MICROSTRUCTURE AND HIGH TEMPERATURE CREEP OF PLATINUM GROUP METAL MODIFIED NICKEL BASE SUPERALLOYS

by

Jason S. Van Sluytman

A dissertation submitted in partial fulfillment
of the requirements for the degree of
Doctor of Philosophy
(Materials Science and Engineering)
in The University of Michigan
2010

Doctoral Committee:

Professor J. Wayne Jones, Co-Chair
Professor Tresa M. Pollock, Co-Chair
Professor Lumin Wang
Assistant Professor Samantha H. Daly

Acknowledgements

First and foremost, I would like to thank my advisor, Tresa Pollock, for her guidance and support throughout this work. I also wish to acknowledge my committee members, Samantha Daly, J. Wayne Jones, and Lumin Wang, for their helpful comments and suggestions.

Additional recognition goes to the team members who were part of this project. This includes Pat Martin and Dallas Hardwick (Air Force Research Laboratory, Dayton, OH), Randolph Helmink and Ann Bolcavage (Rolls-Royce PLC, Indianapolis, IN), Andy Heidloff (University of Iowa, Ames, IA), Brian Gleeson (University of Pittsburgh, PA), and Fan Zhang (CompuTherm LLC, Madison, WI).

My fellow group members and staff of the Pollock-Jones group from 2005 - 2010 deserve additional thanks. I am extremely grateful to Chris Torbet for his help on maintaining laboratory equipment. Additional gratitude goes to my fellow group members, Fang Cao, Dipak Das, Jonathan Madison, Nicholas Saddock, Akane Suzuki, and Christopher Szczepanski, all of whom have provided useful discussions and support. I also wish to acknowledge undergraduate Charles Moceri. His work pertaining to coarsening studies and dislocation density measurements within this thesis was most useful and appreciated. I would also like to acknowledge my office mates over the past years. This includes Clinique Brundidge, Mclean Echlin, Kaitlyn Gallup, and Brian Wang, whose discussions, support, and camaraderie throughout the past 5 years helped

me get through many days, nights, and, of course, weekends.

I wish to additionally recognize the members and staff within the Electron Microscopy Unit at the University of Sydney. This includes Julie Cairney, Alexandre La Fontaine, and Simon Ringer. Their help on conducting atom probe experiments, and making me feel welcome during my stay in Australia, will always be remembered. Additional thanks goes to Carlos Levi (University of California - Santa Barbara), who helped fund this research.

I am grateful for the support that my mom, dad, and brother have shown these past 5 years. Their ability to never judge, nor question, my decision to pursue a higher degree, rather than getting a 'real job,' is what any student would wish from their family.

Finally, special thanks for my soon-to-be wife, Rachel Collino, whom I have come to see as 'the trailblazer.' Months prior to this thesis, her persistence and determination toward her own PhD allowed me to see the path that must be taken to attain this degree. Thanks for lighting the way.

This research was supported under the Versatile Affordable Advanced Turbine Engines (VAATE) program, sponsored by the Air Force Research Laboratory, in collaboration with Rolls-Royce, PLC. Atom probe work was supported through NSF Research Grant DMR-0605700: Dynamics of Layered, Multifunctional Systems with Evolving Structure.

TABLE OF CONTENTS

List of Figures

List of Tables

ABSTRACT

Increasing efficiency in aeropropulsion and energy generation systems drives the development of higher temperature structural materials with good mechanical properties and environmental resistance. Platinum group metal (PGM) additions are known to be beneficial for the oxidation and corrosion resistance of superalloys and Ni rich intermetallics. However, there is limited understanding of how they influence the microstructure and high temperature mechanical properties of γ-γ′ superalloys. The objective of this research is to examine experimental Ni-base compositions that systematically alter PGM and non-PGM elements. The PGMs used for this study are Pt, Ir, and Ru. The non-PGM elements are ones commonly used in conventional Ni-base compositions, such as Re, W, and Ta. Partitioning studies indicates that platinum preferentially partitions to the γ′ phase, resulting in alloys that exhibit positive misfit behavior – quite uncommon for Ni-base superalloys. Iridium influences the partitioning behavior of PGM and non-PGM elements, which could be useful in manipulating alloying chemistry. The unique partitioning behavior of the PGMs results in a wide range of lattice misfit and, therefore, γ′ morphology. Coarsening studies demonstrate that Pt slows γ′ coarsening and helps maintain unusually high volume fractions at temperatures up to 1200 °C. Such high volume fractions at these elevated temperatures could lead to impressive creep properties. High temperature creep tests at 1000 °C demonstrate variations in creep strength between PGM alloys. Alloys with precipitate

boundary strengthening elements boron, carbon, and zirconium, can increase the creep resistance by at least a factor of three. For alloys that directionally coarsen, the formation of dense, interfacial dislocation networks increases creep strength. Dislocation density measurements within positive misfit alloys indicate, in some cases, that a majority of the dislocations are deposited within the precipitate phase rather than the matrix phase – a very unusual feature for high temperature deformation. The calculation of a creep stress exponent establishes that creep is carried out in the power-law regime. A climb velocity is calculated that can be applied not only to the PGM alloys in this investigation, but other Ni-base systems as well.

CHAPTER 1

INTRODUCTION

Over the past four to five decades, aircraft engines as well as land based power generation turbine manufacturers have continuously pushed the envelope for increased performance and efficiency from turbine engines due to the ever increasing demand for power from the commercial sector. In the mid-1940's, engines capable of operating temperatures in the turbine hot section around 650 - 800 °C (1200 - 1470 °F) were produced [1]. Today, due to improved materials and design, temperatures within the turbine section can reach well over 1100 °C (2370 °F) [2]. Figure 1.1 displays a conventional turbine engine serviced within the aerospace industry, highlighting the suite of alloys needed for an engine to function. Beyond the combustion chamber, inlet temperatures approach 1400 °C. The rotating turbine blades in this region are therefore exposed to harsh environments, and, as a consequence, the materials used to fabricate these blades must possess properties that are sufficient to endure the high temperatures and stresses. As seen in Figure 1.1, nickel (Ni)-base alloys are the material of choice. Some of the key performance requirements for Ni-base materials are [3, 4]: (1) resistance to mechanical deformation due to the rotation of the blades or foreign object damage at high temperatures; (2) resistance to high temperature oxidation and corrosion in combustion gases; and (3) thermal stability. This chapter details the factors that can

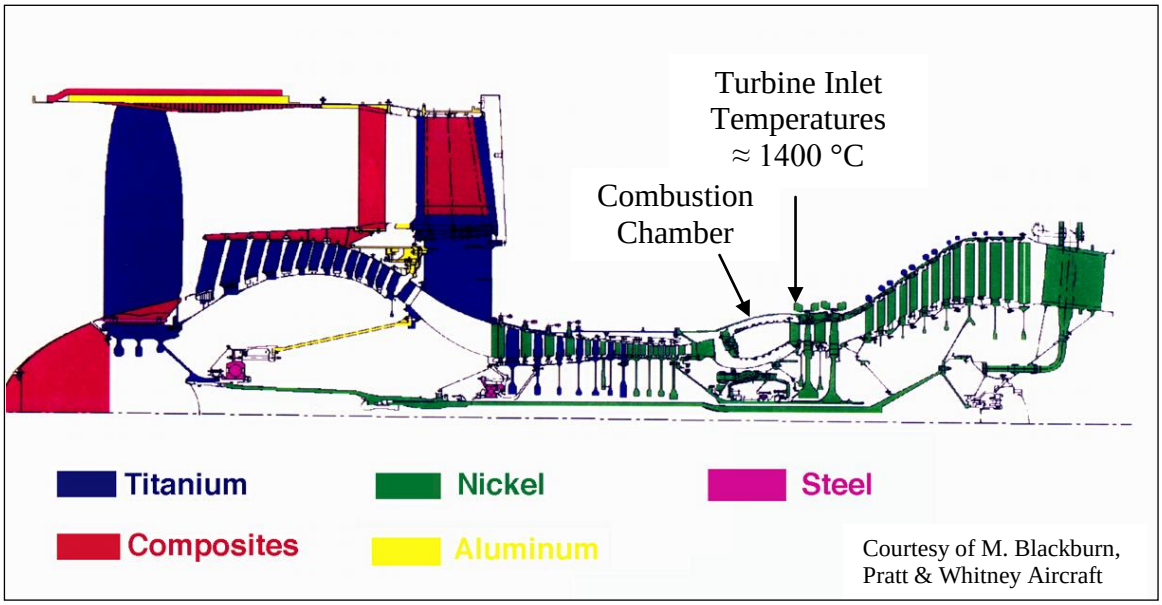

Figure 1.1: Cross section of conventional turbine engine.

influence Ni-base superalloy performance and the current challenges in the design of new alloys for extreme environments.

1.1 Nickel-Base Superalloys

Ni-base superalloys possess an unusual set of features and properties [3-5]; (1) alloying and processing techniques which allow these alloys to operate close to $0.8T_M$ (T_M: melting temperature), (2) resistance to high temperature creep and fatigue, and (3) resistance to high temperature corrosion and oxidation. The following sections provide further background on these properties of nickel-base superalloys.

1.1.1 Ni-Base Superalloys: Microstructure, Chemistry, and Phases

The microstructure of Ni-base systems develops from a precipitation transformation [6]:

$$\gamma^S \rightarrow \gamma + \gamma' \qquad \text{Equation 1.1}$$

where γ^S is a supersaturated solid solution, gamma (γ) is a disordered f.c.c. solid solution, and gamma prime (γ') is a stable or ordered intermetallic precipitate that forms in the γ matrix. In the γ' intermetallic compound, Al atoms are preferentially located on the edges of the f.c.c. unit cell while Ni atoms preferentially occupy the face sites. This two-phase system of γ-γ' forms the structural basis of most commerical Ni-base superalloys today. In the binary systems, the ordered $L1_2$ precipitates have a composition of Ni_3Al, and as indicated in the phase diagram of Figure 1.2 [7], can exist over a relatively wide compositional range, permitting alloying of this phase. The micrograph inset in Figure 1.2 is a SEM image showing the two phase γ-γ' system. The dark contrast cuboidal phase is the Ni_3Al precipitate, embedded within the parent matrix shown with brighter contrast. Furthermore, the micrograph also shows a relatively large volume fraction of γ' within the matrix. Most superalloys usually contain a γ' volume fraction in

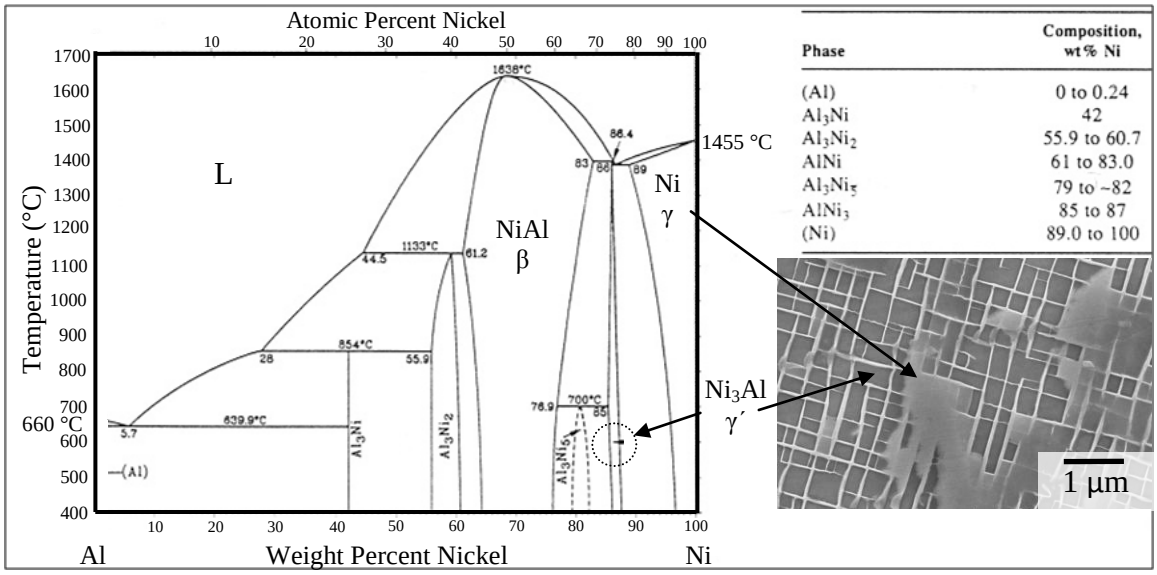

Figure 1.2: Binary Ni-Al Phase Diagram [7]. Inset micrograph depicts γ-γ´ system.

the range 0.6 - 0.7 to help promote mechanical strength [8, 9]. In addition, average precipitate size strongly influences the mechanical properties of the system [4, 5, 10].

1.1.2 Ni-Base Superalloys: Elemental Compositions

As stated in section 1.1.1, one of the primary elemental additions to Ni-base superalloys is Al. Not only does this element promote a stable precipitate phase within the system, but Al is a key element for high temperature oxidation resistance [3, 11-13]. However, at temperatures near 1000 °C, the binary Ni-Al system becomes very ineffective for creep strength. Above $0.6T_M$, γ´ coarsening occurs, changing the overall particle size distribution. Not only are alloying elements used to suppress this coarsening, but are needed for the optimization of other properties such as oxidation, corrosion, and strength. Figure 1.3 shows a variety of elements that have been studied for solid solution additions to the γ and γ´ phases within superalloys [14]. Generally, for solid solution alloying, an atomic radius within ± 15% of nickel (r_{Ni} ≈

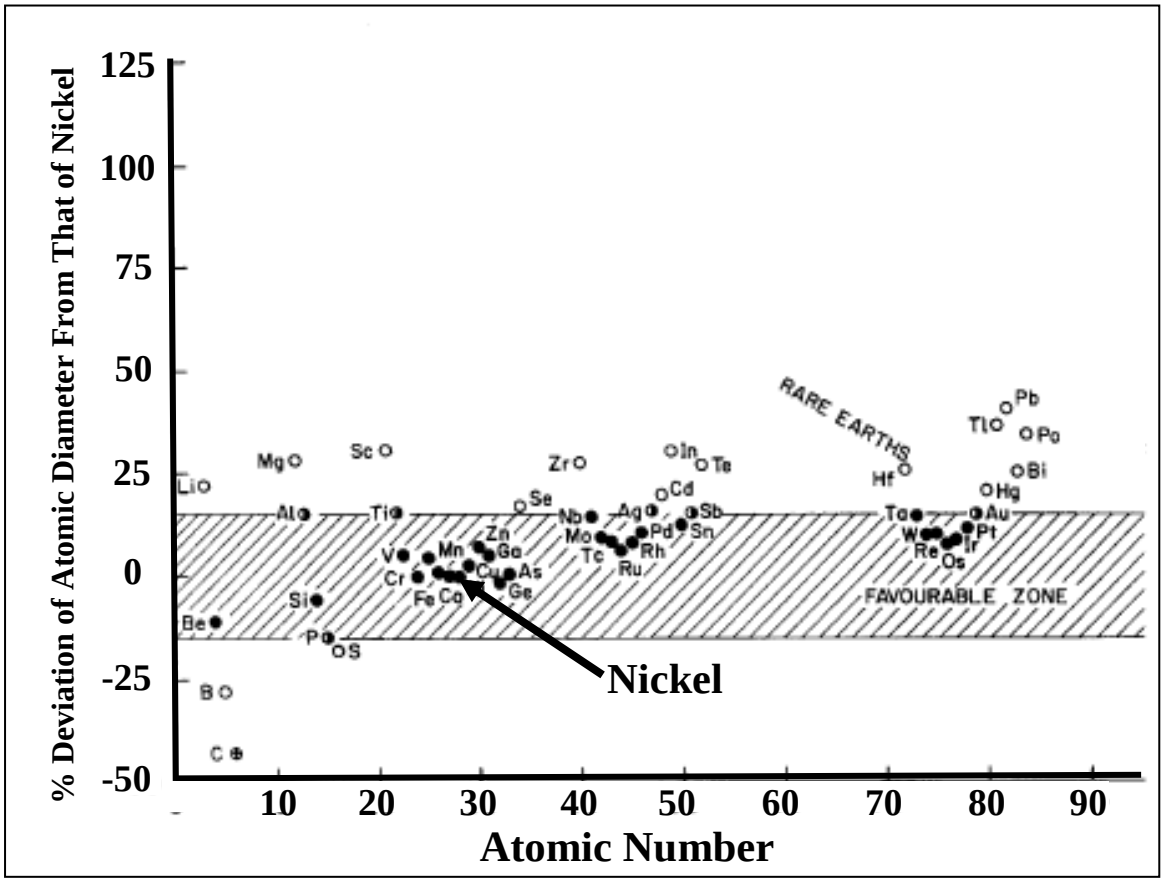

Figure 1.3: Atomic elements used for substitution and/or interstitial replacements within the γ-γ′ system [14].

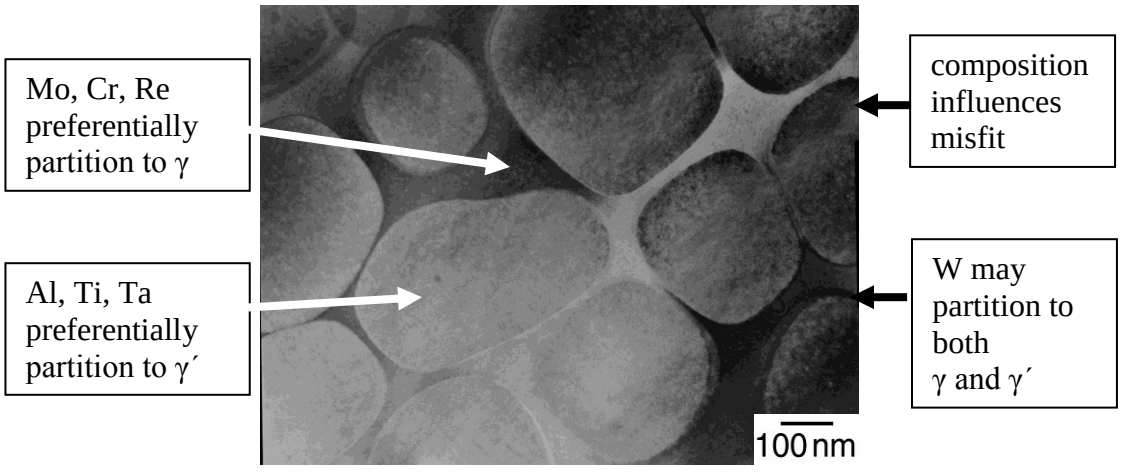

Figure 1.4: Micrograph displaying two phase γ-γ′ system. Each text box highlights atoms which partition either to the matrix or precipitate.

0.125 nm) is required [4, 14]. Many elements that fall within this range provide phase and surface stability to the two phase material at high and low temperatures while simultaneously allowing for strengthening of both phases.

Figure 1.4 highlights elements commonly found in commercial alloys [4, 9, 14]. Elements such as tantalum (Ta), and Al preferentially partition to the intermetallic $L1_2$ phase. Other elements, including chromium (Cr), rhenium (Re), and molybdenum (Mo) preferentially partition to the matrix. Elements such as tungsten (W) can be found in near equal amounts in both phases. Table 1.1 provides typical alloy compositions for a range of 1st, 2nd , and 3rd generation single crystal Ni-base superalloys [15]. A common rule of thumb in differentiating between the first three generations is the level of Re additions, where 1st generation contain no Re, 2nd generation contain approximately 3 wt% Re, and 3rd generation up to 6 wt%.

Table 1.1: Compositional profile of 1st - 3rd generation single crystal Ni-base superalloys [16].

	Alloy	Composition (wt%)								
		Cr	Co	Mo	Re	W	Al	Ti	Ta	Hf
1st Generation	CMSX-3	8	4.6	0.6	--	8	5.6	1	6	0.1
	SRR 99	8	5	--	--	10	5.5	2	3	--
2nd Generation	CMSX-4	6.5	9	0.6	3	6	5.6	1	6.5	0.1
	PWA 1484	5	10	2	3	6	5.6	--	8.7	0.1
3rd Generation	René N6	4.2	12.5	1.4	5.4	6	5.75	--	7.2	0.15
	TMS-75	3	12	2	5	6	6	--	6	0.1

1.1.3 Ni-Base Superalloys: Lattice Misfit / Elastic Strain Energy

As mentioned in section 1.2.1, one important aspect of nickel base superalloys is that the γ and γ' phases share f.c.c-like lattice structures along with similar lattice misfit parameters, so the interface between the phases is coherent. There is a small degree of

misfit, defined as:

$$\delta = 2 \times \frac{a_{\gamma'} - a_{\gamma}}{a_{\gamma'} + a_{\gamma}} \qquad \text{Equation 1.2}$$

where a_{γ} and $a_{\gamma'}$ are the lattice parameters of the matrix and precipitate, respectively. The lattice misfit is important in the design of superalloy compositions [4, 5, 17]. When the two phase system has a high lattice misfit, the interfaces become semi-coherent with interfacial dislocations developing. The degree of misfit between gamma and gamma prime dictates the morphology of gamma prime particles, Figure 1.5. Shapes that are close to spherical occur when misfit is near-zero, whereas shapes that take on cuboidal characteristics occur when misfit values are in the range of 0.002 to 0.005 [6, 18, 19]. Commercial cast superalloys usually contain $\delta < 0$ ($a_{\gamma'} < a_{\gamma}$) [4, 5] with $|\delta|$ approximately 0.002 - 0.003 (cuboidal precipitates).

The lattice misfit also indicates the amount of elastic strain energy that is stored between the precipitate and matrix. Minimizing the elastic strain energy contributes to reducing the total free energy of the alloy system [6]. In Ni-base alloys, a spherical precipitate coherent with the matrix ($\delta \approx 0$) provides the lowest elastic strain energy. The common design of Ni-base alloys, however, requires strong partitioning of elements either to the γ or γ′ phase which, in turn, increases the $a_{\gamma'}$ or a_{γ} lattice parameter, resulting in a lattice misfit deviating away from zero. As lattice misfit increases, so does the elastic strain energy [20]. The minimization of the elastic strain energy in such systems occurs with precipitate particles grown along the least energetic {001} plane [21, 22], changing the morphology from spherical to cuboidal in the process. These cuboidal

particles carry excess strain energy at the precipitate-matrix interface, which is relieved by the deposition of interfacial dislocations during creep. The formation of interfacial dislocations not only lowers the elastic strain energy, but provides effective barriers at the interface for high temperature creep resistance, which is further discussed in Section 1.2. This is one reason why designing commercial Ni-base superalloys purposely tailors nominal compositions that provide a uniform distribution of cuboidal particles.

1.1.4 Ni-Base Superalloys: Coarsening Kinetics

During high temperature exposure, coarsening of γ′ particles occurs to reduce the interfacial surface energy of the system [6, 23, 24]. The growth of larger γ′ particles at the expense of smaller ones may reduce the strengthening imparted by the high density of finely dispersed γ′ particles. Ardell and Nicholson studied the γ′ coarsening behavior in Ni-Al alloys in the temperature range of 625 - 775 °C [25]. It was demonstrated that coarsening of Ni_3Al precipitates can occur at temperatures as low as 645 °C. With the incorporation of refractory elements into superalloy compositions, Giamei and Anton investigated how increases in Re would influence coarsening between 815 - 1065 °C for a single crystal Ni-base superalloy [26]. The study demonstrated that Re helped reduce coarsening up to 982 °C. However, Figure 1.6 depicts an array of particles (a) transitioning to irregularly faceted precipitates (b) after exposure at 1065 °C for 8 h and 16 h, respectively. For superalloys to operate at temperatures exceeding 1000 °C, particle coarsening must be minimized so that particle morphology remains unaltered over time.

1.2 Creep Deformation

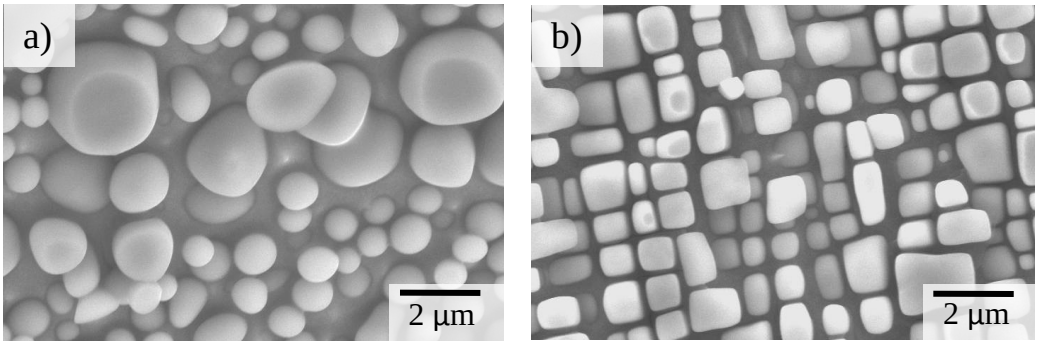

Figure 1.5: The morphological effect due to lattice misfit of Ni-base superalloys. Lattice misfit ranges from (a) near-zero to (b) 0.005.

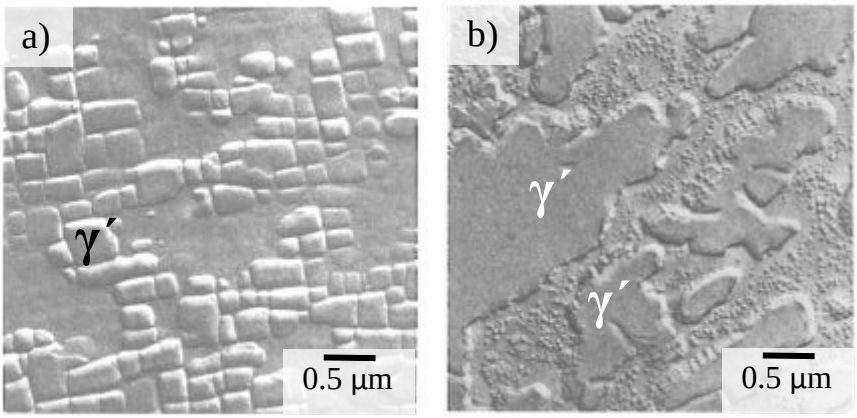

Figure 1.6: Micrographs displaying the change in γ´ morphology due to coarsening at 1065 °C at times of (a) 8 h and (b) 16 h for a Re-containing Ni-base superalloy [26].

Creep is a time-dependent, thermally activated plastic deformation mechanism that occurs at temperatures in excess of $0.4T_M$ [3, 4, 27]. Superalloys must operate at high temperture where creep deformation is a concern. When turbine blades rotate at high temperatures, the Ni-base superalloys experience not only thermal stresses, but also mechanical stresses associated with centrifugal forces. Figure 1.7 displays a creep curve and the associated stages of deformation that can occur at high temperature [3, 4, 9, 27]. The following sections addresses the basic issues of creep within metals and the deformation mechanisms associated with high temperature creep.

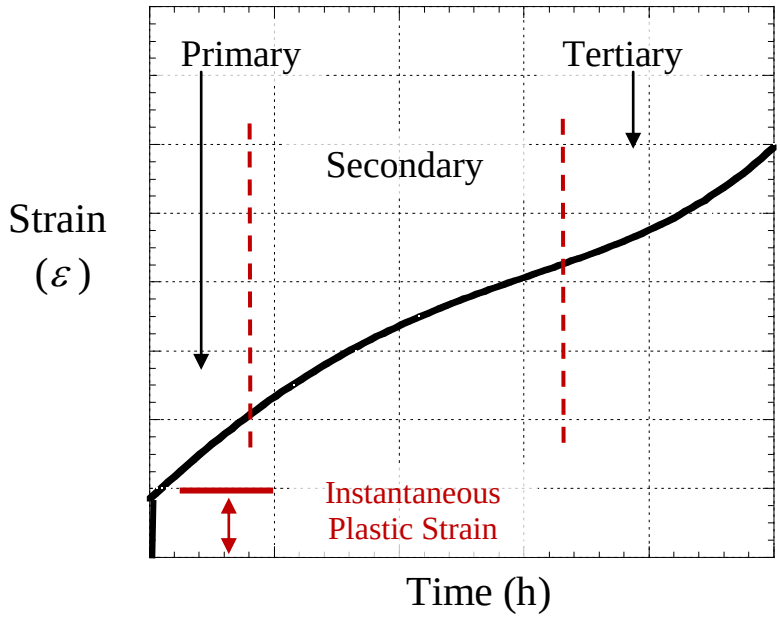

Figure 1.7: Typical creep curve. Various stages of creep are highlighted.

1.2.1 The Creep Process

Upon initial loading, Figure 1.7, there is a near instantaneous response from the material that is completely elastic in nature, followed by a period of time dependent decreasing creep rates, termed primary creep. From primary creep, the material enters the second stage, termed secondary or steady-state creep. Throughout this creep regime, dislocation glide and climb processes occur within both the γ and γ′ phases.

During the primary and steady-state time period, dislocations typically glide within the gamma phase. The slip system is the standard f.c.c. system: $\frac{a}{2}$<110>{111}. Throughout this process, dislocations not only accumulate within the matrix, but are also deposited at the γ-γ′ interfaces. Figure 1.8 displays the structure of a Ni-base superalloy after creep deformation [28]. By measuring the distances between the interfacial dislocations, D_{net}, and knowing the lattice parameter of the deformed material,

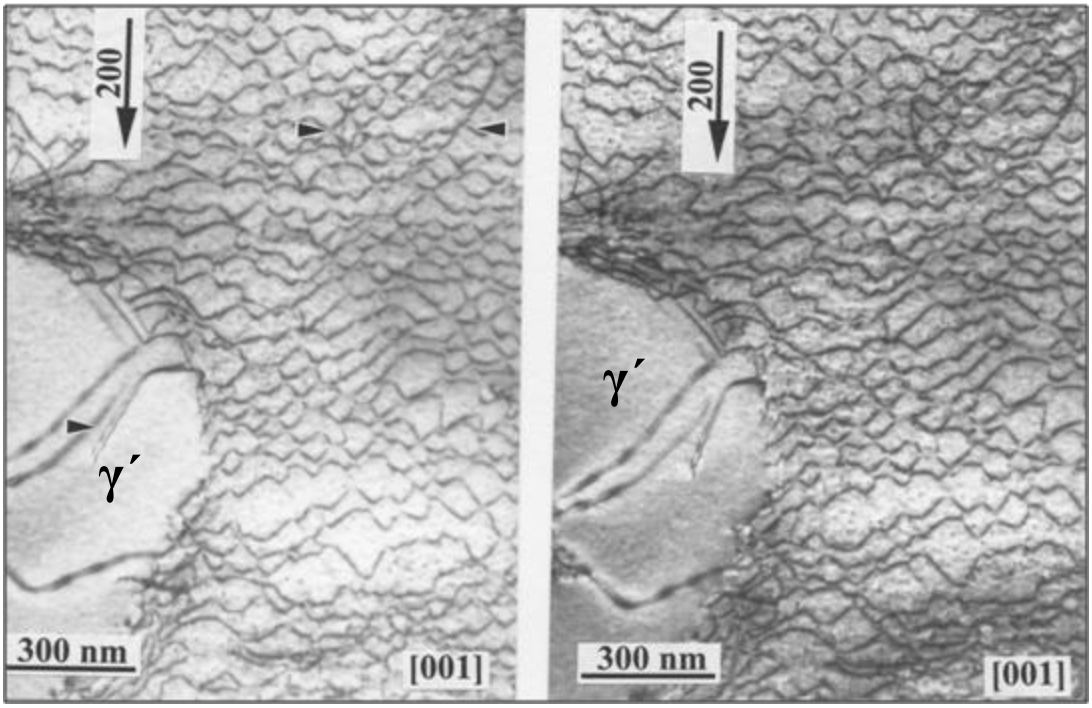

Figure 1.8: Deformed specimen highlighting interfacial dislocations at the γ-γ´ interface [28].

information regarding lattice misfit magnitudes can be attained though Equation 1.3:

$$\delta = \frac{\vec{b}}{D_{Net}} \qquad \text{Equation 1.3}$$

where $\vec{b}$ is the Burgers vector, and δ is the precipitate-matrix misfit of the system.

By differentiating the strain-time curve, a creep-rate can be determined from the creep test. For example, an upper bound limit on creep rates for alloys operating to temperatures close to about 1000 °C (1273K) with applied stresses in the range of 100 MPa (14.5 ksi) are of the magnitude of 10^{-8} s^{-1}. It would take approximately 2,800 h for a creep sample to deform 1% at a creep-rate of 10^{-8} s^{-1} [4]. Commercial blades are meant to provide close to 10,000 h of active service before 1% deformation occurs.

Over time, within the steady-state regime, damage begins to accumulate in the

form of cracks and voids, located preferentially at grain boundaries or in the interdendritic regions of single crystals, accelerating deformation to failure. During this process, the magnitude of the creep-rate accelerates by several orders of magnitude. This deviation marks the onset of the *tertiary* creep stage, where ultimate failure, or fracture occurs.

1.2.2 Creep Deformation: High Temperature Creep

Creep deformation exceeding 900 °C for Ni-base superalloys is referred to as 'high temperature' creep [29]. At intermediate temperatures, 600 - 900 °C, dislocations primarily glide through the γ phase and subsequently shear the γ′ precipitate for continual deformation. Beyond 900 °C, dislocation glide is still a factor, but the elevated temperatures initiate vacancy-assisted diffusion of atoms within the matrix, thereby activating dislocation climb at the matrix-precipitate interface [3, 4, 27, 29]. The interdiffusion coefficients for various elements in Ni at elevated temperature are presented in Figure 1.9 [30]. Self-diffusion data for Ni are provided for comparison. At 1000 °C, Re and W diffusion in Ni is an order of magnitude slower than nickel self-diffusion. If dislocation climb is the rate-limiting mechanism that governs high temperature creep life, then additions of Re and W within the γ matrix must be accounted for when measuring this diffusive process.

High temperature creep mechanisms may also be indirectly characterized by measurement of the creep stress exponent, *n*, within the Arrhenius-type creep-rate equation [4, 27]:

$$\dot{\varepsilon} = A\sigma^{n} \exp(\frac{-Q}{RT}) \qquad \text{Equation 1.4}$$

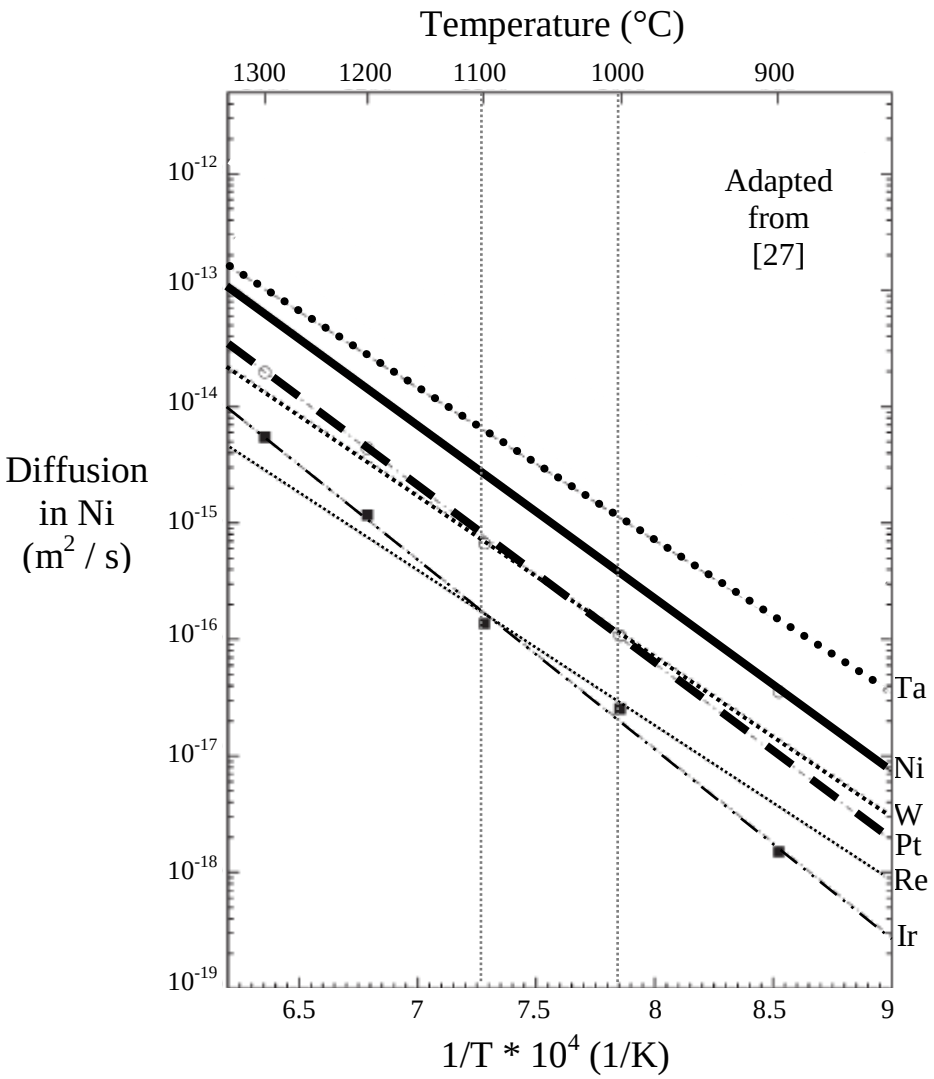

Figure 1.9: Interdiffusion coefficients of various elements within Ni at elevated temperatures [30].

where $\dot{\varepsilon}$, A, σ, Q, R, and T, are the creep rate (s^{-1}), materials constant, applied stress (MPa), activation energy (J/mol), gas constant (J /mol·K), and temperature (K), respectively. For polycrystalline Ni crept in the temperature range of 400 - 1100 °C, n = 5 [31]. Experimental studies have shown, however, that n can range from 6 - 11 for γ-γ′ superalloys containing considerable refractory content (up to 10 – 14 wt%) [29, 32]. These creep stress exponents indicate that high temperature creep operates in the 'power-

law' regime. This implies that deformation proceeds through 'dislocation creep' [3, 4, 27]; the combination of dislocation glide and climb.

The mode of deformation for high temperature creep can also be characterized with use of deformation mechanism maps [33, 34]. Using the example from section 1.2.1, a Ni-base superalloy exposed at 1000 °C ($0.7T_M$) typically experiences a tensile stress approximately 100 MPa. Using a shear modulus, G, of a superalloy varying between 50 - 80 GPa [4, 29], an average value of 65 GPa is used to normalize the tensile load, which is $\frac{\sigma}{G} \cong 1.5 \cdot 10^{-3}$. Figure 1.10 plots deformation maps of (a) pure Ni and (b) a superalloy. The intersection of the red lines indicates the dominant mode of deformation. Both intersection points indicate superalloys operate within the dislocation creep regime. Note that the intersection point within Figure 1.10(a) lies on the boundary between dislocation glide and dislocation creep but resides entirely within the dislocation creep regime for a precipitate strengthened alloy, Figure 1.10(b). This comparison illustrates how solid solution and precipitation strengthening by additions of Re, Ta, and/or W, permit superalloys to operate within the power-law region at high temperatures.

1.2.2 Creep Deformation: Directional Coarsening

During creep at high temperatures (≥ 900 °C) the precipitates in Ni-base alloys typically undergo a directional coarsening process, termed "rafting." [28, 35-44]. This deformation phenomenon occurs within the secondary stage although studies have indicated that rafting may also initiate in the primary stage [43, 45]. Figure 1.11 displays the four possible modes of directional coarsening when either a compressive or tensile stress is applied to the material [45]. The arrows within each picture indicate the direction of applied stress. Directional coarsening that occurs with resultant precipitates

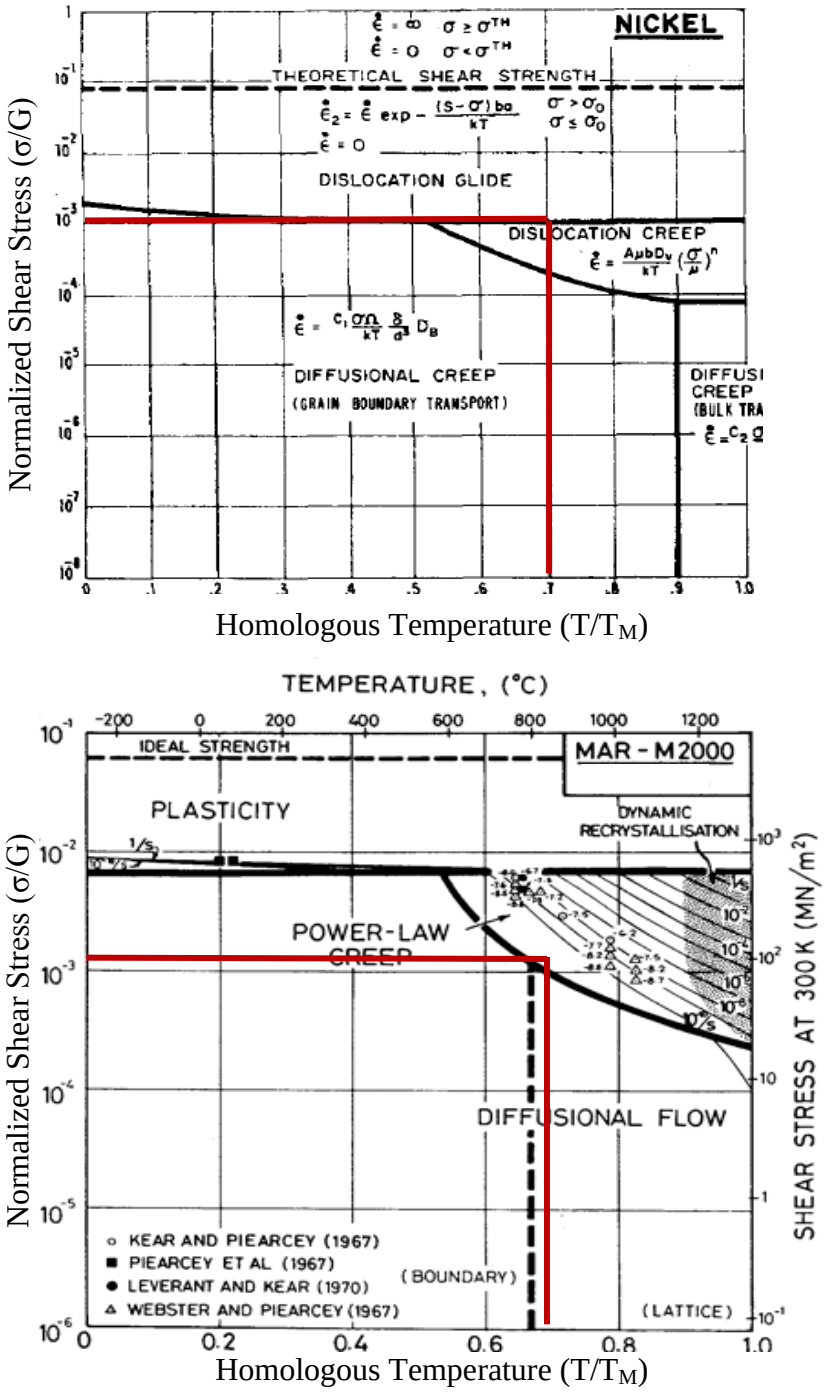

Figure 1.10: Deformation maps of (a) pure Ni [33] and (b) a superalloy [34]. The intersection of the red lines indicates general location for high temperature creep of superalloys.

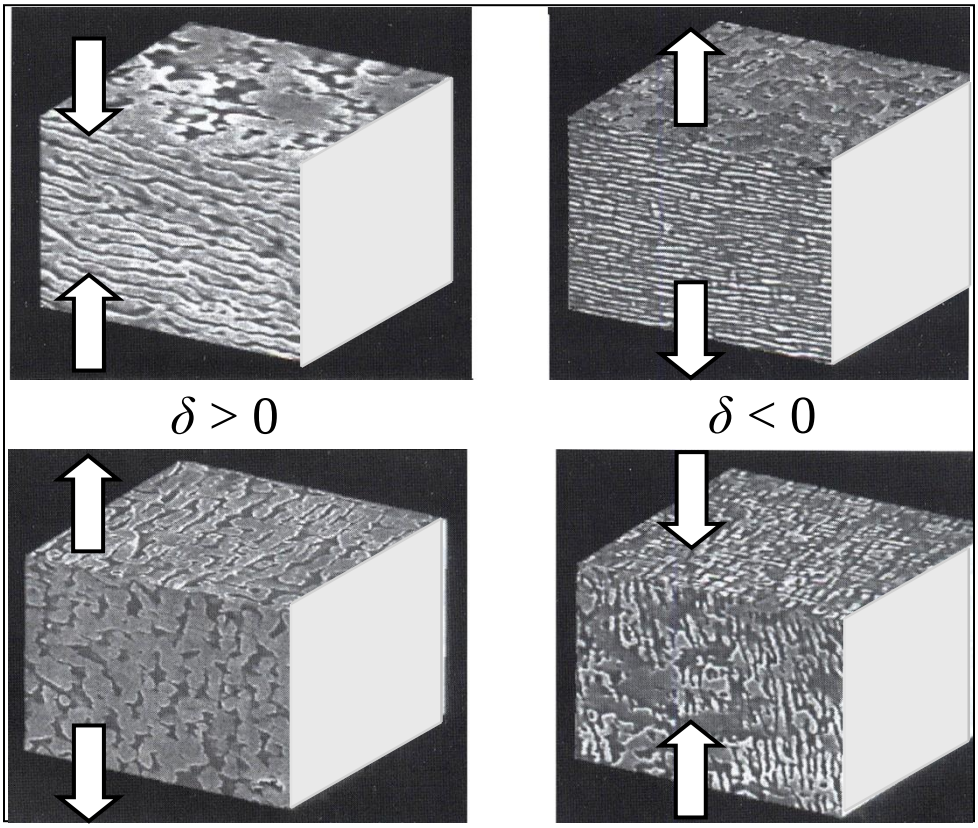

Figure 1.11: Rafting due to misfit and direction of applied stress [45].

perpendicular to the applied stress axis under tension indicates negative misfit, while under compression implies positive misfit. Similarly, directional coarsening parallel to the applied stress axis during a tensile test indicates the material possesses positive misfit or negative misfit if the test occurs under compression. In contrast, alloys that display non-directional coarsening indicate near-zero misfit behavior.

Due to the fact that the most creep resistant alloys contain rhenium, which strongly partitions to the matrix [26, 46], commercial superalloys often possess negative misfit. Since these materials experience tension during service, directional coarsening of γ′ occurs transverse to the applied stress axis.

1.2.3 Creep Deformation: Dislocations

During high temperature creep in superalloys, the lattice misfit may dictate how dislocations are distributed between the γ and γ′ phases. Precipitates that display spherical γ′ morphology, Figure 1.5(a), correspond to near-zero misfit. Alloys with $\delta \approx 0$ have dislocations dispersed throughout the matrix, Figure 1.12(a), with no development of interfacial networks [4, 28]. Precipitates displaying cuboidal morphology ($|\delta| \sim 0.2$ - 0.3 %) will directionally coarsen at temperatures near 1000 °C. Based on the applied uniaxial stress and whether the alloy exhibits positive or negative misfit behavior, dislocation glide becomes restricted to either horizontal or vertical matrix channels relative to the rafting of the precipitates. Since commercial superalloys generally exhibit negative misfit behavior, once rafting has occurred, dislocations accumulate within horizontal matrix channels [37, 44], which is believed to benefit creep life [28, 37, 47]. Alloys which exhibit positive misfit rafting behavior, and are crept in tension, display a greater accumulation of dislocations within the precipitates, Figure 1.12(b), instead of the matrix [4, 28]. It has been suggested that rafts formed parallel to the stress axis might enhance creep and fatigue properties [48]. However, few positive misfit Ni-base superalloys have been studied to date [18, 44, 48].

A lattice misfit that promotes rafting will also drive the formation of interfacial networks. Network formation relieves misfit strain existing between matrix and precipitate [4, 22, 29, 49]. Interfacial networks may assume a variety of configurations as shown in Figure 1.13 [29]. A combination of creep resistant precipitates and dense interfacial networks are associated with good creep properties [4, 28, 29, 50, 51]. This is because excess gliding dislocations (dislocations beyond those which deposit at

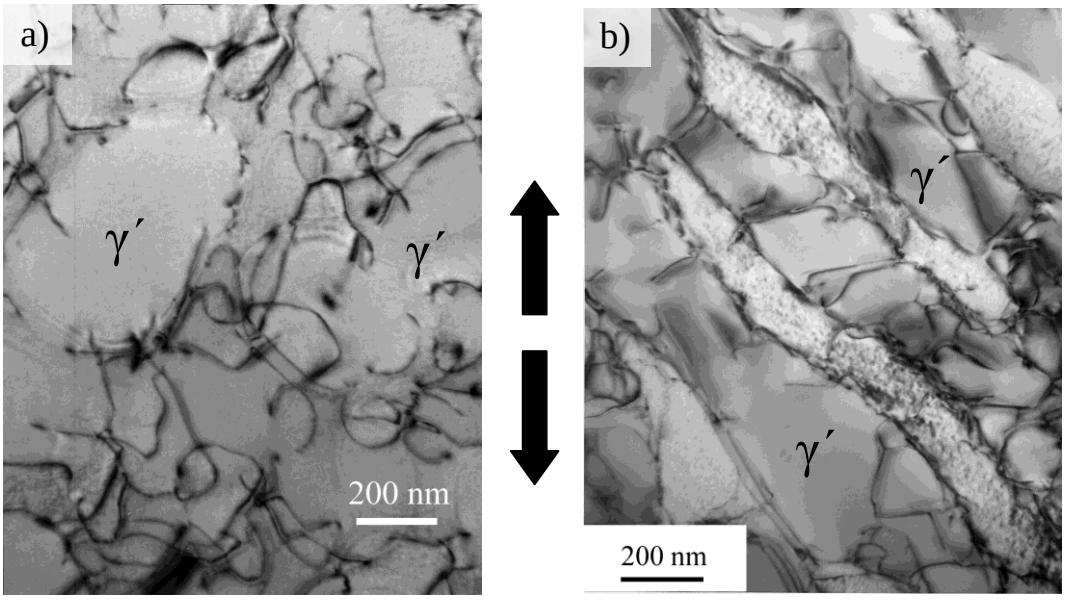

Figure 1.12: Deformed specimen highlighting dislocations for $\delta \approx 0$ (a) and $\delta > 0$ (b) [52]. Arrows indicate applied stress direction.

the γ/γ´ interface to relieve misfit strain) are now inhibited in their climb along the γ´ precipitate interface and in their ability to form pairs of dislocations that can shear the precipitate. It has been argued that decreasing the interfacial network spacings, D_{net} from Equation 1.3, increases the difficulty an excess gliding dislocation has to climb around the precipitate, which should enhance creep strength. Studies conducted on negative δ superalloys where creep strength was a function of network spacing show that this is not necessarily true over a broad range of composition [28]. Evidently, additional factors must be considered to accurately describe high temperature creep within these superalloy materials.

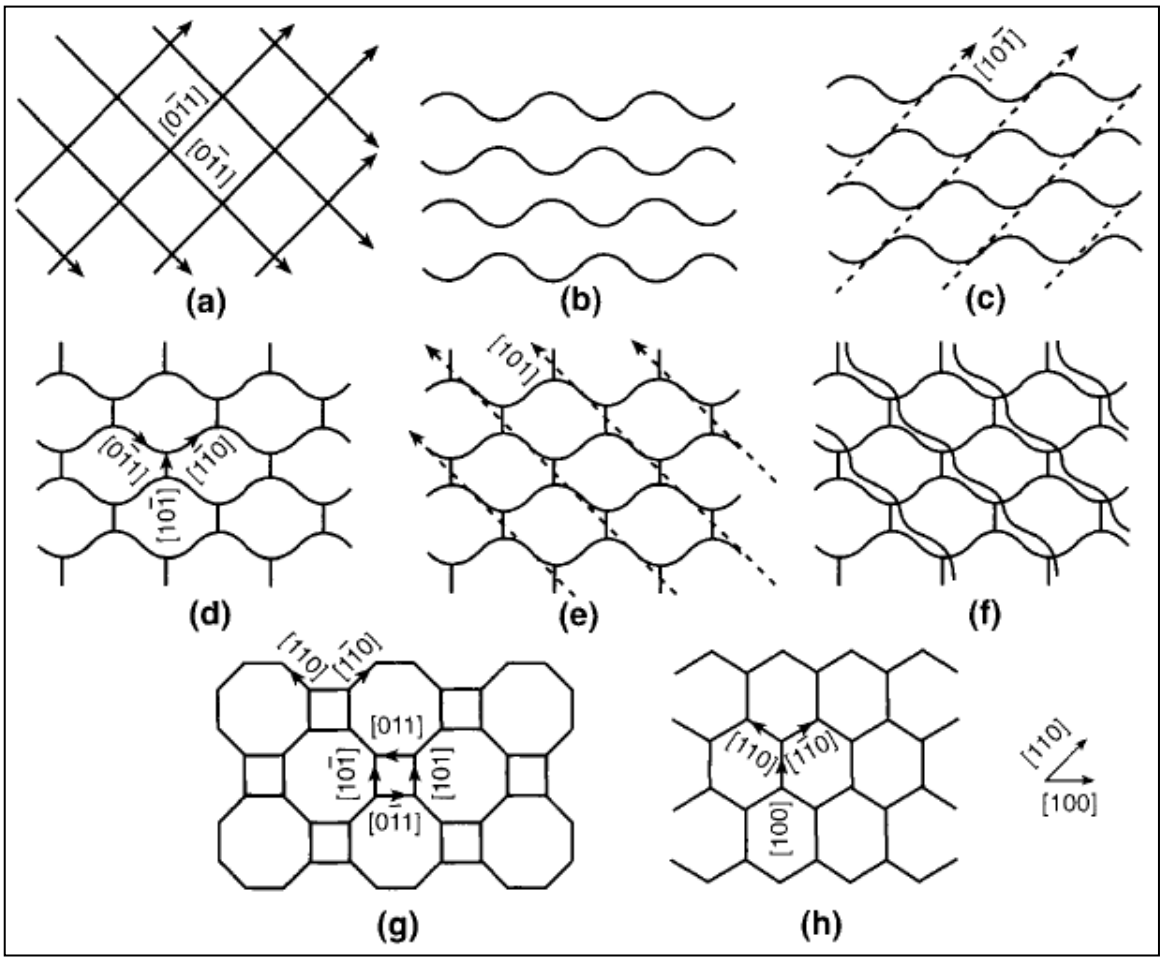

Figure 1.13: Various types of networks that may develop at the γ/γ′ interface [29].

1.3 Current Challenges for Ni-Base Superalloy Design

Figure 1.14 provides a brief summary of alloys developed over the past few decades along with improvements in their temperature capability [4]. As shown in the graph, the trend of superalloy development has gone from wrought to conventionally cast as temperatures increased. Over time, research was directed at controlling grain structure in order to improve high temperature mechanicial properties [4, 53]. The next stage involved directional solidification, where grain boundaries were aligned

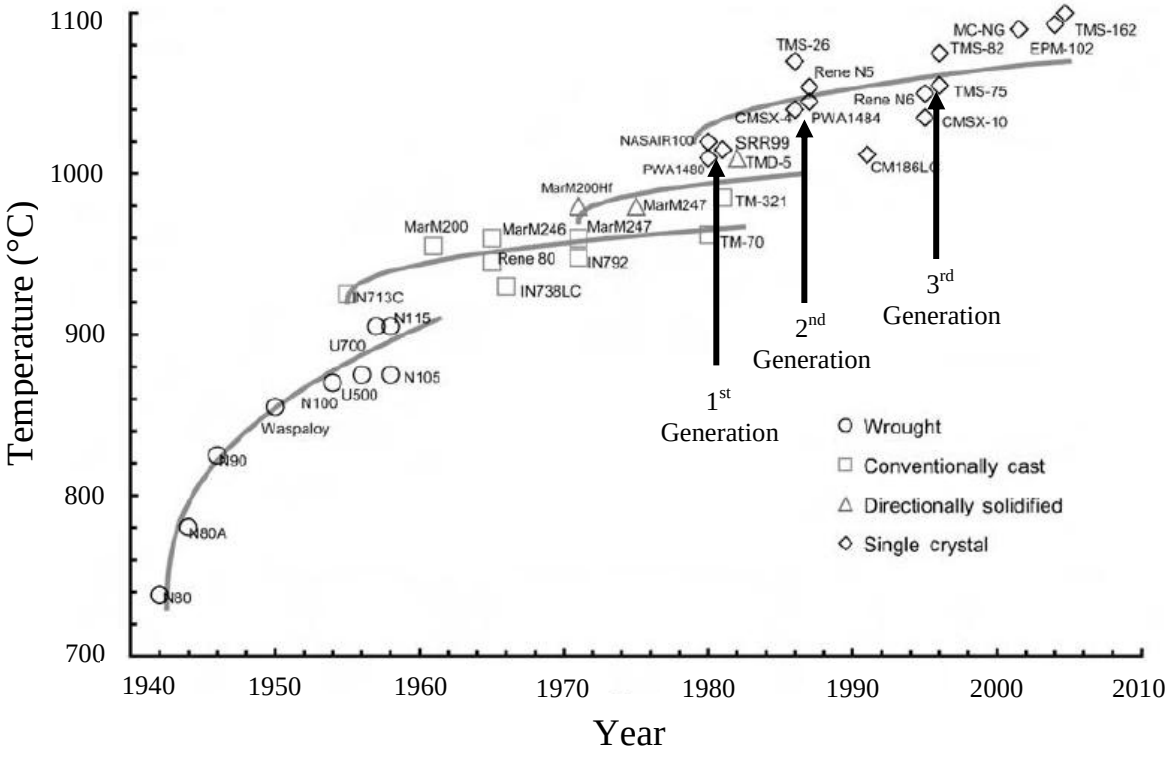

Figure 1.14: Historical development of superalloys [4]. Arrows highlight regions for development of X-generation single crystals.

perpendicular to the applied stress axis in order to remove weak grain boundary sites where initiation defects (cracks, porosity) can occur [5, 54]. Then, around the early 1980's, processes to completely remove grain boundaries were developed and single crystals introduced. Arrows within Figure 1.13 indicate the generations of single crystals listed in Table 1.1. Its apparent that each new generation results in incremental increases in high temperature capability. The following sections highlight how modifications in composition for enhancing creep strength brought about new capabilities.

1.3.1 Alloying Challenges: Topologically Close Packed (TCP) Phases

TCP phases, Figure 1.15(a), are detrimental phases which form during high temperature creep or aging [19, 35, 55-59]. These deleterious phases are associated with

the continual increases in refractory content (Re, Cr, Mo). TCP phases preferentially form within the matrix, and are primarily composed of the refractory additions, which deplete the γ phase of solid solution strengthening elements. Their morphology, as depicted in Figure 1.15(b), is usually plate-like or needle-like with incoherent boundaries within the γ-γ′ system. Table 1.2 lists the more common TCP phases observed within Ni-base superalloys, along with their crystal symmetry and morphology [58]. These phases serve as initiation sites for damage such as cracks, voids, or dislocations and should be avoided.

1.3.2 Alloying Challenges: Oxidation Resistance

The increase in Re from 2nd to 3rd generation single crystals came at the cost of reduced Cr levels to avoid formation of TCP phases. This alloying trend has resulted in poor high temperature superalloy oxidation resistance [60-62]. Ideally, a protective layer of Al_2O_3 or Cr_2O_3 would form on a superalloy surface to protect against further oxidation, Figure 1.16(a). However, reduced Cr levels promote formation of transient mixed oxides, Figure 1.16(b), prior to the formation of a protective alumina (or chromia) scale [4, 11]. Through continual high temperature cyclic oxidation, these oxides tend to spall, exposing the subsurface to further oxidative attack.

1.3.3 Alloying Challenges: Precipitation

Refractory additions, particularly Ta, have increased gamma prime solvus (γ'_{Solvus}) temperatures closer to the solidus temperatures (T_S), constraining heat treatment windows (T_S - γ'_{Solvus}) and making full solutioning difficult. A superalloy that does not attain a fully solutioned condition prior to precipitation of γ′ may contain eutectic γ/γ′ pools, inhomogeneous segregation of elements, or large, insoluble γ′ [4, 5, 60]. These

Table 1.2: Common TCP phases precipitated from refractory-containing superalloys [58].

TCP Phase	Space Group	Structure	Morphology
σ	$P4_2$ / mnm	Tetragonal	Thin sheets
P	Pa	Orthorhombic	Lathes / rafts / needles
μ	R-3m	Rhombohedral	Needles embedded in σ-phase

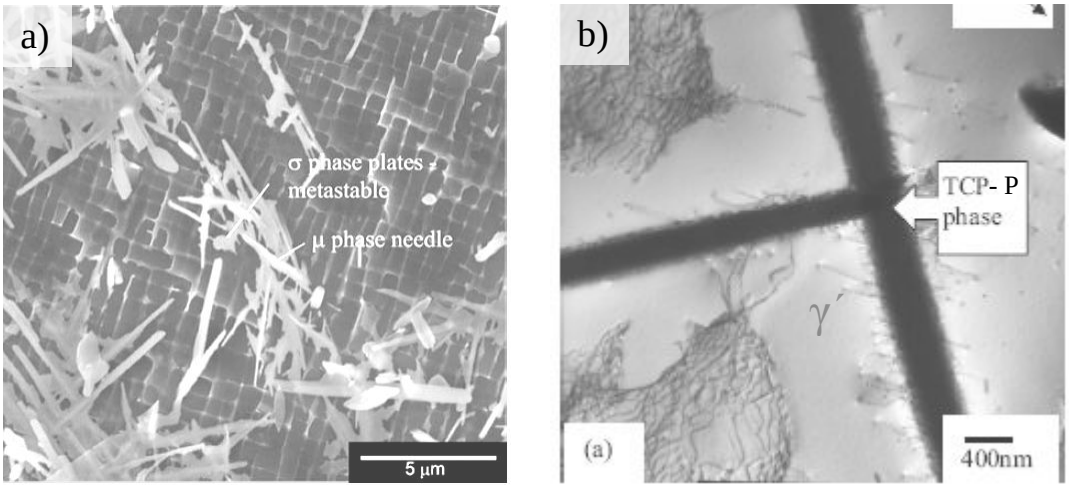

Figure 1.15: Micrographs depicting TCP formation within a superalloy (a) [4]. TCPs can also serve as defect sites (b) [35].

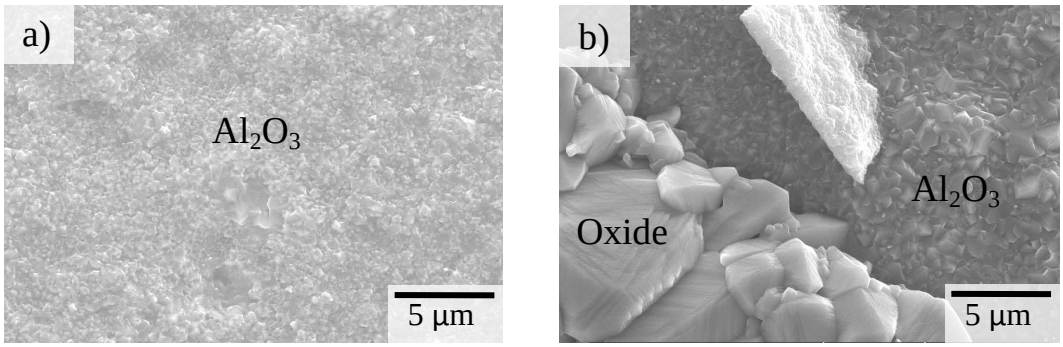

Figure 1.16: Superalloys containing 5 at% Cr (a) and 2.5 Cr (b).

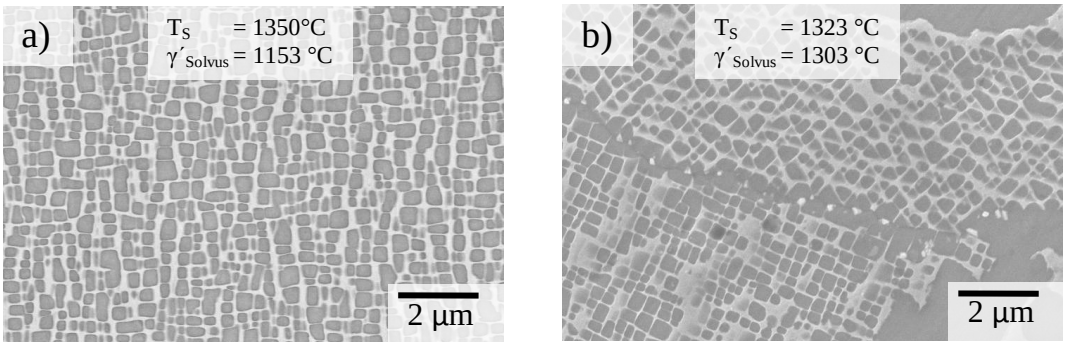

HT: 1250 °C (6 h) → 1050 °C (4 h) HT: 1315 °C (6 h) → 1050 °C (4 h)

Figure 1.17: Alloys without (a) and with (b) Ta and resulting heat treatments (HT).

features can serve as defect sites for fatigue crack initiation similar to TCP phase formation, and degrade creep and fatigue performance. Figure 1.17 depicts the microstructures of two alloys whose compositions are identical, except that 1.17(b) contains 2 at% Ta, which increases the γ'_{Solvus}. Note the differences in heat treatment procedures due to the Ta addition.

1.3.4 Alloying Challenges: Platinum Group Metals

The platinum group metals have been integrated selectively into superalloy compositions that have been studied since the early 1980s [63, 64] and continue to be investigated in recent alloy design studies [4, 30, 56, 65-67]. The PGMs have favorable solubility in Ni, Figure 1.3, and so controlling coherency is still possible. However, the cost and density associated with PGMs is an important consideration and so the payoff for PGM additions must be high to motivate their use.

Ruthenium (Ru), currently the least expensive of the PGMs, suppresses precipitation of TCP phases formed through high temperature creep or aging [19, 35, 55-57]. Platinum (Pt) reduces environmental degradation caused by high temperature corrosion and oxidation [55, 65, 68, 69]. Ir reduces lattice misfit and increases solidus

temperatures [65, 67]. To date, most studies have focused only on the addition of individual PGMs but the synergistic effects of their additions are not well understood.

Analysis of the high temperature creep properties of PGM-modified Ni-base superalloys has focused mostly on ruthenium additions. Ru-modified Ni-base superalloys result in no discernable differences in: *i)* preferential partitioning of the strengthening elements (Re, W, Ta) from their respective phases *ii)* lattice mismatch between γ and γ', and *iii)* γ' volume fractions [28, 35, 57, 70, 71]. High temperature creep tests on Ir-modified Ni-base superalloys have been conducted but are limited [72]. It has been demonstrated that Ir substitution for Ru at T > 900 °C degrades creep performance, although it was not ascertained whether Ir reduces partitioning of other elements or reduces volume fraction of precipitates. Limited high temperature creep experiments have also been conducted on a Pt-modified Ni-base superalloy [73]. The alloy studied contained a good combination of high temperature intrinsic oxidation resistance and creep strength, but whether or not Pt affected volume fraction, lattice misfit, or influenced partitioning of non-PGM elements, was not investigated. These aspects of PGM additions to superalloys are investigated in detail in this thesis.

1.3.5 Alloying Challenges: Thermal Barrier Coatings and Bond Coats

The advent of superalloy single crystals has led to large performance benefits. Further benefits have been gained with the introduction of thermal barrier coatings (TBCs). TBCs are used to sustain a thermal gradient between the hot combustion gases and the superalloy surface [74-76]. To reduce oxidative attack of the superalloy surface, an additional material is layered between the TBC and superalloy substrate, and is termed the bond coat [4, 11, 17, 62]. Bond coats also improve the adhesion between the thermal

barrier coating and the alloy substrate so that spalling, cracking, or delamination is reduced. Bond coats should be mechanically resistant to deformation and must limit diffusion of any elements from the substrate surface into the coating and vice versa. Figure 1.18 depicts a substrate layered with a thermal bond coat and thermal barrier coating. The adherent, thermally grown oxide (TGO) is the oxide layer that is produced due to high temperature oxidation. Note also the intermediate diffustion layer between bond coat and substrate, which must be minimized in order to achieve optimal properties for the entire system.

Bond coats have been the subject of many recent investigations in the metallurgical field due to their dual roles of providing environmental resistance and mechanical integrity [11, 62, 77, 78]. Figure 1.19 depicts various bond coat materials intended for high temperature oxidation and/or corrosion resistance [79]. Among the classes of bond coats shown, the Pt-aluminides possess qualities that are most beneficial not only to oxidation resistance but hot corrosion as well [69, 80-82]. Overall, just as the Pt-aluminides and bond coats serve multiple roles in superalloy development, it should not be unrealistic for the superalloys themselves to possess intrinsic qualities other than mechnical resistance.

1.4 Research Motivations and Objectives

High temperature creep for superalloys has been extensively studied, but the mechanisms that govern the creep performance for PGM-modified alloys have been investigated in detail for only ruthenium. Ru additions have improved high temperature

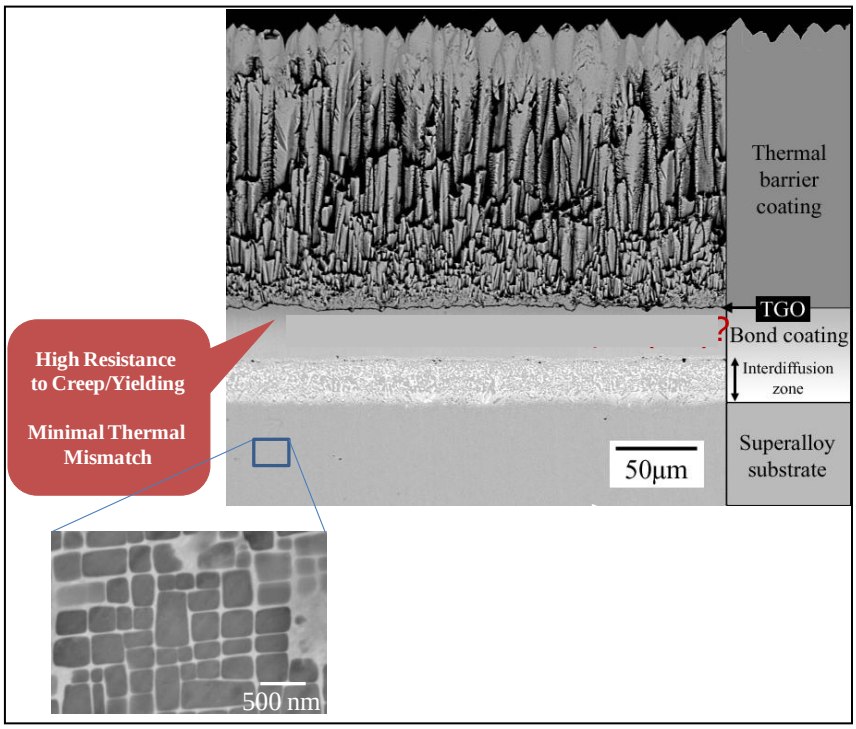

Figure 1.18: Cross-section of turbine blade layered with thermal bond coat and thermal barrier coating [78]. Inset micrograph depicts γ-γ′ microstructure.

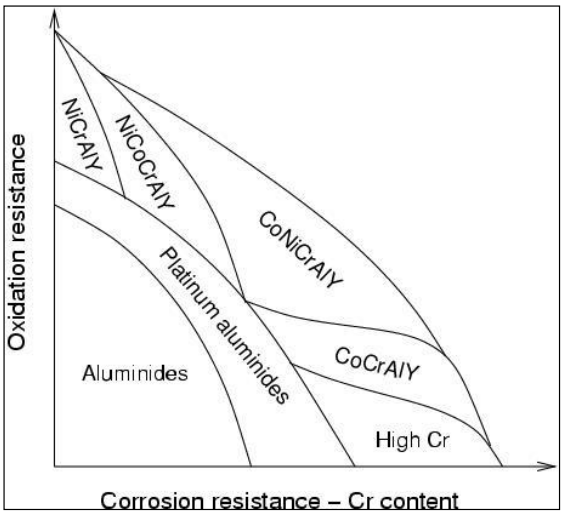

Figure 1.19: Various classes of bond coats and coatings for either oxidation or corrosion resistance [79].

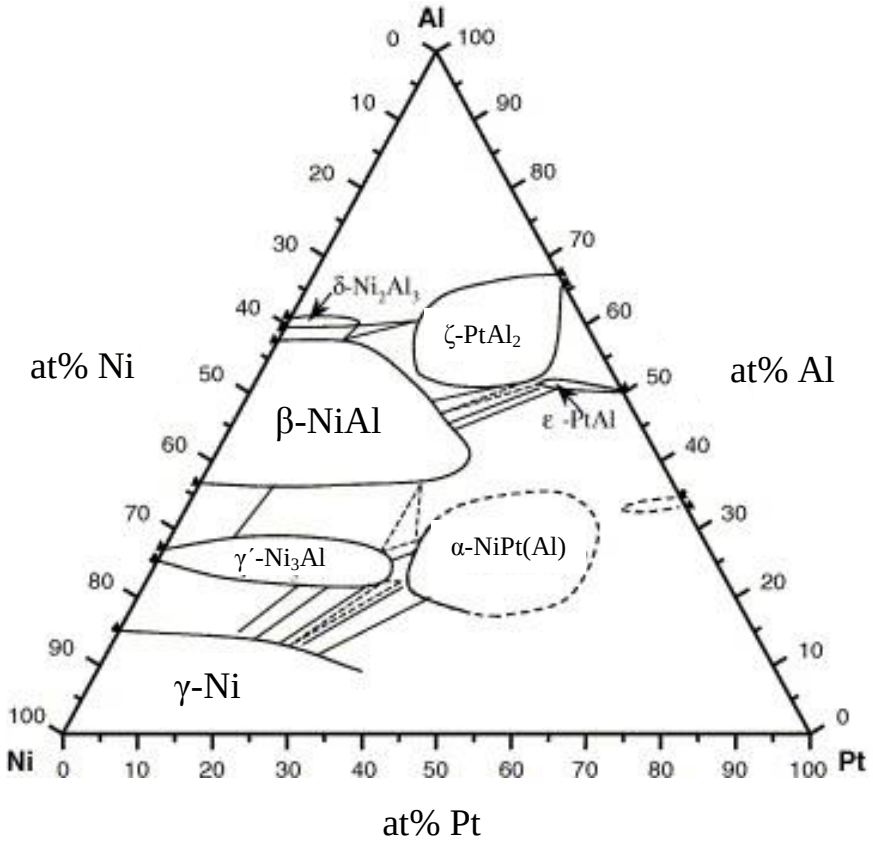

Figure 1.20: Ternary Ni-Al-Pt phase equilibrium at 1150 °C [68].

creep performance by reducing the fraction of harmful TCP phases. The PGMs Pt and Ir may provide additional substantial improvements in high temperature capabilities. This section highlights the motivation and objectives for this thesis.

1.4.1 Research Motivation

The ternary Ni-Al-Pt phase diagram, Figure 1.20, indicates solubility of platinum in Ni-Al at 1150 °C and its equilibrium phases [68]. The phase diagram provides the framework for designing a Pt-containing $\gamma + \gamma'$ alloy system. High temperature cyclic oxidation tests at 1150 °C on $\gamma + \gamma'$ PGM alloys have demonstrated impressive Al_2O_3

scale adhesion with no indication of spallation or transient oxides after 500 one-hour cycles [83]. As shown in Figure 1.18, it would be ideal for a bond coat to contain a similar nominal composition to the substrate. This may help minimize thermal expansion mismatch with the superalloy substrate, slow the growth of the thermally grown Al_2O_3, and improve interfacial adhesion between bond coat and substrate during thermal cycling. Another possibility would be for the superalloy to possess intrinsic oxidation resistance in the event that a bond coat fails; this would once again require the thermally grown oxide to evolve from a γ-γ′ microstructure.

1.4.2 Research Objective

PGM alloys containing γ-γ′ phases possess desirable oxidation properties. The objective of this investigation is to study the influence of PGM additions on the microstructure and high temperature mechanical strength of Ni-base superalloys containing systematic variations of Pt, Ir, and Ru. This study explores a wide range of nominal compositions that vary PGM and non-PGM additions. The variation in compositions allows comparisons on the PGMs influence of γ′ volume fractions, precipitate morphology, and lattice misfit. Determining whether PGM additions effect homogenization behavior is also of importance and presented. It is also useful to evaluate the elemental partitioning behavior of PGM alloys with and without refractory additions. Analyzing whether the PGMs significantly impact coarsening kinetics at temperatures of 1050 - 1200 °C is also investigated. The differences in observed creep strengths are reviewed based on grain boundary damage, directional coarsening behavior, diffusion of the PGMs in the Ni-matrix, and dislocation density distributions throughout the matrix and precipitate phases. It is shown that PGM additions may allow superalloys

to have considerable creep resistance at temperatures surpassing 1100 °C, and demonstrates the impressive creep strength provided by an uncommon class of superalloys – those which exhibit positive misfit behavior.

CHAPTER 2

EXPERIMENTAL PROCEDURES

Assessing the high temperature mechanical properties of PGM-modified Ni-base superalloys requires a systematic examination of PGM additions as well as the non-PGM elements. The quantity of a particular element and its tendency to partition to either the γ or γ′ phases has a strong influence on microstructure and properties. Rather than integrating PGM additions within Ni-base commercial compositions that have been fully studied and reported, the potential benefits of PGM additions are examined in detail within Ni-base compositions containing a wide range of minor, and major, alloying elements. This chapter details how this is accomplished. In addition, specimen preparation, mechanical testing, and the various electron microanalysis techniques, are presented.

2.1 Alloy Design Approach

A total of 55 alloys were fabricated for this study. To explore a broad compositional space in an alloying regime where thermodynamic databases do not yet exist, a design of experiments (DOE) approach was taken [84]. Each DOE matrix phase consisted of nominal compositions that systematically varied key elements while other elements remained fixed.

Each DOE table with alloy compositions is provided in at% and wt% for comparison. In this investigation, at% is used for discussion unless stated. Tables 2.1, 2.3, 2.5, and 2.7, list the range of compositions used within each matrix and the purpose of each alloying addition. Compositions are given in at% and wt%, with the final column summarizing the motivation for each elemental addition. DOE Phase I, Table 2.2, fixed Al and Hf levels, while systematically varying the PGMs Pt and Ir, as well as Cr, Re, and Ta. In DOE Phase II - high Al, Table 2.4, alloys with constant levels of Al, Cr, Re, Ta, and Hf with varying levels of Pt, Ir, Ru, and W, were investigated. An additional set of alloys, Table 2.6, was later developed, referred to as DOE Phase II - low Al, in which the PGM Pt, as well as Re, Ta, and Hf were constant. Aluminum levels remained fixed except that the quantity decreased from 15 at% present in Phase I and II - high Al matrices, to 13 at% in Phase II - low Al. Variations of Ir, Cr, Ru, and W were incorporated as well. Alloys E13 - E16 were similar in nominal composition to alloy E8, except Cr levels increased from 5 → 7.5 at% for all four alloys and either there was a 1 at% increase in Re (alloy E13) or additions of Co, Mo, or Ti. For the final phase, DOE Phase III, Table 2.7, Pt is held constant and becomes the only PGM used in the PX-

Table 2.1: DOE Phase I range of compositions in at% and wt%. The application for each element is provided in the final column.

Elements	Range of Composition (at%)	Range of Composition (wt%)	Purpose
Al	15	6.3 - 6.9	$L1_2$; Oxidation
Pt	0 - 5	7.6 - 16.1	$L1_2$; Oxidation
Ir	0 - 2.5	7.5 - 8.4	Lattice Misfit
Cr	2.5 - 5	2 - 4.6	Oxidation; Corrosion
Re	0 - 1	0 - 3.1	Matrix Strengthener
Ta	0 - 2	0 - 6.1	$L1_2$ Strengthener
Hf	0.1	0.3	Oxidation

Table 2.2: DOE Phase I compositions in at% (left column) and wt% (right). Constant levels for specified elements are listed above each column.

·15Al·0.1Hf·

Alloy	Element Composition				
	Pt	Ir	Cr	Re	Ta
D1	0	2.5	2.5	0	2
D2	0	2.5	2.5	1	0
D3	0	2.5	5	0	0
D4	0	2.5	5	1	2
D5	2.5	0	2.5	0	2
D6	2.5	0	2.5	1	0
D7	2.5	0	5	0	0
D8	2.5	0	5	1	2
D9	2.5	2.5	2.5	0	0
D10	2.5	2.5	2.5	1	2
D11	2.5	2.5	5	0	0
D12	2.5	2.5	5	0	2
D13	2.5	2.5	5	1	0
D14	5	0	2.5	0	0
D15	5	0	2.5	1	2
D16	5	0	5	0	0
D17	5	0	5	0	2
D18	5	0	5	1	0

·6.7Al·0.3Hf·

Alloy	Element Composition				
	Pt	Ir	Cr	Re	Ta
D1	0	8.1	2.2	0	6.1
D2	0	8.2	2.2	3.2	0
D3	0	8.4	4.6	0	0
D4	0	7.9	4.3	3.1	6
D5	8.2	0	2.2	0	6.1
D6	8.3	0	2.2	3.2	0
D7	8.5	0	2.5	0	0
D8	8	0	4.3	3.1	5.9
D9	8	7.9	2.1	0	0
D10	7.6	7.5	2	2.9	5.6
D11	8.1	7.9	4.3	0	0
D12	7.8	7.6	4.1	0	5.8
D13	7.9	7.8	4.2	3	0
D14	16.1	0	2.1	0	0
D15	15.1	0	2	2.9	5.6
D16	16.1	0	4.3	0	0
D17	15.5	0	4.1	0	5.7
D18	15.8	0	4.2	3	0

Table 2.3: DOE Phase II - high Al range of compositions in at% and wt%. The application for each element is provided in the final column.

Elements	Range of Composition (at%)	Range of Composition (wt%)	Purpose
Al	15	6 - 6.5	$L1_2$; Oxidation
Pt	2.5 - 5	7.3 - 14.8	$L1_2$; Oxidation
Ir	0 - 2.5	0 - 7.6	Lattice Misfit
Cr	5	3.8 - 4.2	Oxidation; Corrosion
Re	1	2.8 - 3.2	Matrix Strengthener
Ta	2	5.3 - 5.8	$L1_2$ Strengthener
Ru	*1 - 2*	*1.6 - 3.1*	*Matrix Strengthener*
W	*1 - 2*	*2.8 - 5.8*	*Matrix Strengthener*
Hf	0.1	0.3	Oxidation

Table 2.4: DOE Phase II - high Al range of compositions in at% (left column) and wt% (right). Constant levels for specified elements are listed above each column.

·15Al·5Cr·1Re·2Ta·0.1Hf·

Alloy	Element Composition			
	Pt	Ir	Ru	W
D19	2.5	0	1	1
D20	2.5	0	1	2
D21	2.5	0	2	1
D22	2.5	0	2	2
D23	2.5	2.5	1	1
D24	2.5	2.5	1	2
D25	2.5	2.5	2	1
D26	2.5	2.5	2	2
D27	5	0	1	1
D28	5	0	1	2
D29	5	0	2	1
D30	5	0	2	2

·6.3Al·4Cr·3Re·5.6Ta·0.3Hf·

Alloy	Element Composition			
	Pt	Ir	Ru	W
D19	7.8	0	1.6	2.9
D20	7.6	0	1.6	5.8
D21	7.7	0	3.2	2.9
D22	7.6	0	3.1	5.7
D23	7.5	7.6	1.6	2.9
D24	7.4	7.6	1.5	5.8
D25	7.5	7.6	3.2	2.9
D26	7.3	7.6	3.2	5.8
D27	14.8	0	1.5	2.8
D28	14.5	0	1.5	5.5
D29	14.7	0	3	2.8
D30	14.4	0	3	5.4

series. The refractory elements Re, Ta, and W are also fixed. Systematic additions of Al, Cr, Si, Ti, and Mo, were also investigated. Minor additions of grain boundary strengtheners, C, B, and Zr, were also introduced. It is important to note that grain boundary strengtheners were added to one alloy that did not contain refractory additions

Table 2.5: DOE Phase II - low Al range of compositions in at% and wt%. The application for each element is provided in the final column.

Elements	Range of Composition (at%)	Range of Composition (wt%)	Purpose
Al	13 - 14	5.6 - 6	$L1_2$; Oxidation
Pt	2.5	7.7	$L1_2$; Oxidation
Ir	0 - 2.5	0 - 7.6	Lattice Misfit
Cr	5 - 10	4.1 - 8.2	Oxidation; Corrosion
Re	1 - 2	3.1 - 5.9	Matrix Strengthener
Ta	2	5.7	$L1_2$ Strengthener
Ru	1 - 2	1.6 - 3.1	Matrix Strengthener
W	1 - 2	2.8 - 5.8	Matrix Strengthener
Hf	0.1	0.3	Oxidation
Ti	*0.025*	*0.2*	*$L1_2$ Strengthener*
Mo	*1*	*1.5*	*Matrix Strengthener*
Co	*10*	*9.3*	*Matrix Strengthener*

Table 2.6: DOE Phase II - low Al range of compositions in at% (left column) and wt% (right). Constant levels for specified elements are listed above each column.

·13Al·***2.5Pt***·1Re·2Ta·0.1Hf·

Alloy	Element Composition			
	Ir	Cr	W	Ru
E1	0	5	1	1
E2	0	5	2	2
E3	0	7.5	2	1
E4	0	7.5	1	2
E5	0	10	1	1
E6	0	10	2	2
E7	2.5	5	2	1
E8	2.5	5	1	2
E9	2.5	7.5	1	1
E10	2.5	7.5	2	2
E11a	2.5	10	2	1
*E11b	E11a but 14Al			
E12	2.5	10	1	2
**E13	E8 but ***7.5***Cr·***2***Re			
E14	E8 but ***7.5***Cr·0.25Ti			
E15	E8 but ***7.5***Cr·1Mo			
E16	E8 but ***7.5***Cr·10Co			

·5.6Al·***7.7Pt***·3.1Re·5.7Ta·0.3Hf·

Alloy	Element Composition			
	Ir	Cr	W	Ru
E1	0	4.1	2.9	1.6
E2	0	4.1	5.8	3.2
E3	0	6.2	5.8	1.6
E4	0	6.2	2.9	3.2
E5	0	8.2	1.6	2.9
E6	0	8.2	5.8	3.2
E7	7.6	4.1	5.7	1.6
E8	7.6	4.1	2.9	3.2
E9	7.6	6.2	2.9	1.6
E10	7.6	6.2	5.8	3.2
E11a	7.6	8.2	5.8	1.6
*E11b	E11a but 6Al			
E12	7.6	8.2	2.9	3.2
**E13	E8 but ***6.2***Cr·***5.9***Re			
E14	E8 but ***6.2***Cr·0.2Ti			
E15	E8 but ***6.2***Cr·1.5Mo			
E16	E8 but ***6.2***Cr·9.3Co			

Table 2.7: DOE Phase III range of compositions in at% and wt%. The application for each element is provided in the final column.

Elements	Range of Composition (at%)	Range of Composition (wt%)	Purpose
Al	13.5 - 15	5.8 - 6.8	$L1_2$; Oxidation
Pt	2.5	7.8	$L1_2$; Oxidation
Ir	0 - 2.5	0	Lattice Misfit
Cr	5 - 10	4.4 - 8.3	Oxidation; Corrosion
Re	1	3	Matrix Strengthener
Ta	2	5.8	$L1_2$ Strengthener
Ru	0 - 2	0 - 3.2	Matrix Strengthener
W	1	2.9	Matrix Strengthener
Hf	0.1 - 0.2	0.3 - 0.6	Oxidation
Ti	0 - 0.5	0 - 0.4	$L1_2$ Strengthener
Mo	0 - 2	0 - 3.1	Matrix Strengthener
C	*0 - 0.1*	*0 - 0.2*	*Grain Boundary Strengthener*
B	*0 - 0.087*	*0 - 0.015*	*Grain Boundary Strengthener*
Zr	*0 - 0.025*	*0 - 0.039*	*Grain Boundary Strengthener*

(alloy 8A) as well as the refractory-containing alloys (alloys PX-3, PX-4, and PX-5). Furthermore, alloys PX-5 and PX-6 have similar nominal compositions, except PX-5 contains grain boundary strengtheners.

2.1.1 Density and Cost

When determining alloy compositions, it is useful to consider that blade density impacts mechanical stresses imposed upon the superalloy turbine disk and on overall engine weight. During service rotation, the blade density is directly proportional to the applied mechanical stress [4, 85], and so keeping alloy density low results in lower stresses imposed on the alloy. Table 2.9 provides the densities of a few commercial single crystals listed in Table 1.1, as well as experimental alloys within this investigation. Since the densities of Ni-base superalloys containing Pt and/or Ir are not listed in the literature, a general calculation was performed using the rule of mixtures formula

Table 2.8: DOE Phase III range of compositions in at% (top table) and wt% (bottom table). Constant levels for specified elements are listed above each table.

·***2.5Pt***·1Re·2Ta·1W·0.1Hf·

Alloy	Elemental Composition									
	Al	Cr	Ru	Si	Mo	Ti	Hf	C	B	Zr
DS-1	14	10	2	0	---	---	0.1	---	---	---
DS-2	14	10	2	0.5	---	---	0.1	---	---	---
8A	15Al·***2Pt·2Ir***·5Cr·0.15Hf							0.1	0.081	0.025
PX-1	15	7.5	---	---	2	0.5	0.1	---	---	---
PX-2	14.5	7.5	---	0.5	1	0.5	0.1	---	---	---
PX-3	14	7.5	---	0.5	1	---	0.1	0.1	0.087	0.014
PX-4	14	7.5	---	0.5	1	0.5	0.2	0.1	0.087	0.014
PX-5	13.5	7.5	---	0.5	1	0.5	0.1	0.1	0.087	0.014
PX-6	13.5	7.5	---	0.5	1	0.5	0.1	---	---	---

·***7.8Pt***·3Re·5.8Ta·2.9W·0.3Hf·

Alloy	Elemental Composition									
	Al	Cr	Ru	Si	Mo	Ti	Hf	C	B	Zr
DS-1	6	8.3	3.2	0	---	---	0.3	---	---	---
DS-2	6	8.3	3.2	0.2	---	---	0.3	---	---	---
8A	6.8Al·***6.6Pt·6.5Ir***·4.4Cr·0.5Hf							0.02	0.015	0.039
PX-1	6.5	6.2	---	---	3.1	0.4	0.3	---	---	---
PX-2	6.3	6.3	---	0.2	1.5	0.4	0.3	---	---	---
PX-3	6.1	6.3	---	0.2	1.5	---	0.3	0.02	0.015	0.02
PX-4	6.0	6.2	---	0.2	1.5	0.4	0.6	0.02	0.015	0.02
PX-5	5.8	6.2	---	0.2	1.5	0.4	0.3	0.02	0.015	0.02
PX-6	5.8	6.2	---	0.2	1.5	0.4	0.3	---	---	---

presented by Hull [86]. This formula was used to calculate the densities of commercial single crystals as well, whose density values have been measured experimentally [87]. On average, calculated values for the commercial alloys were 0.44 g/cm^3 lower than measured. As such, values listed for the experimental PGM alloys are probably 0.45 - 0.50 g/cm^3 higher than reported. Note that the PGM-containing superalloys have densities in the same range as present Ni-base single crystals.

Table 2.9: Density of PGM alloys and cost of materials. Commercial alloys are provided for comparison.

Commercial	Generation		Density (g/cm^3)		Material Cost ($ US / kg) *(As of 05/2010)*
			Measured [87]	Calculated	
CMSX-3	1st		8.56	8.22	30
PWA 1484	2nd		8.95	8.45	225
René N6	3rd		8.97	8.49	375
Alloy	PGMs	DOE Phase	Calculated Density (g/cm^3)		
D4	Ir	I	8.28		1,420
D8	Pt	I	8.26		4,190
D12	Pt + Ir	I	8.47		5,030
D19	Pt	II - high Al	8.47		4,175
D24	Pt + Ir + Ru	II - high Al	8.99		5,105
E1	Pt + Ru	II - low Al	8.61		4,135
DS-1	Pt + Ru	III	8.49		4,270
8A	Pt + Ir	III	8.14		4,430
PX-2	Pt	III	8.37		4,080
PX-5	Pt	III	8.43		4,085

Another pertinent factor to alloy design is cost. It would be useful to assess the material cost for the nominal compositions presented in Table 2.9. Using current stock prices of metals within the market today (05/2010) and assuming that approximately 2 kg of charge material is the minimum amount needed for the Bridgman directional solidification process [88], the costs of materials needed to cast single crystal bars approximately 13 mm in diameter and 150 mm in length are provided in the final column of Table 2.9. Its shown that the PGM alloy cost is an order of magnitude higher than the single crystals. To justify these costs, these alloys would need to provide an exceptional set of properties, such as high temperature intrinsic oxidation resistance along with high creep resistance.

2.2 Alloy Melting and Solidification

Alloys were fabricated within facilities located at the Ames Laboratory at Iowa State University (Ames, IA). A vacuum arc melter with a Cu mold for dropcasting, was utilized to create the polycrystalline ingots. This approach helps attain a uniform distribution of alloying elements while minimizing contaminants from the atmosphere or a crucible. Ingots weighed from 10 - 25 g and were approximately 10 mm diameter by 14 mm length. As-cast ingots were subsequently shipped to the University of Michigan for further preparation and testing.

Directional solidification (DS) was performed on two alloys (DS-1 and DS-2) using a Crystalox MCGS5 levitation-melting system with a Cu crucible under an Ar atmosphere and pressure of approximately 10^{-2} Torr. The Czochralski method was used for DS growth with a CMSX-4 single crystal starter seed. Charges, initially created through arc melting, weighed 50 - 75 g before being placed within the crucible. Rotational and translational speeds ranged from 8 - 10 rotations per minute and 1.5 - 3 mm/min, respectively. The step-by-step process is illustrated in Figure 2.1. Total times for complete withdrawal varied from 0.5 - 1 h. A withdrawal was considered ‘complete’ when the molten ingot was no longer absorbed by the rest of the continuously withdrawing DS bar and detached. Alloys developed through this method averaged 6 - 10 mm diameter and lengths varied from 40 - 150 mm.

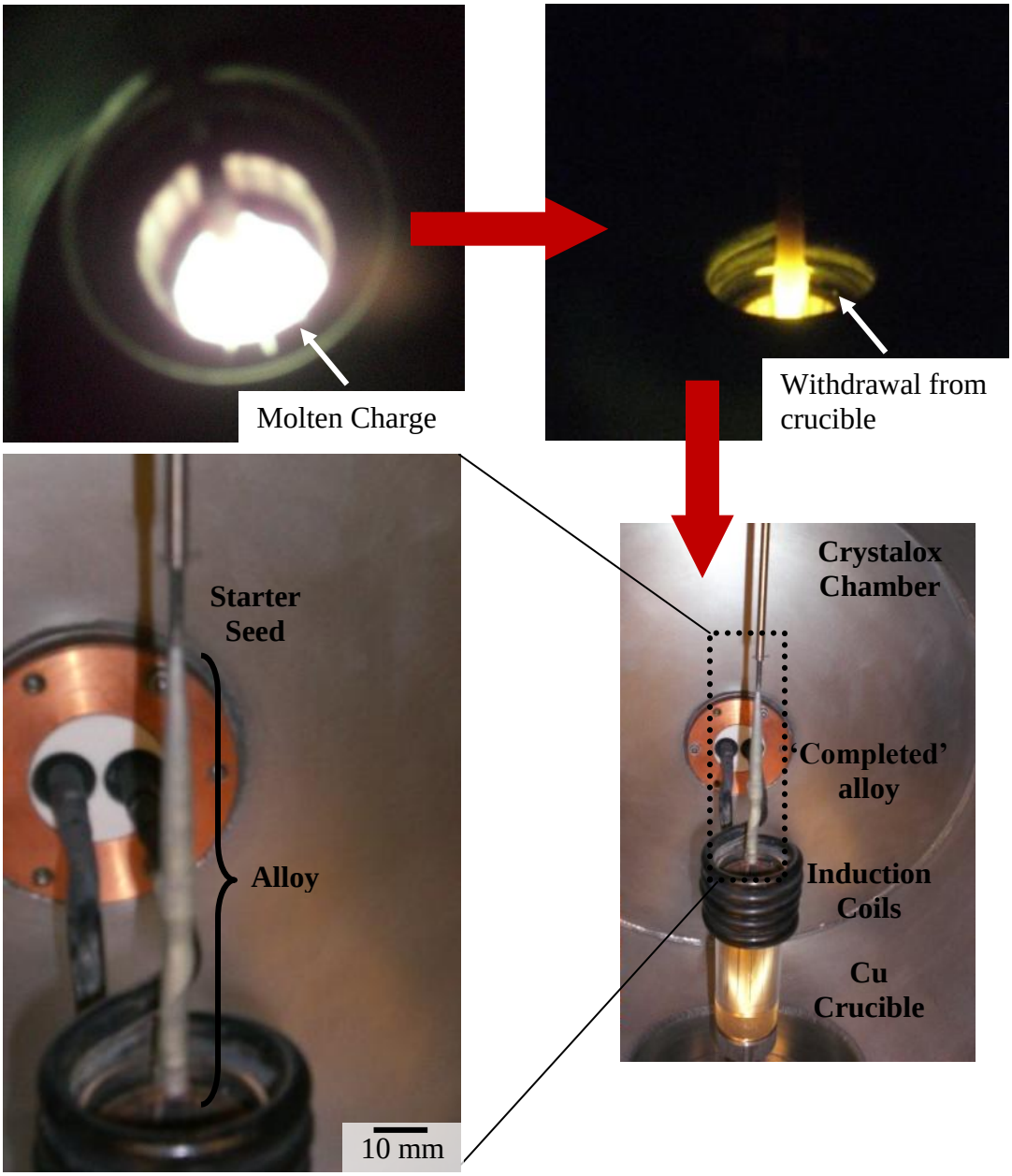

Figure 2.1: Step-by-step process using the Czochralski method.

2.3 Metallographic Preparation

Ingots received from Iowa State were wire electric discharge machined (EDM) to fabricate specimens for further testing and analysis. For some alloys, Isomet slow speed diamond saws were used to cut material. A mechanical grinding wheel was used to remove surface scratches and contaminants. Surfaces were ground from 120 to 2400 grit followed by an alumina micropolish of 1, 0.5, and 0.03 μm to produce a mirror surface finish.

To examine the as-cast microstructure, or γ-γ′ microstructure once heat treatment or creep testing was performed, a solution which selectively etches away the γ′ microstructure, was utilized. This consists of 33% acetic acid (CH_3COOH), 33% deionized water (H_20), 33% nitric acid (HNO_3), and 1% hydrofluoric acid (HF). In other instances, an electrolytic technique, which preferentially etches away the matrix, was used. This solution consisted of 45% sulfuric (H_2SO_4), 43% nitric (HNO_3), and 12% phosphoric (H_3PO_4) acid. A DC power source supplied 6 - 9 A over 15 s intervals.

2.4 Microstructural Analysis

2.4.1 Optical Microscopy

To examine post-crept sample surfaces, a Nikon Epiphot Optical 300 was utilized. Images were acquired using NIS - Elements software, developed by Nikon. All final images were created by initially capturing multiple images of the sample surface and subsequently stitching them together using Adobe Photoshop software.

2.4.2 Scanning Electron Microscopy

A FEI Philips XL-30 FEG scanning electron microscope (SEM) was utilized to image microstructures in the as-cast, heat treated, and crept conditions. Either a back-scatter electron (BSE) or secondary electron (SE) detector was used for imaging with a voltage of 20 kV, beam spot size of 4 - 5, and working distance of 7.5 - 8.5 mm.

2.4.3 Differential Thermal Analysis (DTA) and Heat Treatments

DTA samples were fabricated using wire EDM to provide cylindrical samples with a diameter of 3.5 mm. After EDM, sample surfaces were hand polished using 600 grit followed by submerging in acetone for approximately 5 minutes to ensure the removal of any surface contaminants.

A Setaram SETSYS 16/18 apparatus was used for DTA. Samples weighing approximately 250 - 300 mg were placed within alumina crucibles and tested under an argon atmosphere. A 0.999% pure Pt reference was used for all tests with an optimal scan rate of 5 °C/min to determine solidus (T_S) and liquidus (T_L) temperatures [54]. In some instances, a second DTA run was conducted on the same alloy to verify reproducibility and to acquire the gamma prime solvus (γ'_{Solvus}) temperature. However, some alloys did not provide enough material for two DTA samples and so γ'_{Solvus} temperatures were not determined. All DTA plots display the heat flow (μV) as a function of temperature [89]. The heat flow indicates the difference in voltage measured between the tested and reference samples as both are heated to elevated temperatures. This difference arises because the pure Pt reference and Ni-base superalloy sample contain different thermodynamic properties.

Once the T_S was determined, appropriate heat treatments were performed to

acquire the γ-γ′ microstructure. Heat treatments were conducted in a standard cylindrical tube furnace. Samples were first sealed in quartz tubes back-filled with Ar to mitigate high temperature oxidation. After homogenization, tubes were immediately shattered in iced water (IW). Aging was conducted in laboratory air and alloys were air cooled (AC) following aging. DOE Phase I matrix alloys and alloy 8A, that did not contain Ta, were heat treated with the following steps: 1250 °C / 6h (IW) → 1050 °C / 4h (AC). Alloys within DOE Phase I containing Ta, as well as the alloys in the other DOE matrices, used the following treatment: (T_S – (10 – 15) °C) / 6h (IW) → 1050 °C / 4h (AC).

2.4.4 Electron Microprobe Analysis

Samples for electron microprobe analysis (EMPA) were mounted in bakelite and mechanically polished to 4000 grit, followed by micropolishing using 0.05 μm alumina solution. A CAMECA SX-100 microprobe with five WDS detectors was used to acquire compositional profiles. The WDS detectors were standardized for the elements within the investigated alloy(s). Table 2.10 lists the parameters used for standardization. A NiAl standard was used for the determination of Al peaks. Spot scans were conducted using a current of 10 nA, voltage of 20 kV with a beam diameter of approximately 2 μm. At least 10 spot scans were conducted on each alloy, with each spot scan measured on at least 5 different γ′ particles.

2.4.5 Atom Probe Tomography

To acquire appropriate specimen geometry for data acquisition, atom probe samples were rough polished using a solution of 25% perchloric acid ($HClO_4$) with glacial acetic acid, followed by fine polishing with a solution of 2% perchloric acid with 2-butoxyethanol ($C_6H_{14}O_2$). Tomography studies were conducted within an Imago Local

Table 2.10: Parameters used for EMPA.

Element	Line	Standard	WDS Detector #	Crystal	Offsets
Al	K_α	NiAl	2	TAP	-700 to +1000
Ta	M_α	Ta	2	TAP	+1800; slope: 0.95
Re	L_α	Re	3	LLIF	-400 to +600
Ni	K_α	Ni	3	LLIF	-600 to +1300
Cr	K_α	Cr	5	PET	± 500
Pt	M_β	Pt	1	LTAP	-320 to +400
Hf	L_α	Hf	4	LLIF	-400 to +600
Ru	L_α	Ru	5	PET	-700 to +600
W	L_α	W	4	LLIF	-480; slope: 1.0
Si	K_α	Si	1	LTAP	+2075; slope: 1.0
Mo	L_α	Mo	5	PET	-1360 to +530
Ti	K_α	Ti	4	LLIF	-780 to +1160
* For Si, the element overlap feature must be used for W and Ta due to these two elements having line overlap of Si K_α					

Electrode Atom Probe (LEAP) with a chamber temperature of 22K, pulse fraction of 20% and pulse repetition rate of 200 kHz at the University of Sydney. The flight path between detector and sample was 90 mm. At least two runs were performed on each sample. Data analysis and reconstruction was performed on IVAS 6.0 software.

2.4.6 Elemental Partitioning

Using EMPA data of the γ′ phase, $C_{\gamma'}$, the γ phase composition, C_γ, was calculated using the Lever Law:

$$C_\gamma = \frac{C_n - V_f C_{\gamma'}}{1 - V_f} \qquad \text{Equation 2.1}$$

using the nominal alloy composition, C_n, and the volume fractions of γ′ (V_f). Gamma prime V_f was measured from SEM images using a systematic point count procedure [90].

For APT experiments, phase compositions of the γ and γ′ were independently determined through a 3D reconstruction of each sample and measured within each phase

using a spherical range of interest (ROI). At least 15 different ROIs were evaluted from either the matrix or precipitate(s) phases.

Rearranging Equation 2.1:

$$V_f = \frac{C_n - C_\gamma}{C_{\gamma'} - C_\gamma} \quad \text{Equation 2.2}$$

This rearrangement of the Lever Law allows APT data to be plotted on a x-y chart, providing quantitative values of the volume fraction through the slope. Additionally, partitioning behavior can be analyzed [15]. Finally, partitioning coefficients, *p*, were acquired from both microanalysis tools by Equation 2.3:

$$p = \frac{C_\gamma}{C_{\gamma'}} \quad \text{Equation 2.3}$$

2.4.7 Coarsening Kinetics

Alloy PX-5 was chosen for coarsening studies. Specimens 4 x 4 x 3 mm were homogenized and aged. Homogenization was performed at 1325°C / 6 h, after which tubes were shattered in ice water. Aging treatments were conducted in air for the following times: 0.5, 2, 4, 8, 16, and 24 h, followed by an iced water quench. Aging temperatures were 1050 °C, 1100 °C, 1150 °C and 1200 °C. Samples were etched using the electrolytic etch. Using SEM images taken at a magnification of 10K, a minimum of 200 measurements on particle length/diameter were performed on coarsened precipitates for each aging treatment. Verifying that changes in particle size were due to precipitate coarsening and not the formation of new γ′ particles, the γ′ volume fraction was measured for each testing time and temperature. Subsequent processing and analysis were conducted using *ImageJ* software.

To measure precipitate compositions, an extended aging time of 720 h at 1250 °C was conducted to produce precipitates approximately 4 - 5 μm diameter. Afterwards, the sample was prepared for EMPA. At least 25 spot scans were acquired on coarsened precipitates.

2.4.8 Thermodynamic Calculations

The PANDAT thermodynamic package was employed using a Ni-database to assess how elemental phase compositions and γ′ volume fraction measurements were influenced by the PGM additions of Pt, Ir, and/or Ru. PANDAT calculations helped in narrowing down the final alloy compositions within the PX-series of DOE Phase III.

2.5 High Temperature Mechanical Testing

High temperature compression creep tests were conducted to assess the deformation mechanisms in the experimental polycrystalline PGM-modified Ni-base superalloys. Compression creep experiments were performed due to the high cost of the alloys and the lower amounts of material needed for producing compression samples compared to tension samples.

2.5.1 Sample Preparation

Parallelpiped creep samples 4 mm x 4 mm x 8 mm were sectioned by EDM. An average of two samples per alloy was tested. Alloy surfaces were polished by using 240 grit up toward a 600 grit using a mechanical polishing wheel. For each alloy, one surface face that was parallel to the applied stress axis was polished to 2400 grit and subsequently micropolished using 1 μm alumina. On this finely polished surface, vertical

fiducial lines were placed to check for the occurrence of grain boundary sliding. Samples were then submerged in acetone for 5 minutes. Length, width, and height were measured using a standard micrometer. Specimens were placed in a compression creep cage between two silicon nitride (SiN) ceramic tiles. Prior to specimen placement, each SiN tile was lightly coated using boron nitride spray to prevent sticking between tile and sample during high temperature testing.

2.5.2 Compression Creep

A TZM alloy compression creep fixture was mounted within an OXY-GON creep furnace, Figure 2.2, located at the University of Michigan. Below the creep fixture were two linear voltage displacement transducers used to measure creep strains. Creep tests were conducted at 1000 °C with a vacuum of approximately 10^{-7} Torr. Type-C control thermocouples regulated thermal ramp rates and dwell times within the chamber. Unfortunately, these thermocouples do not accurately measure testing temperatures within the heat zone, where the sample is placed. To overcome this, two type-R thermocouples are positioned near the sample instead (inset of Figure 2.2) to provide continuous monitoring of high temperature conditions.

Due to the limited amount of material for each PGM alloy, creep testing was restricted to 1 - 2 tests per alloy. Stress levels for testing were selected with a goal of achieving a minimum creep-rate of 10^{-8} s^{-1}. While creep-rates varied from 10^{-8} s^{-1} by about a factor of 10x, the creep strengths for the selected stress levels of the alloys were compared by extrapolating a reference creep strength based on a standard creep-rate magnitude of 10^{-8} s^{-1}. The reference creep strength was deduced from the applied stress by fitting a measured creep stress exponent. The value of the stress exponent and an

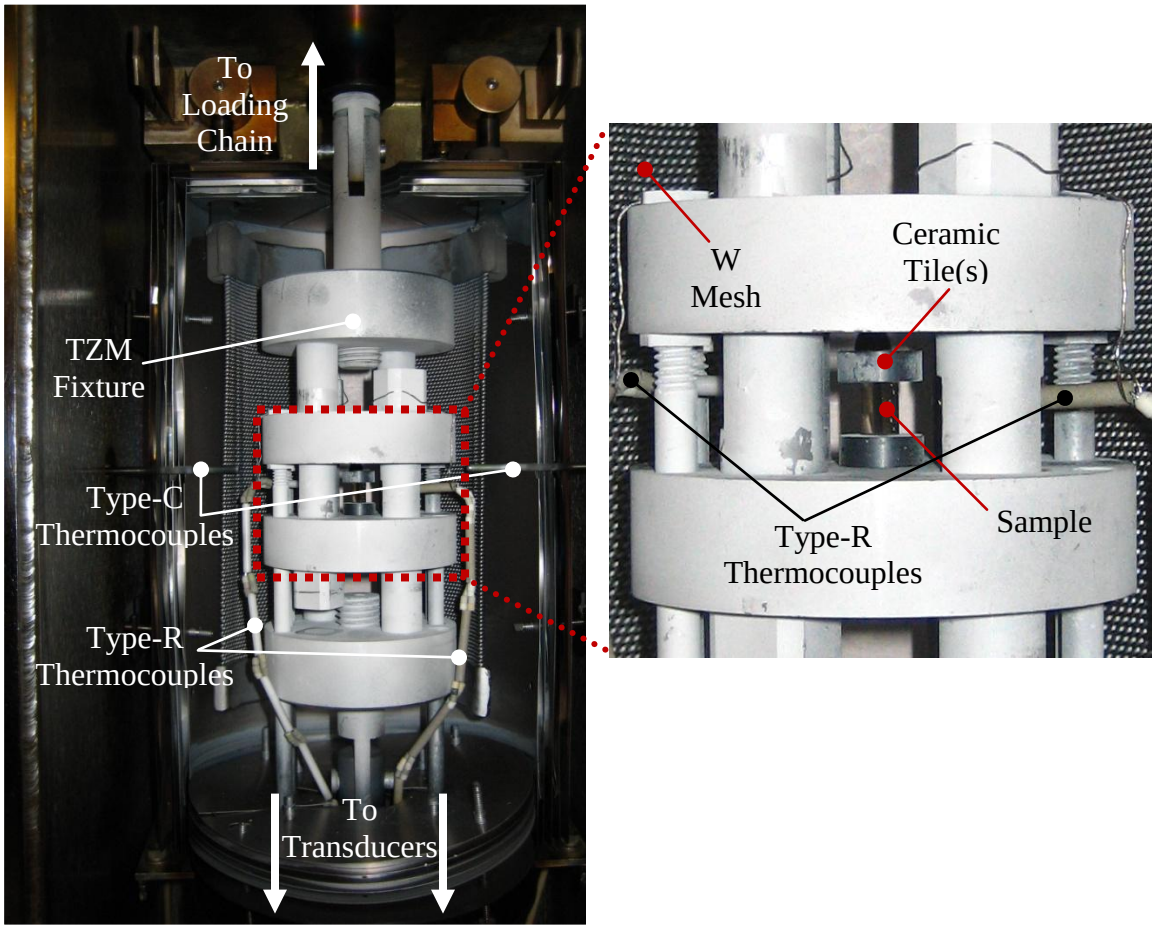

Figure 2.2: Set-up of sample within compression creep fixture.

example of this procedure is provided at the beginning of Chapter 6. Samples were compressed to 1% creep strain upon which tests were immediately terminated. Samples were cooled under load to preserve substructures [28].

Creep data was collected on a Labview 8.0 program. Appendix A provides a general schematic of the program interface and the parameters which were recorded and saved during each test. A legend is provided for clarification of a few parameters. The recorded engineering strain values, along with time, were used to acquire the minimum creep rates ($\dot{\varepsilon}$). Once tests were completed and samples removed from the OXY-GON

chamber, specimen height was re-measured using a micrometer to acquire the total strain.

2.5.3 Directional Coarsening

The compression crept samples were examined to assess their misfit-type through directional coarsening behavior. In addition, the formation of TCP phases, either within grain interiors or at grain boundaries, was documented by SEM.

2.6 Transmission Electron Microscopy (TEM)

Transmission electron microscopy (TEM) was used to examine γ′ microstructure after heat treatments were performed. It was also utilized for analysis of dislocation sub-structure within deformed samples. TEM was imperative for dislocation density analysis within the γ and γ′ phases.

2.6.1 Sample Preparation

Samples were cut using EDM to provide thicknesses 0.42 - 0.62 mm. Foils used to analyze heat treated microstructures were cut randomly from the alloy. TEM foils from compression crept alloys were cut parallel to the applied stress axis. This assisted with the characterization of dislocation networks at the directionally coarsened γ/γ′ interface. Cut samples were hand polished to 0.22 mm thickness using 400 grit paper. Afterwards, a Gatan disc punch (model #659) provided discs 3 mm in diameter. Further hand polishing was employed to go from 0.22 mm down to 0.10 - 0.11 mm thickness using 600 grit paper. Once a thickness of 0.10 - 0.11 was achieved, a final hand polish using 2400 grit was used to provide a mirror surface finish to both sides of the foil. Foils with a thickness below 0.085 mm were considered too thin for electropolishing.

The electropolishing solution consisted of 10% perchloric acid ($HClO_4$), 13% butyl cellusolve ($C_6H_{14}O_2$), and 9% distilled water, in methanol (CH_3OH). Unfortunately, alloys from DOE Phase II - low Al and DOE Phase III could not be successfully electropolished with this solution. Instead, another solution using 10% $HClO_4$ in CH_3OH was employed. This provided foils thin enough for transmission. A Fischione twin-jet electropolisher was utilized with a current and voltage ranging from 44 - 52 A, and 18 - 24 V, respectively. Due to the wide range in alloy composition, polishing temperatures varied from -42 to -30 °C.

2.6.2 Transmission Electron Microscopy

A Philips CM-12 with an accelerating voltage, V_0, of 120 kV was utilized for TEM imaging. The microscope provides a Gatan modified Philips Double-Tilt stage holder (X = ± 45 degrees, Y = ± 30 degrees), which allows access to several low-index zone axes. For Ni-base superalloys, γ′ precipitate faces are parallel to the {001} planes [25]. If images are acquired from **g**-vectors that are parallel to [001], this allows optimal contrast of the γ-γ′ system. For this reason, alloys were imaged from the [001] ZA using a (200) or (020) two-beam condition with a slightly positive deviation parameter [91, 92]. A convergent beam electron diffraction (CBED) image, Figure 2.3, highlights the [001] ZA with the (200) and (020) indicated by the **g**-vector. Images were acquired mostly in bright field (BF) mode. Dark-field was utilized for imaging heat treated microstructures.

2.6.3 Dislocation Analysis

Dislocation densities (ρ_{dis}) in TEM micrographs were calculated as [27]:

$$\rho_{dis} = \frac{\Sigma L}{AD} \qquad \text{Equation 2.4}$$

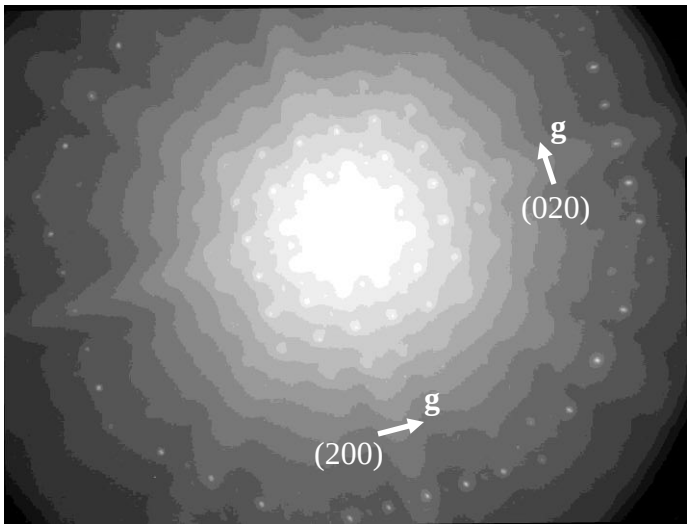

Figure 2.3: Selected area diffraction pattern of [001] ZA. (200) and (020) are highlighted by **g**-vector.

where ΣL is the total measured dislocation line lengths within the γ or γ′ phases, A is the area of the micrograph, and D is foil thickness. The foil thickness was assumed to be equivalent to the average precipitate size in the aged alloy prior to creep.

Interfacial dislocation networks were measured in directionally coarsened alloys, as shown in Figure 2.4. The network spacing, D_{net}, was calculated by a linear intercept method, and inserted into Equation 1.3 ($\vec{b}$ = 0.254 nm) to acquire $|\delta|$. The average network spacing value was assessed by at least 25 - 35 linear measurements per alloy.

2.7 Statistical Analysis

Standard deviations, *SD*, were measured for the γ and γ′ phase compositions, γ′ volume fractions, precipitate edge lengths/diameters, dislocation network spacings, and dislocation density distributions within the γ and γ′ phases:

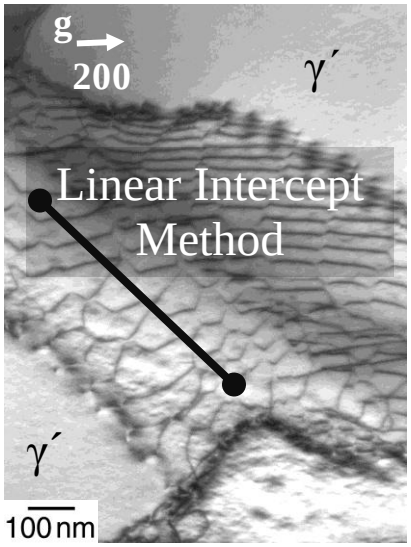

Figure 2.4: Interfacial network post-creep for alloy D12. Network spacing was averaged through multiple linear intercept measurements.

$$SD = \sqrt{\frac{\Sigma(A_x - \bar{A}_x)^2}{(n-1)}}$$ Equation 2.5

with A_x and $\bar{A}_x$ being the individual and average variables, respectively, in accordance with each specified measurement. Error bars within plots represent the 5% standard error of the mean, *5% SE*, divided by the square root of *n*:

$$5\%\ SE = \frac{SD}{\sqrt{n}}$$ Equation 2.6

CHAPTER 3

PHYSICAL PROPERTIES AND MICROSTRUCTURE OF PGM-CONTAINING ALLOYS

Systematic variations in alloy composition were investigated with the use of a design of experiments (DOE) approach. The four DOE matrices investigated in this study encompass a broad range of composition. This chapter presents how systematic shifts in elemental additions influence physical properties and microstructure. In the first matrix, DOE Phase I, the PGMs Pt and Ir were alloyed alongside variations in Cr, and the refractory elements Re, and Ta. The second matrix, DOE Phase II, introduced the solid solution strengthener W, as well as the PGM Ru. Another matrix similar to DOE Phase II was later developed, except Al levels decreased from 15 at% to 13 at%. Systematic variations of Ir, Ru, Cr, and W were assessed in this matrix as well. The final matrix, DOE Phase III, developed alloys containing Pt as the only PGM addition, while continuing to modify Al and Cr content. This chapter also introduces the use of 2-D moment invariants [93, 94] to provide a more quantitative description of the γ' morphology.

3.1 Differential Thermal Analysis (DTA)

The heat treatment windows used for attaining a supersaturated matrix solution, without inducing incipient melting, are influenced by variations in alloy composition. This section illustrates how PGM and non-PGM elements shift the gamma prime solvus, γ'_{Solvus}, and solidus, T_S, temperatures. Alloys used for analysis in Sections 3.1.1 - 3.1.3 are listed in Table 3.1. Alloys that did not contain Ta additions exhibited heat treatment windows (T_S - γ'_{Solvus}) of approximately 200 °C. The addition of Ta reduced this value to less than 50 °C. Increases in refractory content reduced the heat treatment windows to as low as 10 °C in alloys containing 15 at% Al. Decreasing Al content to 13 at% expanded the heat treatment window, shown in Table 3.2. The detailed effects of PGM and non-PGM additions on these thermodynamic properties are discussed in more detail in subsequent sections. A complete list on alloys subjected to DTA and their γ'_{Solvus}, T_S, and liquidus, T_L, temperatures are provided in Tables 3.2 and 3.3.

3.1.1 PGM Additions

An initial assessment of how the PGMs affect the γ'_{Solvus} and T_S temperatures without the additions of refractory elements was conducted. Figure 3.1(a) displays DTA curves for alloys D3 (Ir) and D7 (Pt) that both contain a nominal composition of 15Al·5Cr. The γ'_{Solvus} for Ir is lower than Pt, at approximately 1140 °C compared to 1150 °C, respectively. However, the T_S for the Ir-containing alloy is 15 °C higher than the Pt alloy. If the nominal composition includes refractory additions 15Al·5Cr·(1Re·2Ta), Figure 3.1(b), the γ'_{Solvus} for both alloys increases at least 200 °C. The Ir-containing alloy D4 displays a higher T_S temperature than the Pt-containing alloy

Table 3.1: Nominal compositions (at%) of PGM alloys used for DTA comparisons.

DOE PHASE I	Composition: 15Al·0.1Hf				
Alloy	Pt	Ir	Cr	Re	Ta
D3	0	2.5	2.5	0	0
D4	0	2.5	5	1	2
D5	2.5	0	2.5	0	2
D6	2.5	0	2.5	1	0
D7	2.5	0	5	0	0
D7 plus 2Ta	2.5	0	5	0	2
D8	2.5	0	5	1	2
D11	2.5	2.5	5	0	0
D13	2.5	2.5	5	1	0
D14 minus 2.5Cr	5	0	0	0	0
D14	5	0	2.5	0	0
D16	5	0	5	0	0
D17	5	0	5	0	2
D18	5	0	5	1	0
D18 plus 1Re	5	0	5	2	0
DOE PHASE II - high Al	Composition: 15Al·5Cr·1Re·2Ta·0.1Hf				
Alloy	Pt	Ir	Ru	W	
D19	2.5	0	1	1	
D23	2.5	2.5	1	1	
D27	5	0	1	1	
DOE PHASE II - low Al	Composition: 13Al·2.5Pt·1Re·2Ta·0.1Hf				
Alloy	Al	Ir	Cr	W	Ru
E11a	13	2.5	10	2	1
E11b	14	2.5	10	2	1

DOE PHASE III	Composition: 2.5Pt·1Re·2Ta·1W·0.1Hf									
Alloy	Al	Cr	Ru	Si	Mo	Ti	Hf	C	B	Zr
DS-1	14	10	2	0	0	0	0.1	0	0	0
DS-2	14	10	2	0.5	0	0	0.1	0	0	0
PX-5	13.5	7.5	0	0.5	1	0.5	0.1	0.1	0.087	0.014
PX-6	13.5	7.5	0	0.5	1	0.5	0.1	0	0	0

Table 3.2: DTA for DOE Phases I and II containing high Al (15 at%). Solidus, liquidus, and gamma prime solvus temperatures are provided.

PGMs	Alloy	Differential Thermal Analysis (°C)			
		Solidus (T_S)	Liquidus (T_L)	γ'_{Solvus}	Δ (T_S -γ'_{Solvus})
DOE PHASE I					
Ir	D1	1379	1398	1337	42
	D2	1404	1444	1120	284
	D3	1387	1420	1143	243
	D4	1365	1406	1337	28
Pt	D5	1368	1398	1321	47
	D6	1385	1426	1141	243
	D7	1373	1405	1153	220
	D8	1351	1398	1337	14
Ir / Pt	D9	1393	1428	1105	288
	D10	1375	1417	1333	42
	D11	1386	1419	1150	236
	D12	1363	1400	1336	27
	D13	1366	1407	1172	194
Pt	D14	1377	1409	1095	282
	D15	1362	1403	1341	21
	D16	1367	1401	1170	197
	D17	1347	1383	1333	14
	D18	1373	1424	1262	111
DOE PHASE II - high Al					
Pt / Ru	D19	1361	1401	N/A	N/A
	D20	1357	1401	1352	5
	D21	1361	1398	1340	21
	D22	1360	1400	N/A	N/A
Ir / Pt / Ru	D23	1369	1410	1353	16
	D24	1366	1406	N/A	N/A
	D25	1373	1408	N/A	N/A
	D26	1368	1405	1352	16
Pt / Ru	D27	1356	1392	N/A	N/A
	D28	1354	1390	N/A	N/A
	D29	1357	1393	1342	25
	D30	1356	1398	N/A	N/A

Table 3.3: DTA for DOE Phase II - low Al (13 at%) and Phase III.

PGMs	Alloy	Differential Thermal Analysis (°C)			
		Solidus (T_S)	Liquidus (T_L)	γ'_{Solvus}	Δ (T_S -γ'_{Solvus})
DOE PHASE II – low Al					
Pt / Ru	E1	1379	1414	1291	88
	E2	1381	1418	1304	77
	E3	1367	1400	1302	65
	E4	1377	1405	1290	87
	E5	1356	1395	1280	76
	E6	–	–	–	–
Ir / Pt / Ru	E7	1391	1423	1318	73
	E8	1390	1423	1294	96
	E9	–	–	–	–
	E10	–	–	–	–
	E11	1364	1411	1299	65
	E11 (14Al)	1359	1406	1308	51
	E12	–	–	–	–
Ir / Pt / Ru	E13	1382	1413	1299	83
	E14	1378	1411	1303	75
	E15	1375	1409	1298	77
	E16	1368	1411	1291	77
DOE PHASE III					
Pt / Ru	DS-1	1351	1385	1300	51
	DS-2	1345	1385	1293	52
Pt / Ir	8A	1390	1413	1150	240
Pt	PX-1	1332	1370	N/A	N/A
	PX-2	1325	1373	N/A	N/A
	PX-3	1333	1380	N/A	N/A
	PX-4	–	–	–	–
	PX-5	1341	1377	1321	20
	PX-6	1352	1389	1317	35

D8 by 15 °C. Whereas the heat treatment window (T_S minus γ'_{Solvus}) for the alloys in Figure 3.1(a) is approximately 220 °C, the refractory additions have decreased the window approximately 30 °C when compared to Figure 3.1(b).

Figure 3.2 compares the combination of both PGMs (Pt + Ir) with the same nominal composition presented in Figure 3.1(a). Alloys D3 and D7 are included for

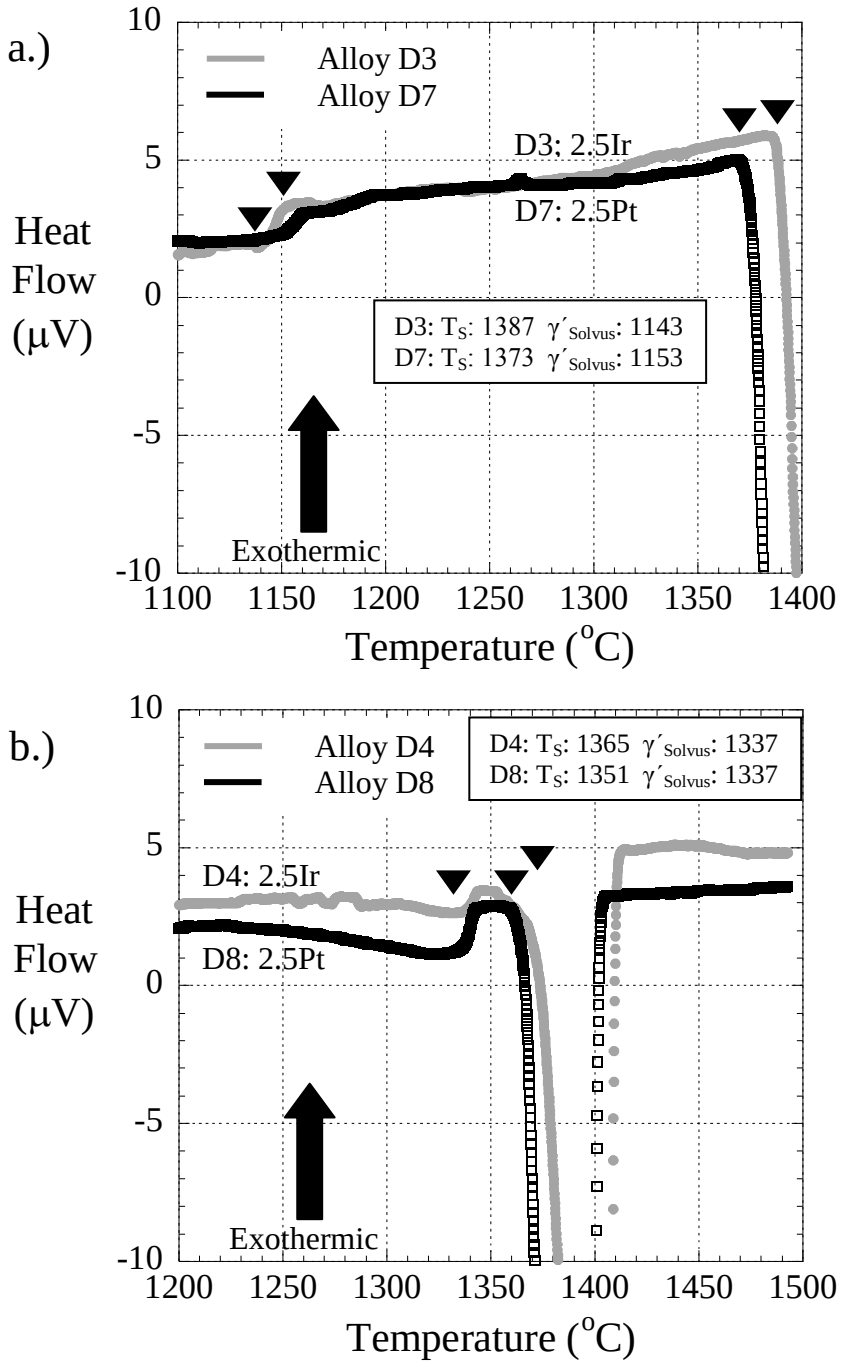

Figure 3.1: Change of γ'_{Solvus} and T_S due to Pt or Ir (a) without refractory additions and (b) with 1Re·2Ta.

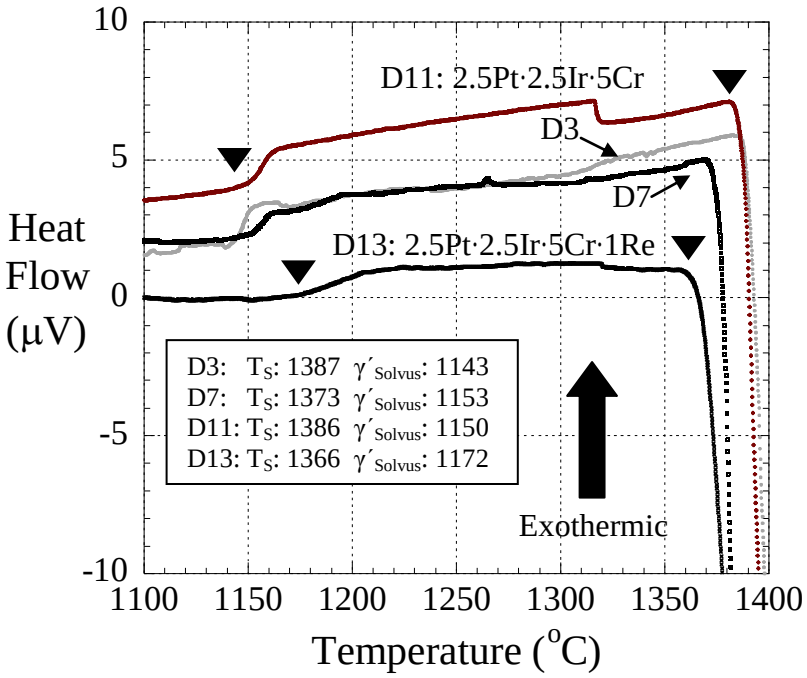

Figure 3.2: Effect of an alloy containing the PGMs Pt and Ir, as well as Re. Both alloys from Figure 3.1 are included for comparison (two middle curves).

for comparison. Alloy D11 (2.5Pt·2.5Ir·5Cr) has a T_S temperature similar to the Ir-only alloy D3, but has a γ'_{Solvus} equivalent to the Pt-only alloy D7. Figure 3.3(a) demonstrates that Ir increases the T_S temperature by 8 °C with the presence of the PGMs Pt and Ru. Increasing Pt content from 2.5 → 5 at%, or Ru from 1 → 2 at%, does not shift the T_S temperature for either, Figure 3.3(b) and Figure 3.4, respectively. Additionally, it has been demonstrated that increasing Ru additions beyond 2 at% within Ni-base superalloys does not change the T_S appreciably [52].

3.1.2 Refractory Additions

Additions of refractory elements such as W and Re impart crucial strengthening to the γ-γ′ system. Table 3.4 presents DTA data for conventional polycrystalline and single crystal superalloys. As refractory additions were continuously increased from

polycrystalline and 1st generation single crystals to 2nd and 3rd generation single crystals, the heat treatment windows diminished. It is therefore necessary to determine whether refractory additions within the PGM alloys alter the γ'_{Solvus} or T_S temperatures appreciably. From Figure 3.4, increasing W content from 1 to 2 at% does not alter the T_S temperature. Figure 3.2 illustrates how adding 1 at% Re reduces the T_S temperature while increasing the γ'_{Solvus} with Pt and Ir as part of the nominal composition. Figure 3.5 compares the effects of adding either Re or Ta. In alloy D5, Ta additions lower the T_S temperature more so than Re by approximately 25 °C. The effect of Ta is demonstrated by Figure 3.6, which verifies that Ta increases the γ'_{Solvus} by approximately 200 °C while lowering the T_S temperature. Figure 3.7 illustrates the effects of increasing Re content from 1 to 2 at%. The γ'_{Solvus} temperature does not shift but the T_S increases approximately 5 °C.

3.1.3 Additional Alloying Elements

Elements such as Cr and Al are added into Ni-base superalloys by as much as 5 - 10 at% (Cr) or 10 - 15 at% (Al). Additionally, Si and grain boundary strengtheners (C, B, and Zr) may be added in minute quantities (< 0.5 at%). These large, or minor, additions can influence the thermodynamic properties of the system. Figure 3.8 displays the influence of increasing Cr from 0 → 5 at%. The incremental increases in Cr continuously reduce the T_S temperature while increasing the γ'_{Solvus}. Once Re is introduced, the T_S temperature increases. This is in contrast to Figure 3.2 where Re reduces the T_S temperature. The one major difference for the PGM alloys in Figure 3.8 compared to those in Figure 3.2 is the absence of Ir. Figure 3.8 further shows that Ta lowers the T_S while dramatically increasing the gamma prime solvus. Figure 3.9

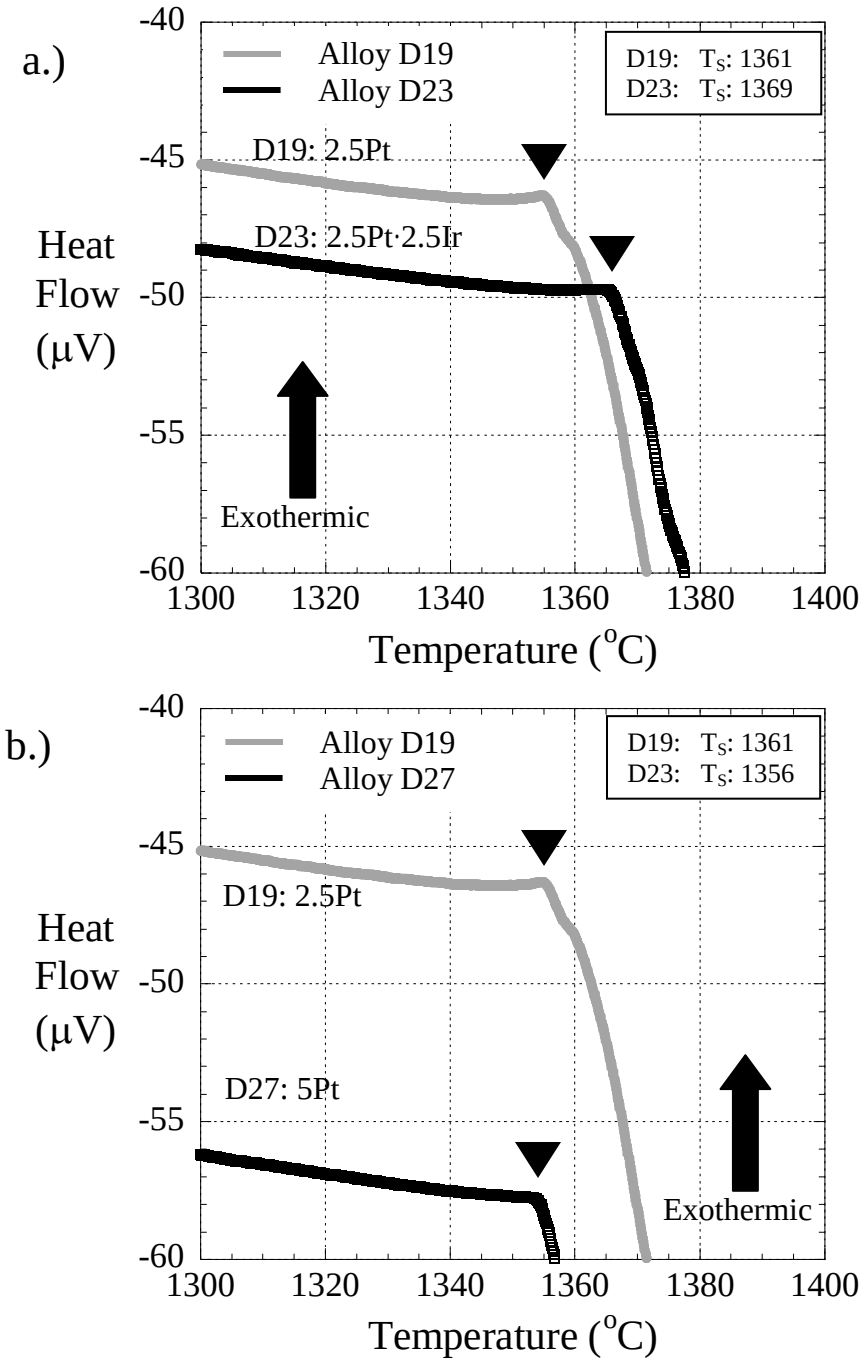

Figure 3.3: Change in the T_S temperature due to (a) Ir or (b) higher Pt.

Table 3.4: Compositional profile of conventional Ni-base superalloys and their DTA data.

	Alloy	Composition (wt%)							
		Cr	Co	Mo	Re	W	Al	Ti	Ta
Polycrystalline	MAR-M247	8.5	10	0.6	0	9.7	5.2	1.4	3
1st Generation	CMSX2	8	5	0.6	0	8	5.6	1	2
	SRR99	8	5	0	0	10	5.5	2	3
2nd Generation	René N5	7	8	2	3	5	5.8	0	7
3rd Generation	CMSX10	2	3	0.4	6	5	5.7	0.2	8

DTA (°C)				
Alloy	T_S	T_L	γ'_{Solvus}	Heat Treatment Window: $T_S - \gamma'_{Solvus}$
MAR-M247 [95]	1360	1410	1250	110
SRR 99 [96]	1305	1370	1260	45
CMSX 2 [96]	1325	1375	1265	60
René N5 [97]	1337	1387	1304	33
CMSX 10 [98]	1366	1414	1337	29

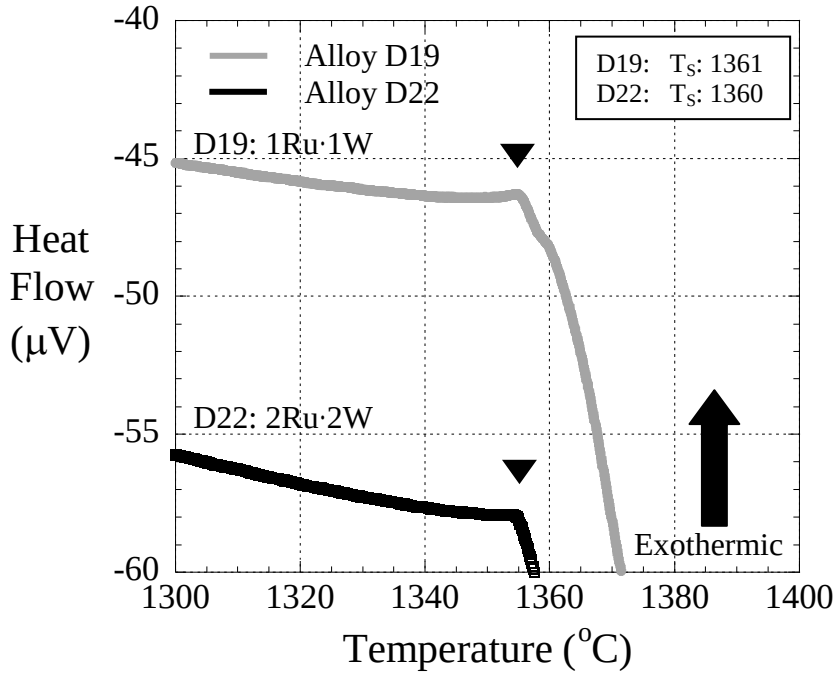

Figure 3.4: Effect of Ru on T_S, where T_S is indicated by arrows.

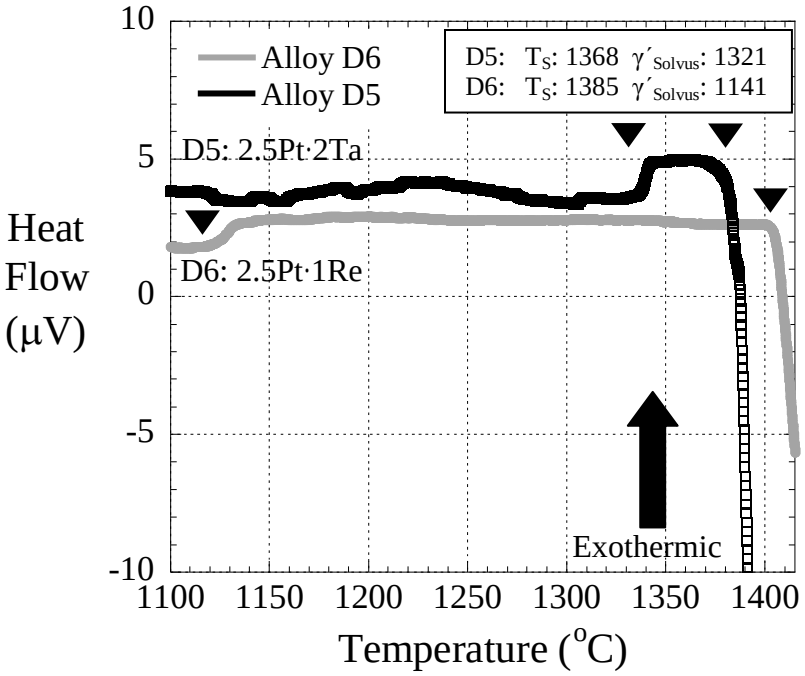

Figure 3.5: Alloying effects of Re versus Ta.

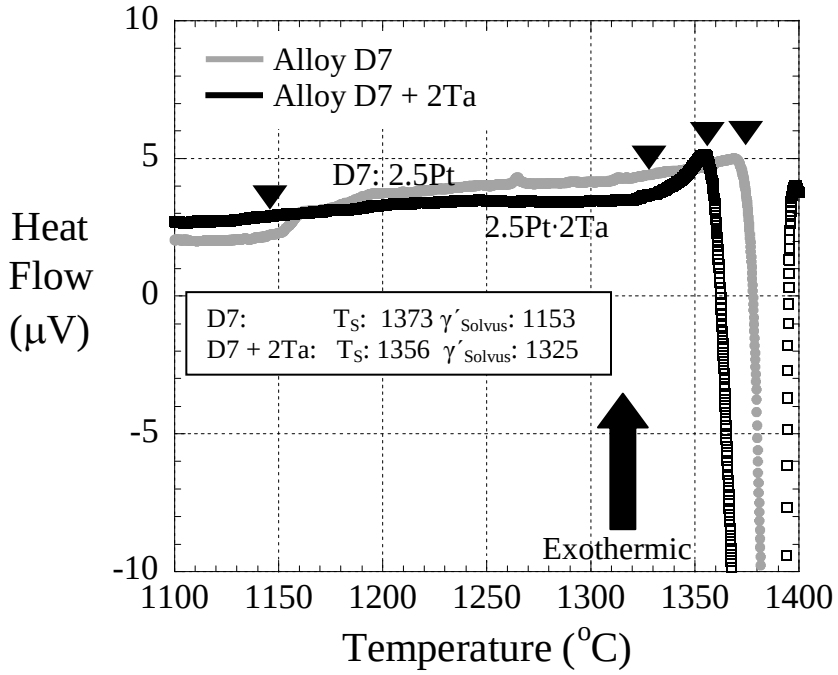

Figure 3.6: Effects due to Ta.

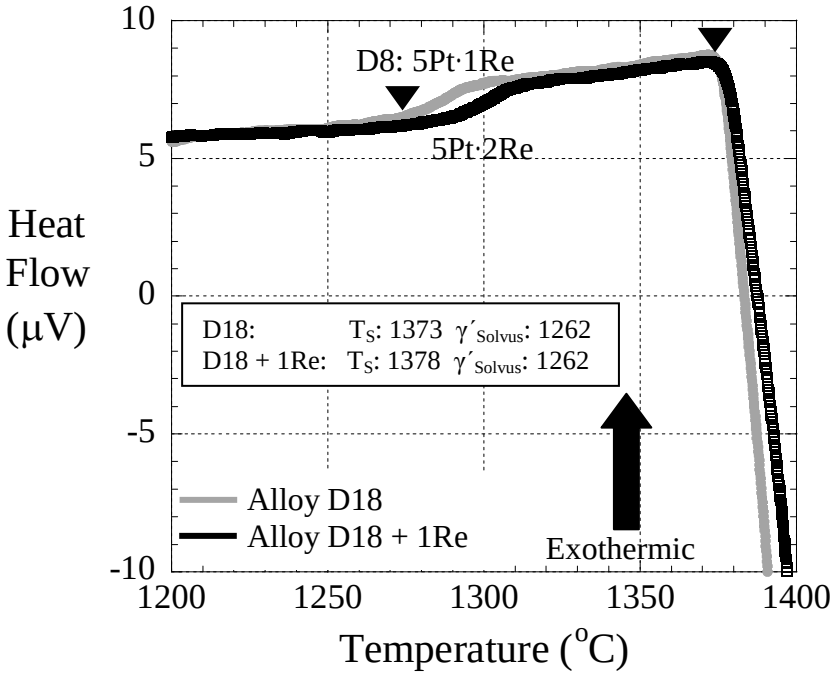

Figure 3.7: Effects due to increasing Re.

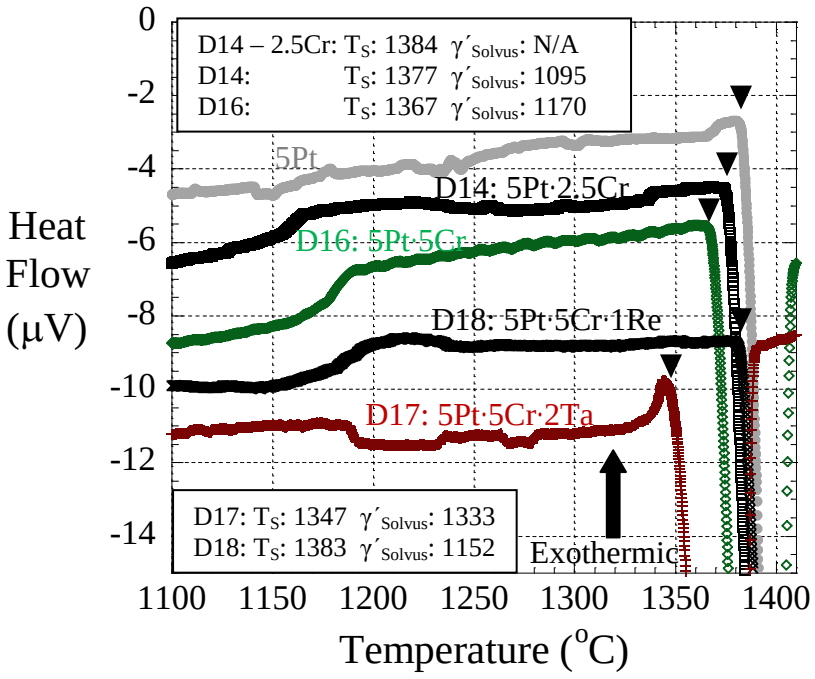

Figure 3.8: Effects due to Cr and additions of either Re or Ta.

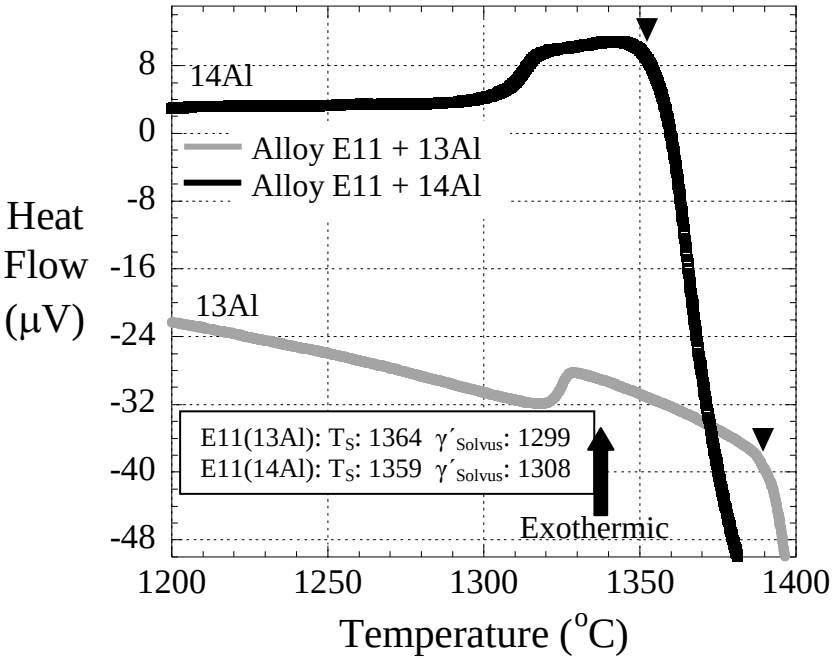

Figure 3.9: Effects due to Al.

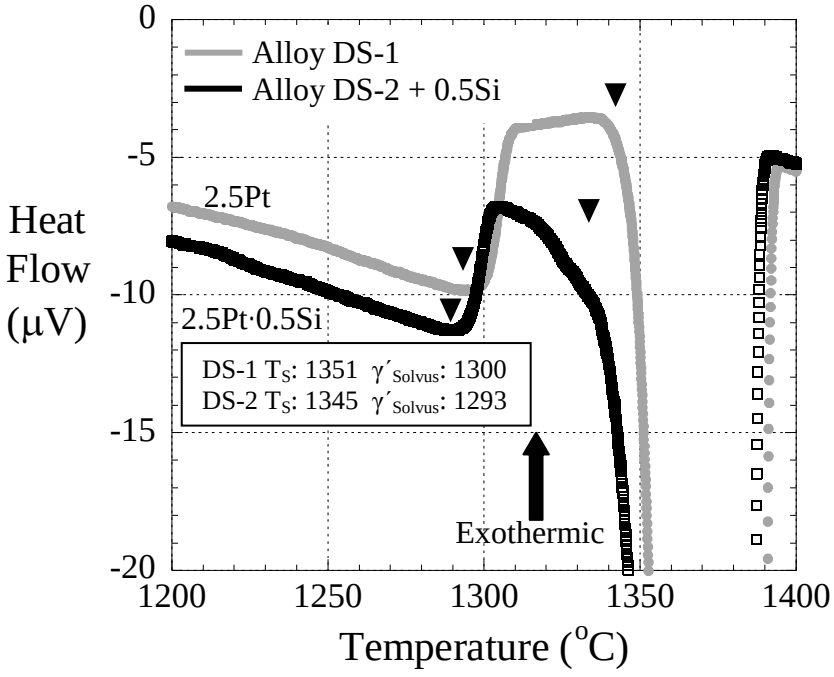

Figure 3.10: Effects due to Si.

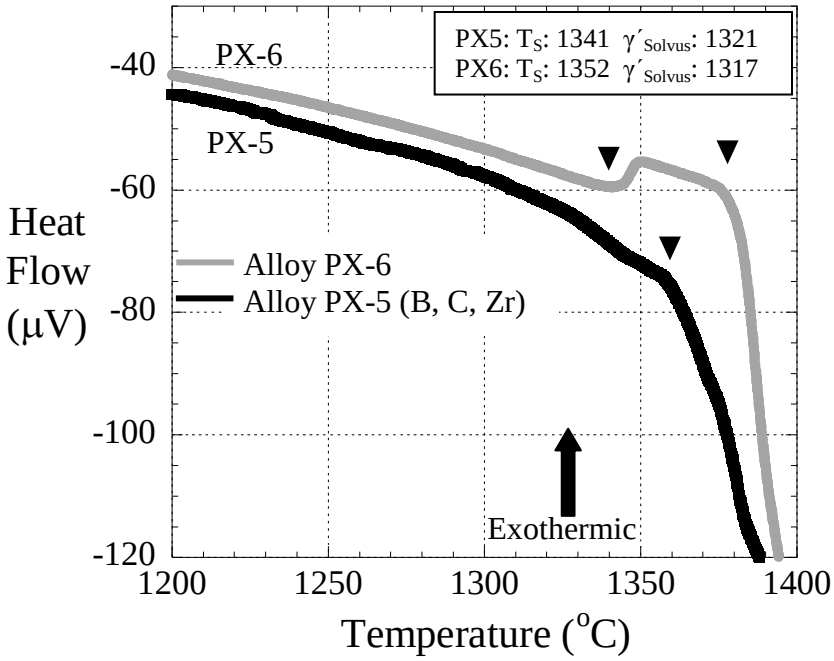

Figure 3.11: Grain boundary strengtheners and their effects on the T_S.

highlights the effects of shifting Al content. Decreasing the Al by 1 at% increases the T_S temperature nearly 30 °C. If 0.5 at% Si is added to the alloy composition, Figure 3.10, there is no appreciable shift in the γ'_{Solvus} but there is a lowering of the T_S by approximately 10 °C. Similarly, minute additions of C, B, and Zr (total of 0.2 at%) decrease the T_S temperature by approximately 10 °C, as shown in Figure 3.11.

3.2 Gamma Prime Morphology

Systematic variations of PGM and non-PGM additions will influence the lattice misfit and, therefore, alter γ' morphology. This section addresses the changes in gamma prime microstructure due to incremental shifts in composition. Volume fractions of precipitates were measured for alloys following aging treatments. A complete listing for

precipitate volume fractions is provided in Table 3.5. Alloys lacking Ta in the DOE Phase I matrix contained V_f ranging from 0.45 - 0.52. Tantalum additions increased volume fractions to the range of 0.55 - 0.65. Alloys in the DOE Phase II - lower Al matrix displayed lower precipitate volume fractions compared to the higher Al DOE Phase II and Phase III matrices.

The usual characterization of precipitate morphology within Ni-base superalloys typically refers qualitatively to the shapes as 'semi-spherical', 'cuboidal with rounded edges' or 'platelet-type'. To remove the ambiguity in describing precipitate morphology, a quantitative method developed by MacSleyne and co-workers involving the analysis of moment invariants has been utilized [93, 94].

Through use of two-dimensional phase-field analysis, more than 15,000 particles of varying morphology were assessed. An aspect ratio, η, classifies particle morphology based on two shape parameters, A and B, shown in Figure 3.12. The dotted lines overlaid on the shape termed 'particle' in Figure 3.12 are always drawn right at the transition from the corner radius to a contour that is straight, as illustrated by the small black arrows in Figure 3.12. The lines always begin and end on the shapes perimeter. The shape parameter 'A' must always constitute the length of a square, which is generated by the intersection of the dotted lines. The shape parameter 'B' refers to the actual length of the particle measured horizontally and vertically. Figure 3.13 illustrates the use of aspect ratios on precipitate morphology within Ni-base superalloys. Figure 3.13(a) demonstrates how aspect ratios can vary within a single alloy specimen. In some instances, aspect ratios are near equal to one another, which can either relate to a 'near-cuboidal' morphology, Figure3.13(b) in which $\eta = 0.77$, or one that is 'near-

Table 3.5: Volume fractions for fully heat treated alloys. The volume fractions beyond DOE Phase I did not change appreciably between certain alloy groups. An average value is provided instead, with the standard deviation listed in parenthesis.

PGMs	Alloy	Volume Fraction (standard deviation)
DOE PHASE I		
Ir	D1	0.52
	D2	0.51
	D3	0.45
	D4	0.61
Pt	D5	0.64
	D6	0.53
	D7	0.57
	D8	0.63
Ir / Pt	D9	0.45
	D10	0.57
	D11	0.54
	D12	0.61
	D13	0.60
Pt	D14	0.45
	D15	0.55
	D16	0.55
	D17	0.65
	D18	0.56
DOE PHASE II – high Al		
Pt / Ru	D19	0.66 (± 0.02)
	D20	
	D21	
	D22	
Ir / Pt Ru	D23	0.62 (± 0.02)
	D24	
	D25	
	D26	
Pt / Ru	D27	0.65 (± 0.02)
	D28	
	D29	
	D30	

PGMs	Alloy	Volume Fraction (standard deviation)
DOE PHASE II – low Al		
Pt / Ru	E1	0.56 (± 0.02)
	E2	
	E3	
	E4	
	E5	
	E6	
Ir / Pt Ru	E7	0.52 (± 0.02)
	E8	
	E9	
	E10	
	E11	
	E11 (14Al)	
	E12	
Ir / Pt Ru	E13	0.53 (± 0.01)
	E14	
	E15	
	E16	
DOE PHASE III		
Pt / Ru	DS-1	0.56 (± 0.01)
	DS-2	
Pt / Ir	8A	0.45
Pt	PX-1	0.62 (± 0.03)
	PX-2	
	PX-3	
	PX-4	
	PX-5	
	PX-6	

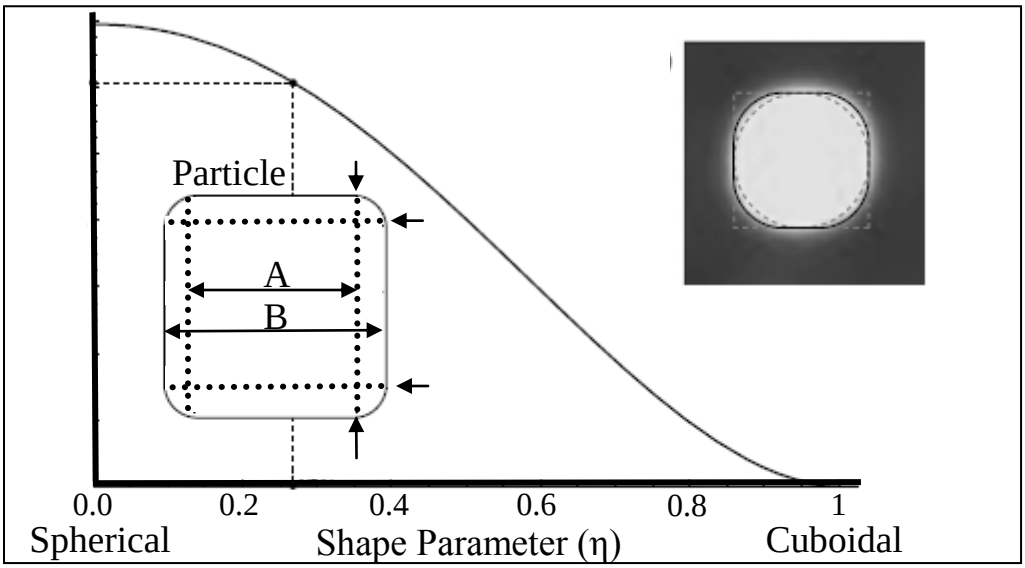

Figure 3.12: Shape parameter (η) to quantitatively assess γ′ morphology. Adapted from [93].

spherical', Figure 3.13(c), where the calculated aspect ratio is 0.21. Based on the x-axis of Figure 3.12, η = 0 indicates spherical while η = 1 corresponds to cuboidal. The aspect ratio is assumed to be independent of γ′ particle size. For the remaining part of this chapter and all subsequent chapters, γ′ morphology in the aged condition will be described based on its aspect ratio. Alloys presented in Sections 3.2.1 - 3.2.3 are listed in Table 3.6 along with measured aspect ratios.

3.2.1 PGM and Refractory Additions; Low Cr

Alloys within the DOE Phase I matrix displayed the widest variation in γ′ morphology of all the matrices. Figure 3.14 shows how elemental additions of Cr, Ta, Re, and Ir change the morphological characteristics of the γ′ precipitates. All samples shown in Figure 3.14 were placed within the SEM chamber simultaneously and were imaged using the same brightness/contrast values in BSE mode. Images that appear to have Z-contrast differences arise due to etching effects as all samples in Figure 3.14 were

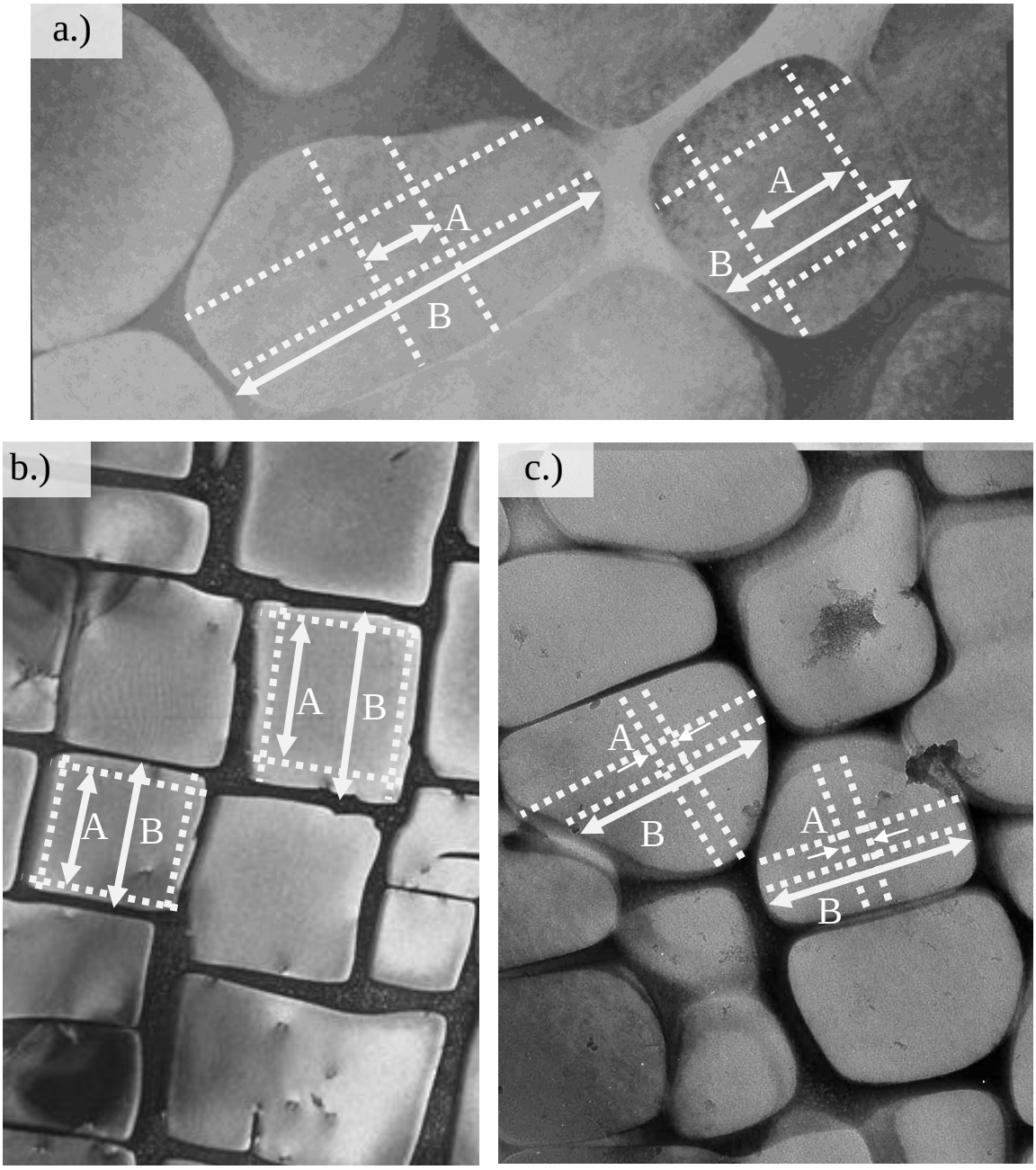

Figure 3.13: Using ‘A’ and ‘B’ shape parameters to define aspect ratios for the γ′ precipitates within Ni-base superalloys. Whereas the TEM image in (a) would provide an aspect ratio near η = 0.5, the precipitates in (b) are closer to η = 1, while those in (c) indicate η near 0.

Table 3.6: Nominal compositions of PGM alloys used for microstructural analysis. The average standard deviation for the measured aspect ratios was ± 0.24.

DOE PHASE I	Composition: 15Al·0.1Hf					Aspect Ratio (η)
Alloy	Pt	Ir	Cr	Re	Ta	
D3	0	2.5	2.5	0	0	0.22
D4	0	2.5	5	1	2	0.29
D5	2.5	0	2.5	0	2	0.14
D7	2.5	0	5	0	0	0.45
Dx	2.5	0	5	0	2	0.66
D8	2.5	0	5	1	2	0.77
D11	2.5	2.5	5	0	0	0.55
D12	2.5	2.5	5	0	2	0.58
D14 – 2.5 Cr	5	0	0	0	0	0.46
DOE PHASE II - high Al	Composition: 15Al·5Cr·1Re·2Ta·0.1Hf					
Alloy	Pt	Ir	Ru	W		
D19	2.5	0	1	1		0.21
D21	2.5	0	2	1		0.14
D22	2.5	0	2	2		0.14
D23	2.5	2.5	1	1		0.18
D27	5	0	1	1		0.32
DOE PHASE II - low Al	Composition: 13Al·2.5Pt·1Re·2Ta·0.1Hf					
Alloy	Ir	Cr	W	Ru		
E1	0	5	1	1		0.70
E2	0	5	2	2		0.11
E5	0	10	1	1		0.08
E6	0	10	2	2		0.67

DOE PHASE III	Composition: 2.5Pt·1Re·2Ta·1W·0.1Hf										
Alloy	Al	Cr	Ru	Si	Mo	Ti	Hf	C	B	Zr	
DS-1	14	10	2	0	0	0	0.1	0	0	0	0.74
DS-2	14	10	2	0.5	0	0	0.1	0	0	0	0.82
PX-2	14.5	7.5	0	0.5	1	0.5	0.1	0	0	0	0.61
PX-3	14	7.5	0	0.5	1	0	0.1	0	0	0	0.14
PX-5	13.5	7.5	0	0.5	1	0.5	0.1	0.1	0.087	0.014	0.08

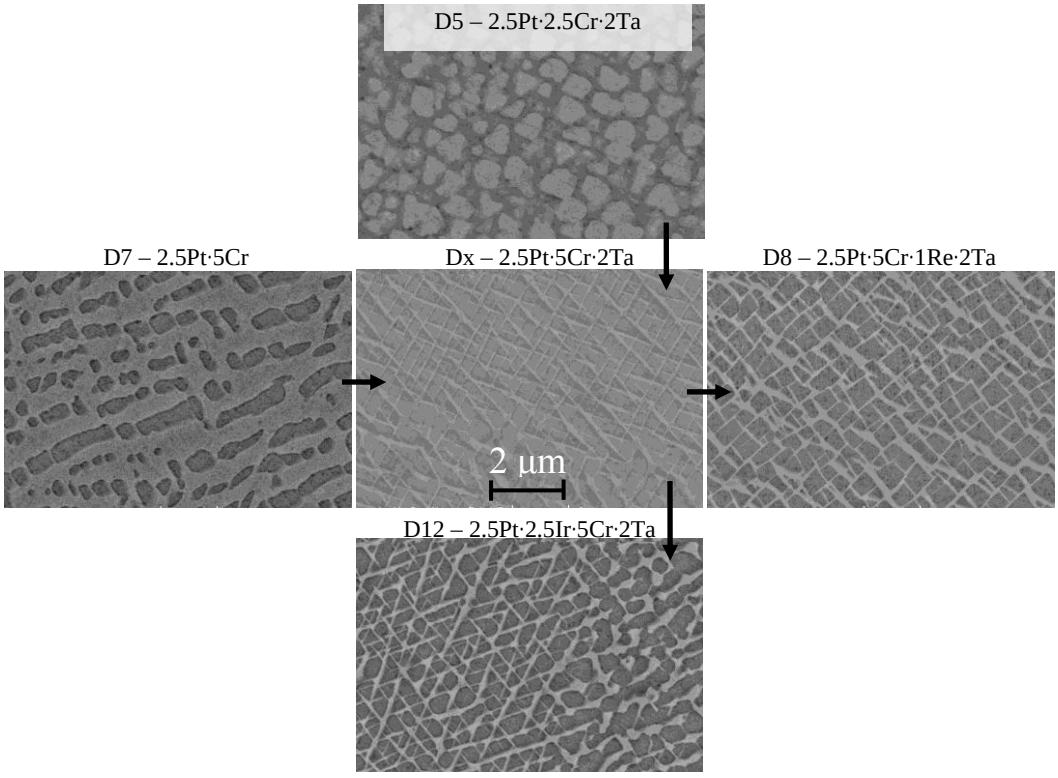

Figure 3.14: Changes in microstructure (Phase I) due to additions of various elements. All alloys contain (in at%) 15Al·0.1Hf. Alloy 2.5Pt·5Cr·2Ta was used for microstructural studies only and was heat treated similarly to Phase I containing Ta.

imaged prior to etching with no appreciable Z-contrast variation. Not all grains that were used for microstructural imaging were oriented in the [001] direction. As a result, alloys such as Dx and D12 appear to have triangular γ′ precipitate shapes. However, this is merely a cube shaped particle sectioned along the {111} plane. Comparing alloy D7 with Dx, which contains an additional 2 at% Ta, increases volume fraction of precipitates and changes the aspect ratio that transitions from $\eta = 0.45$ toward 0.66. Adding Re to Dx results in alloy D8, which has $\eta = 0.77$. Adding Cr from D5, $\eta = 0.14$, to Dx results in 0.66. Considering Dx compared to D12, the Ir addition, changes the aspect ratio to 0.60.

Figure 3.15 compares the effect of PGMs Pt or Ir on precipitate morphology in

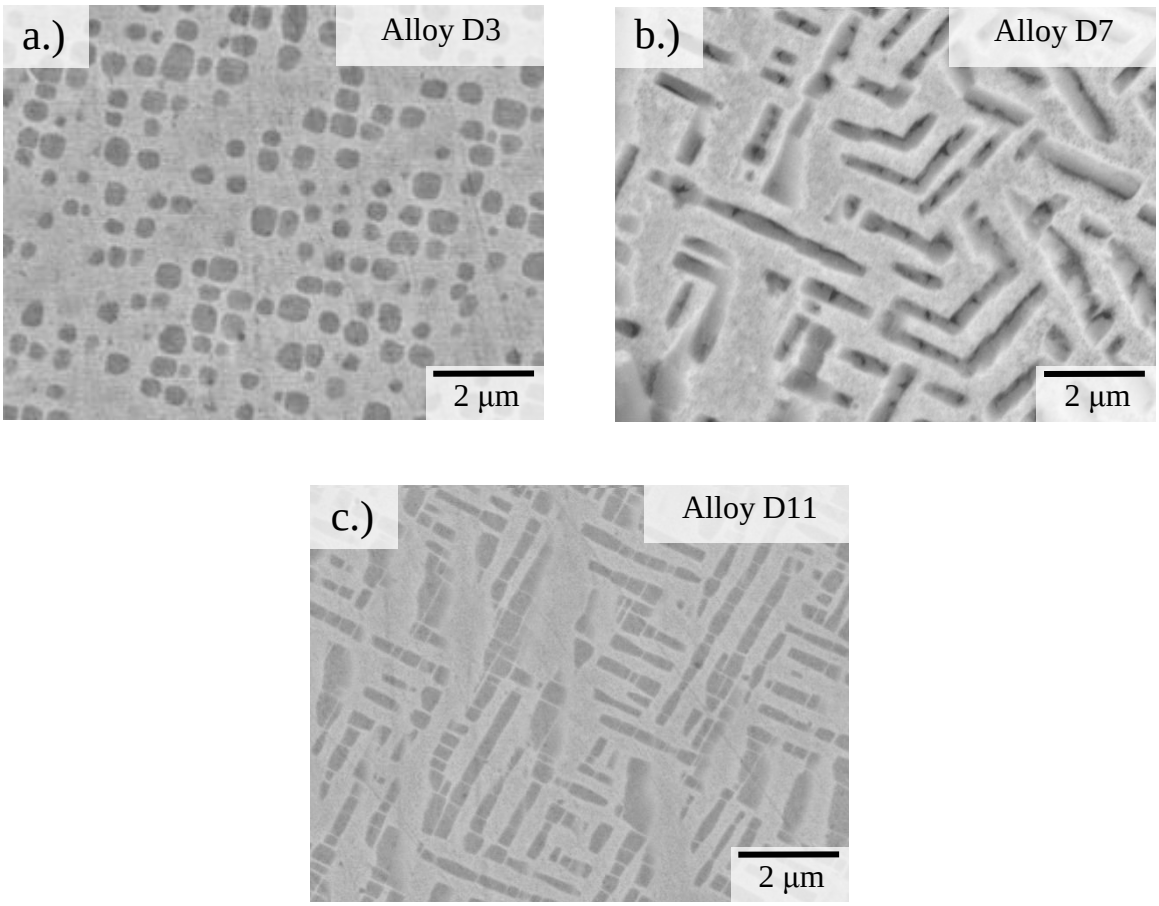

Figure 3.15: Precipitate morphology due to (a) Ir, (b) Pt, and (c) Ir + Pt. Alloys have the following nominal composition: 15Al·5Cr.

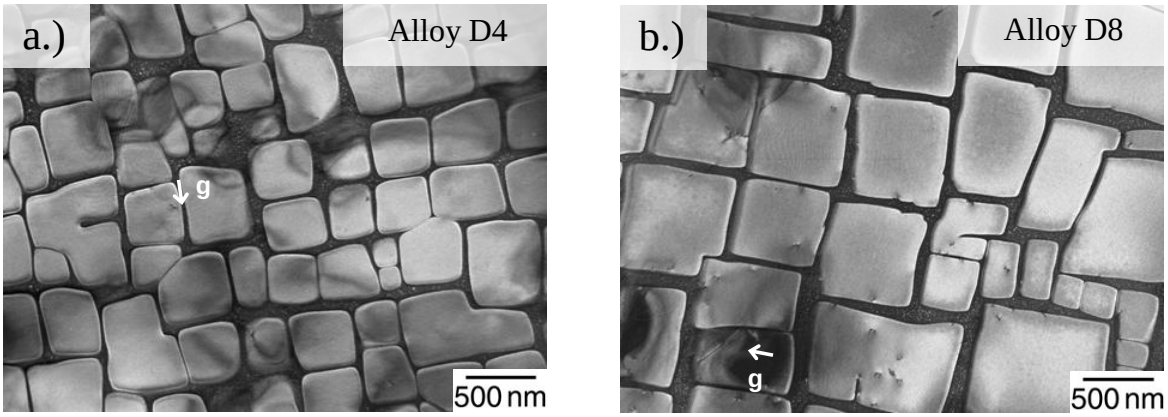

Figure 3.16: Average particle sizes due to (a) Ir or (b) Pt additions. Both alloys contain the following nominal composition: 15Al·5Cr·1Re·2Ta·0.1Hf.

alloys without refractory additions. The iridium addition results in $\eta = 0.22$, Figure 3.15(a) while a Pt addition, 3.15(b), obtains an aspect ratio of 0.47. An aspect ratio that increases toward $\eta = 1.0$ indicates a misfit magnitude deviating further from zero as compared to $\eta = 0.22$. When Pt and Ir are combined, the resultant microstructure, Figure 3.15(c), is similar to the Pt-only morphology, Figure 3.15(b), in which η is near 0.55. Measured volume fractions of alloy D3 (Ir) versus D7 (Pt) are 0.50 and 0.55, respectively. The volume fraction for alloy D11 is 0.54.

The TEM images of Figure 3.16 depict the differences in microstructure due to PGM content in alloys with refractory elements (1Re·2Ta). Both alloys have measured volume fractions of approximately 0.62. Alloy D4 (Ir) has a parameter $\eta = 0.29$ and the Pt-containing alloy D8 illustrates $\eta = 0.77$. The precipitate edge length for the Ir-containing alloy D4 is, on average, smaller compared to the Pt-containing alloy D8 (350 nm versus 530 nm, respectively).

3.2.2 Near-Zero and Negative Lattice Misfit

Ru and W additions preferentially partition to the matrix, thereby increasing a_γ. This partitioning behavior results in morphologies of precipitates not observed within the DOE Phase I alloys. Figure 3.17 shows precipitate morphologies from D19 (Pt-only) and D23 (Pt + Ir). Measured volume fractions for all DOE Phase II – high Al alloys ranged from 0.6 - 0.7. The measured aspect ratios are (a) 0.21 and (b) 0.18. The TEM micrograph of Figure 3.18, showing the 2Ru·2W at% alloy, reveals a morphology with an aspect ratio of 0.14.

In the DOE Phase II matrix the high Al resulted in insoluble γ' particles, as revealed in Figures 3.19(a) and 3.19(b). These particle sizes range in diameter from 1 - 6

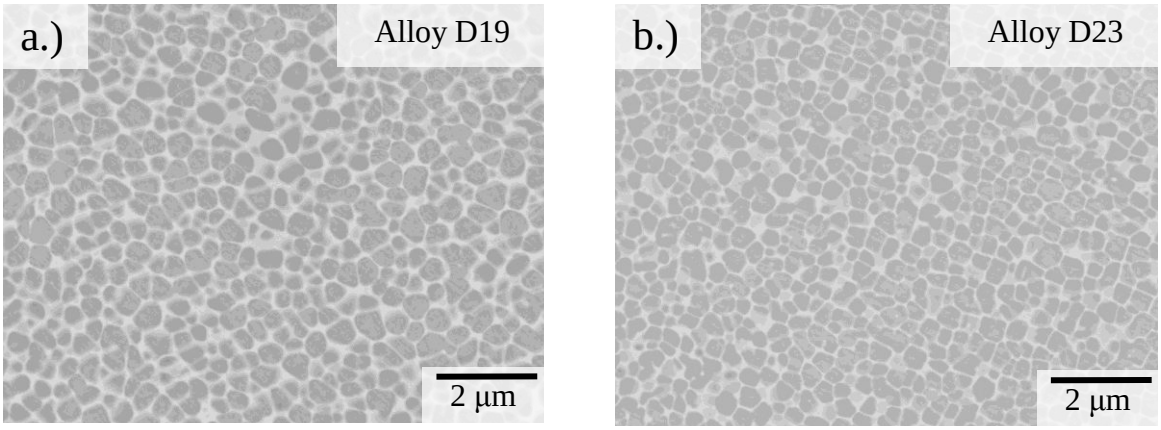

Figure 3.17: γ′ morphology due to Ru/W additions.

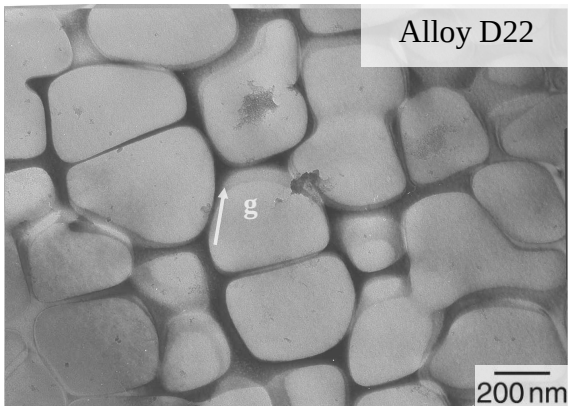

Figure 3.18: TEM micrograph highlighting variation in γ′ precipitates.

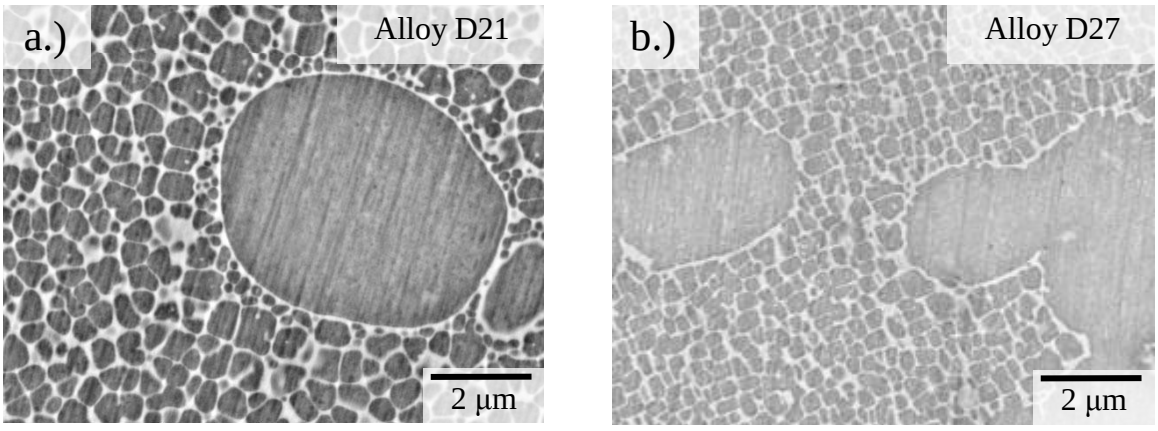

Figure 3.19: Insoluble γ′ particles.

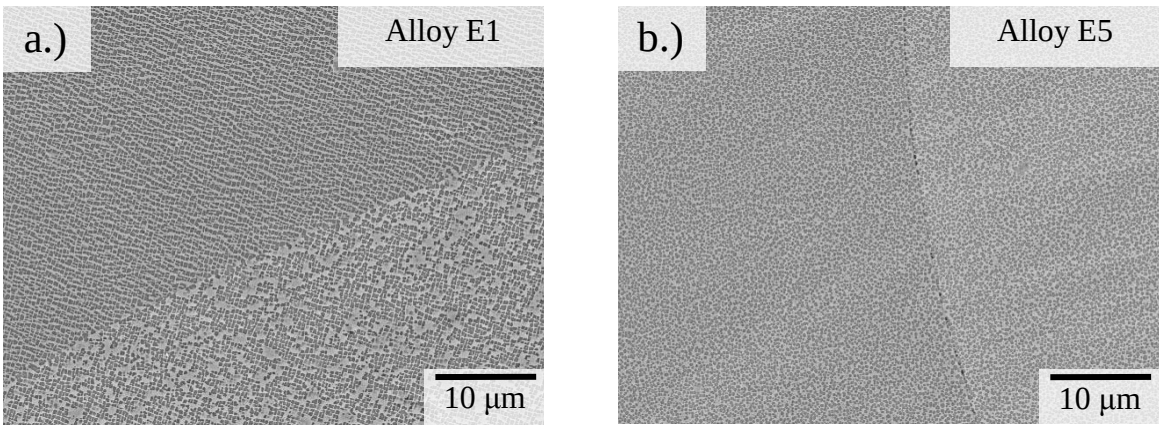

Figure 3.20: No observation of insoluble γ′ at grain boundaries or within grain interior upon full heat treatment for DOE Phase II – low Al alloys.

μm and often displayed a low aspect ratio of 0.10. Reduction of Al to 13 at% reduced the fraction of these insoluble γ′ precipitates. No insoluble γ′ at grain boundaries or within grain interiors were observed for DOE Phase II - low Al alloys. Figures 3.20(a) and 3.20(b), alloys E1 and E5, respectively, represent alloys from the DOE Phase II - low Al matrix upon full heat treatment. Measured volume fractions for all Phase II - low Al alloys ranged from 0.48 - 0.55, which, on average, was a 7% decrease from the range of volume fractions measured for Phase II - high Al.

Increasing Cr, Ru and W content induced further morphological changes, as depicted in Figure 3.21. All four alloys in Figure 3.21 contain Pt as the only PGM addition. The γ′ morphology in Figure 3.21(a) depicts $\eta = 0.70$. Increasing the Ru and W additions by 1 at% each, Figure 3.21(b), shifts η to 0.11. This low aspect ratio is observed again, $\eta = 0.08$, if Cr, instead of Ru and W, is increased from $5 \rightarrow 10$ at%, Figure 3.21(c). When Cr, Ru, and W are all increased simultaneously by the same amounts as in Figures 3.21(b) and (c), then the microstructure of Figure 3.21(d) shares an

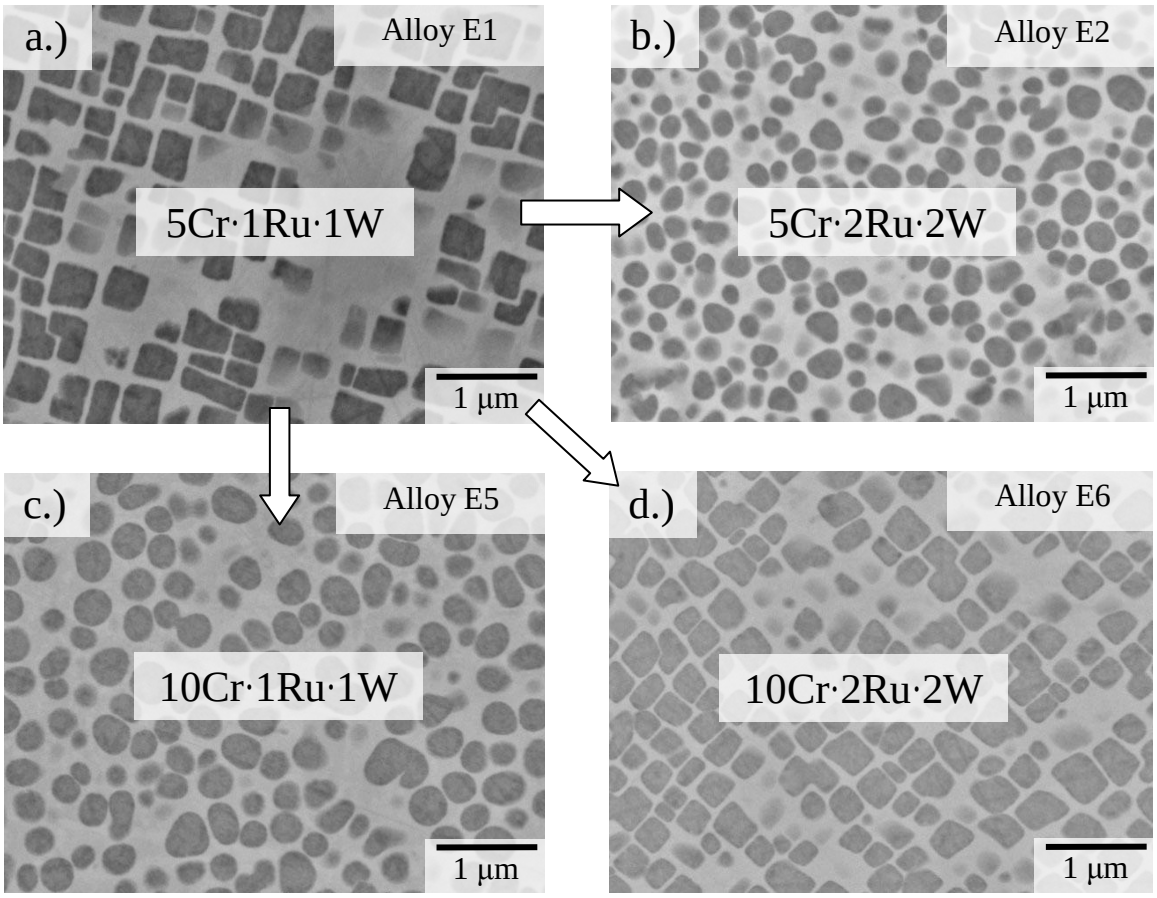

Figure 3.21: Change in γ′ morphology due to Cr, Ru, and W additions. Alloys (a – d) have the following nominal composition: 13Al·2.5Pt·1Re·2Ta·0.1Hf.

aspect ratio similar to Figure 3.21(a), which is 0.67. Cr, Ru, and W preferentially partition to the matrix, increasing a_γ, resulting in a lattice misfit that is negative, Figure 3.21(d), implying that the δ in Figure 3.21(a) must be positive. Comparing the images of Figure 3.17(a) to Figure 3.21(a) demonstrates the change in morphology when Al decreases from 15 → 13 at%, respectively. This is attributed to stronger partitioning of elements into their respective phases. In this instance, the 13 at% Al must increase the $a_{\gamma'}$ to a greater extent than the a_γ. The effects of Al on elemental partitioning is addressed in Chapter 4: Elemental Partitioning.

3.2.3 Optimization of the PGM and non-PGM Additions

Since Ir and Ru did not demonstrate considerable benefits for creep strength or mitigation of TCP phases (discussed in Chapters 5 and 6), respectively, the final matrix did not consider these two PGMs, leaving Pt as the only PGM addition. At the same time, Cr and Al levels were altered in an attempt to achieve an aspect ratio near 1.0. Figures 3.22(a) and (b) depict the microstructures of DS-1 and DS-2 with an average volume fraction of 0.56. Both alloys displayed an average aspect ratio of 0.78 and contained insoluble γ′, Figure 3.22(b).

Levels of Al were decreased from 15 → 13.5 at% within the Pt-containing PX-series (PX-1→ PX-6, respectively). The aspect ratio of PX-2, Figure 3.23(a), is 0.61. Once the Al content is reduced from PX-2 to PX-3, the aspect ratio shifts to 0.14 as is shown in Figure 3.23(b). Lowering the Al content to 13.5 at% provides an even lower aspect ratio of 0.08, as shown for alloy PX-5 in Figure 3.23(c). The TEM micrographs of Figure 3.24 illustrate the variation in morphology through changes in Al for PX-2 and PX-5, Figures 3.24(a) and (b), respectively. The aspect ratio of alloy PX-2 in Figure 3.24(a) is 0.64, which is similar to the measurement made through the SEM image, Figure 3.23(a). Similar agreement is demonstrated with the microstructures of Figure 3.24(b) to that of Figure 3.23(c), indicating $\eta = 0.10$. In addition, the inset of Figure 3.24(b) indicates the presence of tertiary γ′ within the matrix phase, with η below 0.05.

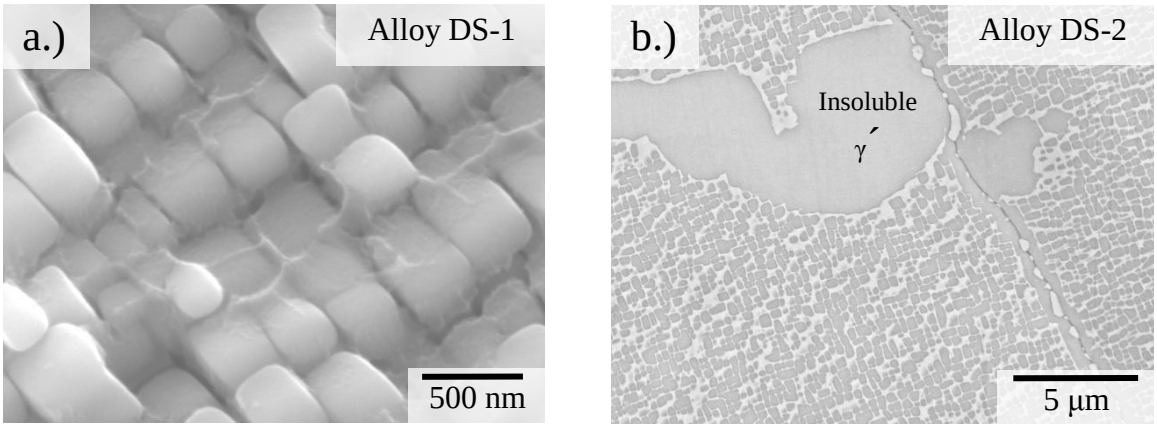

Figure 3.22: (a) Cuboidal and (b) unsoluble γ´ precipitates observed in both alloys DS-1 and DS-2.

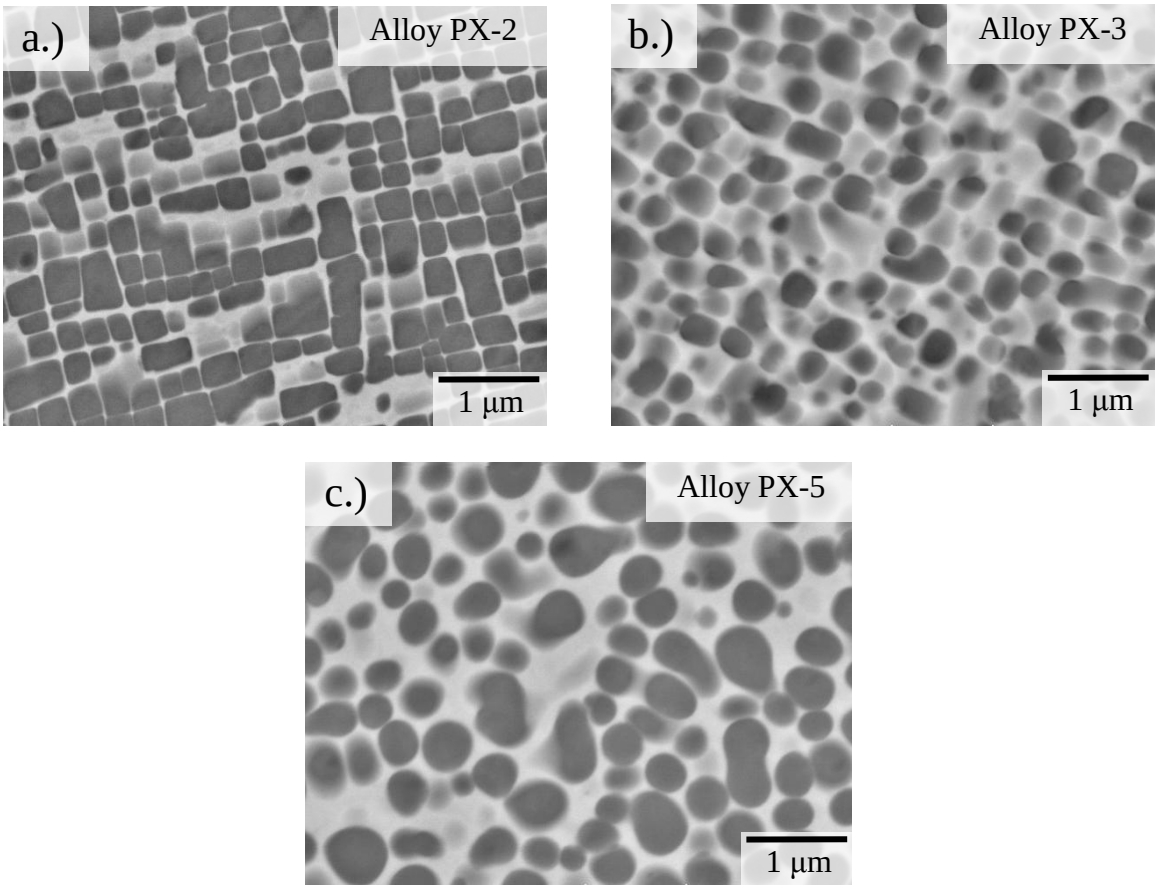

Figure 3.23: Change in γ´ morphology within PX-series due to Al.

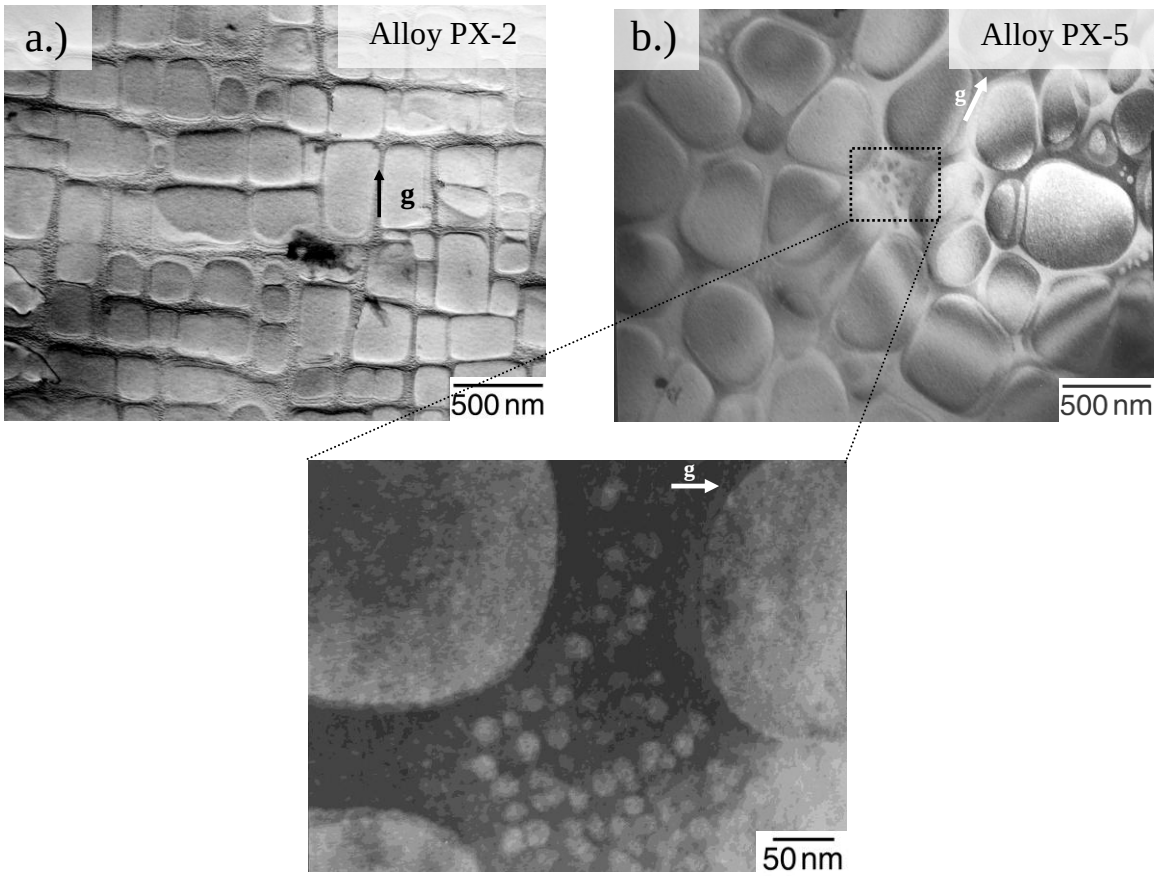

Figure 3.24: Change in γ′ morphology within PX-series due to Al. Inset highlights tertiary γ′ particles.

3.3 Summary

The systematic variation of PGM and non-PGM elemental additions alters the γ'_{Solvus} and T_S temperatures. Overall, Pt reduces the solidus temperature, while Ir increases it. Ru does not affect T_S within the range of compositions investigated. Additions of the refractory element Ta increase the γ'_{Solvus} by approximately 200 °C, narrowing the heat treatment windows to less than 30 °C. The heat treatment windows can be further influenced by modifying the Cr or Al content. The trends for Ta, Re, and

Table 3.7: DTA comparison of heat treatment windows of conventional superalloys versus PGM alloys.

Generation	Alloy	Total Refractory (wt%) (W, Mo, Re, Ta)	Heat Treatment (T_S - γ'_{Solvus})
Polycrystalline	MAR-M247	13.5	110
1st	CMSX 2	10.6	45
1st	SRR 99	13	60
2nd	René N5	17	33
3rd	CMSX 10	19.4	29
DOE PHASE	Alloy	Total Refractory + PGM (wt%) (W, Mo, Re, Ta) + (Pt, Ir, Ru)	Heat Treatment (T_S - γ'_{Solvus})
I	D3	8	243
I	D7	8.5	220
I	D8	17	14
II – high Al	D23	27	16
III	PX-5	21.5	20

W are consistent with those observed for conventional superalloys, as shown in Table 3.7.

The gamma prime morphology is influenced by the PGM and non-PGM elemental additions. Positive, near-zero, and negative lattice misfit is attained, which is quite unusual in multi-component refractory-containing superalloys. Pt additions result in precipitate morphology with high aspect ratios, usually above $\eta = 0.50$, while Ir tends to lower lattice misfit and provide parameters ranging from $0.20 < \eta < 0.30$. Adding Ru and W shifts precipitate morphologies toward $0.10 < \eta < 0.20$. Chromium and aluminum influence precipitate morphology, but their effects are dependent on the additional alloying elements within the nominal composition. With a wide range in γ' morphology, Figure 3.25 displays the relationship of the aspect ratio as a function of an alloy misfit magnitude, which was calculated through TEM analysis of interfacial dislocations on post-crept specimens using Equation 1.3. The TEM images are of as-aged

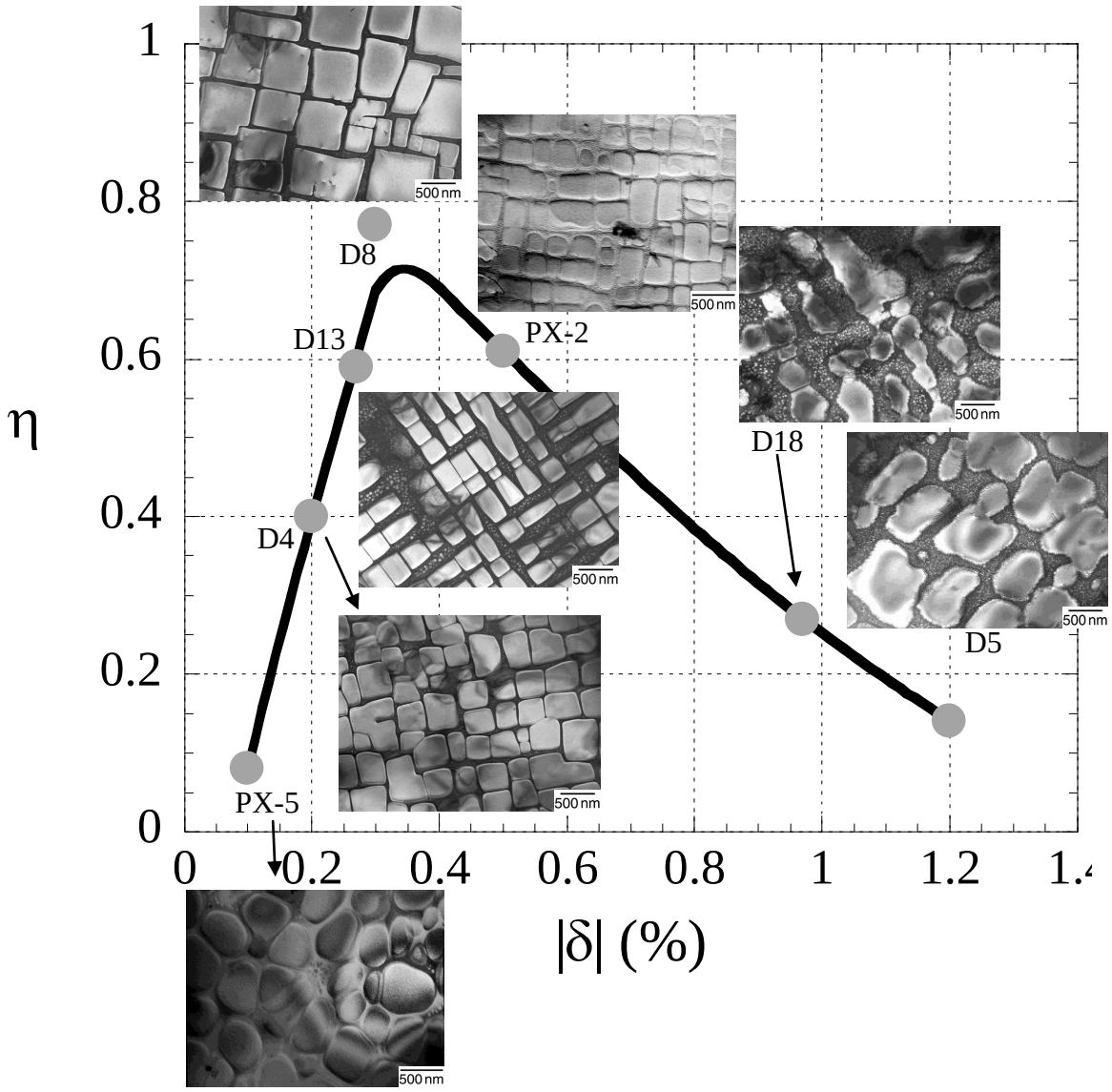

Figure 3.25: Particle aspect ratio (η) as a function of misfit magnitude (|δ|).

microstructures prior to creep. The curved fit peaks at a magnitude of approximately 0.3%. Prior to |δ| = 0.3%, particles display well-faceted morphology. As |δ| increases from 0.3 → 1.2%, particle morphology becomes ellipsoidal, and eventually transitions back toward an aspect ratio approaching zero at misfits around 1.0%, apparently due to loss of coherency. It is interesting to note that many of the strongest commercial single

crystal alloys have misfits in the range of 0.2 - 0.3%, where the aspect ratio peaks at a value of 0.80 in Figure 3.25.

CHAPTER 4

ELEMENTAL PARTITIONING ASSOCIATED WITH HIGHER ORDER ALLOYING ADDITIONS

PGM-modified Ni-base superalloys are candidate materials for high temperature applications such as turbine blades or bond coats. Thus, the study of PGM-containing alloys must include refractory additions as part of the nominal composition. Investigations on the influence of PGMs on the elemental partitioning behavior of Ni-base superalloys with moderate refractory content are detailed in this chapter. Alloys are studied with the use of electron microprobe analysis and a local electrode atom probe detector. The partitioning behavior of the PGMs was assessed in alloys with and without refractory additions, and any unusual partitioning trends associated with the non-PGM elements are presented.

4.1 Elemental Partitioning

Development of new Ni-base superalloys requires an understanding of system thermodynamics in order to control element partitioning to the constituent phases [4, 17, 99]. The partitioning of strengthening elements can also be indirectly influenced by higher order alloying additions. This section addresses the influence of PGM additions on elemental partitioning in "lean" alloys without refractory additions as well as those containing Re, W, Ta, and the PGM Ru. Table 4.1 lists the alloys that were examined for their partitioning behavior by EMPA and APT, along with their measured solidus and gamma prime solvus temperatures.

4.1.1 Microstructural Characteristics

DTA scans for alloys listed in Table 4.1 show γ'_{Solvus} temperatures less than 15 °C below the solidus temperature. As a result, populations of coarse, unsolutioned γ' precipitates were present in the aged microstructures, Figure 4.1. In addition, alloys D19, D22, D23, and D26 had measured aspect ratios of 0.21, 0.14, 0.18, and 0.21, respectively. This implies a relatively low misfit magnitude, $\delta \approx 0$. Alloy D27 with 1Ru·1W exhibited $\eta = 0.35$, while the addition of 2Ru·2W, alloy D30, shifted η from 0.35 to 0.24. Alloys D19, D22, D27, and D30 contained V_f in the range 0.64 - 0.68. Alloys D23 and D26, which contained Ir, had measured volume fractions of 0.63 and 0.60, respectively. Figure 4.2 displays the microstructure of alloys used for atom probe studies. Alloys D3 and D7 exhibited aspect ratios of 0.21 and 0.33, respectively. Alloys D21 and D25 measured η = 0.11 and 0.08, respectively. Average precipitate diameters were between 150 - 200 nm except for alloy D7, which was 200 - 250 nm.

Table 4.1: PGM alloy compositions. Alloys with an asterisk were examined by APT. DTA on solidus, T_S, and γ′-solvus, T_{Solvus}, are included.

Alloy compositions (at%): 15Al-5Cr-0.1Hf						DTA	
PGM Addition	Alloy	Composition				T_S (°C)	T_{Solvus} (°C)
		Pt	Ir	Ru	W		
Ir	*D3	0	2.5	0	0	1387	1143
Pt	*D7	2.5	0	0	0	1373	1153
Alloy compositions (at%): 15Al-5Cr-1Re-2Ta-0.1Hf						**DTA**	
PGM Addition	Alloy	Composition				T_S (°C)	T_{Solvus} (°C)
		Pt	Ir	Ru	W		
Pt	D19	2.5	0	1	1	1361	1352
	*D21	2.5	0	2	1	1361	1340
	D22	2.5	0	2	2	1360	1351
Pt-Ir	D23	2.5	2.5	1	1	1368	1353
	*D25	2.5	2.5	2	1	1373	1354
	D26	2.5	2.5	2	2	1370	1352
Higher Pt	D27	5	0	1	1	1356	1343
	D29	5	0	2	2	1356	1342

4.1.2 Electron Microprobe Analysis

Table 4.2 provides average phase compositions for C_γ and $C_{\gamma'}$ and partitioning coefficients for each element. Compositional phase analysis was conducted on unsolutioned γ′ particles that measured at least 3 μm in diameter. Hf is not reported due to low amounts within all alloys (0.1 at%). Partitioning coefficients, *p*, with a value greater than 1.0 imply preferential partitioning to the γ phase while values less than 1.0 imply preferential partitioning to the γ′ phase. Values near $p = 1.0$ indicate near equal partitioning between phases. The elements Al, Ta, and Pt preferentially partition to the γ′ phase, with Ta displaying very strong partitioning toward the precipitate. Cr, Ru, W, and Re preferentially partition to the γ phase, with Re partitioning the strongest of the four elements into the matrix. Ni and Ir partition equally between phases. Concerning the

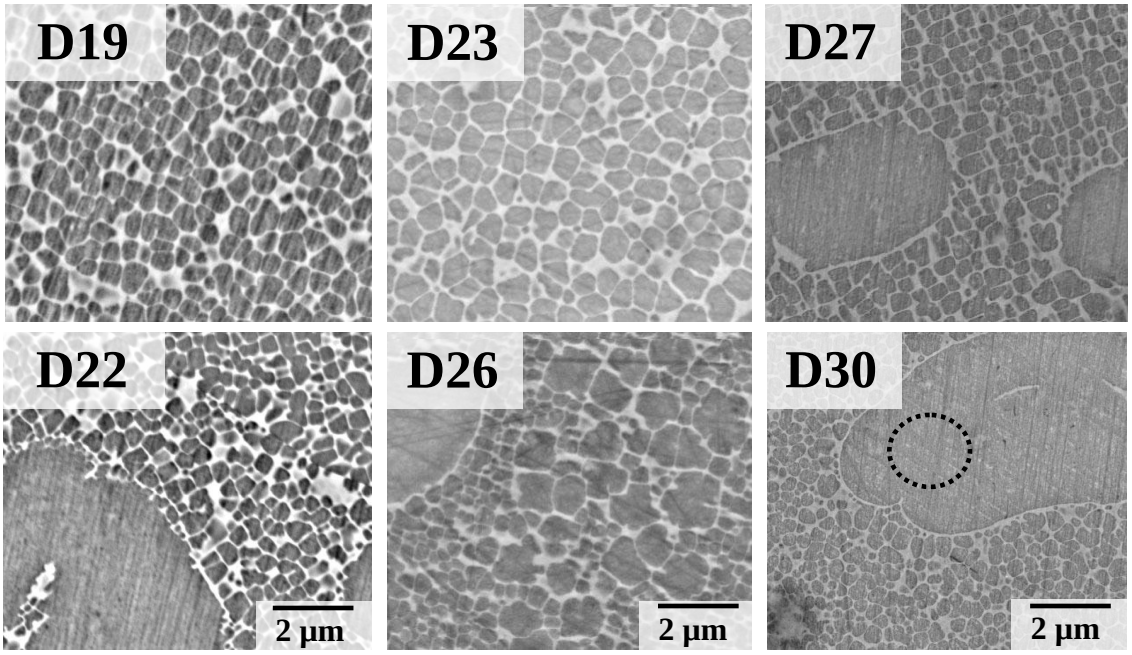

Figure 4.1: Images of alloys following heat treatment. Dotted circles have a diameter of 2 µm, which is the approximate spot size of the EMPA.

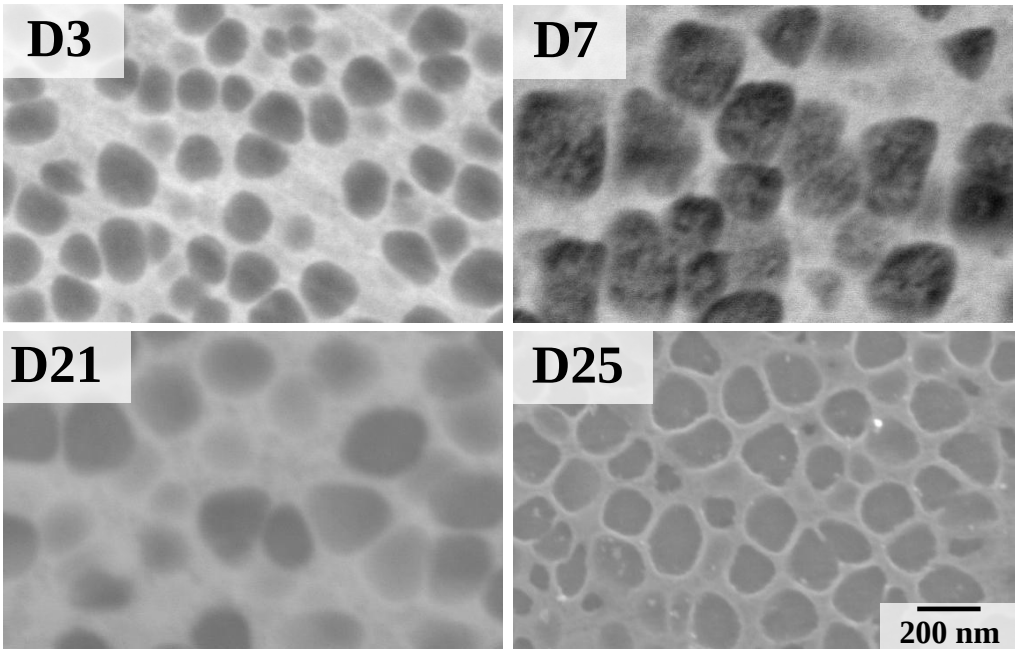

Figure 4.2: Images of alloys after homogenization used for APT.

Table 4.2: Elemental compositions of γ and γ′ phase measured by EMPA. Partitioning coefficients, $p = C_\gamma/C_{\gamma'}$, have also been included.

Alloy	Phase Comp	Element								
		Al	Cr	Ni	Ru	Ta	W	Re	Ir	Pt
D19	C_γ	10.5	6.4	75.2	1.4	0.9	2.3	2.1	0	1.4
	$C_{\gamma'}$	17.0	4.4	71.1	0.8	2.5	0.4	0.5		3.0
	$\boldsymbol{p\ (C_\gamma/C_{\gamma'})}$	***0.6***	***1.5***	***1.0***	***1.7***	***0.4***	***5.5***	***4.1***		***0.5***
D22	C_γ	9.3	8.4	71.6	3.0	0.1	4.1	2.2	0	1.3
	$C_{\gamma'}$	17.4	3.6	69.9	1.6	2.8	1.1	0.5		3.0
	$\boldsymbol{p\ (C_\gamma/C_{\gamma'})}$	***0.5***	***2.4***	***1.0***	***1.9***	***0.1***	***3.7***	***4.6***		***0.4***
D23	C_γ	12.4	7.4	71.4	1.3	0.5	1.6	1.6	2.1	1.7
	$C_{\gamma'}$	16.6	3.6	69.0	0.9	2.9	0.6	0.6	2.7	3.0
	$\boldsymbol{p\ (C_\gamma/C_{\gamma'})}$	***0.8***	***2.0***	***1.0***	***1.5***	***0.2***	***2.6***	***2.6***	***0.8***	***0.6***
D26	C_γ	11.9	6.8	68.4	2.5	1.1	2.8	1.5	2.7	2.3
	$C_{\gamma'}$	17.1	3.8	67.6	1.7	2.6	1.4	0.6	2.4	2.7
	$\boldsymbol{p\ (C_\gamma/C_{\gamma'})}$	***0.7***	***1.8***	***1.0***	***1.5***	***0.4***	***2.0***	***2.4***	***1.1***	***0.8***
D27	C_γ	12.0	7.5	71.3	1.3	0.9	1.7	1.6	0	3.7
	$C_{\gamma'}$	16.7	3.6	69.1	0.8	2.6	0.6	0.7		5.7
	$\boldsymbol{p\ (C_\gamma/C_{\gamma'})}$	***0.7***	***2.1***	***1.0***	***1.6***	***0.3***	***2.7***	***2.5***		***0.7***
D30	C_γ	11.5	8.7	67.4	2.7	0.7	3.4	2.0	0	3.5
	$C_{\gamma'}$	16.8	3.1	68.2	1.6	2.7	1.3	0.5		5.8
	$\boldsymbol{p\ (C_\gamma/C_{\gamma'})}$	***0.7***	***2.8***	***1.0***	***1.7***	***0.3***	***2.6***	***4.4***		***0.6***

PGMs, Ru, Ir, and Pt have average segregation ratios of 1.7, 1.0, and 0.6, respectively. These values agree with earlier measurements of Ru-containing [55, 67, 100], Ir-containing [67], and Pt-modified [55, 67] Ni-base superalloys.

Figure 4.3 demonstrates the effects of Ru and W additions on partitioning in alloys with 2.5Pt, 5Pt, and 2.5Pt·2.5Ir (at%), respectively. Partitioning of the γ′-formers, Al, Pt, and Ta, do not vary significantly due to Ru and W. However, matrix

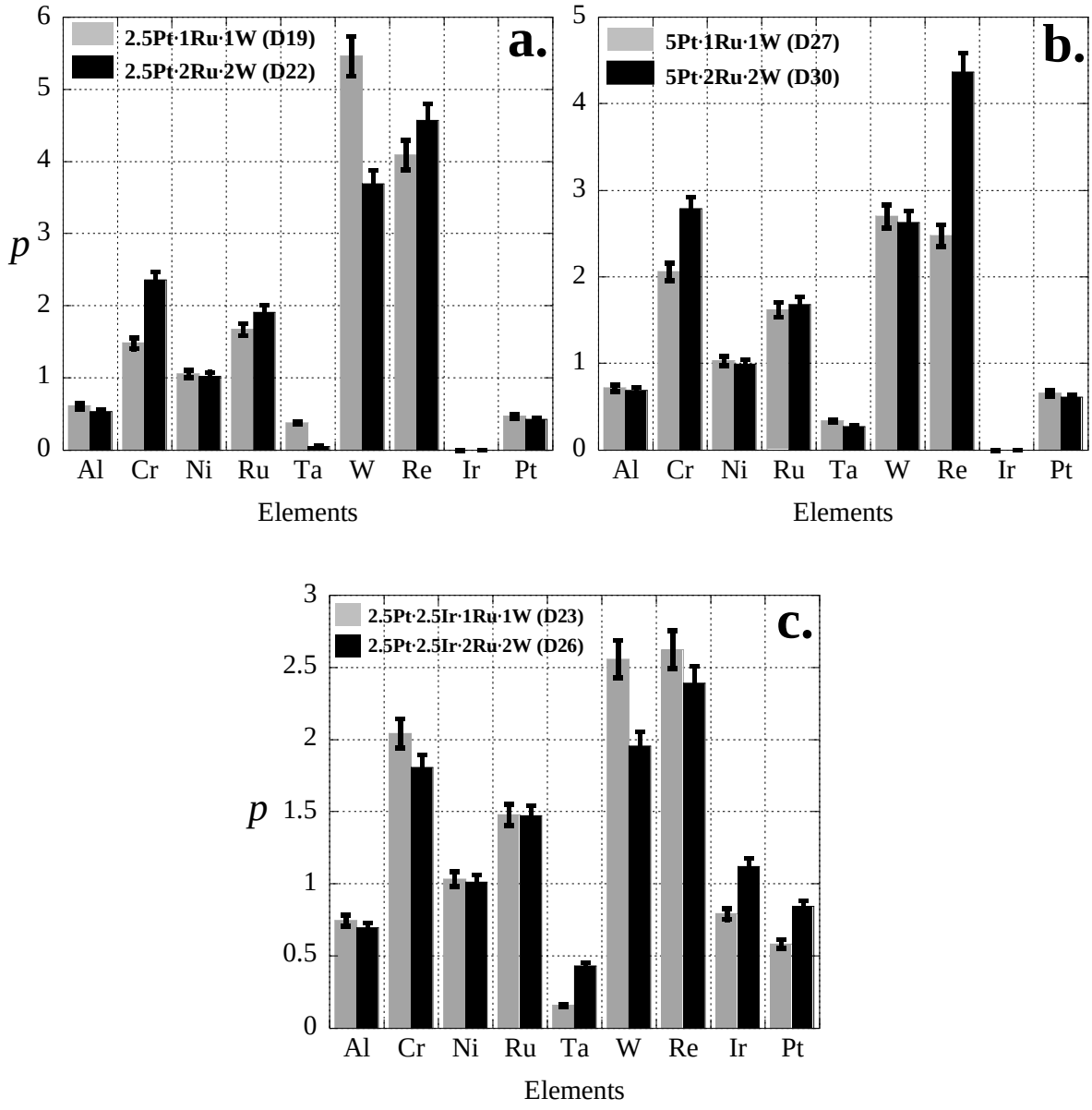

Figure 4.3: EMPA column plots displaying changes in elemental partitioning due to Ru and W additions. All plots contain the following elemental compositions (at%): 15Al·5Cr·1Re·2Ta·0.1Hf.

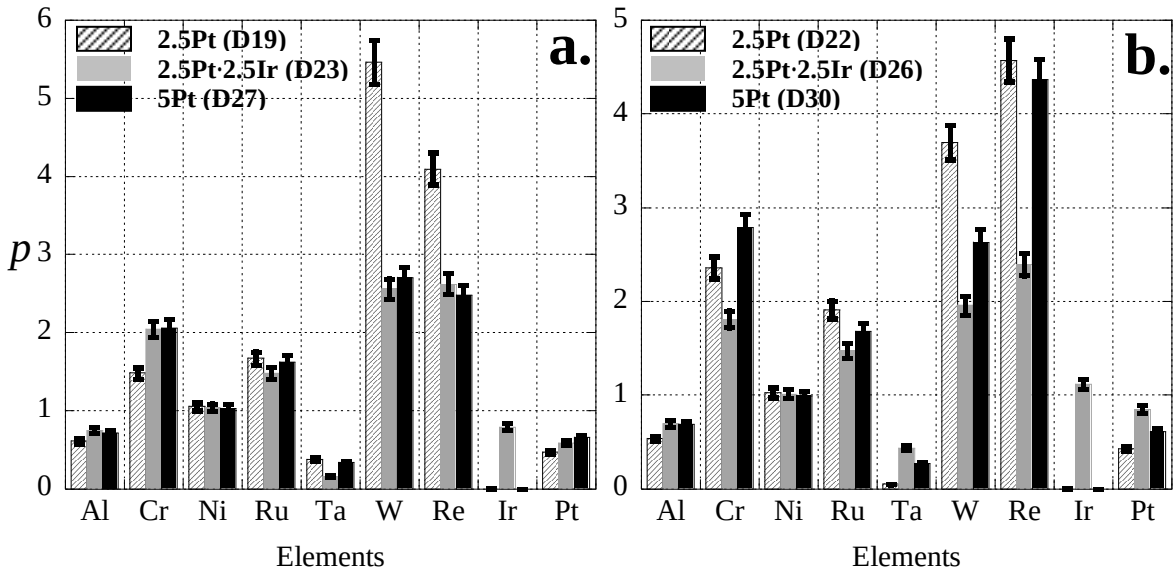

Figure 4.4: EMPA column plots displaying changes in partitioning behavior due to Pt and/or Ir PGM additions. All plots contain the following elemental compositions (at%): 15Al·5Cr·1Re·2Ta·0.1Hf. Alloys in plot A) contain 1Ru·1W and B) 2Ru·2W.

strengthening elements, such as W and Re, partition less strongly into the matrix with the additions of Ru and/or W, as demonstrated in Figures 4.3(a) and 4.3(c), respectively. Chromium partitions more strongly to the matrix due to Ru and W additions, Figures 4.3(a) and 4.3(b), when compared to alloys containing Ir, as shown in Figure 4.3(c).

Figure 4.4 summarizes the partitioning behavior due to the PGM additions (2.5Pt, 2.5Pt·2.5Ir, and 5Pt) while Ru and W additions stay constant at either 1Ru·1W, Figure 4.4(a), or 2Ru·2W, Figure 4.4(b). Despite Ru and W each increasing from 1 → 2 at%, Figure 4.4(a) → Figure 4.4(b), the γ′-partitioning elements, Ta, Al, and Pt, do not shift their partitioning behavior from the γ′ phase. With the addition of Ir, however, partitioning of W, Re, Ru, Al, and Pt is reduced. Unlike Ru and Pt, the PGM Ir shifts partitioning tendencies of both PGM and non-PGM elements.

4.1.3 Atom Probe Tomography

Table 4.3 provides phase compositions as well as partitioning ratios for each element examined by APT. Standard deviations measured for all elements were less than 0.01 at%. In alloys D3 and D7, Al and Cr partition toward the matrix to the same degree, regardless of the PGM addition. For the PGMs, Pt partitions to γ′ (p = 0.6) while Ir again shows near equal partitioning (p = 1.0). Alloys D21 and D25 shows similar partitioning for Pt and Ir, regardless of refractory content. The Al, Ta, and Ru do not shift from their respective phases with varying the Ir additions, as demonstrated by comparing alloys D21 to D25. Partitioning of Re increases and Cr decreases, into the matrix, respectively, with the addition of Ir. Surprisingly, W has partition coefficients of 0.5 and 0.7 for alloys D21 and D25, respectively, indicating preferential partitioning to the γ′ phase, in contrast to the EMPA results in Table 4.2 that show W preferentially partitioning to the γ phase.

The image in Figure 4.5 is a reconstruction from the data collected by the LEAP detector for alloy D3. The image has been false colored so as to provide phase contrast between the gamma prime precipitates (green) and gamma matrix (blue). Figure 4.6 shows reconstructed APT data for alloys D3 and D7. Each image represents a 'slice' of data, ~10 nm thick taken from the bulk 3D dataset. The slice is viewed in transmission, approximating the atomic distribution in 2D. Iridium partitions equally between phases, while Pt weakly partitions to the γ′ phase. Similarly, Al and Cr partition to their respective phases, regardless of PGM content.

Figure 4.7 displays slices of alloy D25. The top row shows elements that partition preferentially to γ′, the middle row those that partition to the γ matrix, and those that partition near equally are displayed along the bottom. Although the W image shows, to

Table 4.3: Elemental compositions of γ and γ′ phase measured by APT. Partitioning coefficients, *p*, have also been included.

Alloy	Phase Composition	Element								
		Al	Cr	Ni	Ru	Ta	W	Re	Ir	Pt
D3	C_{γ}	11.3	6.6	79.3	0	0			2.8	0
	$C_{\gamma'}$	19.9	4.4	72.5					2.7	
	***p* ($C_{\gamma}/C_{\gamma'}$)**	***0.6***	***1.5***	***1.1***					***1.0***	
D7	C_{γ}	10.2	6.0	81.9	0	0			0	1.8
	$C_{\gamma'}$	19.0	3.9	73.9						3.0
	***p* ($C_{\gamma}/C_{\gamma'}$)**	***0.5***	***1.5***	***1.1***						***0.6***
D21	C_{γ}	7.4	13.9	68.3	4.3	0.4	1.2	2.8	0	1.5
	$C_{\gamma'}$	19.2	3.4	66.9	1.7	1.8	2.2	0.9		3.6
	***p* ($C_{\gamma}/C_{\gamma'}$)**	***0.4***	***4.1***	***1.0***	***2.5***	***0.2***	***0.5***	***3.0***		***0.4***
D25	C_{γ}	8.6	10.5	68.2	3.9	0.4	1.2	2.6	2.4	2.0
	$C_{\gamma'}$	18.3	3.0	66.0	1.8	2.4	1.7	0.6	2.7	3.1
	***p* ($C_{\gamma}/C_{\gamma'}$)**	***0.5***	***3.5***	***1.0***	***2.2***	***0.2***	***0.7***	***4.3***	***0.9***	***0.6***

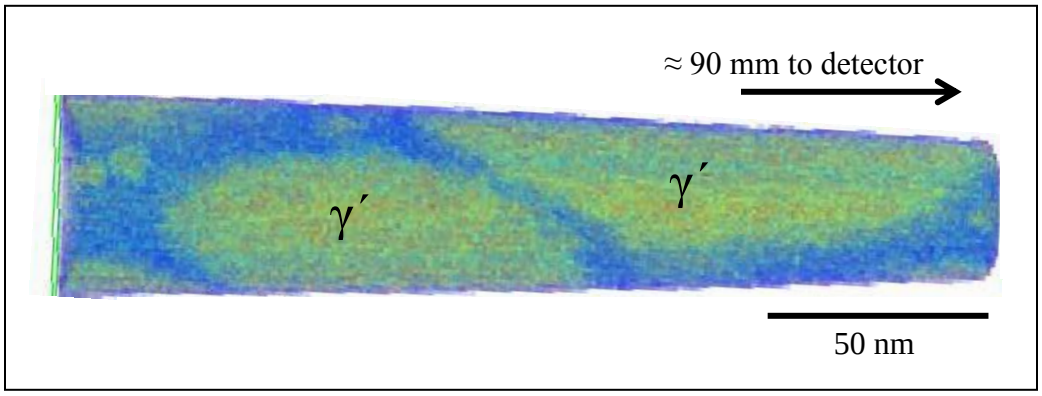

Figure 4.5: Reconstruction of atom probe dataset for alloy D3. Image has been false colored to highlight γ′ particles (green) and γ matrix (blue).

some extent, near equal partitioning, partitioning coefficients listed in Table 4.3 indicate preferential partitioning to the γ′ phase. Platinum and Ir show weak and near equal partitioning, respectively, whereas Ru weakly partitions to the γ phase. It is emphasized that these 2D images depict only a fraction of the total amount of ions collected from the

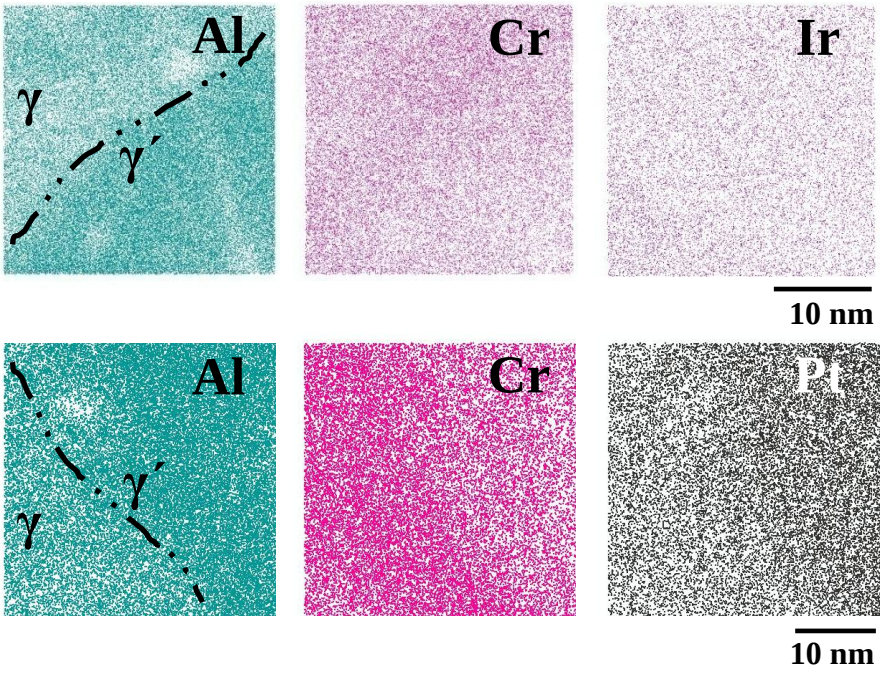

Figure 4.6: Atom probe data showing partitioning in alloys D3 (top row) and D7 (bottom row). Ni and Hf are omitted. Dotted lines help in locating the γ/γ′ interface.

LEAP detector for each element. Thus compositional analysis using multiple ROI's within the phase of interest is important for acquisition of accurate quantitative measurements.

Figure 4.8 highlights compositional profiles of alloys D3 and D7 and how the PGMs affect γ′ volume fraction, represented by the slope, Equation 2.2. Volume fractions of γ′ for alloys D3 and D7 are 0.41 and 0.55, respectively. The location of iridium near the origin of the plot indicates equal partitioning between phases, while Pt shows weak partitioning to the precipitate. Al and Cr do not shift their degree of partitioning with either PGM being present in the system. Figure 4.9 displays alloys D21 and D25, with the bottom inset highlighting elemental partitioning around the origin. Volume fractions measured 0.65 and 0.63 for alloys D21 and D25, respectively. From

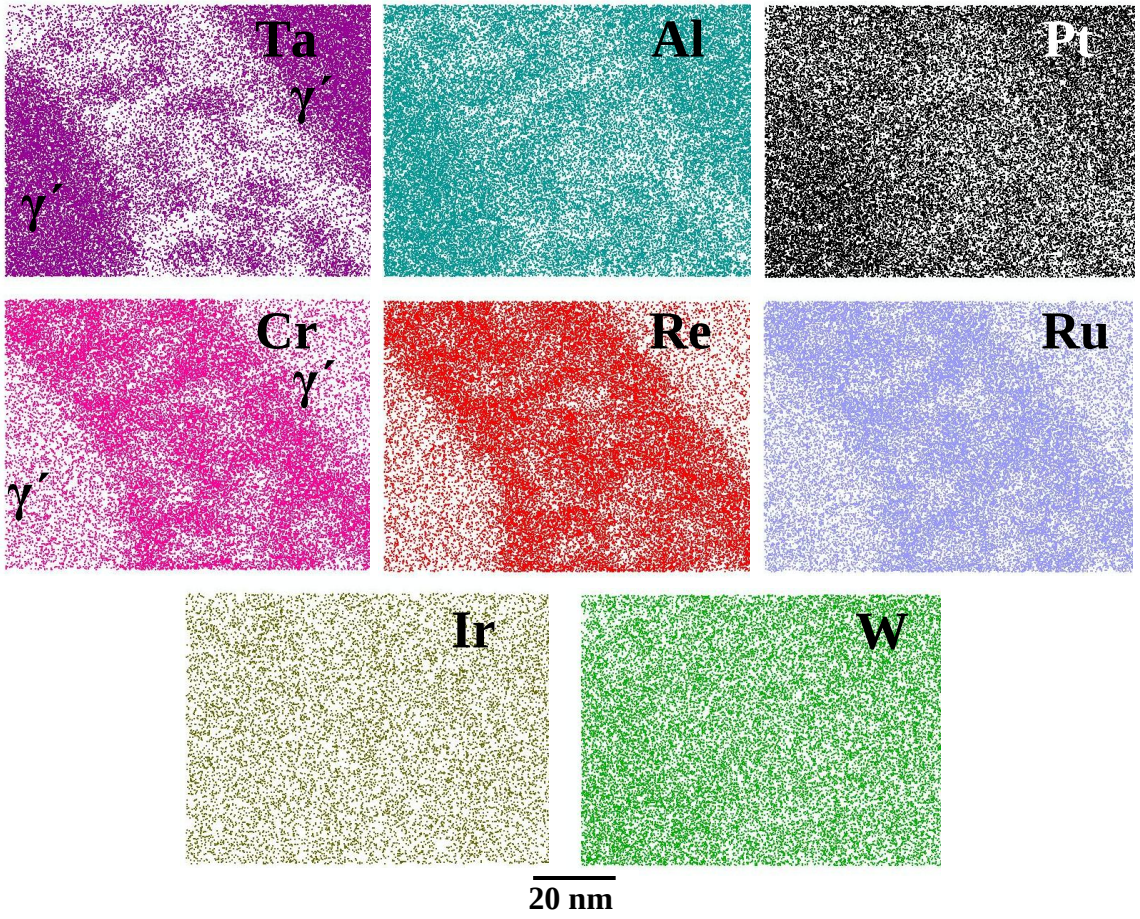

Figure 4.7: Atom probe data showing partitioning in alloy D25 (Ni and Hf are omitted). Displayed within the images are two γ´ particles separated by the γ matrix. Tertiary γ´ precipitates are observed within the matrix.

the top plot, Cr partitions more strongly into the matrix compared to its position in Figure 4.8. Figure 4.9 displays, from the bottom inset, that elements from both phases tend to cluster closer to the origin with the addition of Ir. Furthermore, W preferentially partitions to γ´, but with the addition of Ir, partitions less strongly into the precipitate.

Within the range of PGM alloys studied, the Ta refractory addition strongly partitions to γ´, while Re displays strong partitioning toward the matrix ($p_{Re} \approx 3.5$). When refractory additions are part of the nominal composition, iridium can influence

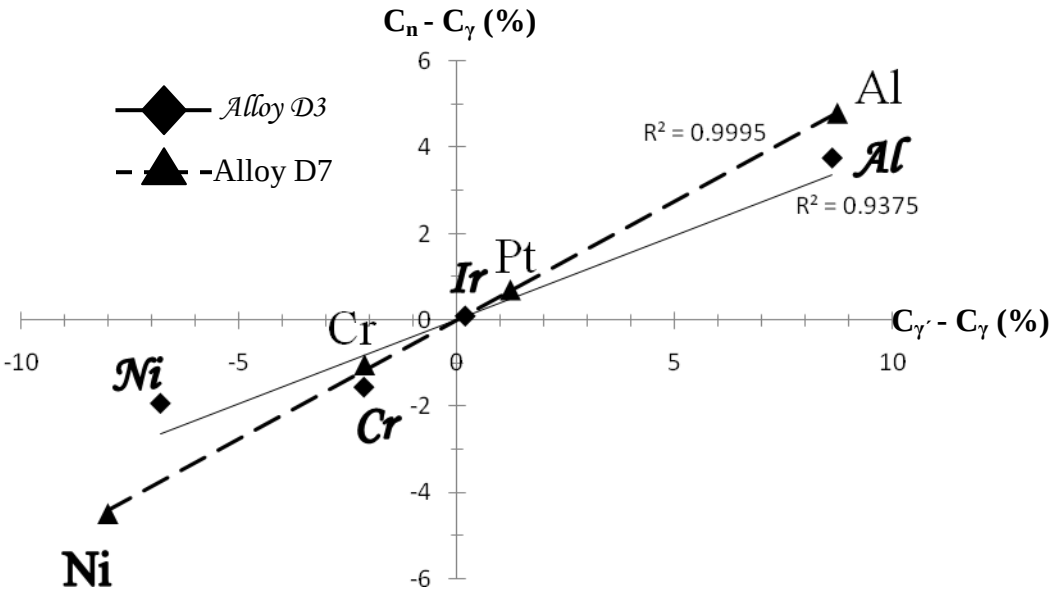

Figure 4.8: Atom probe compositional profile between alloys D3 (Ir) and D7 (Pt) and PGMs effect on volume fraction.

partitioning of PGM and non-PGM elements. Iridiums influence on partitioning of additional elements and tungstens unusual partitioning behavior post-homogenization, and post-aging, are new and uncommon within Ni-base compositions.

4.2 Discussion

Design of Ni-base alloy compositions that contain PGMs requires new alloying strategies due to significant differences in partitioning behavior of most of the superalloy constituents, compared to previous generations of single crystal alloys. This partitioning behavior, which has been examined by EMPA and APT techniques, has led to a wide range in lattice misfit and precipitate morphology. Since the compositions of the γ and γ′

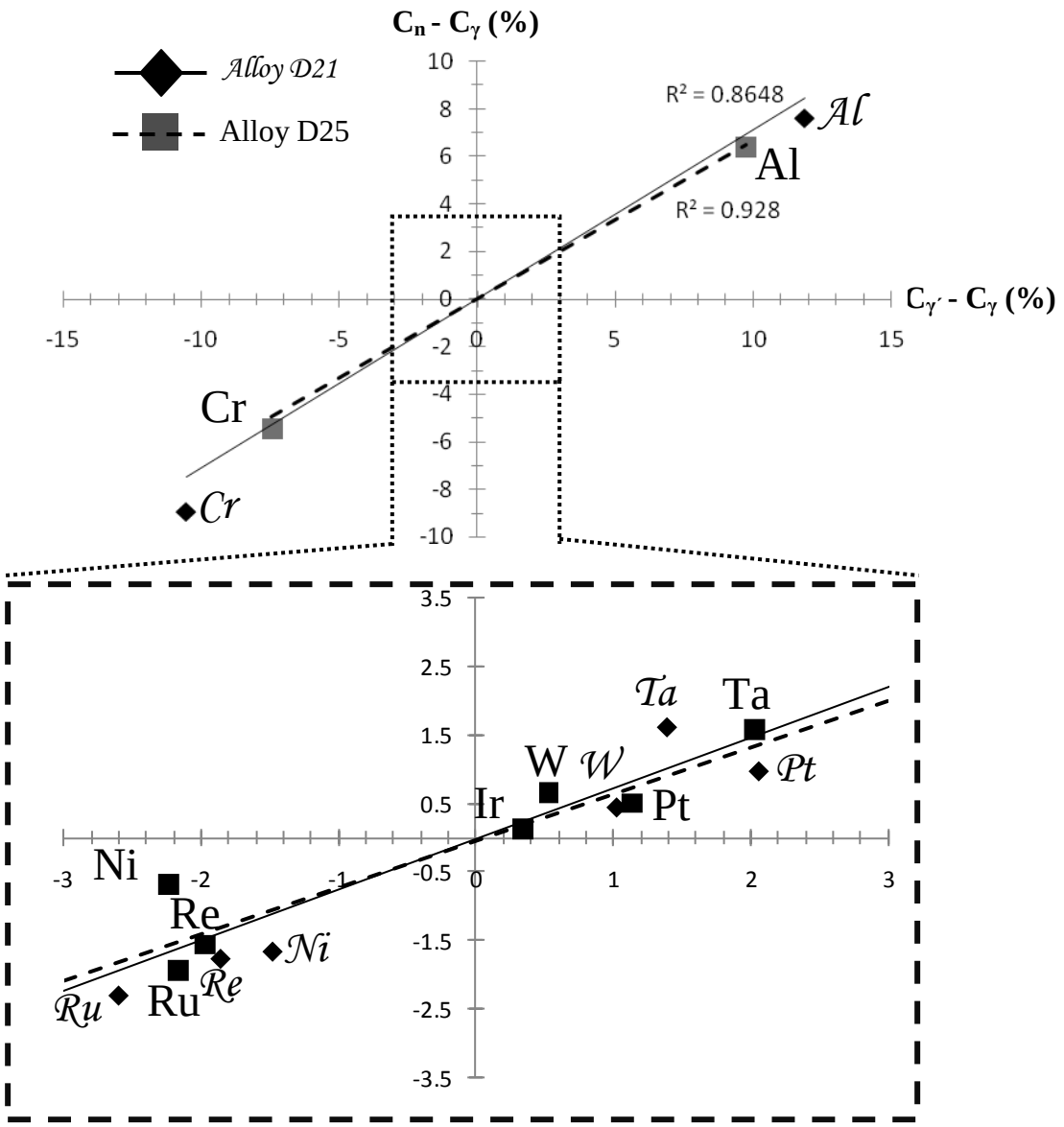

Figure 4.9: Atom probe compositional profile of alloys D21 (without Ir) and D25 (+2.5 at% Ir). Top profile illustrates changes in Al and Cr content along with changes in volume fraction. Bottom inset displays elemental profiles around the origin.

phases influence creep properties, this section reviews the influence, if any, the PGMs have on partitioning behavior. The unusual partitioning behavior of the refractory elements, Re and W, are addressed as well.

4.2.1 Elemental Partitioning

The refractory elements, Re and Ta, show strong partitioning behavior toward the γ and γ′ phases, respectively, with PGM additions. However, the Re partitioning coefficient, which averages 3.5 for the investigated alloys, is lower in comparison to conventional single crystal alloys, such as René N5, or a PGM modified RR2100 [29, 55]. Measurements of Re partitioning within René N5 indicates a partitioning coefficient of 14.4 [29], which is 4x greater than the average coefficient of Re within this study. This is significant as high levels of strongly partitioning Re have resulted in substantial improvements in the creep properties of nickel-base single crystals [4, 5]. The alloys in DOE Phase I and Phase II - high Al, contained 15 at% Al compared to Al levels of 13.5 - 14 at% in the above mentioned single crystals. Recent studies by Zhu *et al*. [101] on the ternary Ni-Al-Re system indicates that with 15Al-1Re (at%), the solubility of Re in the γ′ phase is greater than a system with a reduced Al content, thereby lowering partitioning of Re to the matrix. Such low partitioning for Re to the matrix would likely contribute to poor high temperature mechanical strength.

Overall, Pt and Ru display near-equal partitioning with a slight preference for the γ′ and γ phases, respectively. The presence of refractory elements or Ru, Figures 4.3(a), 4.5, and 4.7, do not significantly influence Pt partitioning. The work by Hayashi *et al.* [68] demonstrates that with 15at% Al, a Pt content of 2.5 or 5% provides similar tie-lines within the two phase region of γ and γ′. Rutheniums partitioning to the γ phase occurs within the ternary Ni-Al-Ru system with a base composition of 15Al-(1 - 2)Ru (at%) [102], and this study demonstrates rutheniums partitioning behavior to the matrix extending to multi-component systems. Recent studies of other individual alloys also

observed weak partitioning of Ru to the matrix [19, 55, 65].

Like Pt, Ir partitioning is not strongly influenced by refractory additions or Ru, in agreement with two previous studies on Ni-base superalloys with Ir additions [65, 103]. The most recent study on the Ni-Al-Ir ternary phase diagram at high temperature suggests that with 15at% Al, and 2.5at% Ir, preferential partitioning of Ir to γ occurs [104], which is not the case in the present alloys. The near equal partitioning of Ir apparently occurs only with Al and Cr additions to the Ni-base composition, shown in Figure 4.8. Coupled with a Ni-Al-Ir ternary, availability of a Ni-Cr-Ir phase diagram would be quite useful for understanding Ir partitioning behavior. Furthermore, Figures 4.4(a) and 4.4(b), as well as Figure 4.9, indicate that Ir reduces partitioning of elements whether the element is a PGM or among those alloying additions typically found in previous generations of single crystals. In this regard, Ir additions may be useful in manipulating and altering alloying chemistry in the event where strong segregation of certain elements is not desired.

4.2.2 Microanalysis Techniques

Although alloys used for EMPA were homogenized and aged and alloys used for APT were only homogenized, the partition coefficients, particularly the PGMs, were in good agreement between techniques. APT provided accurate quantitative measurements between the γ and γ′ phases, with standard deviations less than 0.01at%. In contrast, EMPA does not provide as accurate phase composition values, as highlighted by the standard deviations. Causes of high standard deviation in the EMPA data include x-ray line overlap between elements, as demonstrated by the parameters presented in Table 2.10, and the interaction volume of the electron beam. It is also important to consider the strong bimodal phase distribution between solutionized and unsolutionized γ′, which can

lead to slight variations in precipitate composition, causing shifts in partitioning coefficients. Finally, unlike APT, where phase compositions are individually measured for each phase, an inaccurate calculation of $C_{\gamma'}$ by the EMPA technique leads to inaccurate values of C_{γ}, shown by Equation 2.1. One obvious limitation of APT is the sample volume investigated, averaging around (20 x 20 x 100) nm^3. For single crystals, if the volume sampled by the LEAP detector occurs within a dendrite core, quantitative assessments could be misleading if homogenization times and temperatures were insufficient for elimination of solidification-induced segregation. EMPA, however, allows for sampling over a larger volume of material, reducing bias between interdendritic and dendritic regions of a Ni-base superalloy. Compositional analysis error from APT can also originate from inaccurate peak identification of the mass spectrum, which includes overlap of elemental isotopes, particularly from refractory and PGM elements, although all care was taken in this study to avoid such effects and, as such, do not strongly influence the data presented.

4.2.3 Tungsten Partitioning

The measured partitioning behavior of W was quite unusual. EMPA showed preferential partitioning to the γ phase, yet APT indicated γ′ partitioning. Considering that APT samples were in the quenched state prior to aging and the EMPA samples were aged, these differences might be due to the thermal cycle.

Prior investigations of W partitioning behavior within Ni-base systems have been confined to ternary and quaternary systems [105, 106]. Direct comparisons between $C_{\gamma,W}$ of alloy D21 (Table 4.3) versus alloy D19 (Table 4.2) shows a 1.1 at% increase in $C_{\gamma,W}$ upon aging. To investigate the temperature dependence of the composition of the γ and

γ′ phases, PANDAT *ver*. 7.0 with accompanying Ni database was employed. Figure 4.10(a) shows the Ni-Al-W ternary, while Figure 4.10(b) is the Ni-Al-W pseudo-ternary adjusted for the alloying elements present in D21. Both phase diagrams were calculated for a temperature 30 °C below the solidus in an effort to include undercooling effects on the APT alloys. The elements in the multi-component system shift the γ + γ′ phase region toward lower Al content. Also, for a fixed volume fraction of γ′, there are large shifts in the W content of the γ phase for changes in Al level, Figure 4.10(a). For the multi-component system, these changes in W content at a temperature just below the solidus are less pronounced. Figure 4.11 displays the change in W partitioning from T_S - 30 °C down to the aging temperature for the D21 alloy, indicating stronger partitioning toward the matrix at lower temperatures, in agreement with the experimental observations. Furthermore, the $C_{\gamma,W}$ increases approximately 1 at% from T_S - 30 °C to ~ 1.8 at% at the aging temperature, indicating that these changes in partitioning arise from the thermodynamics of the system. The W content of the γ′ phase is near-constant over this large temperature range, varying between 0.5 and 0.7 at%. As a result, as the temperature decreases and the V_f increases the γ phase becomes progressively enriched in W to balance the overall 1 at% addition of tungsten. This results in an increase of the partitioning coefficient for W at lower temperatures, where V_f are higher.

4.3 Summary

The PGMs Pt and Ru demonstrate preferential partitioning behavior toward the precipitate and matrix, respectively. Platinum partitions in a similar manner with the

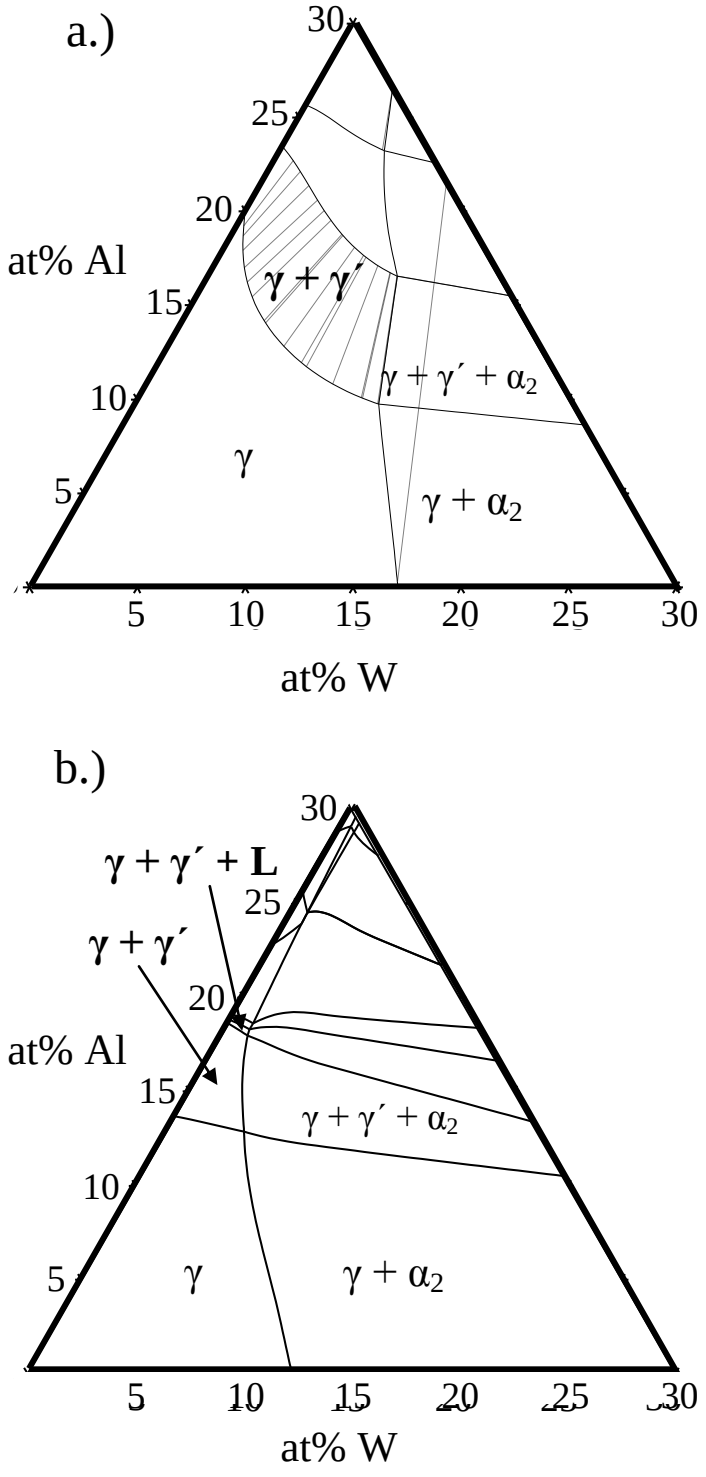

Figure 4.10: PANDAT calculation of Ni-Al-W ternary (a) and pseudo-ternary for alloy D21 (b) at 30 °C below the solidus temperature.

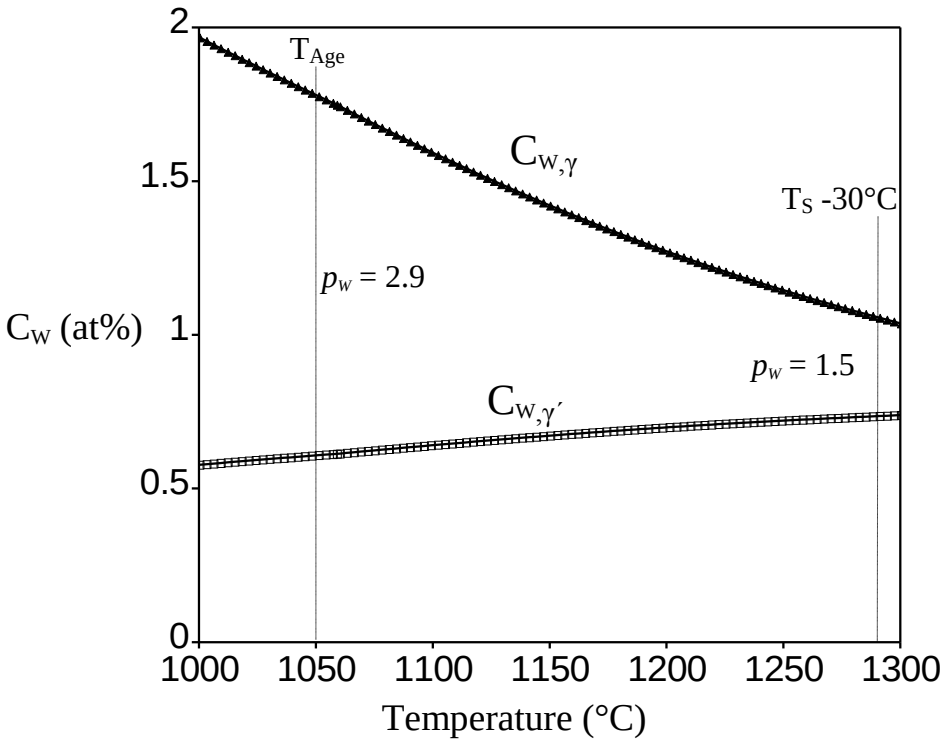

Figure 4.11: PANDAT calculation of W composition in alloy D21 at aging temperature and 30 °C below the solidus temperature. Partitioning coefficients are included near each specified temperature.

inclusion of refractory elements. Even though Ir partitions nearly equal between phases with and without refractory content, this PGM alters the partitioning behavior of other PGM and non-PGM elements in alloys composed of higher order additions. The reduced volume fractions of precipitates in Ir-containing alloys are due to shifts in the tie-line within these multi-component systems. Furthermore, there was considerably weaker partitioning of Re to the matrix when compared to conventional single crystals, as well as unusual partitioning behavior observed for W, both of which can have adverse effects on high temperature creep strength.

CHAPTER 5

COARSENING KINETICS OF A PT-CONTAINING SUPERALLOY WITH MODERATE REFRACTORY ADDITIONS

The strength imparted by the gamma prime phase is dependent on the volume fraction, size, and chemical composition of the precipitates. These factors influence the behavior of the material during long term exposure at high temperature – a serious issue since the operating conditions for superalloys can exceed 950 °C and blades may be used for up to 40,000 h. For this reason, this chapter investigates coarsening kinetics, precipitate morphology, and partitioning of γ′-forming elements for a Pt-containing Ni-base superalloy. Determining whether precipitate coarsening is mitigated by PGM additions, particularly Pt, and whether changes in coarsening kinetics may influence high temperature creep resistance, is addressed.

5.1 Precipitate Coarsening

This section addresses the coarsening kinetics of a Pt-containing Ni-base superalloy. Because coarsening requires diffusional redistribution of elements that strongly partition to the gamma prime phase, it is important to determine whether the Pt partitioning behavior influences precipitate coarsening. Table 5.1 provides the nominal composition of alloy PX-5 along with other Ni-base superalloys for comparison. It can be seen from Table 5.1 that alloy PX-5 has a nominal composition that includes Re, Ta, and W. Coarsening studies have been conducted within conventional Ni-base compositional domains [26, 107-109] containing these refractory elements, but there have been no detailed studies that include all three refractory elements within the same nominal composition. These three elements, along with Pt, can heavily influence interdiffusion within the matrix, thereby effecting microstructure, coarsening, and precipitate shape/composition.

5.1.1 Microstructure

To assess coarsening kinetics, precipitate size and morphology at each testing temperature was characterized. Figure 5.1 displays the microstructure of alloy PX-5 after homogenization. A high density of precipitates with $\eta = 0.12$ is present immediately after quenching ($V_f = 0.61 \pm 0.04$). The gamma prime morphology was evaluated at the final aging time, 24 h, for each temperature, Figure 5.2. The aspect ratio in Figure 5.2(a) is equal to 0.26, indicating moderate lattice misfit, ranging from 0.1 - 0.3% [4]. The aspect ratios at T = 1100, 1150, and 1200 °C are 0.22, 0.44, and 0.43, Figures 5.2(b), (c), and (d), respectively. Anisotropic particle coarsening has been reported for precipitates

Table 5.1: Compositions (at%) of PX-5 *vs.* various multi-component Ni-base alloys. γ'_{Solvus}, investigated temperatures (T_{inv}), and *Q* are given for comparison.

Alloy	Composition (at%)											
	Al	Pt	Cr	Re	Ta	W	Ti	Mo	Si	Co	Nb	Other
PX-5	13.5	2.5	7.5	1	2	1	0.5	1	0.5	-	-	0.2 Hf 0.014 Zr 0.1 C 0.087 B
René 88DT [107]	3.8	-	18	-	-	1.3	4.9	2.4	-	12.9	0.4	0.24 C 0.16 B
FGH-95 [109]	7.4	-	14.5	-	-	1.1	3.1	2.1	-	7.7	2.1	-
CMSX-2 [108]	12.5	-	9	-	2	2.6	1.2	0.4	-	4.7	-	-

Alloy	γ'_{solvus} (°C)	$T_{inv.}$(°C)	Q (kJ/mol)
PX-5	1323	1050 – 1200	388 (± 12.5)
René 88DT	1130	760	~ 270
FGH-95	1165	1000 - 1140	288.2
CMSX-2	1265	800 - 1050	260

within Ni-base superalloys coarsened at high temperatures [52, 110, 111], but were not observed for this study.

To assess whether particle coarsening follows a cube-root time dependence, Figure 5.3 plots average particle sizes $\frac{\bar{a}}{2}$ (nm) as a function of time ($t^{1/3}$) for each aged temperature. Figures 5.3(a - d) demonstrates that precipitate coarsening obeys this relationship, in accordance with other Ni-base coarsening studies [26, 107-109, 112]. The fitted slope in Figures 5.3(a - d) provides the rate constant, *k* (nm^3/min), which is listed, along with average edge lengths, *a*, in Table 5.2. Studies which measured the coarsening rate constants of Ni-base superalloys at/near 1050 °C are of the same order of magnitude as the rate constants measured in this study at 1050 °C, as shown in Table 5.3.

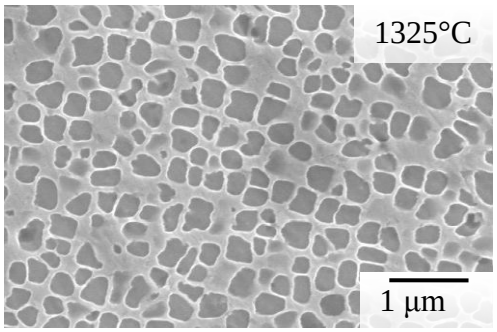

Figure 5.1: Gamma prime post-homogenization and prior to aging. Homogenization was for 6 h followed by an iced water quench.

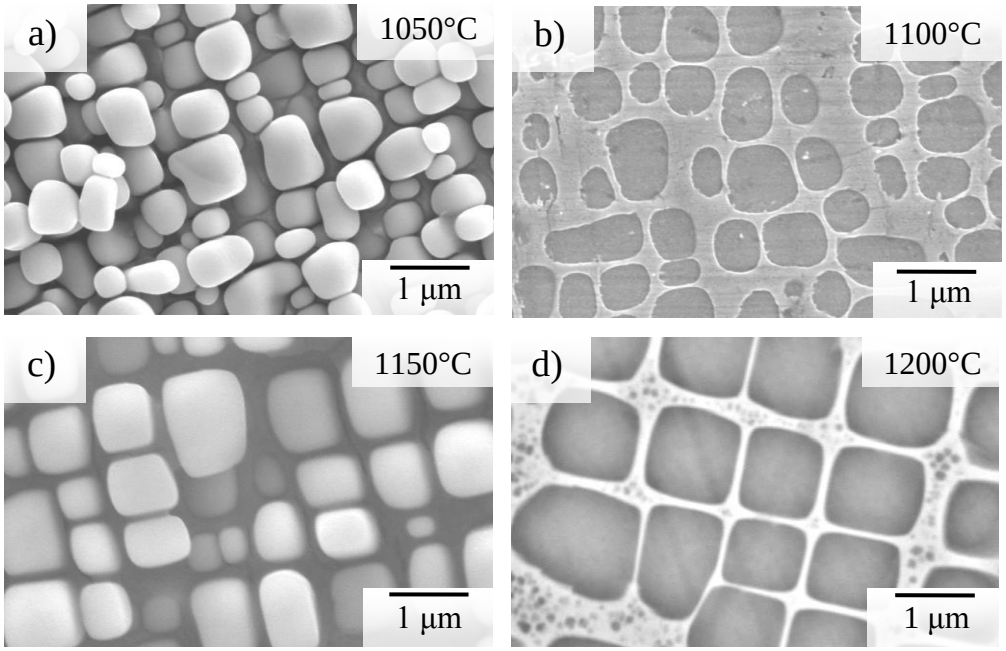

Figure 5.2: Gamma prime morphology after 24 h aging in open air at each temperature.

Even so, the rate constants of the alloys tested by Ges [108] and Giamei [26] at 1050 °C are 5x and 9x faster than that of alloy PX-5, respectively.

5.1.2 Gamma Prime Solvus and Volume Fraction

For a superalloy to retain sufficiently high V_f beyond 1000 °C, the γ'_{Solvus} must be

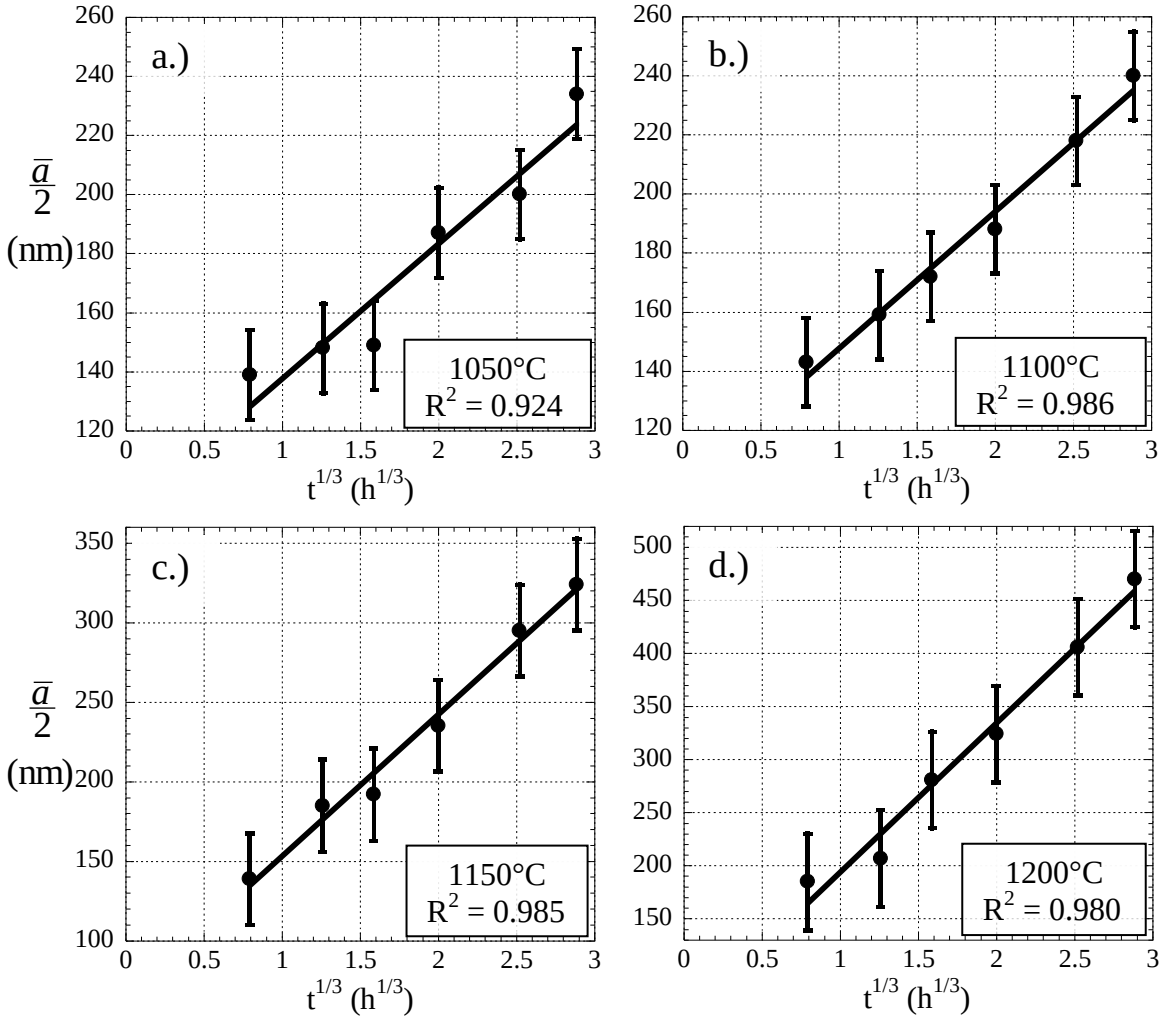

Figure 5.3: Average particle size as a function of time ($t^{1/3}$) for investigated temperatures.

Table 5.2: Experimental values of edge length, *a*, and rate constant, *k*.

T (°C)	*a* / 2 (nm)	*k* (nm^3 / min)
Solutioned (1323)	121 (± 16)	---
1050	168 (± 40)	$1.59 \cdot 10^3$
1100	197 (± 43)	$1.66 \cdot 10^3$
1150	229 (± 71)	$1.18 \cdot 10^4$
1200	312 (± 112)	$4.67 \cdot 10^4$

Table 5.3: Comparison of rate constants measured at/near 1050 °C.

Alloy	Composition (at%)										
	Al	Pt	Cr	Re	Ta	W	Ti	Mo	Co	Nb	*k* (1050 °C) (nm^3 / min)
PX-5	13.5	2.5	7.5	1	2	1	0.5	1	-	-	$1.59 \cdot 10^3$
1444 [26]	11	-	10.4	1.3	0	2.9	2.5	0	0	0.6	$14.0 \cdot 10^3$
CMSX-2 [108]	12.5	-	9	-	2	2.6	1.2	0.4	4.7	-	$8.2 \cdot 10^3$

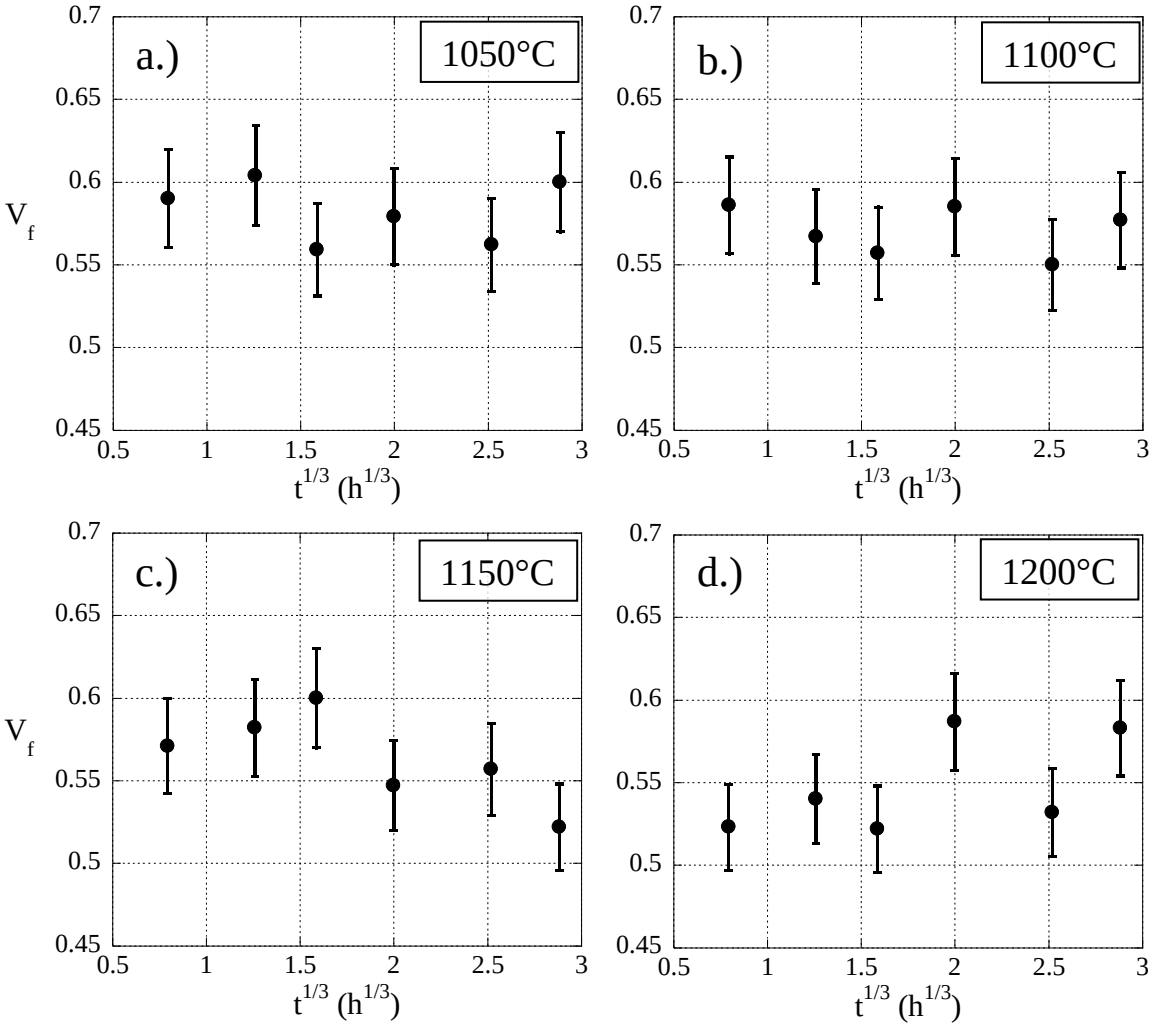

Figure 5.4: Volume fractions (γ′) *vs.* $t^{1/3}$ ($h^{1/3}$). Measurements were conducted at (a) 1050 °C, (b) 1100 °C, (c) 1150 °C, and (d) 1200 °C.

high enough so as not to allow considerable dissolution of the precipitate into the matrix. PX-5 displayed the highest γ'_{Solvus} of all alloys in Table 5.1. Although Ta additions raise the γ'_{Solvus} [113], PX-5 displays a solvus temperature 55 °C higher than CMSX-2. The absence of Ta within René 88DT and FGH95 produces a solvus temperature 170 °C lower than PX-5.

High temperature coarsening studies on Ni-Al alloys conducted by Ardell has demonstrated that γ' volume fractions reach thermodynamic equilibrium shortly after homogenization [25, 114]. To verify this, Figure 5.4 displays measured V_f for each aging time at investigated temperatures. The volume fraction remains constant at each temperature, indicating that equilibrium fractions of γ' were present across the range of experimental conditions. One striking characteristic is the precipitate volume fractions at 1200 °C, measured as 0.54 ± 0.03. Figure 5.4(d) confirms that V_f remains constant up to 24 h. The measurements on precipitate volume fractions at 1200 °C on other Ni-base superalloy single crystals (PWA 1484, AM1, and CMSX-4) ranges from 0.25 - 0.32 [111, 115, 116]. Figure 5.5 plots average V_f at each temperature compared to thermodynamic calculations obtained through the PANDAT 8.1 Ni database. For the two lowest temperatures (1050 °C and 1100 °C), the experimental and thermodynamic data are in agreement.

5.1.3 Phase Compositions

One method toward evaluating precipitate stability is determining which elements preferentially partition to the γ' phase. Table 5.4 provides information on the partitioning of elements to the γ and γ' phases after aging PX-5 at 1250 °C. The volume fraction at 1250 °C was measured as 0.32. Partitioning coefficients, *p*, are listed for each element.

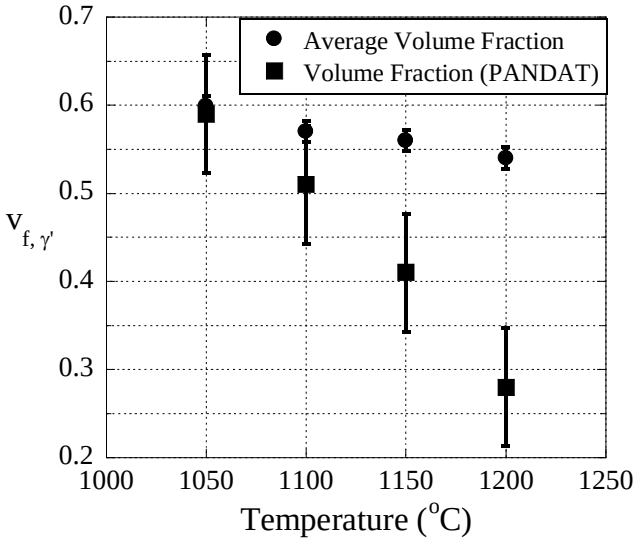

Figure 5.5: Average measured V_f compared against theoretical at investigated temperatures.

Ti and Si are not included due to their minor additions. Pt and Ta strongly partition to the γ′ phase while Re and Mo show strong partitioning to the γ phase. Comparison of the Pt partitioning behavior at 1250 °C, Table 5.4, to its partitioning at 1050 °C presented in Section 4.1 indicates stronger partitioning to the γ′ phase at higher temperatures. A similar comparison, Tables 4.2 and 5.4, indicates stronger partitioning of Re toward the matrix for alloy PX-5. This is attributed to the Al content in PX-5, as discussed in Section 4.2.1. Table 5.4 also indicates that W weakly partitions to the matrix as well.

To quantitatively assess the change in solute concentrations across the γ-γ′ interface at the aged testing conditions, the diffusional flux, *J*, across the interface was calculated for the γ′-forming elements (*A* = Pt, Ta, and Al), using the following equation [6]:

$$J = \Delta C D_{Ni-A} \qquad \text{Equation 5.1}$$

Table 5.4: Elemental compositions measured at 1250 °C. Partitioning values, *p*, are listed for each element.

Alloy		Composition (at%)						
		Al	Pt	Cr	Re	Ta	W	Mo
PX-5	C_{γ}	12.5	1.3	9.6	1.4	1.5	1.2	1.3
	$C_{\gamma'}$	15.7	5.0	3.0	0.2	3.0	0.6	0.3
	p	*0.8*	*0.3*	*3.2*	*7*	*0.5*	*2*	*4.3*

Table 5.5: Diffusional flux, *J*, of γ′-forming elements across the γ/γ′ interface at the investigated temperatures.

Element	$\Delta C_{1050\ °C}$ (mol fraction)	$\Delta C_{1250\ °C}$ (mol fraction)	D (T) (m^2/s)			
			1050 °C	1100 °C	1150 °C	1200 °C
Pt	0.015	0.037	$2.0\cdot10^{-16}$	$6.0\cdot10^{-16}$	$2.5\cdot10^{-15}$	$4.0\cdot10^{-15}$
Ta	0.021	0.015	$2.0\cdot10^{-15}$	$8.0\cdot10^{-15}$	$1.0\cdot10^{-14}$	$3.0\cdot10^{-14}$
Al	0.078	0.023	$5.0\cdot10^{-15}$	$1.0\cdot10^{-14}$	$1.5\cdot10^{-14}$	$7.0\cdot10^{-14}$
Element			$J = \Delta C*D$ (m^2/s)			
			1050 °C	1100 °C	1150 °C	1200 °C
Pt			$3.0\cdot10^{-18}$	$9.0\cdot10^{-18}$	$3.8\cdot10^{-17}$	$1.5\cdot10^{-16}$
Ta			$4.2\cdot10^{-17}$	$1.7\cdot10^{-16}$	$2.1\cdot10^{-16}$	$4.5\cdot10^{-16}$
Al			$3.9\cdot10^{-16}$	$7.8\cdot10^{-16}$	$1.2\cdot10^{-15}$	$1.6\cdot10^{-15}$

where the change in composition across the γ/γ′ interface, ΔC, was acquired through partitioning values listed in Table 4.2. For the diffusional flux at 1200 °C, ΔC at 1250 °C measured in this study was used. This is to provide a more reliable measurement for ΔC at 1200 °C. Interdiffusion values of Pt, Ta, and Al within Ni at high temperatures were acquired through studies conducted elsewhere [30, 117, 118]. Table 5.5 lists the diffusional flux of γ′-forming elements within the Ni-matrix of alloy PX-5. The final three rows provide *J* for each element. Pt and Ta atoms are the slowest to diffuse across the interface in the range of temperatures investigated.

5.2 Discussion

Developing creep resistant Ni-base superalloys that operate at elevated temperature requires a relatively high γ′ volume fraction and stable precipitate morphology. Ni-base superalloys that exhibit high rates of precipitate coarsening, or loss of coherency between the γ and γ′ phases, may degrade during high temperature exposure [26, 119]. It is therefore essential to examine the factors affecting partitioning and interdiffusion in these complex multi-component alloys. Of additional importance is whether Pt retards coarsening behavior in any significant manner. As such, further analysis on the coarsening kinetics examines high temperature diffusion, partitioning behavior, and interfacial energy. This section addresses alloys D3 and D7, Table 4.1, and alloy PX-5, Table 5.1.

5.2.1 Precipitate Morphology and Misfit

Aging treatments performed by Heidloff *et. al.* [110] on alloys D3 and D7 resulted in microstructures that displayed aspect ratios η = 0.38 and near 0.61, respectively. This indicates the lattice misfit of the Ir-alloy is lower in magnitude than the Pt-alloy, since Pt preferentially partitions to γ′, increasing $a_{\gamma'}$. High temperature synchrotron x-ray analysis [110], as well as directional coarsening of the precipitates during high temperature creep testing (addressed in Section 6.1.2) verifies that both alloys possess positive misfit. The semi-spherical precipitate morphology in the refractory-containing PGMs indicates a decrease in lattice misfit to near-zero. Partitioning coefficients of Ir and Pt within alloys D3 and D7, respectively, post-aging [110] matches the values measured in this study, Table 4.3, with and without the

refractory content. It is therefore likely that aspect ratio transitions from $\eta = 0.38$ or 0.61 (alloys D3 and D7) toward $\eta < 0.2$ (D19, 22, 23, and 26) are not influenced by the Pt or Ir, but rather the indirect effect of Pt and Ir on partitioning behavior of the additional refractory elements.

The measured volume fractions from Figures 4.1 and 4.2 and slopes of the fits to the data in Figures 4.8 and 4.9 indicate that Ir additions decrease γ′ volume fractions. Volume fraction measurements of precipitates in alloys D3 and D7 following homogenization were consistent with measurements conducted after aging was performed. Therefore, these two alloys with either Pt or Ir PGM additions reach a thermodynamically stable volume fraction relative to the aging temperature quickly.

It is worth considering the kinetics of precipitate growth where precipitate size (edge length), X, may be limited by Pt or Ir interdiffusion [6]:

$$X = \frac{\Delta C_0}{C_{\gamma'} - C_n}\sqrt{Dt} \qquad \text{Equation 5.2}$$

with ΔC_0 (equal to C_n - C_γ), C_n represents the nominal composition of the element, D is the interdiffusion coefficient, and t is time. Using the results of nickel interdiffusion studies by Karunaratne *et. al.* [117], for a homogenization temperature of 1330 °C, D_{Pt} and D_{Ir} were taken as 2.0 x 10^{-14} and 4.5 x 10^{-15} m^2/s, respectively. Using the phase compositions for alloys D3 and D7 from Table 4.3, and t = 6 h (21,600 s), X_{Pt} and X_{Ir} were approximately 29.1 and 14.8 μm, respectively. Thus the ratio of the precipitate sizes due to differences in Ir and Pt diffusion would be:

$$\frac{X_{Pt}}{X_{Ir}} \propto \sqrt{\frac{D_{Pt}}{D_{Ir}}} \qquad \text{Equation 5.3}$$

Using the numerical values stated above, Pt precipitate thickness would be double that of Ir for the given temperature. Experimentally, the average particle diameter and length for alloys D3 and D7, respectively, post-homogenization were 129.2 nm (± 27.5), and 196.6 nm (± 32), respectively, giving a proportionality, X_{Pt} / X_{Ir}, of 1.5. Considering that interdiffusion may be influenced by other elements in solution and that interdiffusion coefficients of Ir and Pt may have slightly different temperature dependence, the particle size differences are thus likely due to differences in growth rate. However, a lower V_f is more likely due to a shift in phase boundaries due to Pt or Ir, rather than the coarsening kinetics.

5.2.2 Diffusion

At temperatures surpassing 1000 °C, the diffusion of Pt and the refractory additions within Ni play a more prominent role for particle coarsening. It is expected that increasing temperature, in turn, increases diffusion [112]. The rate constants, *k* (nm^3/min), extrapolated from the slopes of the data plotted in Figures 5.3(a - d) indicates an increase in *k* as temperature, and particle size, increases. Figure 5.6 plots the coarsening rate constants, given in Table 5.2, as a function of the diffusional flux for the three elements (Al, Ta, Pt) which strongly partition to the precipitate. At temperatures of 1050 and 1100 °C, the rate constant remains similar but *J* for each element increases. Above 1100 °C, the rate constants increase significantly by at least one order of magnitude, and Pt shows the greatest increase in *J* from 1100 → 1200 °C. Based on Figure 5.6, Pt and Ta provide the lowest diffusional fluxes within the range of investigated temperatures.

It would be useful, therefore, to explore diffusion kinetics. The linear fits of

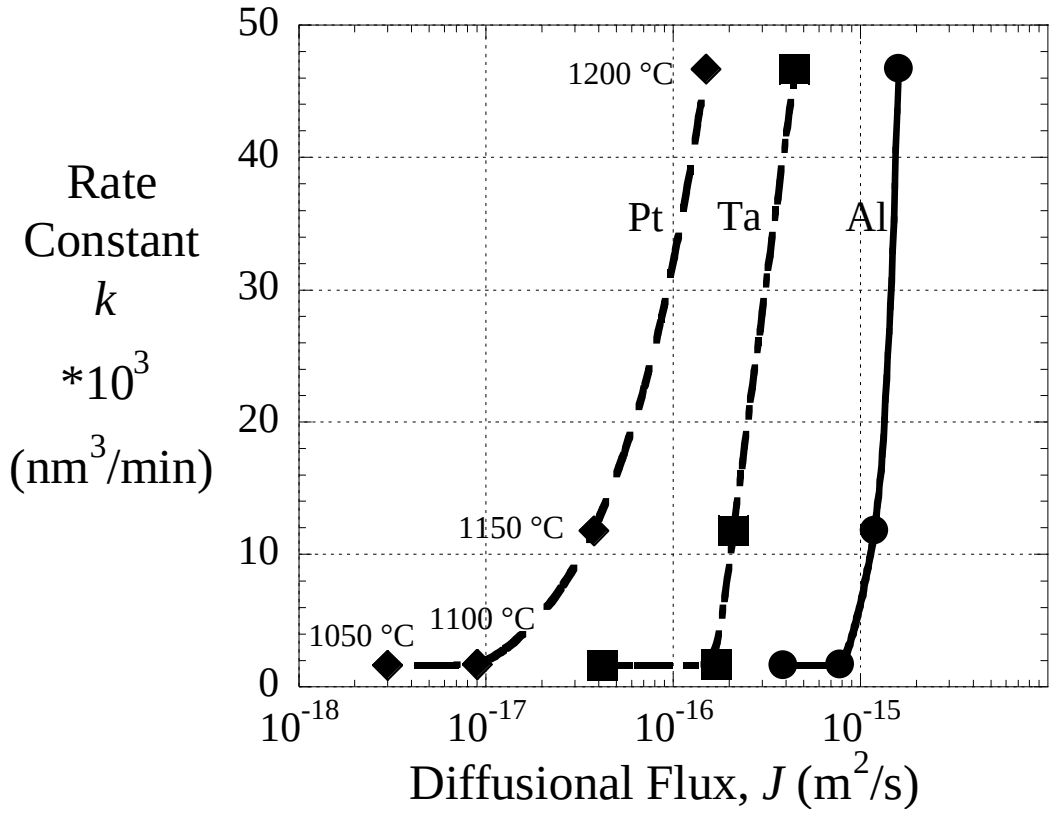

Figure 5.6: Coarsening rate constants as a function of diffusional flux for the elements Pt, Ta, and Al.

the data for alloy PX-5 shown in Figures 5.3(a - d) indicate that the precipitates coarsen as a function of $t^{1/3}$. This relationship is derived from LSW theory [120, 121]:

$$r_t^3 - r_0^3 = kt \qquad \text{Equation 5.4}$$

where r_t (nm) is average particle size at time t (h), and r_0 is average particle size (nm) prior to aging. The rate constant, k, is related to the following material variables [25, 109, 121]:

$$k = \frac{8 \cdot \sigma_{int} \cdot V_m \cdot \Delta C \cdot D_{int}}{9 \cdot R \cdot T} \qquad \text{Equation 5.5}$$

where σ_{int} is interfacial energy of the phase boundary (J / m^2), V_m the molar volume of γ' (~ 10^{-5} m^3/mol), D_{int} the interdiffusion coefficient (m^2/s), R the gas constant (J/mol·K),

and T is absolute temperature (K). Table 5.5 indicates Pt and Ta atoms are the two slowest to diffuse across the γ/γ′ interface. Comparing the flux, *J*, Table 5.5, indicates that Al is transported one order of magnitude faster than Ta, and two orders faster over Pt. Assuming that interdiffusion is governed by the two elements which have the strongest partitioning (Table 5.4) and lowest interdiffusion coefficients within the Ni-matrix (Table 5.5), D_{int} is calculated as follows [6]:

$$D_{\text{int}} = X_{Pt} D_{Ni-Ta} + X_{Ta} D_{Ni-Pt} \qquad \text{Equation 5.6}$$

where X_{Pt} and X_{Ta} are compositional concentrations of Pt and Ta within the matrix, Tables 4.2 and 4.3, and $D_{Ni\text{-}Pt/Ta}$ are interdiffusion coefficients of Ta [117] and Pt [30] within Ni at high temperatures, Table 5.5. Using Equation 5.6, interdiffusion values for Pt and Ta range from 3.4 x 10^{-17} - 1.2 x 10^{-15} m^2/s (at 1050 and 1200 °C, respectively). If Ta and Al limited D_{int}, values would be on the order of ~ 10^{-16} - 10^{-15} m^2/s (at 1050 and 1200 °C, respectively). Consequently, the rate-limiting step of coarsening in alloy PX-5 is the interdiffusion between Pt and Ta through the γ phase.

Assuming ΔC does not change appreciably from 0 - 24 h for each investigated aging temperature, *k* can be used to calculate the activation energy (*Q*) by plotting ln (*k*) versus (1/T), Figure 5.7 [4, 5]. The slope of Figure 5.7 provides *Q*, determined to be 388 kJ/mol. The activation energy, in comparison to the other Ni-base compositions shown in Table 4.4, is considerably higher. The absence of Ta in René 88DT and FGH-95 contribute to lower *Q* since particle coarsening doesn't rely on this refractory element in either alloy. From Table 4.4, alloy PX-5 is the only alloy to contain all three refractory additions (Re, Ta, W).

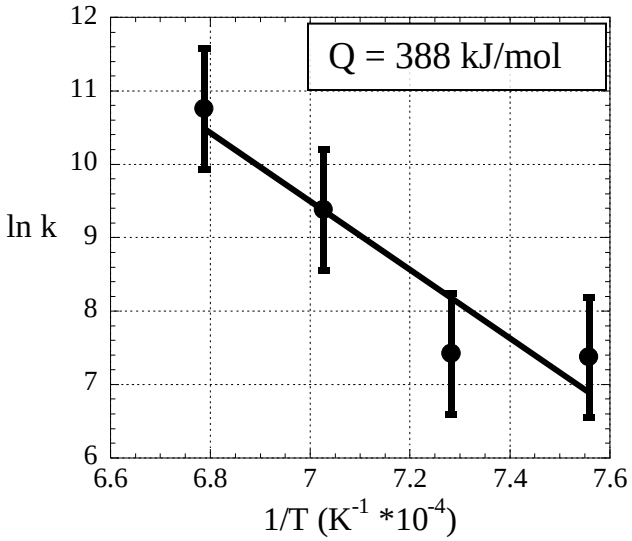

Figure 5.7: Temperature dependence of coarsening kinetics.

5.2.3 Partitioning Behavior of W and Re

The refractory element, tungsten, displayed unusual partitioning behavior as discussed in Section 4.2.3. At 1050 °C, W preferentially partitions to the γ phase, but above 1050 °C, as V_f decreases, the precipitates become enriched in W. Preferential partitioning of W to γ′ could slow coarsening kinetics [95, 122]. To assess the effect of tungsten partitioning in alloy PX-5, PANDAT was employed to calculate phase compositions of the γ and γ′ phases for W, Re, Ta, and Pt. Figure 5.8 plots the compositional changes of these four elements across the range of investigated temperatures. Partitioning coefficients, *p*, at 1250 °C are included within each plot. Comparison of the partitioning values listed in Figures 5.8(a - c) versus those measured through EMPA, Table 5.4, indicates good agreement. The concentration of W in the γ phase decreases from 1050 → 1200 °C, Figure 5.8(a). Interestingly, Re illustrates the same decrease in concentration within the matrix from 1050 → 1200°C, Figure 5.8(b),

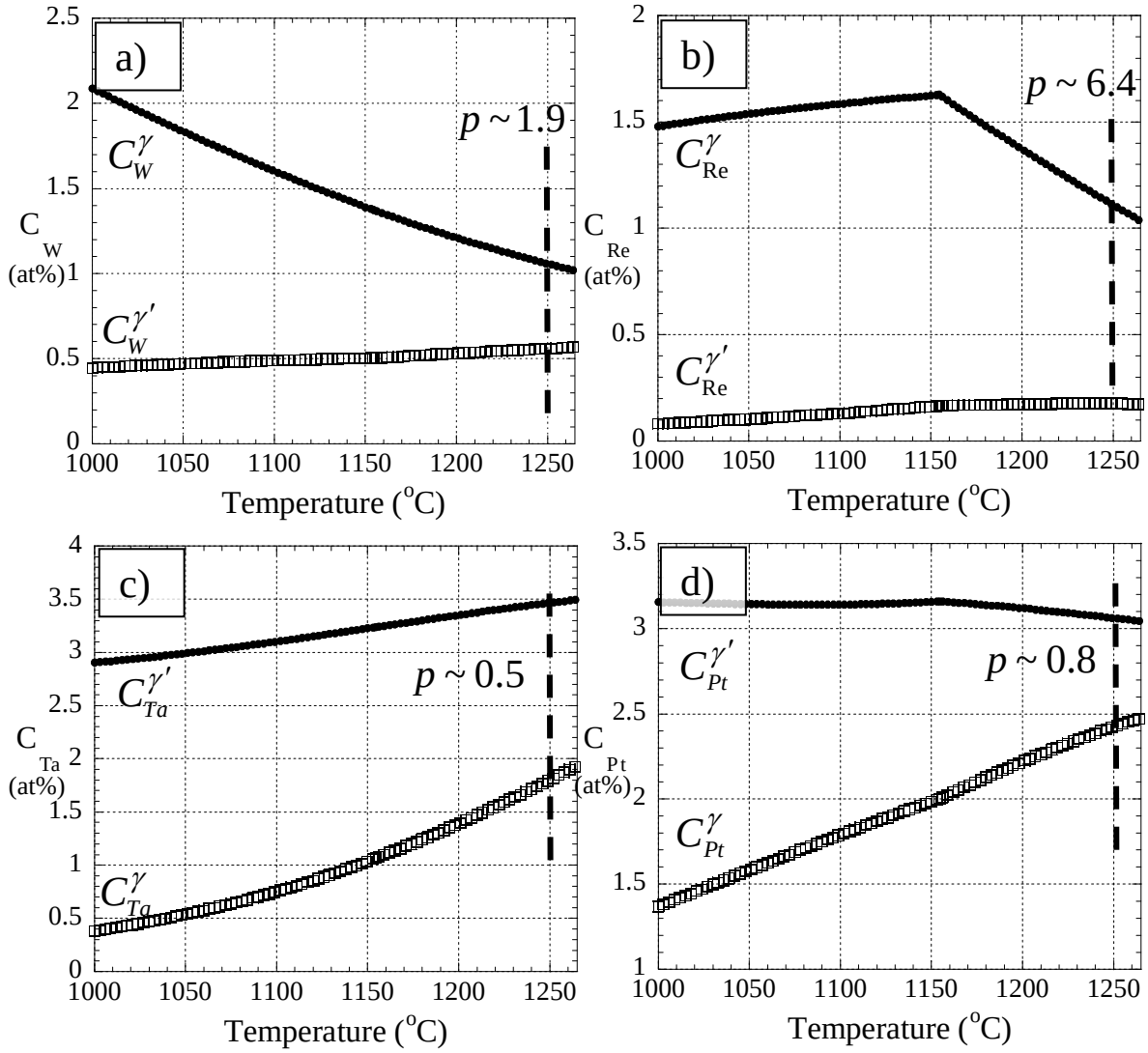

Figure 5.8: PANDAT calculations of phase composition (at%) in the γ and γ′ phases as a function of temperature. The refractory elements, (a) W, (b) Re, (c) Ta, and PGM (d) Pt, are plotted. Partitioning coefficients, *p*, at 1250 °C, are assigned within each plot.

displaying a sharp drop in C_{Re}^{γ} just beyond 1150 °C. Evidently, beyond Ta and Pt, as temperatures increase and volume fraction decreases, Re and W diffuse readily into the precipitate.

Figure 5.9 demonstrates the rate constant as a function of diffusional flux for the four elements presented in Figure 5.8. The fluxes of Re and W were calculated by

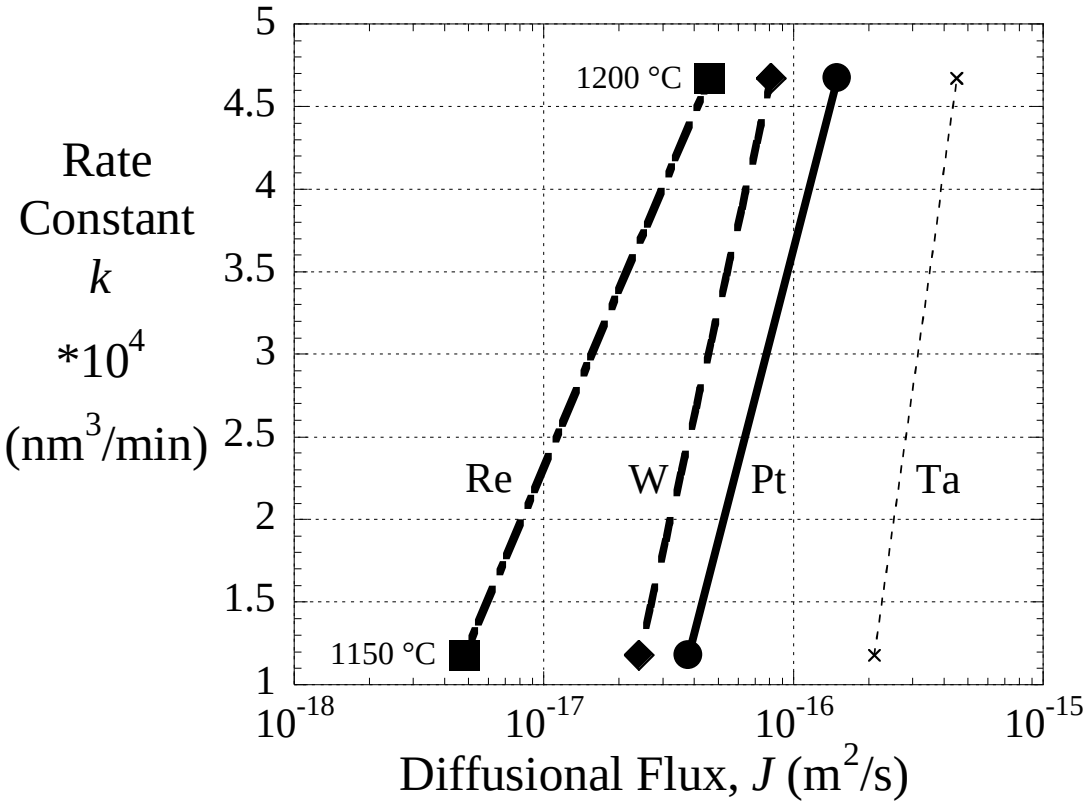

Figure 5.9: Rate constant as a function of diffusional flux for Re, W, Pt, and Ta.

Table 5.6: Six alternatives for the interdiffusion coefficients based on Pt, Ta, Re, and W.

	Interdiffusion Coefficient (m^2/s)	Temperature (°C)	
	$X_A D_{Ni\text{-}B} + X_B D_{Ni\text{-}A}$	1150	1200
(1)	$X_{Pt} D_{Ni\text{-}Ta} + X_{Ta} D_{Ni\text{-}Pt}$	$2.5 \cdot 10^{-16}$	$4.5 \cdot 10^{-16}$
(2)	$X_{Pt} D_{Ni\text{-}W} + X_W D_{Ni\text{-}Pt}$	$1.0 \cdot 10^{-16}$	$9.4 \cdot 10^{-17}$
(3)	$X_{Pt} D_{Ni\text{-}Re} + X_{Re} D_{Ni\text{-}Pt}$	$5.1 \cdot 10^{-17}$	$6.6 \cdot 10^{-17}$
(4)	$X_W D_{Ni\text{-}Ta} + X_{Ta} D_{Ni\text{-}W}$	$2.8 \cdot 10^{-16}$	$4.1 \cdot 10^{-16}$
(5)	$X_{Re} D_{Ni\text{-}Ta} + X_{Ta} D_{Ni\text{-}Re}$	$1.7 \cdot 10^{-16}$	$4.3 \cdot 10^{-16}$
(6)	$X_W D_{Ni\text{-}Re} + X_{Re} D_{Ni\text{-}W}$	$3.5 \cdot 10^{-17}$	$5.9 \cdot 10^{-17}$

Equation 5.1 and the use of compositional values listed in Tables 4.2 and 5.4. Only the temperatures of 1150 and 1200 °C are plotted. At 1200 °C, *J*(Re), *J*(W), and *J*(Pt) display the lowest fluxes. This indicates that Re and W influence particle coarsening at 1150 and 1200 °C. The use of Equation 5.6 for Pt, Ta, Re, and W results in six different possibilities for an interdiffusion coefficient at T = 1150 and 1200°C, and are listed in Table 5.6. Close examination of Figure 5.9 indicates that Ta would not be a rate-limiting factor for interdiffusion since it demonstrates the fastest flux of the four elements. Furthermore, due to stronger partitioning of Pt to the γ′ phase, as shown in Table 5.4, this suggests that Pt must be one of the two elements that would limit interdiffusion across the interface. This eliminates all choices in Table 5.6 except (2) and (3). Considering that the W concentration within the matrix is lower than Re at 1150 and 1200 °C, Figure 5.8, then it is concluded that Pt and Re interdiffusion may be the rate-limiting factor for particle coarsening of alloy PX-5 at temperatures above 1150 °C.

5.2.4 Interfacial Surface Energy

Ardell has suggested that uncertainty in interfacial surface energy (σ_{int}) values arises due to uncertainty in diffusion values [24]. The work of Karunaratne *et al.*, however, provides useful data concerning diffusion of refractory, and PGM, elements within the Ni-matrix at high temperatures [30, 117].

Rearranging Equation 5.5:

$$\sigma_{int} = \frac{9 \cdot R \cdot T \cdot k}{8 \cdot V_m \cdot \Delta C \cdot D_{int}} \qquad \text{Equation 5.5(a)}$$

The interdiffusion value in Equation 5.5(a) incorporates Pt and Ta. In Ni_3Al, Pt prefers to occupy the Ni site [123]. First principles calculations conducted on a Ni (Al,Pt) alloy

Table 5.7: Interfacial energy values.

Alloy	Average $\sigma_{int.}$ (J/m^2)
PX-5	0.26 (± 0.15)
Ni (Al,Pt) [15]	1.8 – 2.4
René 88DT [6]	0.012
Ni-Al (solid solution) [13]	0.008

indicates a preference for platinum on the Ni site, increases the interfacial energy [124]. Table 5.7 lists the average $\sigma_{int.}$ value for PX-5 as 0.26 J/m^2. This is one order of magnitude higher than René 88DT but an order lower than calculated through first-principles studies. It is interesting that of all γ′-formers within PX-5 (Pt, Ta, and Al), Pt is the only element preferring substitution of Ni sites rather than the Al within the $L1_2$ structure. In any case, the presence of Pt in the γ′ phase increases interfacial energy. Due to its preferentially partitioning to γ′, and tendency to partition more strongly into γ′ as temperatures increase from 1050 → 1200 °C, the interfacial energy continues to remain high.

5.3 Summary

Pt-containing alloys contain higher gamma prime volume fractions than Ir-containing alloys. This is caused by shifts in the phase field boundaries between the γ and γ′ phase regions due to Pt or Ir additions. The rate-limiting mechanism for precipitate coarsening within alloy PX-5 is the interdiffusion of Ta and Pt within the Ni-matrix. The interfacial energy of gamma prime is increased due to the partitioning

behavior of Pt. For temperatures exceeding 1100 °C, Re and W display preferential partitioning into the precipitate. This uncommon partitioning behavior leads to a strong possibility of Pt and Re becoming the rate-limiting factor for interdiffusion at temperatures above 1150 °C. Alloy PX-5 retains sufficiently high precipitate volume fractions of 0.56 and 0.54 at 1150 °C and 1200 °C, respectively. Such high volume fractions with a shape parameter near 0.27 could lead to impressive creep properties for temperatures exceeding 1100 °C – unusually high temperatures for Ni-base superalloy creep performance. Prior to conducting creep at these elevated temperatures, however, requires initial evaluation of the PGM alloys at testing temperatures similar to conventional Ni-base superalloys.

CHAPTER 6

HIGH TEMPERATURE CREEP AND ASSOCIATED DEFORMATION MECHANISMS

The partitioning behavior of the PGMs, along with non-PGM elemental additions, yields a range of lattice misfit, which is reflected by the morphology of the γ′ precipitates. The wide range of γ′ microstructures and volume fractions influences the overall creep behavior of the PGM-modified Ni-base superalloys at high temperature. However, particle morphology and V_f are not the only relevant parameters that regulate creep performance. The formation of TCP phases or grain boundary sliding can influence creep. This chapter examines the high temperature behavior of PGM alloys under creep deformation conditions. Differential thermal analysis is used to examine whether the nominal compositions of the studied alloys provide adequate heat treatment windows for full homogenization. Creep strength is assessed based on the effects of rafting and grain boundary damage. TEM investigations were employed to evaluate deformation mechanisms during high temperature creep. Features of the substructure important to creep include dislocation accumulation within the γ and γ′ phases and at the γ/γ′ interface. The influence of the PGM additions with respect to partitioning and the overall effect on creep resistance and associated deformation mechanisms is discussed.

6.1 High Temperature Creep Properties

Because of material limitations, one compression creep test was performed per alloy. Table 6.1 lists all PGM alloys that were crept at 1000 °C to approximately 1% plastic strain in this investigation, along with minimum creep-rates. A wide range of applied stresses were employed to achieve creep-rates on the order of 10^{-8} s^{-1}. Differences in precipitate volume fractions, grain boundary damage, and the formation of interfacial dislocation networks for alloys which exhibited rafting behavior were examined to explain observed differences in creep behavior.

Further creep analysis described in Sections 6.1.2 - 6.1.4, pertains to alloys listed in Table 6.2. Measured volume fractions and edge lengths are provided in Table 6.3. Alloy D4 contained Ir as the only PGM, whereas alloys PX-5, PX-2, E1, DS-1, and PX-6 contained only Pt. Alloys D12, D25, and 8A combined Pt and Ir. Alloy 8A, the only alloy with no refractory additions, displayed the lowest volume fraction of the alloys listed is Table 6.3. It did, however, contain C, B, and Zr grain boundary strengtheners. Alloys PX-5 and PX-6 share similar elemental compositions, except that PX-5 contains B, C, and Zr grain boundary strengtheners as well.

To ensure that creep strengths among the PGM alloys would be compared equally between one another, the applied stress conditions were selected so that minimum creep-rates would be on the order of 10^{-8} s^{-1}. However, creep-rates differed by a factor of 10x, as shown in Table 6.1. In order to accurately compare and contrast creep strength, reference creep strengths (σ_{Ref}) were evaluated instead of the applied stress. To extrapolate σ_{Ref} from the experimental applied stress, a creep stress exponent, n = 5.0, was fitted through each alloys data point from a log creep-rate – log stress scale. The

Table 6.1: PGM-modified Ni-base superalloys creep tested at 1000 °C in this investigation.

DOE Phase	PGMs	Alloy	Applied Stress σ (MPa)	Volume Fraction V_f	Minimum Creep Rate ε_{min}*10^{-8} s^{-1}	Reference Stress σ_{Ref} (Ref ε_{min}: 10^{-8})
I	Ir	D1	55	0.52	1.3	42
	Ir	D3	60	0.45	1.3	52
	Ir	D4	55	0.61	5.6	20
	Pt	D5	80	0.64	1.6	61
	Pt	D7	80	0.57	3.5	52
	Pt + Ir	D10	55	0.57	7.9	8
	Pt + Ir	D12	70	0.61	1.5	56
	Pt + Ir	D13	65	0.60	6.0	25
	Pt	D15	60	0.55	6.2	21
	Pt	D17	60	0.65	4.4	26
	Pt	D18	50	0.56	5.6	9
II Higher Al	Pt + Ru	D21	65	0.66	3.8	48
	Pt + Ru	D22	65	0.67	3.8	48
	Pt + Ir + Ru	D24	75	0.66	8.9	46
	Pt + Ir + Ru	D25	70	0.62	3.4	53
	Pt + Ru	D27	55	0.67	5.7	38
II Lower Al	Pt + Ru	E1	50	0.53	3.4	35
	Pt + Ru	E2	75	0.50	17	26
	Pt + Ru	E3	45	0.52	5.6	24
	Pt + Ru	E5	45	0.52	6.5	21
	Pt + Ir + Ru	E8	65	0.51	7.7	30
	Pt + Ir + Ru	E11(a)	50	0.51	2.0	39
		E11(b)	50	0.57	2.7	35
III	Pt + Ru	DS-1	50	0.55	3.3	25
	Pt + Ru	DS-2	50	0.56	4.4	21
	Pt + Ir	8A	60	0.45	1.5	52
	Pt	PX-2	60	0.58	4.5	38
	Pt	PX-5	95	0.60	5.6	68
	Pt	PX-6	40	0.60	3.2	20

Table 6.2: Nominal compositions of PGM alloys. Experimental and reference loads are provided in the final two columns.

Alloy	Composition (at%)											Applied σ (MPa)	σ_{Ref} (MPa)
	Al	Pt	Ir	Cr	Re	Ta	Ru	W	Mo	Ti	Si		
PX-5 *	13.5	2.5	-	7.5	1	2	-	1	1	0.5	0.5	95	68
D12	15	2.5	2.5	5	-	2	-	-	-	-	-	70	56
D25	15	2.5	2.5	5	1	2	2	1	-	-	-	65	53
8A *	15	2	2	5	-	-	-	-	-	-	-	60	52
PX-2	14.5	2.5	-	7.5	1	2	-	1	1	0.5	-	60	38
E1	13	2.5	-	5	1	2	1	1	-	-	-	50	35
DS-1	14	2.5	-	10	1	2	2	1	-	-	-	50	25
D4	15	-	2.5	5	1	2	-	-	-	-	-	55	20
PX-6	13.5	2.5	-	7.5	1	2	-	1	1	0.5	0	40	20

* Alloys contain the following grain boundary strengtheners: 0.014Zr·0.1C·0.087B

Table 6.3: Measured volume fractions, edge lengths, and aspect ratios of PGM alloys listed in Table 6.2.

Alloy	V_f	l_{edge} (nm)	Aspect Ratio (η)
PX-5 *	0.66	298	0.08
D12	0.61	653	0.58
D25	0.74	294	0.14
8A *	0.45	337	0.35
PX-2	0.69	292	0.61
E1	0.53	325	0.70
DS-1	0.55	281	0.74
D4	0.7	573	0.39
PX-6	0.67	343	0.13

method used to acquire the creep stress exponent is discussed in Section 6.1.4. From this creep stress exponent, the σ_{Ref} was acquired with respect to a creep-rate of 10^{-8} s^{-1}. Figure 6.1 demonstrates the acquisition of σ_{Ref} from the experimental loading conditions and minimum creep-rates of a few creep tested alloys listed in Table 6.2. Reference creep strengths are listed in the final columns of Tables 6.1 and 6.2. Based on σ_{Ref}, from Table 6.2, alloys PX-5 and PX-6 demonstrated the strongest, and least, creep resistance,

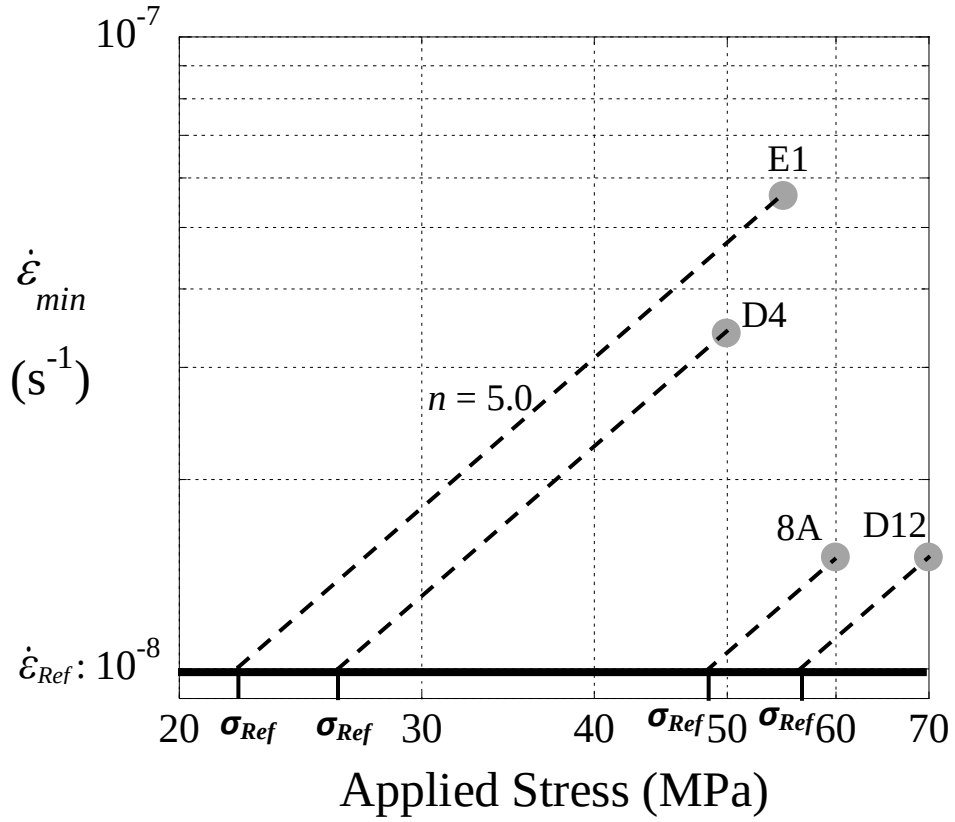

Figure 6.1: Extrapolation of σ_{Ref} from experimental loading conditions and minimum creep-rates.

respectively.

6.1.1 Gamma Prime Volume Fraction

Precipitate volume fractions ranged from 0.45 - 0.67 in the experimental alloys provided in Table 6.3. Alloy 8A contained the lowest V_f due to the absence of Ta [113]. To illustrate how changes in volume fraction impact creep performance, Figure 6.2 plots alloy creep strength, σ_{Ref}, of PGM alloys from design of experiments (DOE) Phase I (♦), Phase II with high Al (●), and Phase II containing low Al concentrations (▲). The observed low V_f for Phase II - low Al alloys is associated with the decrease in Al from 15 at%, Phase II - high Al, to 13 at%, Phase II - low Al. The lower Al content shifts the γ-γ′

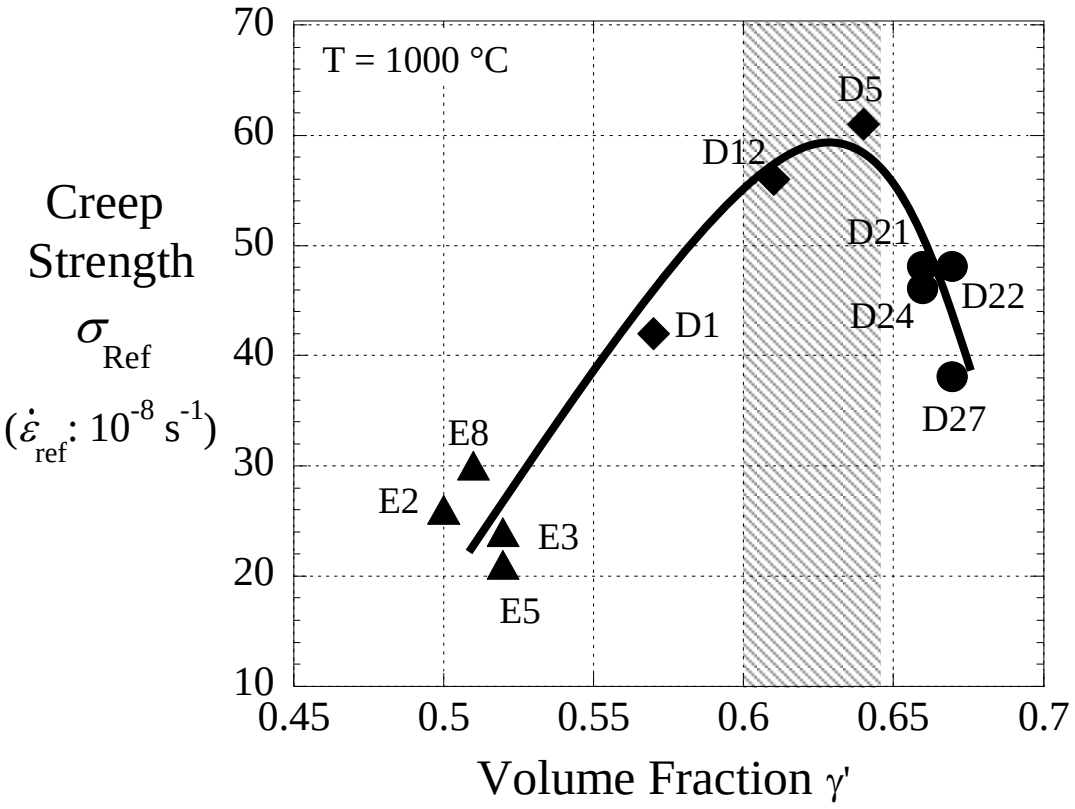

Figure 6.2: Creep strength as a function of γ′ volume fraction. Alloys from DOE Phase I are represented by (♦), Phase II - high Al (●), and Phase II - low Al (▲).

tie-line within the Ni-Al-Pt ternary phase diagram toward the γ phase region [68], lowering γ′ volume fraction. As volume fraction increases, creep strength increases up to $0.60 < V_f < 0.64$, highlighted by the shaded region. Beyond this range, creep strength decreases again. Studies conducted on other Ni-base systems have established the importance of a sufficiently high γ′ volume fraction for increasing the load bearing capacity of a superalloy [4, 85, 125]. Investigations performed on a series of TMS superalloys (T = 900 and 1100 °C, at 392 and 137 MPa, respectively) developed by Murakamo *et al.* containing various γ′ volume fractions demonstrated that, on average, 65% γ′ volume fraction provides the longest creep rupture life [126]. For the PGM alloys

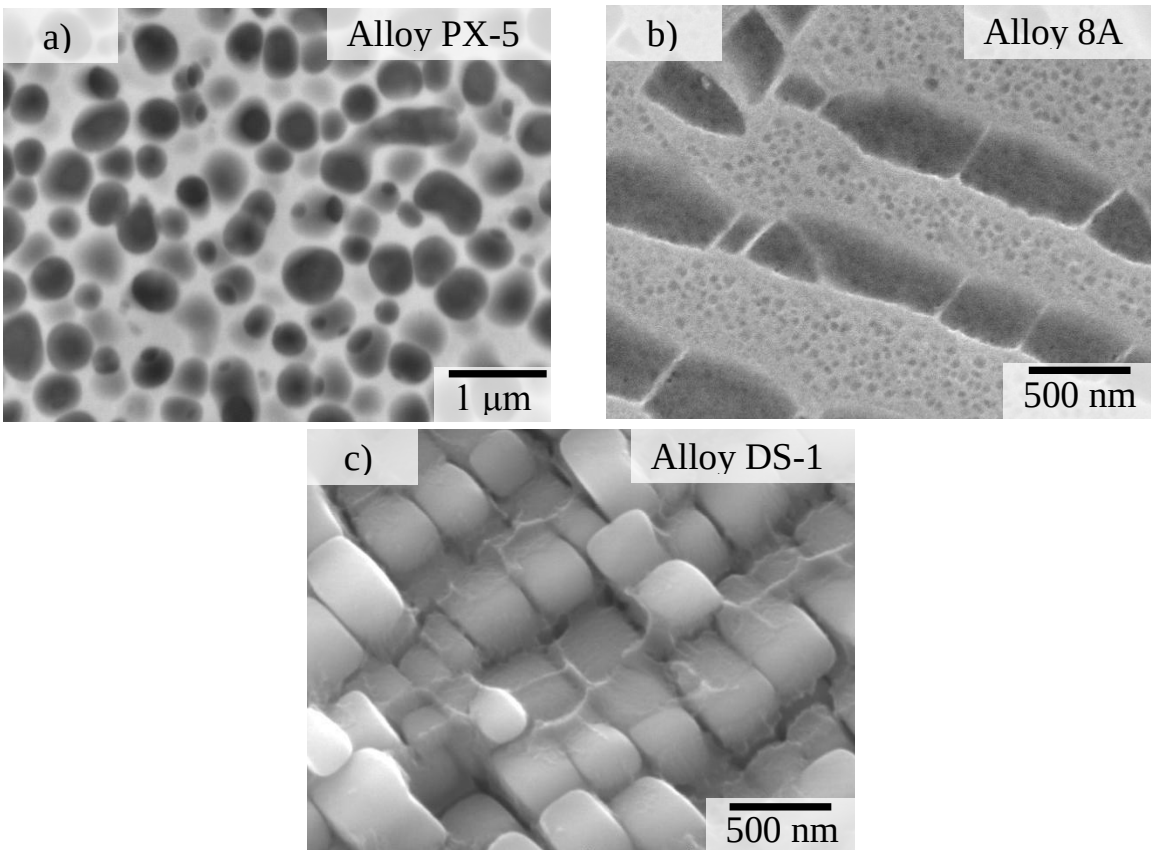

Figure 6.3: Gamma prime morphology upon aging. Images were acquired through SEM using an electrolytic etch.

in this study, volume fractions in the range of 0.60 - 0.65 tend to possess optimal creep strength. Since Pt-containing, or Ir-containing, alloys display lower volume fractions without Ta, it is necessary to include this refractory element in order to achieve the most favorable V_f for these PGM alloys.

6.1.2 Microstructural Evolution During Creep

Changing the nominal alloy composition alters the γ-γ′ lattice misfit and, hence, γ′ morphology. Figure 6.3 displays the microstructures of several alloys prior to compression creep, with aspect ratios of (a) 0.08, (b) 0.35, and (c) 0.74.

Since all creep tests are compressive for this study, precipitates that coarsen

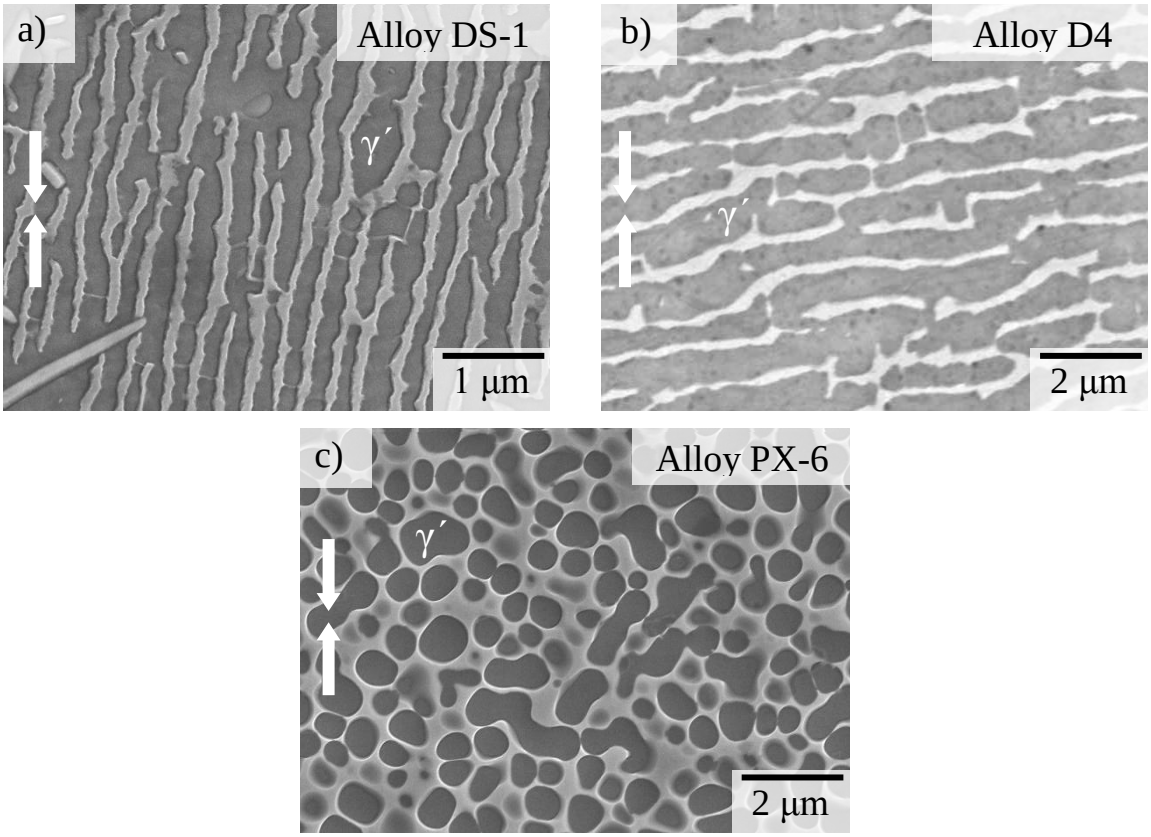

Figure 6.4: SEM depicting directional coarsening of γ´, indicating (a) negative, (b) positive, and (c) near-zero misfit-type behavior. Arrows indicate compressive creep direction.

Table 6.4: Lattice misfit at the γ/γ´ interface following creep. Included are misfit-type behavior (acquired from SEM rafting images) and network spacings (TEM images).

Alloy	Misfit Behavior	
	δ type	Network Spacing (nm)
PX-5	≈ 0	N/A
D12	(+)	41
D25	≈ 0	N/A
PX-2	(-)	51
8A	(+)	59
D4	(+)	79
E1	(+)	57
DS-1	(-)	80
PX-6	≈ 0	N/A

parallel to the applied stress axis indicate negative misfit-type behavior [4, 44]. If rafting is perpendicular to the applied stress axis, this corresponds to positive misfit-type behavior. Figure 6.4 shows directional coarsening associated with negative and positive misfit behavior, alloy DS-1 in Figure 6.4(a) and alloy D4 in 6.4(b), respectively. Alloys, such as PX-5 in Figure 6.3(a) with initially spherical precipitates, did not undergo directional coarsening as illustrated for alloy PX-6 in Figure 6.4(c). A listing of the misfit-type associated with directional coarsening for each alloy is provided in Table 6.4

Dislocation distributions within the γ-γ′ system were examined on post-crept alloys that exhibited positive, near-zero, and negative misfit. Interfacial dislocations were observed in positive and negative misfit alloys as displayed in Figure 6.5(a) for alloy D12. Alloys which did not directionally coarsen contained mainly a distribution of matrix dislocations, shown in Figure 6.5(b) of alloy PX-5. Interfacial dislocation spacings measured from rafted alloys are provided in Table 6.4. Alloys that did not directionally coarsen accumulated no interfacial dislocations [127] and so network spacings are not reported.

6.1.3 Differential Thermal Analysis (DTA)

Table 6.5 provides DTA data for solidus (T_S) and gamma prime solvus (γ'_{Solvus}) temperatures. The final column indicates heat treatment windows for homogenization. The refractory additions influence γ'_{Solvus} and T_S temperatures [98], especially Ta [113], which increases the γ'_{Solvus} more strongly than the T_S or T_L temperatures. Aside from alloys 8A and E1, heat treatment windows ranged from 17 - 35 °C. These narrow windows are due to Ta and the PGM Pt [113], known to lower the T_S as well. The solvus to solidus gap was narrow in alloy PX-5 compared to PX-6 due to the presence of grain

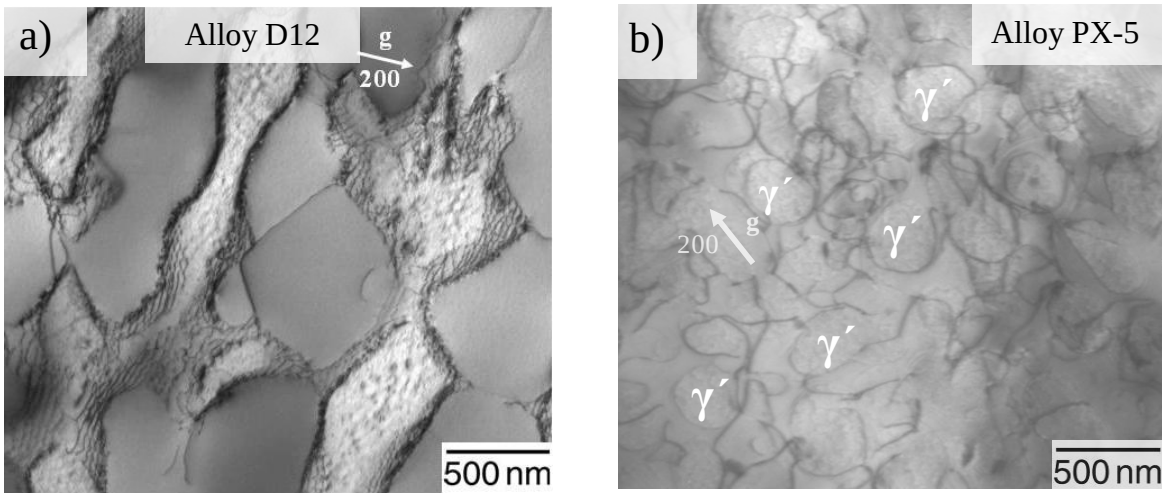

Figure 6.5: Interfacial networks in alloys with (a) directional coarsening, but lacking in (b) non-coarsened alloys.

Table 6.5: DTA for compression crept alloys. Heat treatment windows, labeled TS - γ'_{Solvus}, are given in last column.

Alloy	DTA (°C)			
	γ'_{Solvus}	T_S	T_L	$T_S - \gamma'_{Solvus}$
PX-5	1324	1341	1377	17
D12	1336	1363	1400	27
D25	1352	1370	1406	18
PX-2	N/A	1324	1373	N/A
8A	1150	1390	1413	240
D4	1337	1365	1406	28
E1	1291	1379	1414	88
DS-1	1320	1345	1385	25
PX-6	1317	1352	1389	35

boundary strengtheners, particularly boron [29]. Alloy 8A displayed the widest heat treatment window due to the absence of Ta. The lower Al content in alloy E1 shifts the composition within the Ni-Al-Pt ternary phase diagram toward the γ phase region [68], lowering the γ'_{Solvus} temperature.

6.1.4 High Temperature Creep Behavior

Considering a reference creep-rate of 10^{-8} s^{-1}, the alloys listed in Table 6.2 are ordered from highest to lowest creep resistance. This shows that alloys PX-5 (σ_{Ref} = 68 MPa) and PX-6 (σ_{Ref} = 20 MPa) are the strongest and weakest alloys, respectively. Two polycrystalline Ni-base superalloys creep tested at or near 1000 °C (MAR-M247 and TM-321) [32, 128], sustained applied stresses of 172 and 120 MPa, respectively, for over 3.6 x 10^5 s (100 h). Comparatively, the PGM Ni-base superalloys creep tested in this study display lower creep resistances. However, in comparing experimental loading conditions, the creep resistance of alloy PX-5 is nearly equal to the polycrystalline Pt-modified Ni-base superalloy developed by Selman and co-workers [73]. This alloy, termed alloy *K*, attained a creep rate on the order of 10^{-8} s^{-1} under an applied load of 103 MPa. However, it is important to note that alloy PX-5 contains approximately 3 wt% less Pt than alloy *K*. Furthermore, the creep properties of the PGM alloys examined in this investigation exceed those of Pt-modified NiAl [81], β-rich Ni(Pt,Al) [82], or NiCrAlY [129] bond coat materials.

Creep tests conducted at varying stress levels on alloys PX-5 and PX-6 at 1000 °C are summarized in Table 6.6. Through use of the Arrhenius-type creep-rate equation [4, 27]:

$$\dot{\varepsilon} = A\sigma^{n} \exp\left(\frac{-Q}{RT}\right) \qquad \text{Equation 6.1}$$

where $\dot{\varepsilon}$, A, σ, n, Q, R, and T, are the creep rate (s^{-1}), materials constant, applied stress (MPa), creep stress exponent, activation energy (J/mol), gas constant (J/mol·K), and temperature (K), respectively. The average slopes of the curves in Figures 6.6(a) and

Table 6.6: List of alloys used for determination of creep stress exponent in Figures 5.4(a) and (b).

Alloy Figure 5.6(a)	Applied Stress, σ (MPa)	Creep Rate $\dot{\varepsilon}_{min}$ (s^{-1})	Alloy Figure 5.6(b)	Applied Stress, σ (MPa)	Creep Rate $\dot{\varepsilon}_{min}$ (s^{-1})
PX-5	110	1.5×10^{-7}	PX-6	80	6.7×10^{-7}
PX-5	95	5.6×10^{-8}	PX-6	60	2.4×10^{-7}
PX-5	70	1.6×10^{-8}	PX-6	40	3.2×10^{-8}

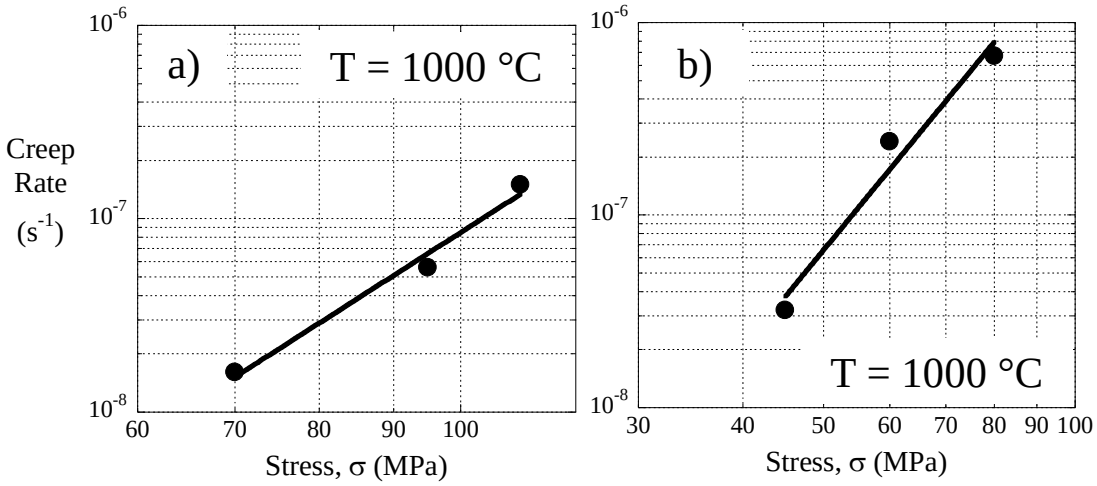

Figure 6.6: Creep-rate as a function of stress plotted on a log-log scale. The slope provides the creep stress exponent, *n*. Plot (a) displays alloys PX-5 while (b) are alloys PX-6.

6.6(b) indicate a creep stress exponent of 5.0 (± 0.5), indicative of power-law creep [4].

Prior to testing, vertical fiducial lines were placed on the specimen surface to check for the occurrence of grain boundary sliding. Figure 6.7 presents optical images of the surface of the compression sample for alloys E1, Figure 6.7(a), and DS-1, Figure 6.7(b). The white arrows in Figure 6.7(a) highlights shifts across grain boundaries following 1.3% creep strain in alloy E1, indicating the operation of grain boundary sliding. This behavior leads to 'wing crack' formation [130], as shown in the upper right inset of Figure 6.7(b) (DS-1 crept ~ 1.1% strain). These cracks continually grow, leading

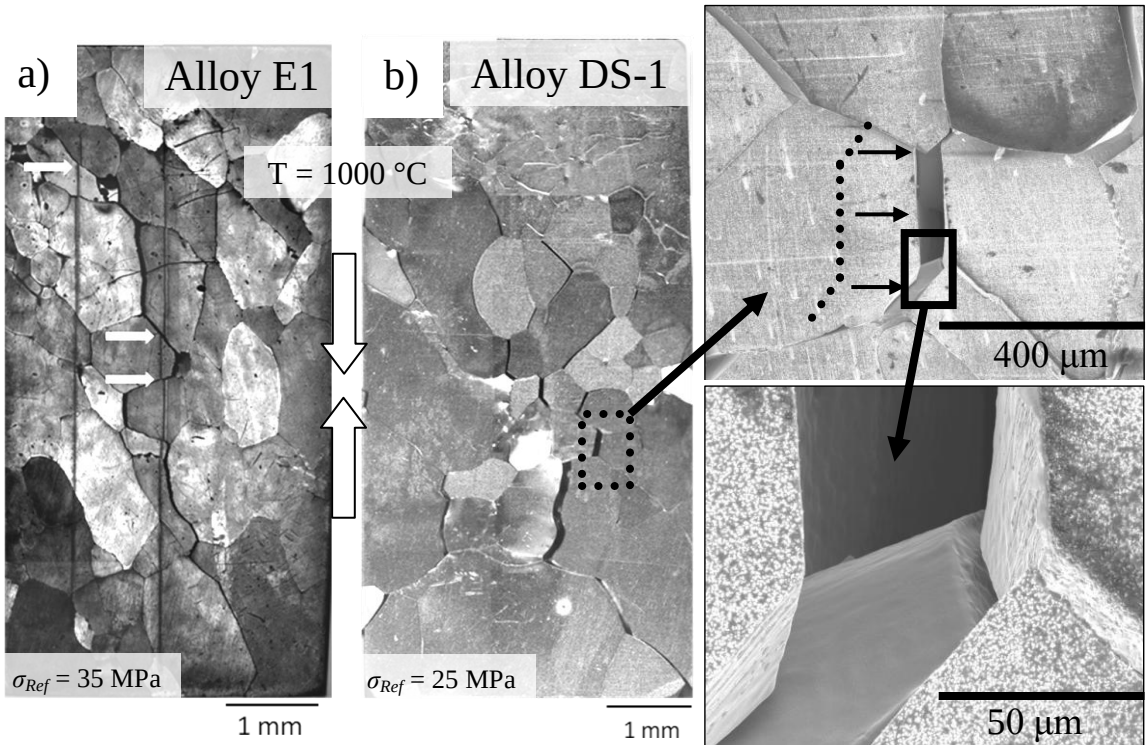

Figure 6.7: Optical images of grain boundary sliding (a), indicated by white arrows, leading to cracks (b). Upper right inset SEM image depicts 'wing crack' formation (illustrated by dotted line), leading to grain separation (lower right SEM inset image). Arrows between (a) and (b) indicate compressive creep direction. Both alloys accumulated at least 1% creep strain.

to grain separation (SEM image highlighted in lower right). The formation of extended cracks parallel to the applied stress axis is typical of plastic failure within compressive tests [27, 130]. From Table 6.2, alloys that did not display grain boundary sliding included PX-5, D12, 8A, and D4.

For alloys that exhibited directional coarsening behavior, creep strength was measured as a function of network spacing and plotted in Figure 6.8. A spacing of approximately 40 nm (alloy D12) was associated with the highest creep strength among all alloys that developed interfacial dislocations. This spacing indicates a misfit

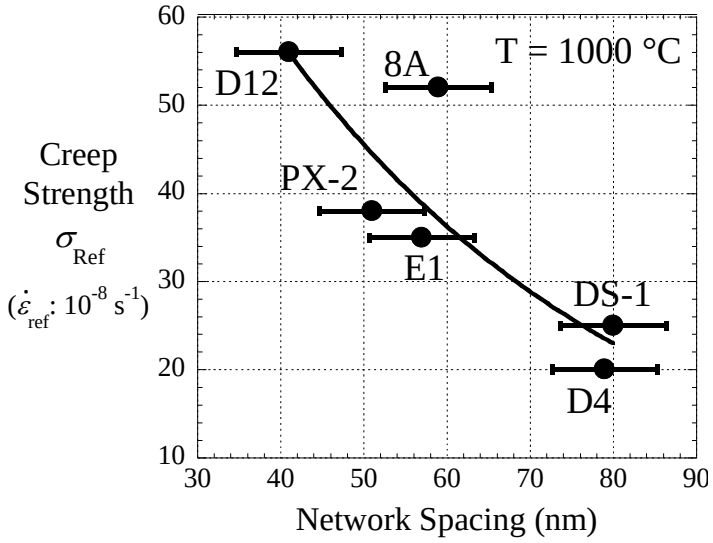

Figure 6.8: Creep strength as a function of network spacing at the γ/γ′ interface.

magnitude approximately 0.6%. Though the fitted line indicates a continual decrease in creep strength up to 80 nm ($|\delta| \approx 0.3\%$) as network spacing increases, it is clear that alloy 8A is an outlier to the observed trend. High temperature creep studies conducted on Ru-modified Ni-base superalloys reported that decreasing $|\delta|$ from 1.0 → 0.2 % does not directly scale with increased creep strength [28]. Thus, network spacings are not the only important factor contributing to variations in creep strength for these PGM alloys.

6.2 High Temperature Deformation Mechanisms

This section examines the deformation mechanisms of positive, negative, and near-zero misfit PGM-modified Ni-base superalloys exposed to high temperature conditions. The preferential partitioning of Pt to γ′ [131, 132] provides superalloys which possess positive misfit rafting behavior. Experiments in Chapter 4 indicate that, in

turn, the strong partitioning behavior of Re to the γ phase within these PGM-modified systems is greatly reduced. These two effects can provide new insight into deformation processes not normally observed for non-PGM (or Ru-containing) superalloys. Nominal compositions (at%) of the alloys discussed in this section are presented in Table 6.7. Alloy D4 contained Ir as the only PGM, while D12 combined Pt and Ir. The remaining alloys contained Pt. All alloys contain 0.1 at% Hf, which shall not be discussed due to its minor additions. Measured volume fractions range from 0.53 - 0.67. Gamma prime aspect ratios, ranging from 0.1 - 0.7, are listed in the final column. The alloys are listed from strongest to weakest in Table 6.7 with respect to reference creep strength, σ_{Ref}, labeled top to bottom, respectively.

6.2.1 γ′ Aspect Ratio and Subsequent Rafting

The range in lattice misfit is apparent through the variation in γ′ morphology, Figure 6.9. An aspect ratio of 0.58 was measured for alloy D12 in Figure 6.9(a), which is near to the aspect ratios of alloys D7, PX-2, and E1, listed in Table 6.7. Alloy D4 measured $\eta = 0.39$, as shown by the image in Figure 6.9(b). Alloys D22 and PX-6 displayed low aspect ratios, $\eta < 0.20$, demonstrated by the microstructure of PX-6 in Figure 6.9(c). Thus, the shift in aspect ratios from $0.58 \rightarrow 0.2$ from Figure 6.9(a → c) is proportional to a decrease in misfit magnitude from $0.6 \rightarrow 0.1\%$ [6].

Once creep testing was performed, the rafting behavior was assessed for each alloy. Figure 6.10(a) demonstrates directional coarsening for alloy D4, whereas alloy D22, Figure 6.10(b), exhibits non-directional coarsening. Table 6.8 lists alloy rafting behavior, determined by similar SEM analysis presented in section 6.1.2. From Table 6.8, four out of five alloys that rafted exhibited positive misfit behavior. Alloy PX-2

Table 6.7: Nominal compositions of PGM alloys used for dislocation analysis.

Alloy	Composition (at%)											v_f	σ_{Ref} (MPa)	η
	Al	Pt	Ir	Cr	Re	Ta	Ru	W	Mo	Ti	Si			
D12	15	2.5	2.5	5	-	2	-	-	-	-	-	0.61	56	0.58
D7	15	2.5	-	5	-	-	-	-	-	-	-	0.57	52	0.47
D22	15	2.5	-	5	1	2	2	1	-	-	-	0.67	48	0.14
PX-2	14.5	2.5	-	7.5	1		-	1	1	0.5	-	0.58	38	0.61
E1	13	2.5	-	5	1	2	1	1	-	-	-	0.53	35	0.70
D4	15	-	2.5	5	1	2	-	-	-	-	-	0.61	20	0.39
PX-6	13.5	2.5	-	7.5	1	2	-	1	1	0.5	0.5	0.60	20	0.13

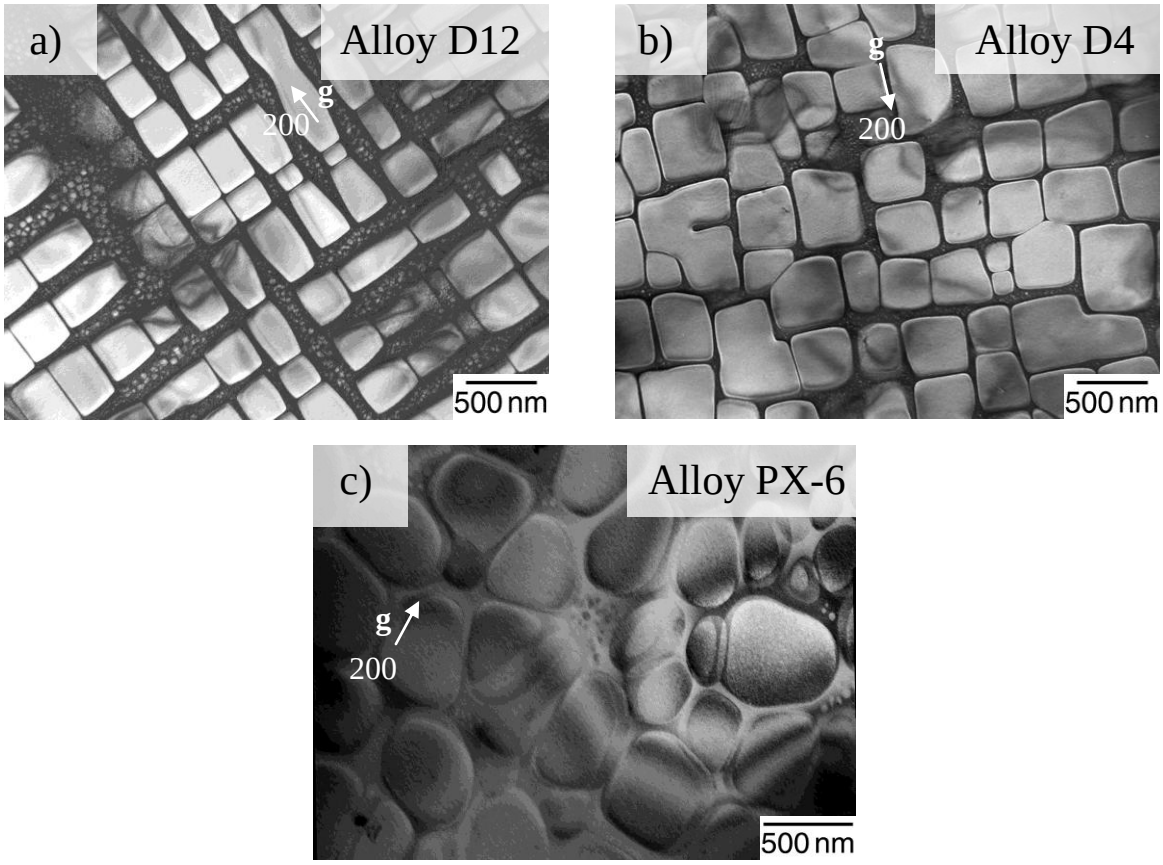

Figure 6.9: Dark field TEM images of heat treated alloys, displaying a range in γ´ morphology.

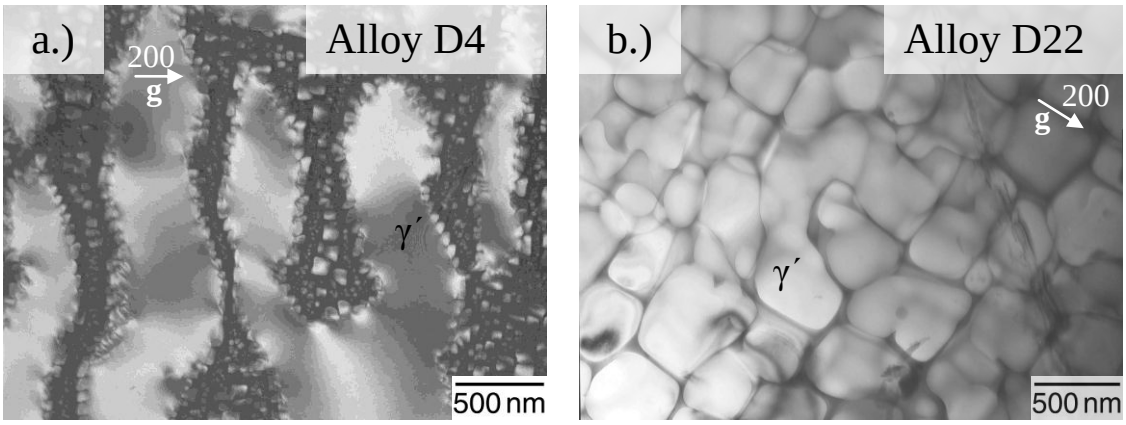

Figure 6.10: (a) Dark field and (b) bright field images of directional and non-directional coarsening, respectively, post-creep.

Table 6.8: Observation of directional coarsening and associated misfit-type.

Alloy	σ_{Ref} (Ref ε_{min} :10^{-8})	Rafting?	Misfit Type
D12	56	Yes	Positive
D7	52	Yes	Positive
D22	48	No	Near-Zero
PX-2	38	Yes	Negative
E1	35	Yes	Positive
D4	20	Yes	Positive
PX-6	20	No	Near-zero

demonstrated negative misfit behavior. Alloys D22 and PX-6 displayed near-zero misfit behavior.

6.2.2 Dislocations

Dislocations were analyzed in regions where directional coarsening was evident. Interfacial network spacings were measured, as well as dislocation densities within the γ and γ´ phases. When compared among one another, alloys in Table 6.8 which rafted did not exhibit similar dislocation networks at the interface. The TEM micrographs in Figure 6.11 show the interfacial dislocation networks following creep deformation. Figures

6.11(a) and 6.11(b) reveal well-developed interfacial networks. These network patterns have been observed within other Ni-base superalloys [29]. Although Figures 6.11(c) and 6.11(d) display directional coarsening, the observation of interfacial network densities are lower in comparison to Figures 6.11(a) or 6.11(b).

The degree by which dislocations accumulated within the matrix or precipitate phases is shown in Figures 6.12(a - d). Figure 6.12(a) represents alloy D7, where dislocations are deposited within the γ′ phase to a greater extent than the matrix. This was observed for alloy D12 as well. Alloy PX-2, Figure 6.12(b), exhibits contrasting behavior where dislocations accumulate to a greater extent within the γ phase. In Figure 6.12(c), alloy E1, dislocations are distributed near equally between phases. Dislocations were observed for non-directionally coarsened alloys, as depicted in Figure 6.13 for alloy PX-6. No evidence of interfacial networks within alloys PX-6 or D22 was observed; this is expected due to near-zero lattice misfit [6, 28].

Dislocations were mostly observed within the γ phase, Figure 6.13(b), with evidence of dislocation climb, shown by the black arrows in Figures 6.11(c) and 6.12(b), and in Figure 6.13(a). A dislocation which glides along the <110>{111} slip system reorients itself into a <001> configuration at the γ/γ′ interface to relieve misfit strain. The orientation of <001> dislocation line segments parallel to the <001> interface indicates the climb process [29]. Dislocation shearing is identified by a pair of closely coupled line segments within the γ′ phase, as indicated by the dotted black arrows in Figure 6.11(b). The observation of climb indicates that creep was carried out in the power-law regime for all three misfit-type behaviors [4, 27], in accord with the calculated creep stress exponent determined from Equation 6.1.

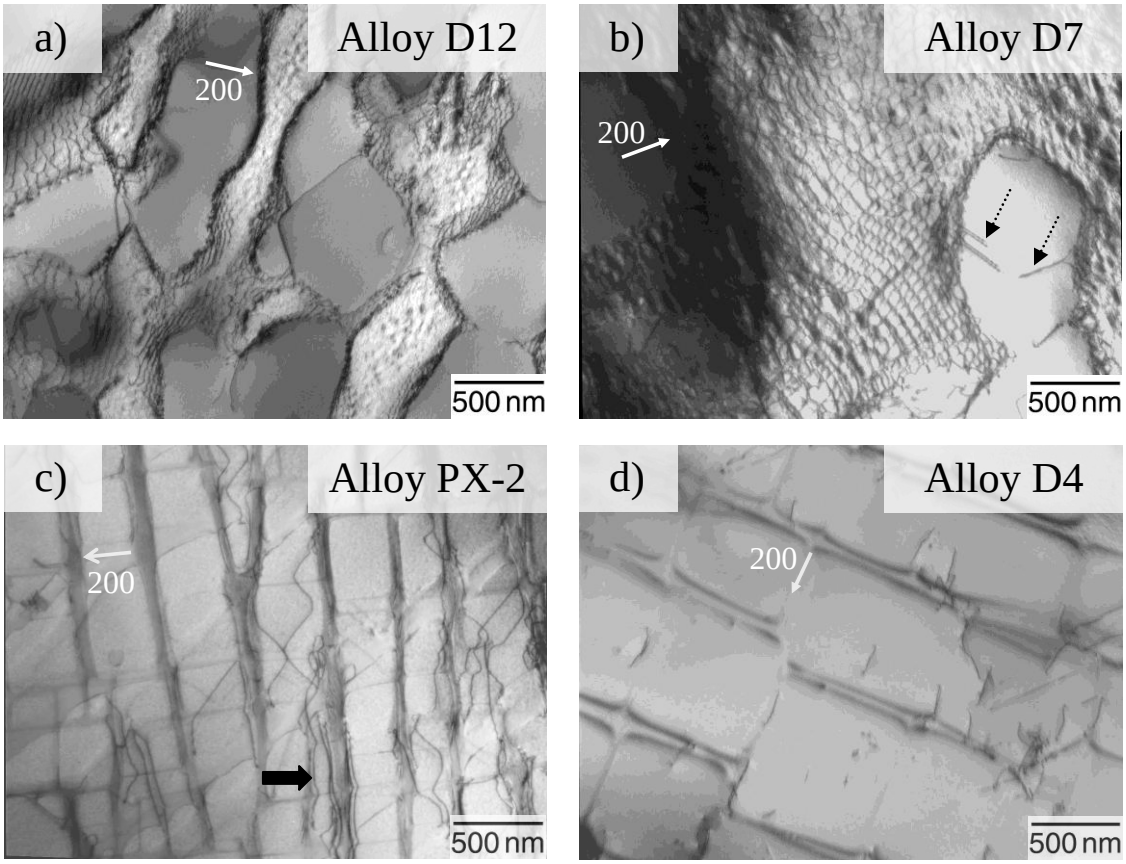

Figure 6.11: Images highlighting formation of interfacial networks in alloys with high creep strength (a) and (b), versus absence of networks with lower strength alloys, (c) and (d). White arrows indicate (200) 2-beam condition

6.2.3 Average Precipitate Thickness

Once dislocations were identified as either within the γ or the γ′ phase, dislocation densities (ρ_{dis}) in each phase were measured using Equation 2.4. Figure 6.14 plots the distribution of normalized precipitate sizes. An average precipitate thickness, *D*, was calculated as 461 nm (± 109). This value falls within the range of other aged γ′ particle sizes [40, 44, 47]. Thus, γ′ precipitates for PGM alloys provide particle sizes similar to conventional Ni-base superalloys.

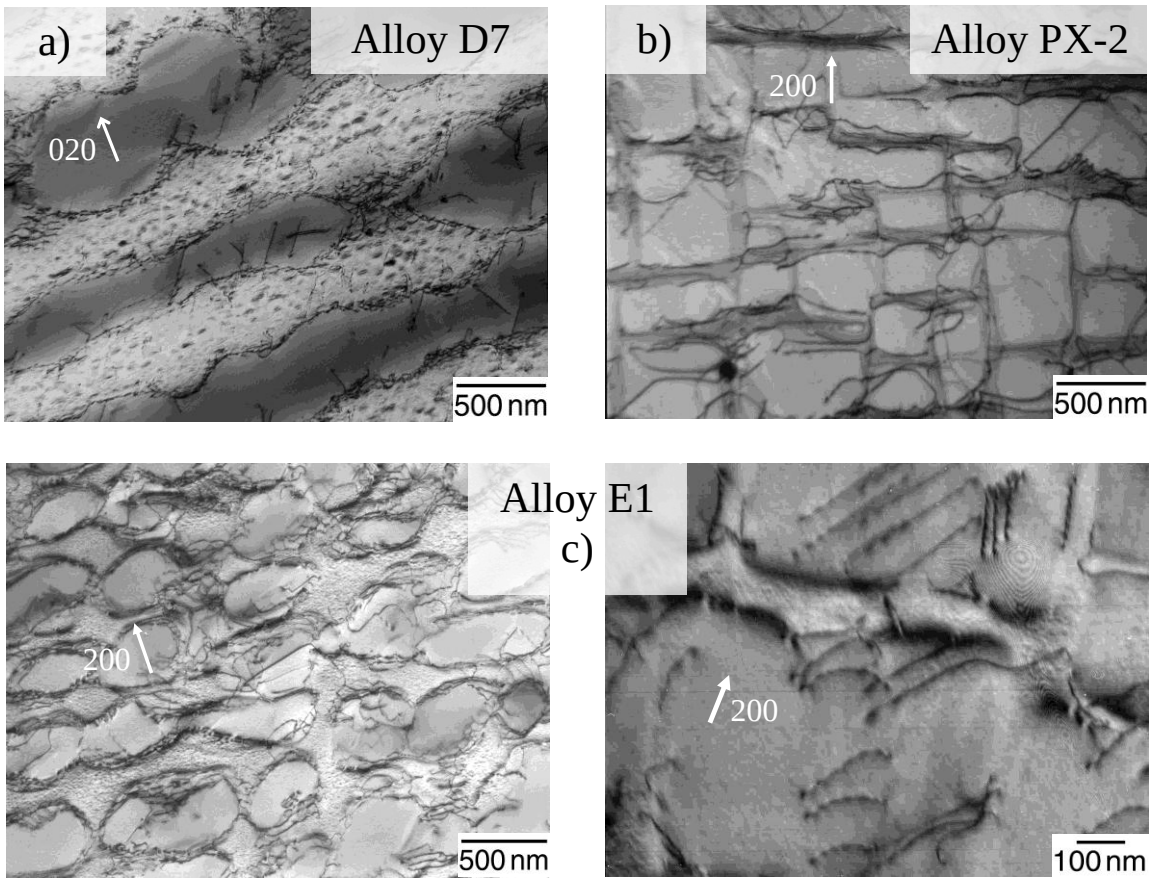

Figure 6.12: For directional coarsened material, alloys with high creep strengths displayed (a) $\rho_{ppt} > \rho_{matrix}$. As creep strength decreased, an inversion occurred, where (b) $\rho_{ppt} < \rho_{matrix}$. As strength continually decreased, (c) $\rho_{ppt} \approx \rho_{matrix}$.

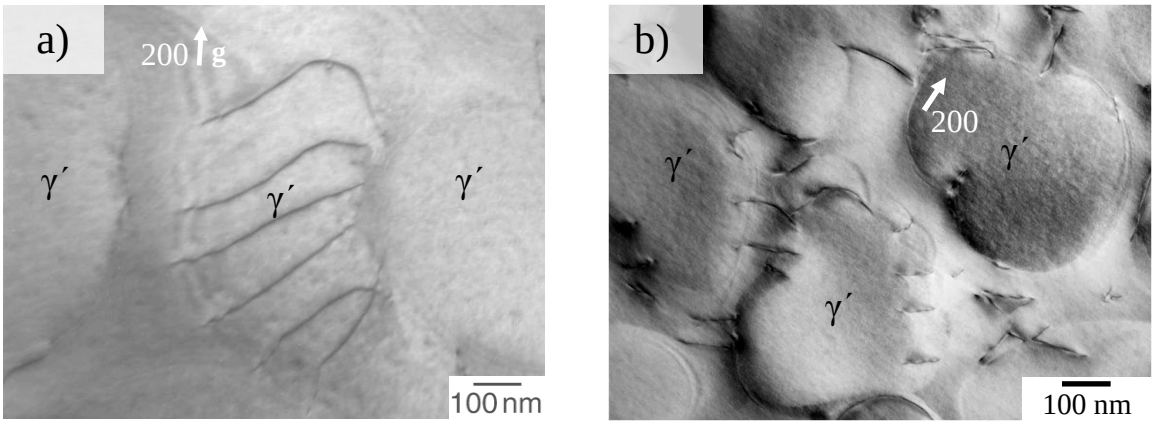

Figure 6.13: Alloy PX-6, highlighting dislocation (a) climb and (b) glide.

6.2.4 Dislocation Density

The dislocation densities in each phase are plotted as a function of reference creep strength in Figure 6.15. As stress increases, no discernable pattern is observed for either the ρ_{matrix} or ρ_{ppt} when viewed individually from alloy to alloy. However, comparing the densities of the ρ_{matrix} and ρ_{ppt} for each reference stress, rather than separately, reveals an unusual observation. At a reference stress of σ_{Ref} = 50 - 60 MPa, the $\rho_{ppt} > \rho_{matrix}$ – a very uncommon feature for high temperature creep deformation within Ni-base superalloys. As stress decreases, an inversion occurs, where the $\rho_{ppt} < \rho_{matrix}$, corresponding to positive misfit alloys D4 and E1, as well as negative misfit alloy PX-2. The matrix densities for alloys D22 and PX-6 are greater than the precipitate densities; similar for alloys that exhibited rafting behavior below the reference creep strength of 50 MPa. In this study, matrix density measurements range on the order of 10^{11} - 10^{13} per m^2, in agreement with matrix densities reported for other high temperature creep deformed Ni-base superalloys [28, 29, 133, 134]. The precipitate densities measured in this study are on the order of 10^{11} - 10^{12} per m^2.

6.3 Summary

The high temperature creep behavior of PGM-modified Ni-base superalloys is influenced by numerous factors. A γ' volume fraction between 0.60 - 0.65 provides the highest creep resistance. Positive, negative, and near-zero misfit-type behavior has been observed through directional coarsening. A creep stress exponent of n = 5.0 indicates the PGM alloys operate within the power-law regime. Grain boundary sliding and damage

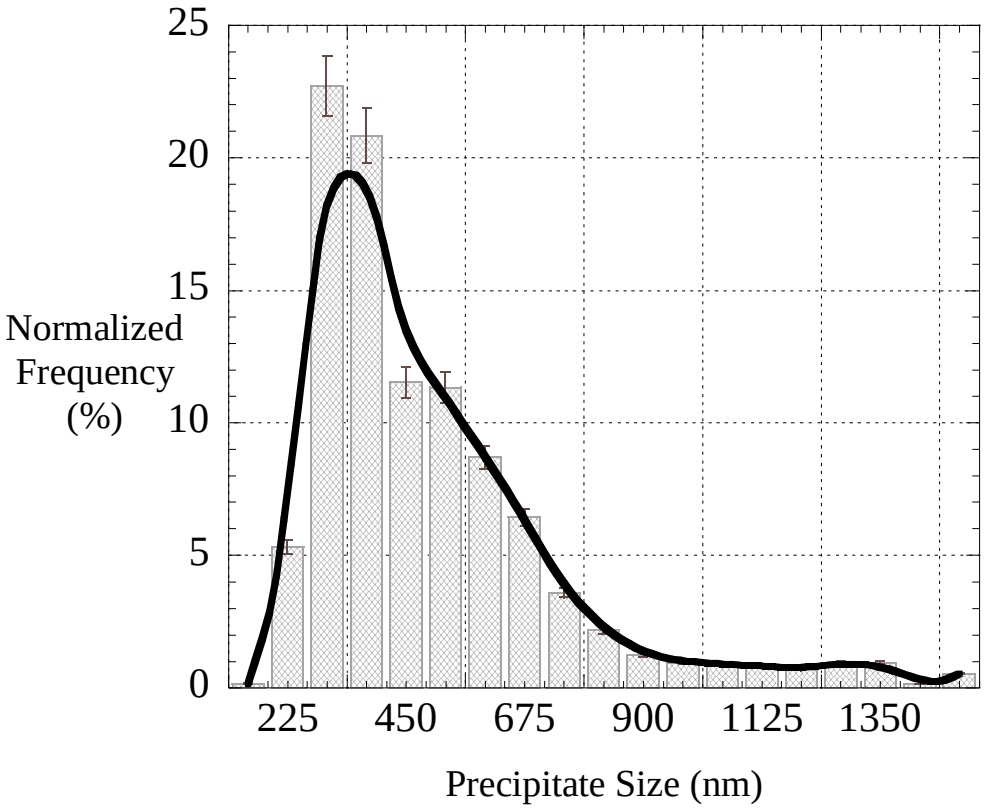

Figure 6.14: Normalized precipitate size used in dislocation density analysis.

has been observed for some, but not all, of the creep tested alloys. High temperature creep tests have demonstrated that: 1) grain boundary strengtheners improve overall creep resistance for alloys containing little or no refractory additions, and 2) the Ir-containing alloys have lower creep resistances compared to Pt-containing alloys.

Dislocation analysis has been performed on alloys exhibiting all three types of misfit behavior. Alloys that directionally coarsen display dissimilar interfacial network densities when compared amongst each another. Alloys with well-developed networks demonstrate higher creep resistances. The degree by which dislocations accumulate within the matrix and precipitate is dependent upon the misfit-type behavior and reference creep strength. Alloys displaying positive misfit behavior with reference creep

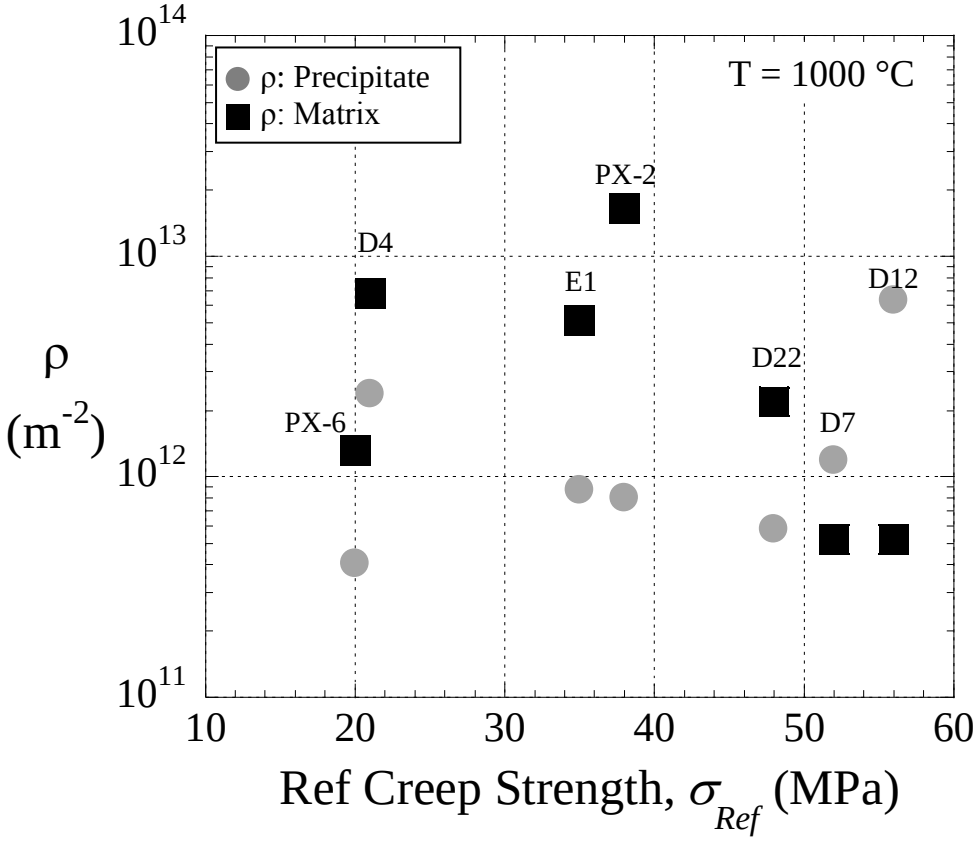

Figure 6.15: Dislocation densities within the matrix and precipitate as a function of reference creep strength.

strengths that range from 50 - 60 MPa exhibit precipitate dislocation densities greater than the matrix, which is an unusual occurrence for high temperature creep deformation of Ni-base superalloys. Creep resistances below the reference creep strength of 50 MPa contain higher dislocation densities within the matrix as opposed to the precipitate, regardless of the misfit-type behavior of the superalloy. TEM reveals dislocation climb operating within non-directionally and directionally coarsened alloys, demonstrating that creep is operating in the power-law region, consistent with the value of $n = 5$ obtained for the creep stress exponent.

CHAPTER 7

HIGH TEMPERATURE CREEP PERFORMANCE OF THE PGM-MODIFIED NI-BASE SUPERALLOYS

Approximately 50 PGM-modified experimental Ni-base superalloys have been investigated in this study. The variation in nominal compositions allows a comparative analysis of the mechanisms that affect creep performance. The influence of PGM additions on γ′ morphology, elemental partitioning, and coarsening kinetics have been examined. Iridium reduces the preferential partitioning behavior of alloying elements, providing one explanation for the observed low creep strengths of Ir-containing alloys. Furthermore, Re does not strongly partition into the γ phase for these PGM alloys, compared to conventional Ni-base superalloys. Despite iridium and rheniums effect on creep strength, their uncommon partitioning behavior can provide new insight into deformation mechanisms not typically observed within conventional Ni-base superalloys.

The high temperature reference creep strengths for these PGM alloys ranged from approximately 10 - 70 MPa. These variations were due a creep strength dependence on precipitate volume fractions, grain boundary strengthening, and the formation of interfacial dislocation networks. This investigation established that creep deformation occurred in the power-law regime, indicating that dislocation climb and the diffusion of solute atoms within the Ni-matrix would affect creep performance. An unusual feature of deformation in some alloys was observed; dislocation densities that measured to be

greater within the precipitate phase rather than the matrix. The preferential partitioning of platinum to the γ′ phase permitted an uncommon group of superalloys to be studied, namely alloys that exhibit positive misfit behavior.

This chapter examines the dependence of high temperature creep strength on the various factors mentioned above. These PGM-modified Ni-base compositions offer new possibilities for the design of Ni-base alloys. As such, understanding the mechanisms which caused differences in creep strengths, and whether PGM additions were beneficial, can help design more creep resistant PGM alloys for the future.

7.1 High Temperature Creep Resistance of PGM-Modified Ni-Base Superalloys

Factors known to influence creep resistance in superalloys include: 1) Orowan resistance due to non-deforming coherent or semi-coherent precipitates, 2) degree of misfit, 3) dislocation densities within each of the phases, and 4) grain boundary sliding and damage accumulation at grain boundaries. Determining whether or not the PGM additions impact any of the above factors and, if so, to what extent, is considered in this section. Table 7.1 lists the alloys used for discussion. Table 7.2 provides volume fractions and precipitate edge lengths, or precipitate diameters, for alloys listed in Table 7.1. The volume fractions range from 0.45 - 0.74 and precipitate lengths/diameters range from 281 - 653 nm. Alloys PX-5 and 8A contain grain boundary strengtheners B, C, and Zr. Alloy 8A did not include Re, W, or Ta refractory additions in its nominal composition, and alloy D4 is the only alloy that contains Ir as the sole PGM addition. Other than alloys PX-5, D12, 8A, and D4, the remaining alloys listed in Table 7.1 succumbed to grain boundary sliding. Calculated interdiffusion coefficients are provided in Table 7.2 as well.

7.1.1 Analysis of Creep Resistance

The bulk of dislocation activity for non-directional and directional coarsened alloys was confined to the matrix, as shown in Figures 7.1(a) and 7.1(b), respectively. Dislocation densities within the matrix will therefore exceed dislocation densities within the precipitate, which has been observed for other Ni-base systems [28, 29, 133, 134]. This suggests that the γ' precipitates are able to resist dislocation shearing, forcing dislocations to glide within the matrix. Dislocation glide and accumulation within the γ

Table 7.1: Nominal compositions of PGM alloys. Extrapolated reference creep strengths are provided in the last column.

Alloy	Composition (at%)											σ_{Ref}
	Al	Pt	Ir	Cr	Re	Ta	Ru	W	Mo	Ti	Si	(MPa)
PX-5 *	13.5	2.5	-	7.5	1	2	-	1	1	0.5	0.5	68
D12	15	2.5	2.5	5	-	2	-	-	-	-	-	56
D25	15	2.5	2.5	5	1	2	2	1	-	-	-	53
8A *	15	2	2	5	-	-	-	-	-	-	-	52
PX-2	14.5	2.5	-	7.5	1	2	-	1	1	0.5	-	38
E1	13	2.5	-	5	1	2	1	1	-	-	-	35
DS-1	14	2.5	-	10	1	2	2	1	-	-	-	25
D4	15	-	2.5	5	1	2	-	-	-	-	-	20
PX-6	13.5	2.5	-	7.5	1	2	-	1	1	0.5	0	20

*Alloys contain the following grain boundary strengtheners: 0.014Zr·0.1C·0.087B

Table 7.2: Measured volume fractions, average edge lengths, and interdiffusion coefficients of PGM alloys listed in Table 7.1.

Alloy	V_f	l_{edge} (nm)	Interdiffusion Coefficient D_{int} (MPa / $m^2 \cdot s^{-1}$)
PX-5	0.66	298	4.97×10^{-18}
D12	0.61	653	2.18×10^{-18}
D25	0.74	294	5.45×10^{-18}
8A	0.45	337	2.18×10^{-18}
PX-2	0.69	292	4.97×10^{-18}
E1	0.53	325	4.97×10^{-18}
DS-1	0.55	281	4.97×10^{-18}
D4	0.7	573	1.05×10^{-18}
PX-6	0.67	343	4.97×10^{-18}

phase or at the γ-γ′ interface is dependent on channel width, w_{ch}, and γ′ volume fraction. The range of V_f and precipitate edge lengths, l_{edge}, listed in Table 7.2 can be used to estimate the creep strength by consideration of the Orowan resistance, τ_{Or} [135]:

$$\tau_{Or} = \sqrt{\frac{2}{3}} \frac{G\vec{b}}{w_{ch}} \qquad \text{Equation 7.1}$$

where the factor $\sqrt{\frac{2}{3}}$ accounts for the orientation of the slip plane and line direction

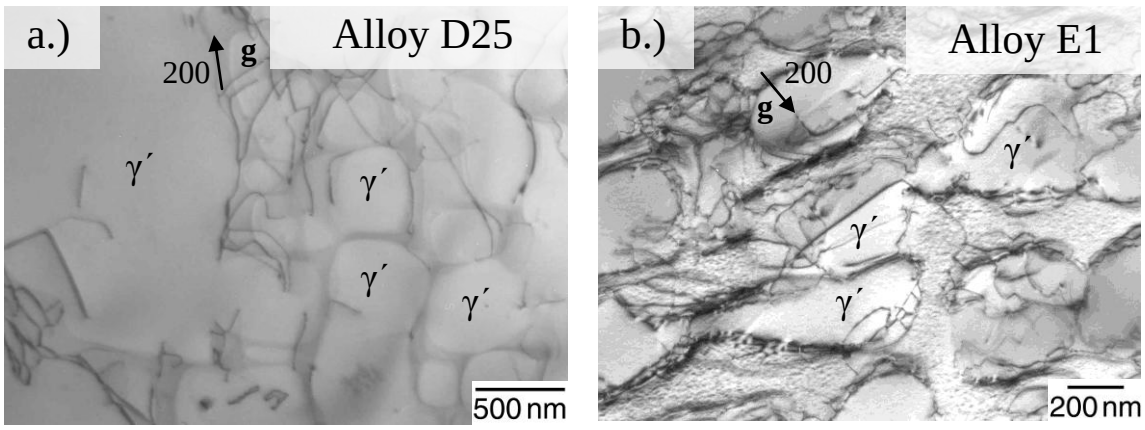

Figure 7.1: Dislocations within the matrix for alloys displaying (a) non-directional and (b) directional coarsening**.**

within the fcc matrix channels, and G (shear modulus) = 50 GPa [29]. The w_{ch} is calculated as:

$$w_{ch} = l_{edge}\left(\frac{1}{(V_f)^{1/3}} - 1\right) \qquad \text{Equation 7.2}$$

The Orowan shear resistance is converted to a normal stress, σ_{Or}, via a Schmid factor, M, for single crystals or a Taylor factor, m, for polycrystalline material:

$$\sigma_{Or} = \frac{\tau_{Or}}{M} \rightarrow M = < m >^{-1} = < m > \tau_{Or} \qquad \text{Equation 7.3}$$

For fcc polycrystals, M is replaced with the average Taylor factor, $< m > = 3.06$ [136, 137]. Orowan resistance calculations are compared to the reference creep strengths in Table 7.3, and plotted in Figure 7.2. Calculated normal stresses are an order of magnitude greater than reference creep strengths. Aside from alloys PX-5, D12, 8A, and D4, the remaining alloys in Figure 7.2 exhibited grain boundary sliding (GBS), similar to the optical images of alloys E1 and DS-1 shown in Figure 6.7. GBS is discussed in

Table 7.3: Comparing Orowan Resistance to reference creep strength.

	PGM Alloy								
	PX-5	D12	D25	8A	PX-2	E1	DS-1	D4	PX-6
Orowan σ_{Orowan} (MPa)	714	481	1019	307	825	413	702	437	645
Creep Strength σ_{Ref} (MPa)	68	56	53	52	38	35	25	20	20

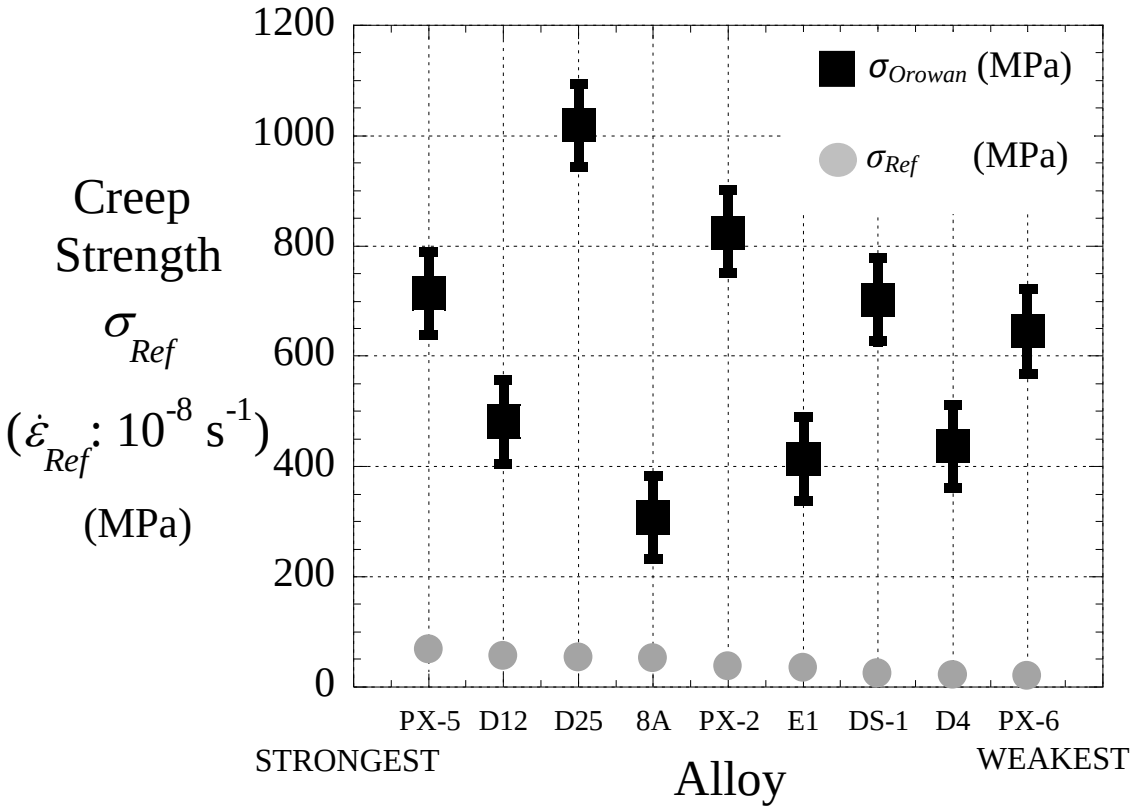

Figure 7.2: Comparison of Orowan resistance to reference creep strengths

further detail in Section 7.1.3.

Although alloys PX-5, D12, 8A, and D4 did not display GBS, their reference creep strengths were still considerably lower than calculated. The Orowan calculation presumes that precipitates resist dislocation shearing. Therefore, this presumption must not be entirely valid for these PGM alloys. In addition, while the Orowan calculation

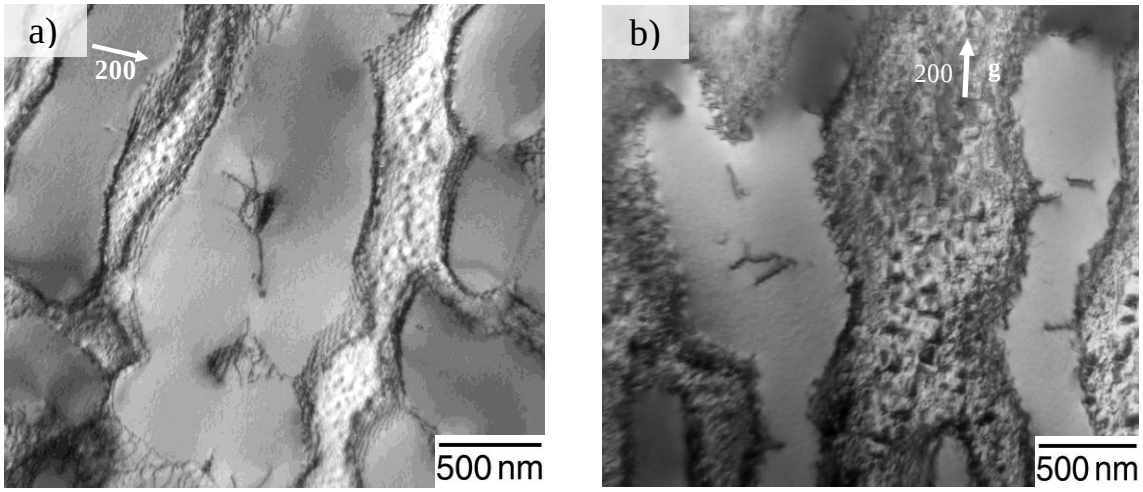

Figure 7.3: Alloys (a) D12 and (b) 8A creep tested at 1000 °C. Dislocations were not evident within γ but observed mainly within γ′.

accounts for dislocations accumulating mostly within the matrix phase, alloys D12 and 8A displayed a greater accumulation of dislocations within the precipitate as compared to the matrix, shown in Figures 7.3(a) and (b), respectively. The density of dislocations being greater within the precipitate phase rather than the matrix was shown in Section 6.2.4, and is further addressed in Section 7.2.

The creep stress exponent, n = 5.0, derived from alloys PX-5 and PX-6, Figures 6.6(a) and 6.6(b), respectively, indicate that these PGM superalloys operate in the power-law regime. Table 7.4 provides the creep stress exponents, n, of various Ni-base alloys tested at high temperatures. Aside from the PGM alloys, stress exponents that are $n = 5.0 \pm 1$ belong to single phase Ni alloys. Creep stress exponents greater than n = 6.0 are more common for two-phase γ-γ′ Ni-base superalloys. Considering that the PGM alloys contain precipitates and additional strengthening elements beyond Ni and Al, its measured stress exponent is rather low. Models for creep deformation indicate that the

Table 7.4: Creep stress exponents of various Ni-base alloys.

Alloy	Investigated Temperature (°C)	Creep stress exponent *n*
DS MAR-M200 [138]	760	12.7
CMSX-3 [135]	850	7.3
PC MAR-M247 [32]	871	7.5 - 9.5
René N6 [60]	982	6.6
	1083	7.2
PC Ni-Al [139]	927	5.9
	1027	5.8
PC Ni-W [140]	1000	3.6
SC γ-alloy [141]	1000	4.2
SC γ′-alloy [141]	1000	3.5
PGM alloys	***1000***	***5.0***
PC Ni [31]	1100	4.6

*PC = Polycrystalline; DS = Directional Solidifed; SC = Single Crystal

rate-limiting mechanism associated with n = 5.0 is dislocation climb [29, 139, 140]. As such, dislocation climb is likely to be the rate-limiting step for these PGM systems.

At high temperature, dislocation climb can occur at the scale of the precipitates or at the scale of the interfacial network. The former is more likely in a near-zero misfit material that does not undergo directional coarsening, and the latter in high misfit alloys where the precipitates are not easily sheared. It is necessary to consider how solute in the matrix can affect this aspect of creep behavior. The PGMs, Pt and Ir, must be accounted for, along with the more common strengtheners, Re and W. Considering:

$$\tilde{D}_{\text{int}} = \sum_{A} X_A^m \cdot D_{Ni-A} \qquad \text{Equation 7.4}$$

where the interdiffusion coefficient, $\tilde{D}_{\text{int}}$ (m^2/s), arises from the summation of the slowest diffusing elements (A = Pt, Ir, Re, W) within the matrix, $D_{Ni\text{-}A}$, multiplied by the mole fraction of A residing in the matrix, X_A^m. Using the partitioning data of solute to the γ

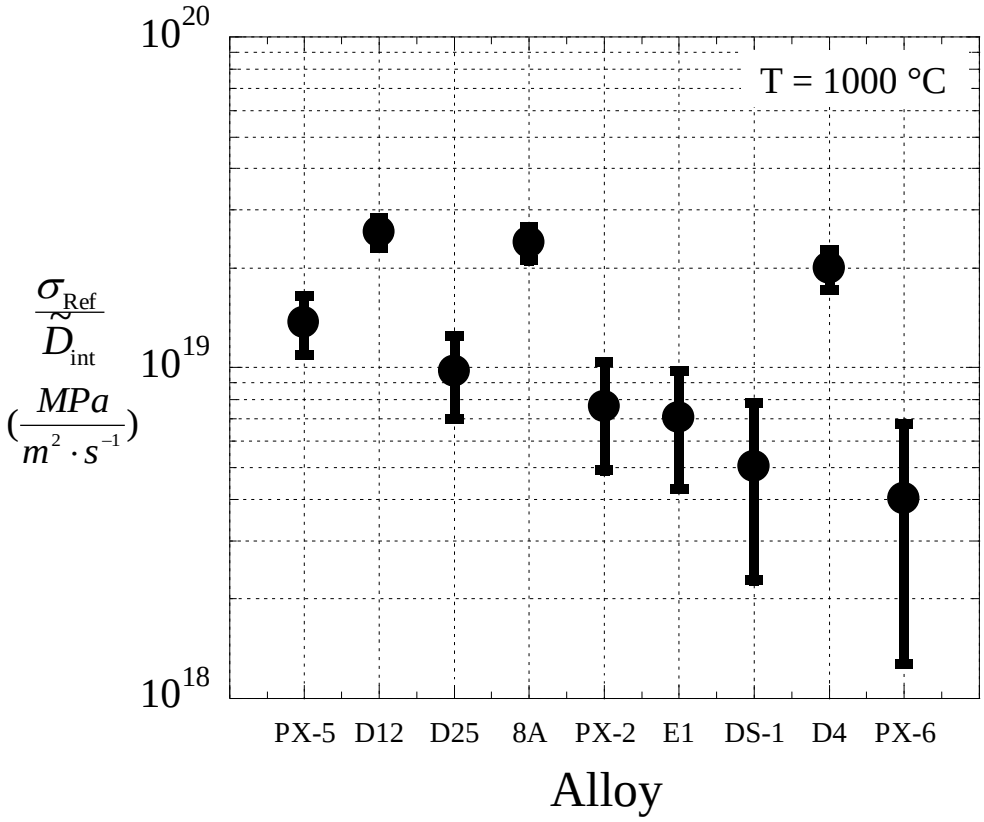

Figure 7.4: Normalization of creep strength.

phase, Tables 4.2 and 4.3, and interdiffusion data, $D_{Ni\text{-}A}$, of refractory and PGM elements at 1000 °C [30, 117], Figure 1.9, an interdiffusion coefficient is provided for each alloy in Table 7.2. This interdiffusion coefficient is used to normalize the reference creep strengths listed in Table 7.1, and plotted in Figure 7.4. Alloys are listed from strongest to weakest (left to right) based on extrapolated reference creep strengths. From Figure 7.4, alloys D12, 8A, and D4, should provide the highest resistance to dislocation climb of all alloys listed in Table 7.1. Considering alloys D12 and 8A are not the two strongest alloys from Table 7.1, and alloy D4 was one of the weakest alloys overall, this indicates that creep strength does not directly scale with interdiffusion and creep is not simply controlled by dislocation climb. Since the variation in creep strength from alloy to alloy

is reduced when normalizing with the interdiffusion coefficient, it is still essential to consider how alloying additions can reduce diffusion kinetics.

7.1.2 Degree of Lattice Misfit

As stated in Section 1.3.3, the degree of lattice misfit between γ and γ′ dictates the morphology and directional coarsening behavior of the precipitate. For alloys that display misfit magnitudes near, or greater than, 0.2%, directional coarsening occurs as well as the formation of dislocation networks at the interface. Misfit magnitudes less than 0.2% display no directional coarsening behavior and are devoid of interfacial networks.

The unique PGM elemental partitioning provided a range of lattice misfit, with particle aspect ratios ranging from 0 - 0.8. Pt additions increase $a_{\gamma'}$, resulting in aspect ratios near 0.7, similar to the micrograph of alloy D12 in Figure 6.9(a). Alloy D4, containing Ir as the only PGM, provides η near 0.4, Figure 6.9(b), with low refractory additions. To offset the preferential partitioning of Pt to the γ′ phase, alloys must include elements that partition to the matrix (W, higher Cr, Mo), increasing a_{γ}. An aspect ratio near 1 with these additions can be achieved, alloy DS-1, shown in Figure 6.3(c). Similarly, near-zero lattice misfit alloys that contain moderate refractory content is also possible, shown for alloy PX-5 in Figure 6.3(a). Overall, Ni-base alloys with Pt additions containing little to no refractory content will provide $\delta > 0$. Introducing higher order solid solution strengthening content increases a_{γ}, resulting in $\delta \leq 0$.

Table 7.5 lists the ten alloys which displayed the highest creep resistance in this investigation, along with the measured aspect ratios. To assess whether particle morphology relates to creep strength, Figure 7.5 plots creep strength as a

Table 7.5: Reference creep strengths and shape parameter for ten highest creep resistant alloys in this investigation.

Alloy	Reference Creep Strength σ_{Ref}	Particle Aspect Ratio η
PX-5	68	0.08
D5	61	0.14
D12	56	0.58
D25	53	0.14
8A	52	0.35
D3	52	0.22
D7	52	0.45
D21	48	0.14
D22	48	0.14
D24	46	0.16

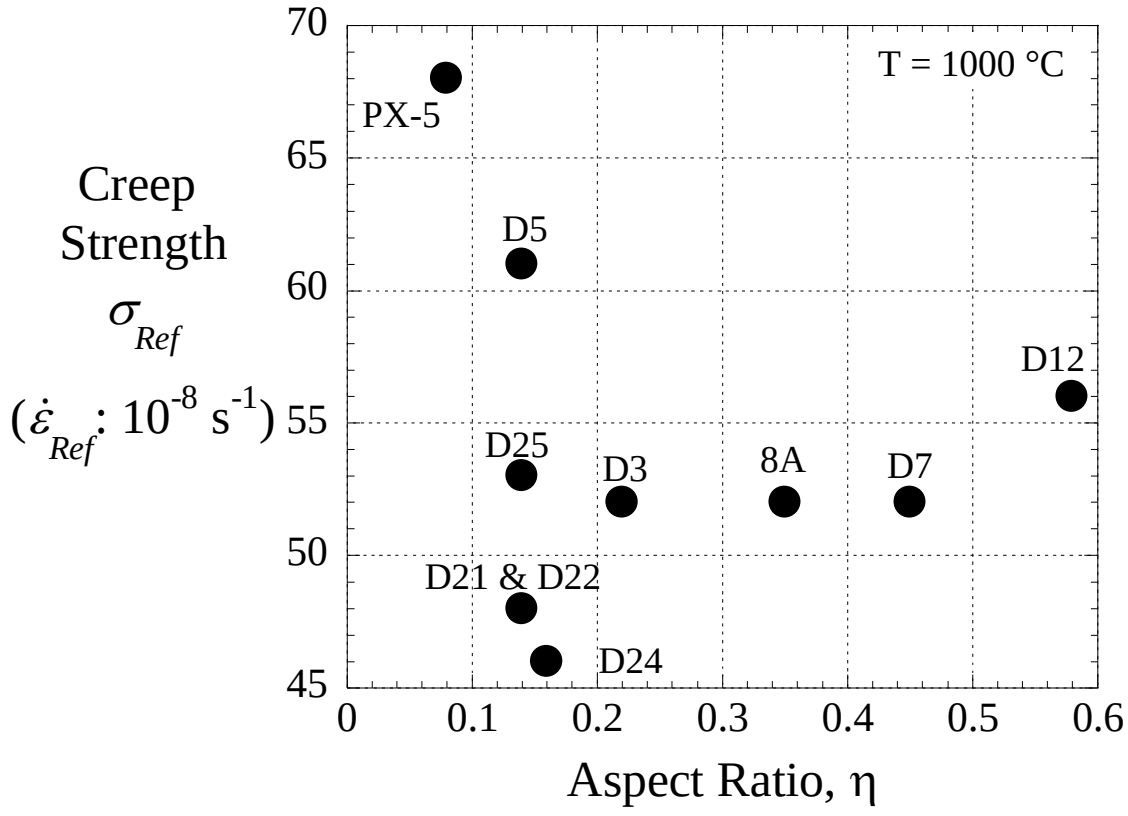

Figure 7.5: Reference creep strength as a function of particle aspect ratio.

function of particle aspect ratio from alloys listed in Table 7.5. Alloy PX-5 demonstrates the greatest creep strength. This can be attributed to the grain boundary strengtheners added to alloy PX-5s composition. Although the aspect ratio for alloy D5 is similar to alloys D21, D22, D24, and D25 in Figure 7.5, the one feature separating D5 from the latter four alloys was its misfit magnitude, 1.2%, as shown in Figure 3.25, for which well-developed interfacial networks formed during creep. Aspect ratio alone does not directly correlate to alloy creep strength. Rather, the combination of gamma prime aspect ratio and misfit magnitude provides a better indication for PGM alloy creep strength.

7.1.3 Grain Boundary Sliding (GBS)

Out of the 29 alloys that were crept within this study, Table 6.1, 13 alloys displayed grain boundary sliding. The observation of GBS has been recorded since the early 1910s, where Rosenhain observed 'inter-crystalline fracture' for Al-Cu-Zn alloys [142, 143]. The deformation of a fcc polycrystalline alloy requires that no less than five independent slip systems be active for deformation to proceed, which the Taylor factor assumes to be true [137]. The nucleation of voids and cracks, however, allow grains to behave and deform independently of one another, as if they were single crystal grains. This leads to an overall reduction in creep strength, as was observed for the PGM alloys which exhibited GBS from Table 7.1.

There was no indication that GBS was associated with specific PGM additions or with positive or negative misfit. From Table 7.1, alloys PX-5, D12, 8A, and D4 were the only alloys not to display grain boundary sliding. DTA, Table 6.5, indicated narrow heat treatment windows for many alloys listed in Table 7.1. Weak, unsolutionized γ', Figure 7.6(a), enhances damage development, leading to crack initiation within the grain interior

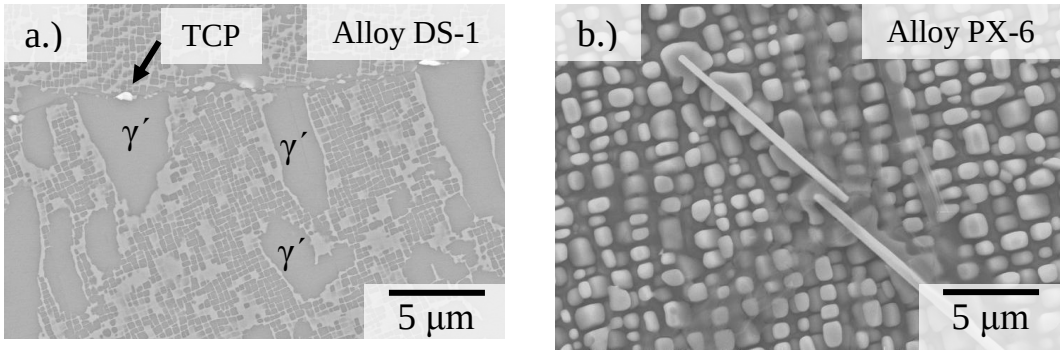

Figure 7.6: (a) Unsolutionized γ´ at a grain boundary and interior and TCP formation, (a) and (b), contributed to sliding and reduction in creep strength.

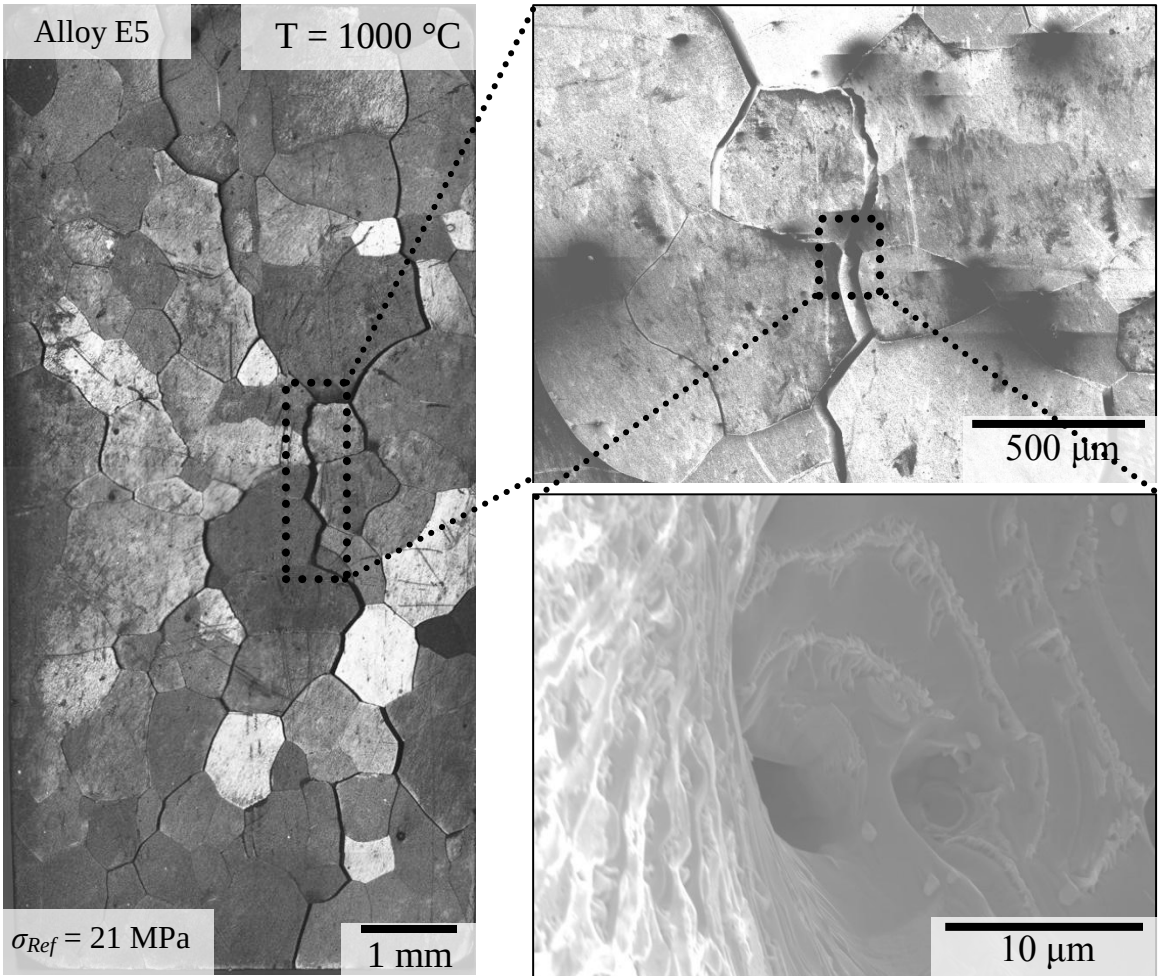

Figure 7.7: Optical image of alloy E5. TCP phase formation and/or insoluble γ´ could be initiation sites for cracks (upper right SEM image). These factors may serve to enhance damage (lower right SEM), leading to GBS.

or at grain boundaries.

High temperature studies conducted on Ni-base superalloys containing Re additions have demonstrated that this refractory element can induce TCP phase formation [19, 127, 144]. TCP phases can form at grain boundaries, causing cracks or porosity, which contributes to GBS. Despite alloy D4 containing 1 at% (~ 3 wt%) Re, no evidence of TCP phases at grain boundaries or grain interiors post-creep was observed for alloy D4. When W was added to the alloys, TCP phases were observed at grain boundaries and interiors, as shown in Figures 7.6(a) and 7.6(b), respectively. All alloys listed in Table 7.1 that contained Re and W displayed TCP phase formation. Insoluble γ′, or TCP phase formation, at grain boundaries may individually, or cumulatively, create damage, displayed in Figure 7.7, which reduces the strengthening effect of the precipitates [4].

Research since the 1960s has established that grain boundary strengtheners, in parts per million, improves the creep life of superalloys [145-149]. Selmen *et al.* included grain boundary strengtheners in the polycrystalline PGM alloys they investigated to prevent GBS [73]. Decker and Freeman conducted creep tests at 871 °C on Ni-base alloys with variations in the boron and zirconium additions [146]. Table 7.6 compares the effects of two alloys studied by Decker and Freeman which contained trace amounts of B and Zr, as well as B and Zr additions similar to those found in alloys PX-5 and 8A.

Table 7.6: Effects of B and Zr for high temperature creep tests at 871 °C.

Alloy	B (at%)	Zr (at%)	ε (%)	Time to 1%	ε_{min} (s^{-1})	Applied Stress (MPa)
V	0.001	<0.006	1.0	117	1.1·10-8	138
V (B+Zr)	0.05	0.006	1.2	214	< 1.0·10-8	207

It can be seen that the time to 1% deformation for alloy V (B + Zr) is nearly double in comparison to alloy V, and that the applied stress for alloy V (B + Zr) is almost a factor of two higher compared to Alloy V. In some instances, Decker stated, the process of GBS could attribute to more than 90% of the total creep deformation [150]. Garosshen *et al.* conducted creep tests at 704 °C and 552 MPa to 0.2% elongation on powder metallurgy (P/M) disk Ni-base superalloys modified with C, B, and Zr additions. Whereas the alloy without grain boundary strengtheners ruptured after 1 hour, alloys containing grain boundary strengtheners achieved a steady state creep-rate on the order of 10^{-8} s^{-1} and recorded, on average, 330 h before 0.2%. Based on these tests, the creep strength for a superalloy would, at least, double with the additions of grain boundary strengheners.

Alloys PX-5 and PX-6 share similar nominal compositions, shown in Table 7.1, except for the grain boundary strengtheners within alloy PX-5. Comparing reference creep strengths of both alloys demonstrates how grain boundary strengtheners provide a higher creep resistance for PX-5. Although TCP phases were observed for PX-5 and PX-6, PX-5 provides a reference creep strength 3.4x that of PX-6, and was the strongest alloy in this investigation. Based on the reports of Decker and Garosshen, as well as the creep strength increase shown for alloy PX-5, it can be concluded that alloys listed in Table 7.1 which demonstrated GBS should exhibit creep strengths 2 - 3x than what is reported, if grain boundary strengtheners are included in their nominal compositions. It is also important to consider grain boundary strengtheners for alloys with no refractory additions, such as alloy 8A. This alloy displayed low V_f, Table 7.2, and lacked Ta, Re, or W additions, yet was the 5^{th} strongest alloy out of those listed in Table 7.5, displaying a

higher reference creep strength against alloys containing moderate refractory additions. For these PGM alloys, grain boundary strengtheners enhance creep properties with and without refractory additions.

7.2 Dislocation Densities and Creep Resistance

The PGM-modified Ni-base superalloys crept in this study exhibited positive, near-zero, and negative misfit-type behavior. Such a broad range in rafting behavior allows dislocation accumulation within the γ and γ′ phases to be studied in finer detail. The calculations of dislocation densities measured within both phases, and interdiffusion coefficients, $\tilde{D}_{\text{int}}$, at 1000 °C, provides useful quantitative input for modeling of the creep process. This section derives a creep model to help explain the differences in creep strength among the PGM alloys. Table 7.7 lists alloys used for discussion within this section, and Table 7.8 lists misfit-type behavior and measured dislocation densities within the γ and γ′ phases. Volume fractions range from 0.53 - 0.67, and edge lengths/diameters range from 280 - 650 nm.

7.2.1 Climb Velocity

Analysis within Section 7.1.1 established that interdiffusion does influence the creep properties of these PGM-containing alloys. As such, determination of the climb velocity for the PGM alloys which exhibit directional and non-directional coarsening would be most useful. The climb velocity is expressed as [151, 152]:

$$v_{cl} = \frac{\tilde{D}_{\text{int}} \sigma_{\text{Ref}} b^2}{kT} \qquad \text{Equation 7.5}$$

Table 7.7: Nominal compositions of PGM alloys used for dislocation analysis.

Alloy	Composition (at%)											v_f	σ_{Ref} (MPa)
	Al	Pt	Ir	Cr	Re	Ta	Ru	W	Mo	Ti	Si		
D12	15	2.5	2.5	5	-	2	-	-	-	-	-	0.61	56
D7	15	2.5	-	5	-	-	-	-	-	-	-	0.57	52
D22	15	2.5	-	5	1	2	2	1	-	-	-	0.67	48
PX-2	14.5	2.5	-	7.5	1		-	1	1	0.5	-	0.58	38
E1	13	2.5	-	5	1	2	1	1	-	-	-	0.53	35
D4	15	-	2.5	5	1	2	-	-	-	-	-	0.61	20
PX-6	13.5	2.5	-	7.5	1	2	-	1	1	0.5	0.5	0.60	20

Table 7.8: Matrix and precipitate dislocation densities of alloys listed in Table 7.7.

Alloy	l_{edge} (nm)	Misfit-Type Behavior	Matrix Density ρ_{matrix} (m^{-2})	Precipitate Density ρ_{ppt} (m^{-2})
D12	653	Positive	5.2×10^{11}	6.3×10^{12}
D7	471	Positive	5.2×10^{11}	1.2×10^{12}
D22	283	Near-Zero	2.2×10^{12}	5.8×10^{11}
PX-2	292	Negative	1.7×10^{13}	8.0×10^{11}
E1	325	Positive	5.1×10^{12}	8.7×10^{11}
D4	573	Positive	6.8×10^{12}	2.4×10^{12}
PX-6	343	Near-Zero	1.3×10^{12}	4.0×10^{11}

where k (Boltzmann constant = $1.38 \cdot 10^{-23}$ J/K)*T (1273 K). Until recently, information on the interdiffusion of refractory, and PGM, elements within Ni at elevated temperatures was relatively unknown. Here, the interdiffusion coefficients were calculated using the same methodology described in Section 7.1.1 and through Equation 7.4, resulting in an average climb velocity of $\bar{v}_{cl}$ = 1.4 (± 0.7) x 10^{-10} m/s for alloys listed in Table 7.7. Taking the standard deviation into consideration, this averaged climb velocity of 1.4 x 10^{-10} m/s matches that obtained by Pollock and Argon (1.4 x 10^{-10} m/s [135]), which is interesting as the two different climb velocities were derived by different methods. The alloy used in the study by Pollock was a single crystal that exhibited negative misfit-type

behavior. This indicates that dislocation climb within Ni-base superalloys proceeds at a similar rate irrespective of misfit-type behavior. Therefore, Ni-base superalloys that exhibit $\delta > 0$ and subsequently raft should offer similar dislocation climb resistance compared to their negative misfit counterparts. Likewise, if rafting behavior degrades creep performance, then designing compositions that exhibit near-zero misfit rafting behavior, similar to alloy PX-5, should offer similar climb resistance to superalloys exhibiting negative or positive lattice misfit behavior.

To assess how creep strength varies with climb velocity, creep-rates were extrapolated from a constant reference stress of 100 MPa, shown in Figure 7.8(a). A creep stress exponent of $n = 5.0$ was used once again. From this reference stress of 100 MPa, reference creep-rates for each alloy are plotted in Figure 7.8(b) as a function of their measured climb velocity. Only alloys that displayed directional coarsening are plotted. This was to ensure that creep analysis for these PGM alloys are similar compared to conventional Ni-base superalloys, which usually develop rafted microstructures. For the PGM alloys presented in this investigation, increasing the climb velocity increases the creep-rate as well. Based on the positions of the PGM alloys in Figure 7.8(b), alloys D7 and E1 are the strongest, and least, creep resistant alloys, respectively, out of those which directionally coarsened.

7.2.2 Modeling High Temperature Creep Deformation

Given the availability of interdiffusion data and information on dislocation densities in both phases of the experimental alloys, it is worth considering the hardening and recovery processes that are operative using the Bailey-Orowan analysis [153, 154]. The shear strain-rate due to glide of dislocations through the matrix phase, v_{glide}, is

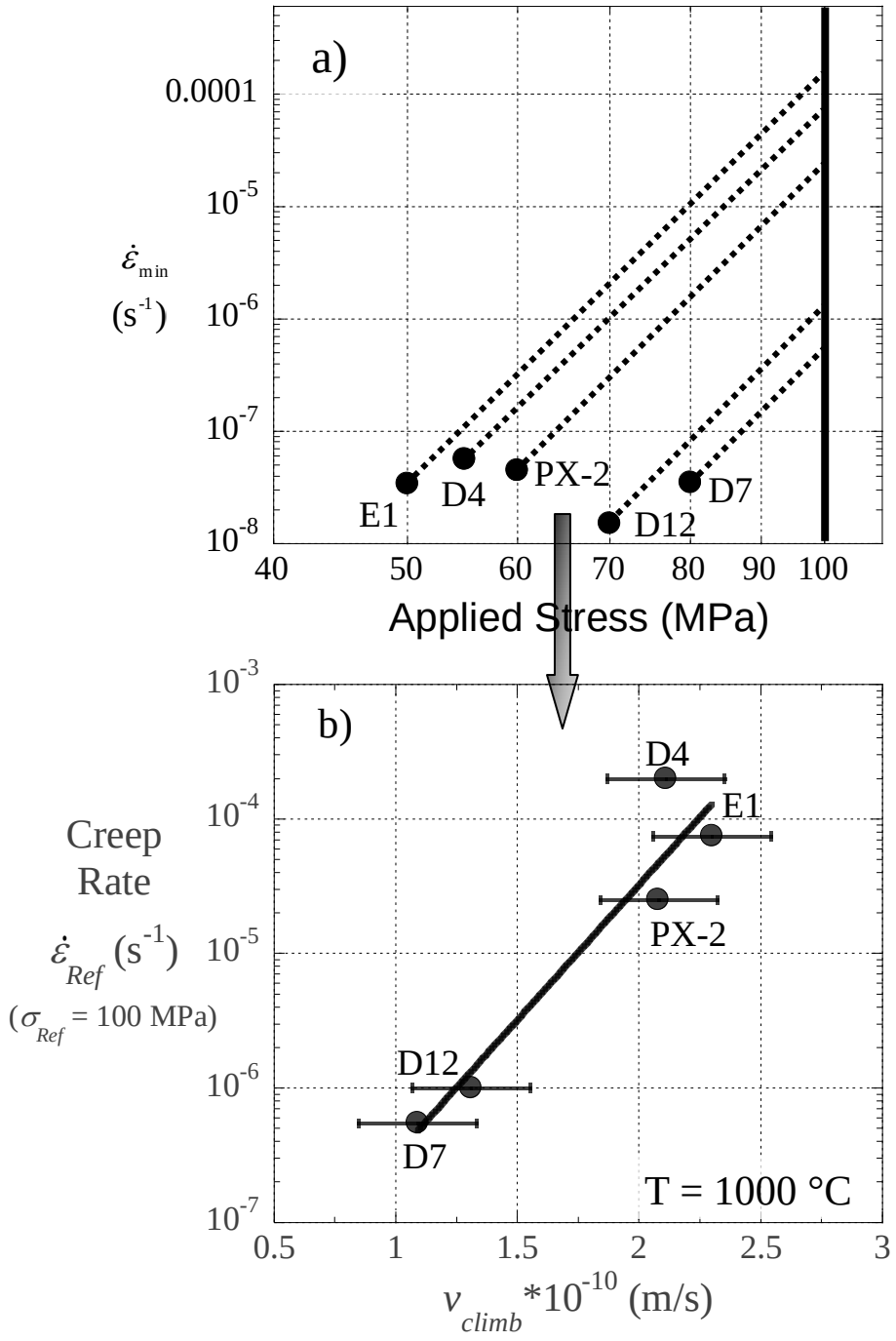

Figure 7.8: A creep stress exponent, n = 5.0, was fitted for each experimentally determined $\dot{\varepsilon}_{min}$ to extract reference creep-rates form a constant reference stress, σ_{Ref} = 100 MPa. The reference creep-rates were plotted as a function of climb velocity (b). Alloys PX-6 and D22 are not included.

represented by the Orowan equation [27]:

$$\dot{\gamma} = \rho_{matrix} \bar{b} v_{glide}$$ Equation 7.6

However, the Bailey-Orowan equation considers the competing processes of hardening and recovery:

$$d\sigma = (\frac{\partial \sigma}{\partial \gamma})_t d\gamma - (\frac{\partial \sigma}{\partial t})_\gamma dt$$ Equation 7.7

where $(\frac{\partial \sigma}{\partial \gamma})_t$ and $(\frac{\partial \sigma}{\partial t})_\gamma$ equal the rate of hardening (*h*) and recovery (*r*), respectively.

Assuming plastic creep deformation occurs under steady-state, $\frac{d\sigma}{dt} = 0$, Equation 7.7 can be rearranged:

$$\frac{d\gamma}{dt} = \dot{\gamma} = \frac{r}{h}$$ Equation 7.7(a)

Recovery (*r*) is represented by a climb velocity component,

$$v_{cl} = \frac{dx^*}{dt} \rightarrow \frac{1}{dt} = \frac{v_{cl}}{dx^*}$$ Equation 7.7(b)

where *dx** = obstacle height. The obstacle height was equivalent to one-half the precipitate edge length/diameter prior to high temperature creep. For hardening (*h*), the Orowan strain expression is used [27]:

$$\gamma = \rho b(dx) \rightarrow \frac{d\gamma}{d\rho} = b(dx) \rightarrow \frac{d\rho}{d\gamma} = \frac{1}{b(dx)}$$ Equation 7.7(c)

where *dx* = dislocation glide distance (within the γ phase). This is equivalent to the matrix channel width, calculated by Equation 7.2, and multiplied by a factor of $\sqrt{\frac{2}{3}}$. Reinserting Equation 7.7(b) and 7.7(c) into 7.7(a):

$$\frac{\frac{1}{dt}}{\frac{d\rho}{d\gamma}} = \frac{d\gamma}{dt}\frac{1}{d\rho} = \frac{\frac{v_{cl}}{dx^*}}{\frac{1}{b(dx)}} \rightarrow \dot{\gamma} = d\rho \cdot b v_{cl} \frac{dx}{dx^*} \qquad \text{Equation 7.7(d)}$$

Assuming incremental changes of the dislocation density within either the γ or γ′ phases is considerably less than the total density magnitude, $d\rho << \rho$, the Bailey-Orowan strain-rate equation is obtained:

$$\dot{\gamma}_{Bailey-Orowan} = \rho_{matrix} b v_{cl} \frac{dx}{dx^*} \qquad \text{Equation 7.8}$$

The calculated average of (dx/dx^*) = 0.31 (± 0.05). The climb velocity determined from Equation 7.5, 1.4 x 10^{-10} m/s, and the matrix dislocation densities pertaining to PGM alloys in Table 7.8 which exhibited near-zero and negative misfit behavior are used, and all variables are re-inserted into Equation 7.8 and plotted in Figure 7.9. Alloys D22, PX-2, and PX-6 are listed from left to right (strongest to weakest) based on reference creep strengths. All predicted strain-rates are approximately one order of magnitude higher than the reference creep-rate of 10^{-8} s^{-1}.

Precipitate resistance to dislocation shearing within these PGM alloys must be lower as compared to conventional Ni-base superalloys, as discussed in Section 7.1.1. However, if the precipitate resistance for all the PGM alloys were the same, then the matrix densities would have been higher compared to the values listed in Table 7.8, and predicted strain-rates would have increased as well. Thus, the precipitates in these PGM alloys do offer some degree of resistance to climb during high temperature deformation.

For alloy PX-2, which exhibited negative misfit behavior, a likely explanation is that the presence of the precipitates induces interfacial networks that interact with the

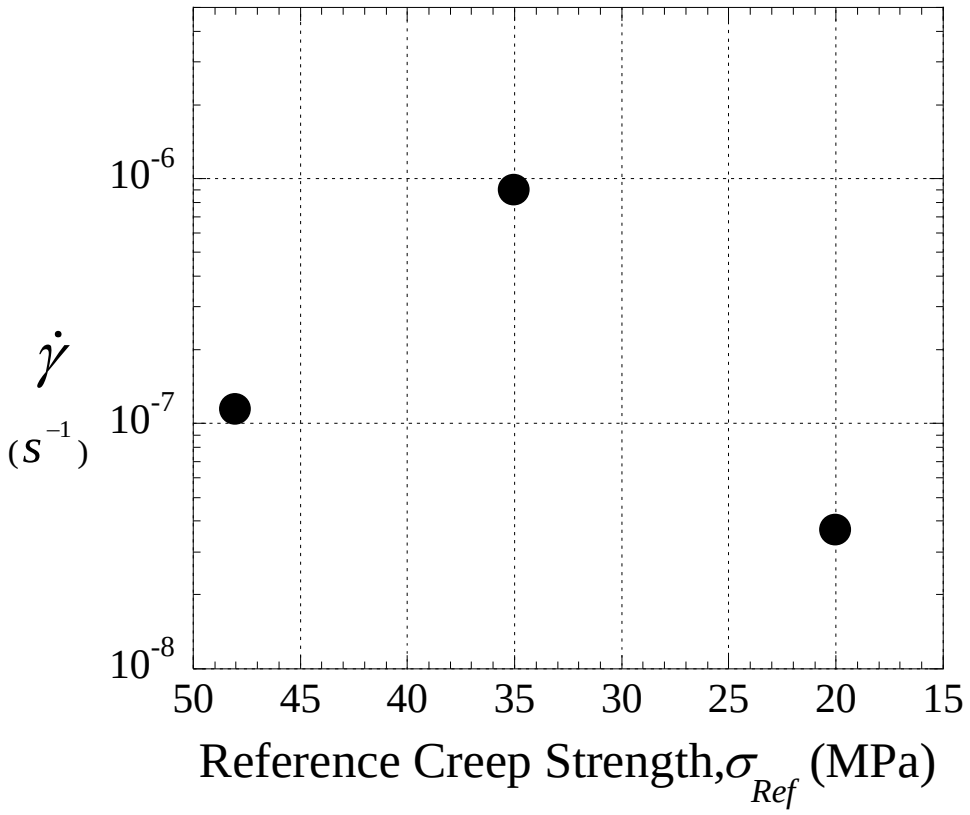

Figure 7.9: Bailey-Orowan strain-rate. Alloys are listed strongest to weakest (left to right).

gliding dislocations. Thus, the climb distance is an order of magnitude lower, or at the scale of the interfacial network spacing rather than the precipitate diameter. Furthermore, neglecting alloy PX-2 for one moment, alloy D22 (σ_{Ref} = 48 MPa) had a predicted strain-rate higher than that of alloy PX-6 (σ_{Ref} = 20 MPa). If the ability to shear the precipitates within both alloys were similar, then the strain-rates would have been similar, too. This must indicate that the alloying chemistry of alloys D22 and PX-6 differs to the point where the precipitates of alloy D22 resist shearing to a greater extent than alloy PX-6. Measuring the anti-phase boundary (APB) energy of the PGM γ′ precipitates would help to assess how various PGM nominal compositions influence precipitate microstructure.

Another possibility for the discrepancy between predicted and reference creep-rates is attributed to the density calculations of Equation 2.4. If insufficient dislocation line segments were measured, or the examined area for dislocation line measurements was too small, these could all factor together in providing density measurements that are at least an order of magnitude different than those listed in Table 7.8.

7.2.3 Microstructure and Subsequent Raft Evolution

Systematic changes in alloy composition alter coarsening and γ′ morphology, demonstrated in Section 3.1, and elsewhere [4, 48]. The averaged precipitate size, *D*, measured from Figure 6.14 indicates that the distribution curve is shifted toward smaller γ′ particle size. Alloys D4, D12, and D7 had, on average, larger precipitate sizes after aging versus the other studied alloys in Table 7.8. These three alloys contained moderate to no refractory elements. High temperature coarsening studies have demonstrated that adding or increasing Re, W, and/or Mo additions into Ni-base compositions decreases γ′ particle size [26, 112, 122]. Five out of seven alloys listed in Table 7.7 contained little to moderate refractory additions, which biased the average particle size to smaller lengths/diameters.

MacKay and Ebert conducted high temperature studies (982 °C) on negative misfit superalloys to evaluate how precipitate size affects overall creep strength [155]. It was concluded that the alloy displaying the smallest γ′ precipitates provided the greatest creep resistance. This arises due to the smaller precipitates producing a greater number of rafts per unit area, restricting dislocation glide within the matrix, and forcing dislocations to either shear or climb the precipitate. From Table 7.8, alloy PX-2 had the lowest precipitate edge length of alloys that directionally coarsened. Micrographs in

Figure 6.11 demonstrate alloy PX-2 exhibiting a greater number of rafts per unit area compared to alloy D12, Figures 6.11(c) and 6.11(a), respectively. However, PX-2 displayed intermediate creep resistance among the group of rafted alloys listed in Table 7.7. For the PGM alloys which raft, the number of rafts developed per unit area is not a leading factor for attaining higher creep resistance.

In some instances, directional coarsening benefits high temperature creep properties of Ni-base superalloys [4, 29, 36, 37, 44]. Alloys that raft have a propensity to form interfacial dislocation networks in order to relieve misfit strain. Not only do excess dislocations (meaning dislocations beyond those required to relieve misfit strain) become restricted either to horizontal or vertical matrix channels (dependent on δ sign), but dislocations must now penetrate these networks if they are to shear the precipitate. Comparison of the density of interfacial networks for alloys shown in Figures 6.11(a – d) and their respective reference creep strengths indicates that a higher network density results in higher creep strength. Orowan analysis presented in Section 7.1.1, however, suggests that the shearing of precipitates in these PGM alloys is considerably easier compared to conventional Ni-base systems, even among alloys which developed dense interfacial networks, Figures 6.11(a) and (b). Figure 6.11(b) displays at least 3 sets of shearing dislocations penetrating the precipitate. This alloy, D7, did not display GBS. Calculation of the Orowan resistance performed for alloy D7 results in σ_{Orowan} = 422 MPa. Interfacial networks formed within some PGM alloys do not inhibit shearing dislocations as effectively as compared to conventional Ni-base superalloys that display well-developed networks.

One of the most unusual observations within this study was the creep behavior of

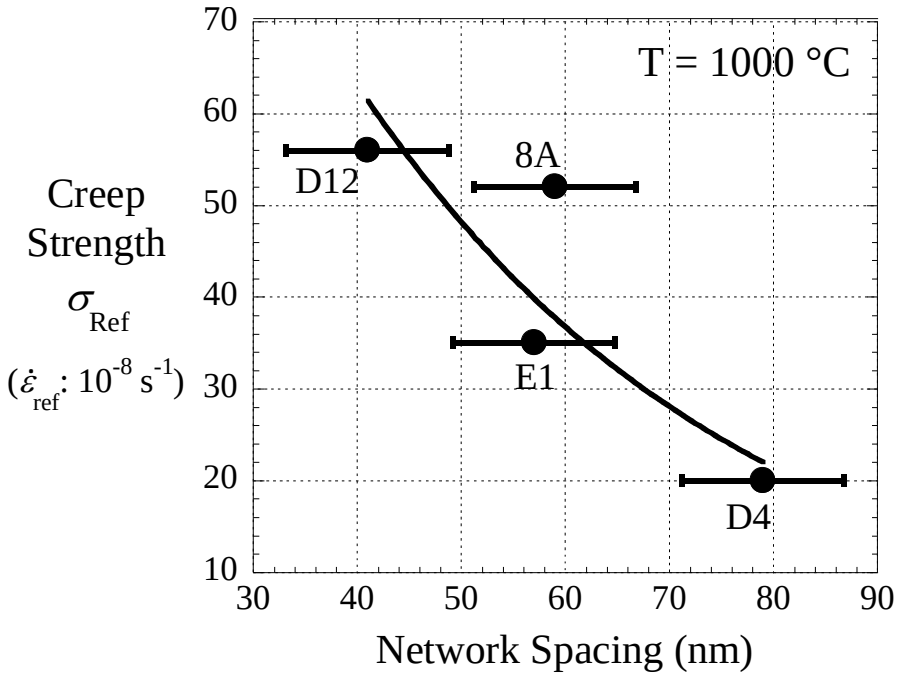

Figure 7.10: Creep strength as a function of network spacing at the γ/γ′ interface for alloys which displayed positive misfit rafting behavior.

alloys exhibiting positive misfit behavior. The plot of alloy creep strength as a function of network spacing in Figure 7.10 compares alloys that displayed $\delta > 0$. This plot indicates that an increase in network spacing decreases creep strength. It seems beneficial, in this case, for a positive misfit PGM alloy to decrease its network spacing in order to increase creep strength. Carroll conducted studies on Ru-modified Ni-base superalloys and reported that network spacings near 40 nm resulted in improved creep life at 950 °C [28].

7.2.4 Dislocation Densities in the γ and γ′ Phases

The anisotropic stress gradients that promote raft coalescence transverse to the applied stress axis for negative misfit-type alloys under tension [37, 44] must act in a similar fashion for alloys that exhibit positive misfit behavior under compression. Once

rafting is completed, however, the subsequent development of dislocation densities, particularly within the γ′ phase, is dissimilar between positive and negative misfit superalloys.

Studies have been conducted on dislocations in γ′ within directionally coarsened Ni-base superalloys exhibiting negative misfit behavior [50, 156-161]. Under tensile stress in negative misfit single crystals, $\frac{a}{2}$<011> type dislocations deposit on the γ/γ′ interface. Back stresses caused by increasing ρ_{matrix} may lead to interaction of interfacial dislocations, resulting in strongly coupled *a*<001> edge components which climb through the precipitate [29, 157]. Sarosi *et al.* [157] suggest dislocations which are deposited in γ′, rather than shearing the precipitate, may be remnants of interfacial dislocations that formed prior to coalescence and inevitably become trapped. The measurements of precipitate dislocation densities for alloys D7 and D12 are too high to be considered 'remnant'. The one key difference between γ′ dislocations studied here compared to those in Refs. 153 - 158 is the PGM content. Partitioning of Pt and Ir into the γ′ phase alters the chemical composition of the precipitate, which may affect the overall density distribution.

From Table 7.8, alloys D22 and PX-6 exhibited a ρ_{matrix} greater than the ρ_{ppt}. This is attributed to an absence of interfacial networks and non-directional coarsening, allowing easy climb or glide of dislocations throughout the matrix [28], depicted in Figures 6.13(a) and (b), respectively.

7.2.5 Dislocation-Dislocation Interactions

PGMs alloys which exhibited negative and near-zero misfit-type behavior accumulated a relatively large amount of dislocation densities within the matrix, as

displayed in Figures 6.11(c) and 7.1(a) for alloys PX-2 and D22, respectively. As shown in Figure 6.11(c), dislocations become entangled with nearby dislocations spread throughout the matrix. Such dislocation interactions act as effective barriers in impeding further dislocation glide, improving creep resistance.

To account for dislocation-dislocation interaction within the matrix and its effect on measured creep strengths, a modified version of Taylors work-hardening equation for Ni-base superalloys is utilized [29, 162]:

$$\tau_{dis-dis} \cong \alpha G M \vec{b} \sqrt{\rho_{matrix}} \qquad \text{Equation 7.9}$$

where α is a constant (0.175) [29, 163], G the shear modulus (50 GPa) [29], and M is the Schmid factor. M is replaced by Taylors factor (3.06) [136], and the matrix densities are provided in Table 7.8. The $\tau_{dis-dis}$ was calculated and plotted in Figure 7.11. In comparison to reference creep strengths listed in Table 7.7, the $\tau_{dis-dis}$ for alloy PX-2 accounts for 75% of the observed creep strength, but, on average, less than 30% for alloys PX-6 and D22, and no more than 10% for alloys D7 and D12. Evidently, the dislocation-dislocation interaction is a significant property for alloys that display negative misfit behavior. Referring to Figure 7.9, the $\tau_{dis-dis}$ is not accounted by the Bailey-Orowan strain-rate calculation. This may be another reason why the alloy with the highest discrepancy between predicted and reference creep-rates is the negative misfit alloy PX-2. For the PGM alloys which exhibit positive misfit-type behavior, the dislocation-dislocation interaction is a relatively minor factor toward overall creep resistance. This can easily be attributed by the propensity for dislocations to accumulate within the precipitate, thereby reducing the interactions within the matrix.

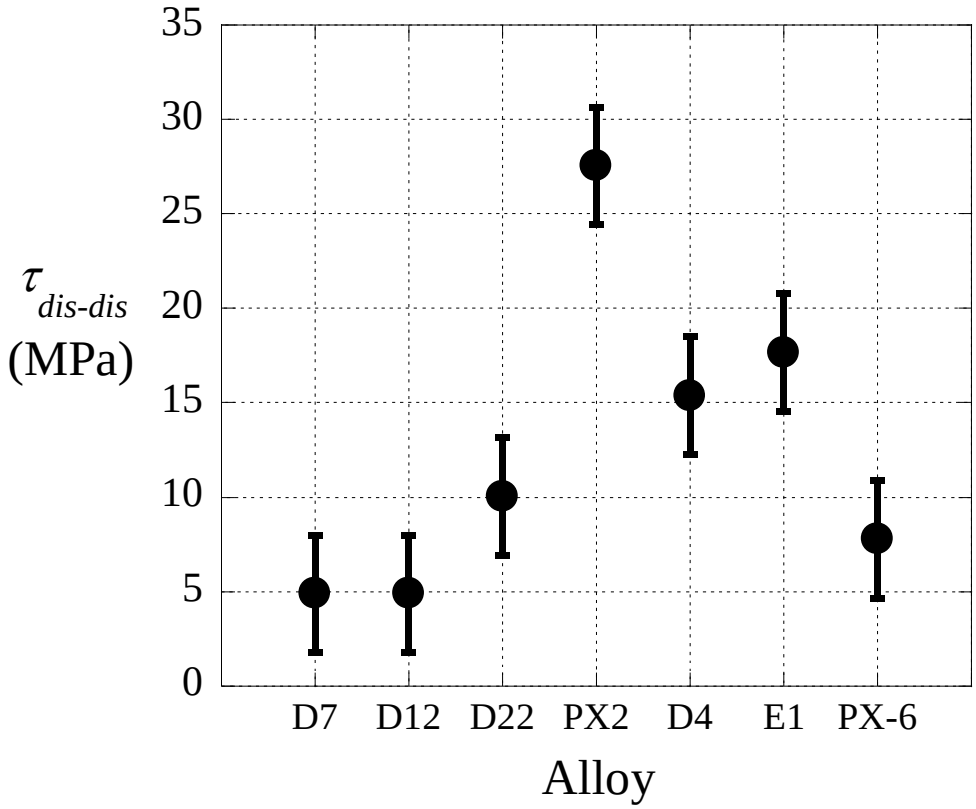

Figure 7.11: Taylor work hardening.

7.3 Summary

The high temperature creep properties for PGM-modified Ni-base superalloys were evaluated. The partitioning of platinum and iridium resulted in crept alloys exhibiting positive, near-zero and negative misfit-type behavior. Orowan resistance calculations demonstrate that the PGM precipitates might not resist dislocation shearing as well as conventional Ni-base superalloys. The power-law creep stress exponent measured for the PGM alloys was lower in comparison to other γ-γ′ Ni-base superalloys. This may be attributed to the easy shearing process. Grain boundary damage was observed for alloys containing the combination of the refractory elements Re and W.

Grain boundary strengtheners mitigate grain boundary sliding for alloys with and without the refractory elements and can improve the creep strength by at least a factor of three. Analyzing particle aspect ratios along with misfit magnitude would provide a better assessment of alloy creep strength. Comparing the reference creep strengths of directionally coarsened alloys demonstrated higher creep resistances for those alloys displaying dense interfacial networks. Although Pt and Ir contribute solute atoms within the matrix for improved creep resistance, the creep strength does not share a direct correlation with the interdiffusion of PGM, or solid solution strengthening, atoms within the Ni-matrix.

Dislocation analysis indicated dissimilar density distributions within the γ and γ' phases. Bailey-Orowan analysis accounts for the climb mechanism associated with high temperature creep. Results from this analysis may be used to compare precipitate resistance to dislocation shearing in each alloy. However, precipitate resistance to dislocation shearing is dependent on the alloying chemistry, which is strongly influenced by the PGM additions. Additional mechanisms, such as dislocation-dislocation interactions within the matrix, were more prominent for alloys with negative misfit behavior, as opposed to near-zero and positive-misfit superalloys.

CHAPTER 8

CONCLUSIONS

This thesis has investigated platinum group metal elements within Ni-base superalloys to assess their influence on microstructure and high temperature mechanical properties. Elemental partitioning, precipitate coarsening kinetics, high temperature creep studies, and deformation analysis, was carried out on these PGM alloy systems. This chapter summarizes the major findings and considers their implications for the design of superalloys and bond coatings. These conclusions suggest future directions for investigations; the details of which are subsequently presented.

8.1 PGM Influence on High Temperature Mechanical Properties

The PGM additions used in this study influence microstructure, lattice misfit, precipitate coarsening, and high temperature creep behavior. The systematic and broad range of nominal compositions permitted valuable assessments toward high temperature creep performance, and the additional factors which influence this property. This section briefly reviews these major findings and indicates unusual features not commonly observed in conventional Ni-base superalloy systems.

8.1.1 Overall Assessment of the PGM-Modified Ni-Base Superalloys

Partitioning studies demonstrated that Pt and Ru partition toward the γ′ and γ phases, respectively. Neither element significantly alters partitioning behavior of other alloying elements in the multi-component system. The PGM Ir partitions near-equal between phases and influences the partitioning behavior of both PGM and non-PGM alloying constituents.

A Pt-containing Ni-base superalloy containing Re, W, and Ta additions was aged at elevated temperatures to assess its coarsening kinetics. This alloy, PX-5, exhibited near-zero misfit behavior and maintained high γ′ volume fractions at 1150 and 1200 °C. The measured activation energy of 388 kJ/mol was considerably higher than activation energies of other superalloys aged under high temperature conditions. At temperatures surpassing 1100 °C, the refractory additions, Re and W, demonstrate a stronger preference to partition into the precipitate. As such, the rate-limiting mechanism of precipitate coarsening at temperatures above 1150 °C would be the interdiffusion of Pt along with refractory additions.

High temperature creep analysis establishes that a combination of particle morphology and lattice misfit helps in determining the highest creep resistances. Additional features, such as precipitate volume fraction, grain boundary strengthening, and/or the formation of rafts during creep, must be considered as well. The most favorable range in gamma prime volume fraction for optimizing creep resistance lies between 0.60 - 0.65. For alloys that directionally coarsen, increasing the density of interfacial networks increases creep strength. Inclusion of grain boundary strengtheners benefits high temperature creep resistance. Orowan calculations suggest that precipitate resistance to dislocation shearing in these PGM alloys is weaker compared to conventional Ni-base superalloys. The calculated creep stress exponent, $n = 5.0$, is lower in comparison to other two-phase Ni-base superalloys.

Dislocation analysis indicates that dislocation climb is an important mechanism toward modeling high temperature deformation. The calculated climb velocity directly correlates to creep strength. Quite surprising were the variations in dislocation densities within the γ and γ' phases. In some instances, alloys which exhibited positive misfit behavior contained a higher amount of dislocation densities within the precipitate phase instead of the matrix. This would indicate that creep deformation for these specific alloys occurs mainly within the γ' phase, which is opposite to what is usually observed within most Ni-base superalloys. Alloys that exhibited directional coarsening behavior and displayed well-developed interfacial networks proved to be the most creep resistant.

8.1.2 Discussion

Further development of Ni-base superalloys with exceptional high temperature properties requires these materials to possess attributes beyond mechanical strength. The

processing technique of the single crystal blade, and the inclusion of the solid solution strengthener element Re, has enhanced blade strength to new levels, as shown in the chart of Figure 1.14. As such, the next generation for superalloys exposed to high temperature conditions will require the material to intrinsically provide strength and environmental resistance.

The different factors that would influence high temperature creep performance were examined in this investigation. With regard to misfit and morphology, PGM-modified Ni-base superalloys offer a wide variety of these two features. The elements Pt and Ir identify a new class of superalloys for further investigation – namely alloys that possess positive misfit along with relatively high creep resistance. The presence of the PGM Ir within a nominal composition affects the partitioning behavior of PGM and non-PGM elements. This may prove useful toward the manipulation of elements that tend to preferentially partition to a specific phase.

Surprisingly, Pt-contaning Ni-base superalloys can provide volume fractions of precipitates in excess of 50% at temperatures up to 1200 °C. The PGM Pt is a key element to slow coarsening kinetics. Also unexpected was the partitioning behavior of the solid solution strengtheners Re and W in the presence of PGMs. Their preferential partitioning to the precipitate at 1150 °C and 1200 °C may influence interdiffusion and subsequent coarsening behavior.

In the absence of grain boundary strengtheners, high temperature creep resistance is best attained with aspect ratios between 0.4 - 0.8 and misfit magnitudes approximately 0.5 - 1.0%. Particle morphologies within this range tend to raft and form dense interfacial dislocation networks. It was established that additions of grain boundary

strengtheners could increase the creep resistance for many alloys by a factor of at least three. The degrees of lattice misfit are influenced by the preferential partitioning behavior of the PGMs, particularly Pt. One fortuitous outcome in assessing PGM alloys which exhibit different misfit-type behavior can be understood with regard to Table 2.9. In this investigation, alloy PX-5 ($\delta \approx 0$) demonstrated the highest creep resistance, followed by alloy D12 ($\delta > 0$). Comparison of alloy densities indicates that both alloys share near equal densities, although the cost of material for alloy PX-5 would be less expensive than alloy D12. However, alloys such as D4 and D8, which both exhibit positive misfit behavior, are similar in cost to alloys PX-5 and D12, but display lower densities than the latter two. Hence, the use of grain boundary strengtheners would permit greater avenues to consider with regard to cost and density toward future use of the PGMs.

The deformation of PGM-modifed Ni-base superalloys demonstrated an unusual dislocation density distribution for alloys displaying positive misfit behavior. In some instances, precipitate dislocation densities were greater than matrix densities. It has always been assumed for Ni-base superalloys which directionally coarsen that the matrix phase captures nearly all of the deformation (i.e., dislocations), whereas the precipitate, resistant to dislocation shearing, provides additional strengthening to the material by shedding deformation to the more resistant matrix phase, analogous to ceramic-matrix composites. This was not the case for the positive misfit PGM superalloys displaying the highest creep resistance, where the precipitates now carried a majority of the deformation. PGM alloys that accumulate dislocation densities greater within the precipitate phase over the matrix phase is unusual for Ni-base superalloys. Increasing the

γ′ volume fraction so that more dislocations would accumulate within the precipitates would not be the best solution. Murakumo demonstrated that increasing the volume fraction to 80% for a single crystal Ni-base superalloy resulted in a lowering of creep strength, in comparison to alloys which contained 40 - 60% V_f [126]. Instead, phase strengthening the precipitate to a greater extent than the matrix, while keeping volume fractions in the range of 60 - 65%, might prove beneficial.

Dislocation climb was established to be the rate-controlling mechanism for deformation. As stated in Section 6.2.2, the availability of interdiffusion data pertaining to refractory and PGM elements, and microanalysis techniques, such as the electron microprobe and atom probe, allows concentrations of these elements within the Ni-matrix to be accurately determined. All these factors help to provide a climb velocity that can be applied not only for PGM-modified Ni-base superalloys, but a majority of superalloys crept at temperatures around 1000 °C. This calculation demonstrates that climb resistance is similar for superalloys exhibiting all three types of misfit behavior and that recovery must be considered when modeling high temperature creep deformation. It is strongly emphasized, however, that while dislocation climb is *a* key component in considering high temperature creep, it is not *the* crucial factor. Instead, it is a combination of multiple features (resistance to dislocation shearing, grain boundary sliding, interfacial networks, γ′ volume fractions, for example) that must be considered for these multi-component systems.

8.2 Future Work

The PGMs have demonstrated uncommon characteristics when integrated within Ni-base compositions containing Al, Cr, and various refractory elements. The conclusions feature the various aspects that affect the high temperature creep properties of PGM-modified Ni-base superalloys. This section suggests future directions to consider if the unique attributes behind these PGM systems are to be further developed and their high temperature capabilities advanced to new levels of performance.

8.2.1 Implications: Positive, Near-Zero, or Negative Misfit?

Do PGM Ni-base superalloys need negative misfit behavior to provide high temperature mechanical strength? Negative misfit alloys generally exhibit improved creep life compared to positive misfit alloys [37, 125], but to develop an alloy whose misfit deviates further negative does not directly correlate to improved creep properties [28], explaining why most commercial superalloys lattice misft is ~ 0.3% [29]. Tetzlaff and Mughrabi provided work on SRR 99 where rafts formed parallel to the applied stress axis *prior* to tensile testing at 1000 °C enhanced creep life [164]. Also, due to increased refractory content, negative misfit material is more susceptible to TCP formation versus positive misfit, shown in this study, and for positive misfit single crystal superalloys [165]. It is difficult to distinguish the role of misfit from the solute effects due to the fact that slow-diffusing solutes such as Re partition strongly to the matrix, thereby giving higher negative misfit. PGM additions such as Ir, reduces the strong partitioning of refractory elements, which can be detrimental to creep strength. Pt seems to offer the best properties in relation to morphology, lattice misfit, and creep resistance. Detailed studies on selected alloys with positive misfit behavior, alloy D8, Figure 3.15(b), or grain boundary strengthened alloys displaying negative misfit behavior, DS-1 or PX-2, could

ascertain which lattice mismatch provides better overall creep properties.

8.2.2 Implications: PGM Influence on γ′ Composition

Orowan calculations strongly suggest that the precipitates of these PGM alloys are easily sheared during high temperature creep. The Bailey-Orowan analysis points out, however, that the γ′ resistance to dislocation shearing differs from alloy to alloy. The nominal compositions, therefore, must continuously alter the precipitate compositions and, thus, change a precipitates ability to retard shearing. In some instances, rather than shearing the precipitates, dislocations accumulated to a greater extent within the γ′ phases.

It is essential to assess the force required for a dislocation, f_{dis}, to enter the PGM γ′ particle. This can be approximated by the following [4]:

$$f_{dis} = \frac{\gamma_{APB}}{\vec{b}} \qquad \text{Equation 8.1}$$

where γ_{APB} is the antiphase boundary energy of the precipitate. Figure 7.1 depicts APBs within alloys (a) D12 and (b) D4. The APB is adjoined by superpartials within each micrograph. Studies conducted on substitution of Al for either Ta [166, 167] or Ti [168] within Ni_3X indicates that Ta and Ti increase APB energy. Thus, the force required for a dislocation in the matrix to enter the precipitate increases as well. This study shows that Pt and Ir partition preferentially, and near-equally, respectively, into the γ′ phase. TEM studies that measure the APB energy of creep deformed positive misfit PGM alloys containing no refractory content (alloys D3 or D7), or moderate refractory additions (alloys D4 or D8), would provide useful information of the PGM behavior within γ′ and their influence on dislocation distributions following creep.

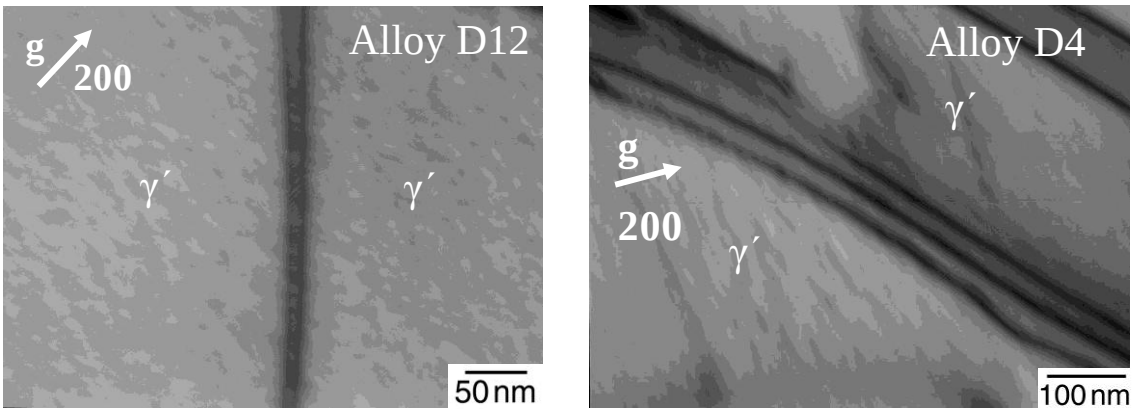

Figure 8.1: (a) Alloy D12 contains a superdislocation in γ´ linked by an APB. (b) Alloy D4 depicts multiple superpartials within the precipitate.

8.2.3 Implications: High Temperature Mechanical Performance

The γ´ precipitates within alloy PX-5 maintain high volume fractions of precipitates at temperatures ranging from 1050 - 1200 °C, Figure 4.13. Volume fractions exceeding 0.50 at temperatures where conventional Ni-base single crystals display rather low fractions of γ´ could lead to impressive creep properties. Caron reported an experimental single crystal Ni-base superalloy (MC653) containing $V_f \approx 0.55$ at 1200 °C [169]. Creep tests on alloy MC653 at 1150°C and 100 MPa resulted in a creep rupture life 1.5 - 3 times that of CMSX-10 and René N6 crept under similar conditions.

To assess creep strength for PX-5, the Orowan resistance was calculated through Equations 6.1 - 6.3. In this case, the resistance for a single crystal, rather than polycrystal, was calculated (Schmid factor = 0.41), and provided for each temperature in Table 7.1. The edge lengths for CMSX2 in the temperature range 1050 - 1200 °C was extrapolated from the provided edge length values reported by Ges *et al.* in the range 850 - 1050 °C [108]. Likewise, volume fractions were averaged by the values provided through measurements conducted on single crystals in the temperature range of 1050 -

Table 8.1: Orowan resistance, σ_{Orowan}, of alloy PX-5 at investigated temperatures.

Temperature (°C)	Average V_f	$\sigma_{App.}$ (MPa)
1050	0.60	405
1100	0.57	312
1150	0.56	259
1200	0.54	178

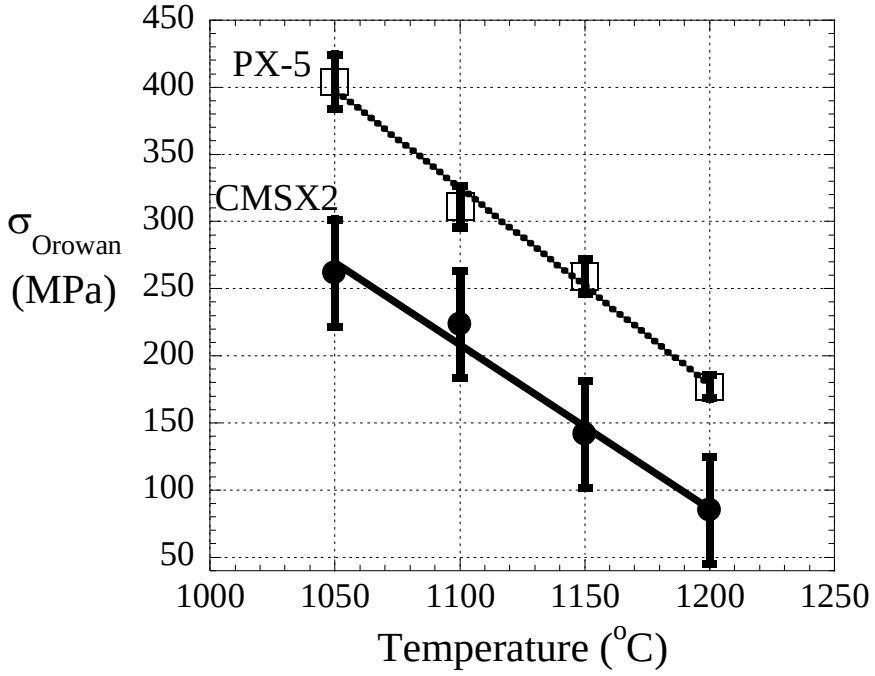

Figure 8.2: Orowan resistance comparing CMSX2 versus alloy PX-5 at elevated temperatures.

1200 °C [111, 115, 116]. The comparison of alloy PX-5 versus CMSX2 is plotted in Figure 7.2. The creep resistance offered by PX-5 for 1150 °C and 1200 °C is double that of CMSX2.

8.2.4 Implications: Frictional Effects

In this study, a wide range in γ′ morphology and volume fractions led to differences in the length of the gamma matrix channels, which can affect the creep

strength due to friction at the precipitate-matrix interface. Schroeder and Webster investigated pressure gradients due to frictional effects between a rigid disk and its surrounding medium [170]. The greater the friction between the disk and medium, the higher the pressure required for the continual deformation of the disk. Pollock and Argon adapted these calculations for non-deforming cuboidal γ′ precipitates surrounded by the gamma matrix to determine the pressure required to force dislocations through the matrix channels [135]. It was estimated that at least one-third of the total applied stress for plastic deformation was attributed to the pressure required to overcome the frictional resistance between the matrix and the precipitate. Thus, to identify PGM alloys with the greatest frictional resistance, and therefore high creep strength, the pressure necessary for plastic deformation within the matrix channels could be calculated for the compositions studied in this work.

8.2.5 Implications: Alloying of PGM Additions

To achieve optimal high temperature creep resistance, refractory additions are necessary within PGM-containing alloys. Grain boundary strengtheners are necessary as well if the combination of Re and W is desired. With Pt lowering the T_S and Ta increasing the γ'_{Solvus} temperature, these PGM systems require tight control on heat treatments for full solutioning without resultant incipient melting. The preferential partitioning of Pt to γ′ creates unusual alloy systems because the refractory content may be added which result in alloys exhibiting near-zero and negative lattice misfit. This study demonstrates, in the absence of grain boundary sliding, that lattice misfits in the range of 0.5 - 1.0% provides precipitate morphologies that improve creep resistance. Alloys which display near-zero misfit behavior may be desired in case of any potentially

negative effects of directional coarsening, thereby preventing any major evolution in properties during long-term, high temperature exposure. Alloy PX-5 displayed the highest creep resistance in this investigation (Table 6.3) with minimal change in morphology post-creep, Figure 5.5(b).

Alloy D4, with $\delta > 0$, displayed cuboidal morphology, observed in Figure 3.15(a). Whereas Ir additions weaken creep strength, Pt can strengthen γ' and does not influence partitioning of PGM or refractory elements. High temperature creep tests on alloy D8, Figure 3.15(b), which replaces Pt for Ir, might lead to greater creep resistance. For $\delta < 0$ where Pt is the only PGM, this requires not only refractory additions but increased Cr content with a reduction in Al, Tables 2.6 and 2.8. Microstructures with aspect ratios near 0.8 are obtained, viewed from Figures 3.20(d), 3.21(a), and 3.22(a). Grain boundary strengtheners are necessary once again. Ru additions mitigate precipitation of TCP phases, but alloy DS-1, which contained 2 at% Ru, displayed TCP phases at grain boundaries and grain interiors post-creep. Whether the fraction of TCP phases observed for DS-1 would have increased post-creep without the Ru addition remains uncertain. The role of Ru in this new class of superalloys needs further attention. The lowering of Al to approximately 13.5 at% allowed volume fractions to remain near 60%, alloys PX2 and PX-5, and resulted in stronger partitioning behavior of Re to the matrix phase, Table 5.4. Removing W, which demonstrated weak partitioning to the matrix, from the nominal composition might resolve the formation of TCP phases. Still, the unique partitioning behavior of the PGMs results in a variation of γ' microstructures and hence, differences in high temperature creep behavior.

8.2.6 Implications: High Temperature Tensile Creep Tests

Due to the high cost and limited amount of PGM material, high temperature creep strengths of PGM alloys were evaluated by compression creep tests only. Creep performance is more commonly investigated through tensile creep tests because the applied tension mimics the service loading of a rotating blade. Care must be taken, however, if tensile tests are performed on these polycrystalline samples due to grain boundary sliding that leads to crack propagation. If loading conditions and testing temperature are the same between two PGM alloys which share identical nominal compositions, it is observed that crack propagation accelerates at a faster rate for the alloy tested under tension compared to the alloy tested under compression [27, 130, 171]. Thus, the total time for the PGM alloy to accumulate 1% plastic strain will be shortened in tension creep tests versus compression creep.

APPENDIX

Labview 8.0 interface for creep data acquisition.

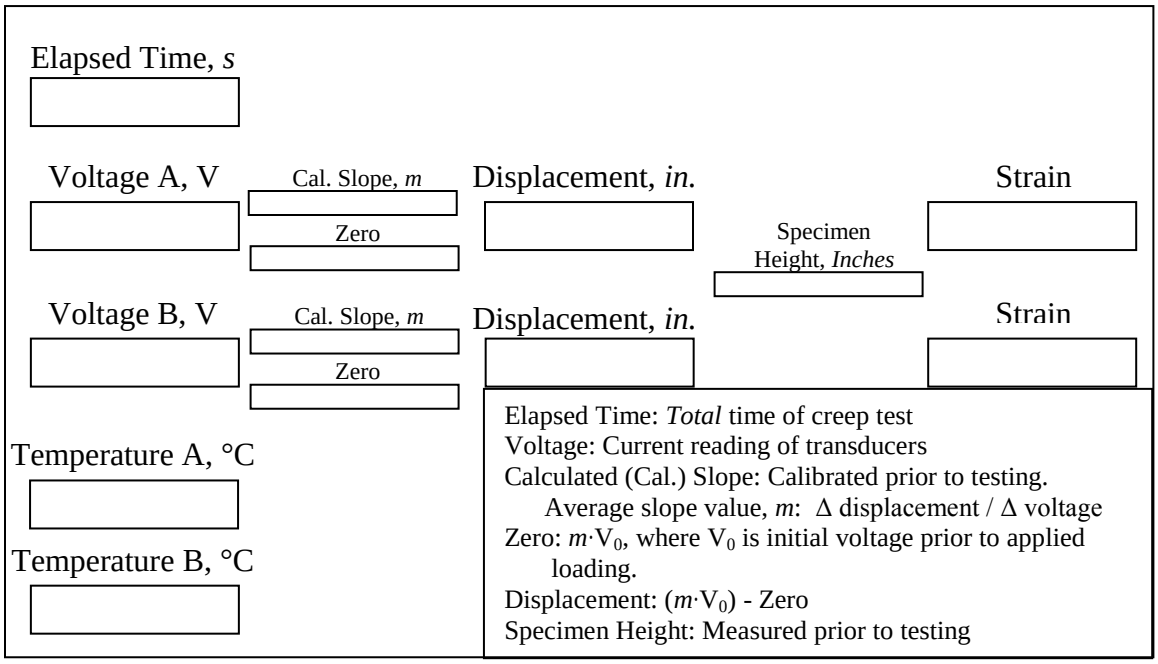

REFERENCES

[1] R. P. Probert, J. R. Singham: *J. Sci. Instruments*, 1946, 23, pp. 72-77.
[2] N. P. Padture, M. Gell, E. H. Jordan: *Science*, 2002, 296, pp. 280-284.
[3] M. Ashby, D. Jones: *Engineering Materials 1: 3rd Ed.*, Butterworth-Heinemann, Burlington, MA, 2005.
[4] R.C. Reed: *The Superalloys: Fundamentals and Applications*, University Press, Cambridge, 2006, p. 372.
[5] T.M. Pollock, S. Tin: *J. Prop. Power*, 2006, 22, pp. 361-374.
[6] D.A. Porter, K.E. Easterling: *Phase Transformations in Metals and Alloys*, Stanley Thornes Ltd, Cheltenham, 1992, p. 514.
[7] P. Nash, M. Singleton, J. Murray: *Phase Diagrams of Binary Nickel Alloys*, ASM International, Metals Park, OH, 2001.
[8] B.H. Kear, A.F. Giamei, J.M. Silcock, R.K. Ham: *Scr. Metall.*, 1968, 2, p. 287.
[9] M. Durand-Charre: *Microstructure of Superalloys*, CRC Press, London, 1997.
[10] T.P. Gabb, D.G. Backman, D.Y. Wei, D.P. Mourer, D. Furrer, A. Garg, D.L. Ellis: in *Superalloys 2000*, T.M. Pollock, R.D. Kissinger, R.R. Bowman, K.A. Green, M. McLean, S.L. Olson, J.J. Schirra, eds., Seven Springs, PA, TMS, 2000, pp. 405-414.
[11] N. Birks, G.H. Meier, F.S. Pettit: *Introduction to the High Temperature Oxidation of Metals 2nd Edition*, Cambridge University Press, New York, 2006, p. 352.
[12] B. Gleeson, W. Wang, S. Hayashi, D. Sordelet: in *High Temperature Corr. Prot. Matls Proc.*, P. Steinmetz, I.G. Wright, G. Meier, A. Galerie, B. Pieraggi, R. Podor, eds., vol 461-464, 2004, pp. 213-222.
[13] Q. Feng, B. Tryon, L.J. Carroll, T.M. Pollock: *Mat. Sci. Eng. A*, 2007, 458, pp. 184-194.
[14] A.K. Jena, M.C. Chaturvedi: *J. Mat. Sci.*, 1984, 19, pp. 3121-3139.
[15] D. Blavette, E. Cadel, C. Pareige, B. Deconihout, P. Caron: *Microsc. Microanal.*, 2007, 13, pp. 464-483.
[16] P. Caron, T. Khan, in: TMS Fall Meeting, J.C. Chao, M. Fahrmann, T.M. Pollock, eds., Indianapolis, IN, TMS, 2001, pp. 1-14.
[17] C.T. Sims, N.S. Stoloff, W.C. Hagel: *Superalloys II*, John Wiley and Sons Inc., 1987, p. 90-93.
[18] M. Fahrmann, P. Fratzl, O. Paris, E. Fahrmann, W.C. Johnson: *Acta Metall. Mater.*, 1995, 43, pp. 1007-1022.
[19] L.J. Rowland, Q. Feng, T.M. Pollock: in *Superalloys 2004*, K.A. Green, T.M. Pollock, H. Harada, T.E. Howson, R.C. Reed, J.J. Schirra, S. Walston, eds., Seven Springs, PA, TMS, 2004, pp. 697-706.
[20] M. Doi, T. Miyazaki, T. Wakatsuki: *Mat. Sci. Eng.*, 1984, 67, pp. 247-253.

[21] T. Miyazaki: in *Proc. Intl. Conf. Solid - Solid Phase Trans.*, W.C. Johnson, J.M. Howe, D.E. Laughlin, W.A. Soffa, eds., Farmington, PA, PTM, 1994, pp. 573-592.
[22] R.A. Ricks, A.J. Porter, R.C. Ecob: *Acta Metall.*, 1983, 31, pp. 43-53.
[23] A. Baldan: *J. Mat. Sci.*, 2002, 37, pp. 2379-2405.
[24] A.J. Ardell: *Interface Science*, 1995, 3, pp. 119-125.
[25] A.J. Ardell, R.B. Nicholson: *J. Phys. Chem.*, 1966, 27, pp. 1793.
[26] A.F. Giamei, D.L. Anton: *Met. Trans. A*, 1985, 16, pp. 1997-2005.
[27] M.A. Meyers, K.K. Chawla: *Mechanical Behavior of Materials*, Cambridge University New York, 2009, p. 1-851.
[28] L.J. Carroll, Q. Feng, T.M. Pollock: *Met. Trans. A*, 2008, 39A, pp. 1290-1307.
[29] T.M. Pollock, R.D. Field: in *Dislocations in Solids Vol. 11*, F.R.N. Nabarro, M.S. Duesbery, eds., Amsterdam, Elsevier, 2002, pp. 547-618.
[30] M.S.A. Karunaratne, R.C. Reed: *Acta Mater.*, 2003, 51, pp. 2905-2919.
[31] J. Weertman, P. Shahinian: *Trans. AIMM*, 1956, 206, pp. 1223-1226.
[32] M.V. Nathal, R.D. Maier, L.J. Ebert: *Met. Trans. A*, 1982, 13, pp. 1767-1774.
[33] M.F. Ashby: *Acta Metall.*, 1972, 20, pp. 887-897.
[34] H. Frost, M. Ashby: *Deformation Mechanism Maps*, Permagon Press, Oxford, 1982.
[35] A.C. Yeh, C.M.F. Rae, S. Tin: in *Superalloys 2004*, K.A. Green, T.M. Pollock, H. Harada, T.E. Howson, R.C. Reed, J.J. Schirra, S. Walston, eds., Seven Springs, PA, TMS, 2004, pp. 677-685.
[36] M. Kamaraj: *Sadhana*, 2003, 28, pp. 115-128.
[37] F.R.N. Nabarro: *Met. Trans. A*, 1996, 27, pp. 513-530.
[38] M.V. Nathal: *Met. Trans. A*, 1987, 18, pp. 1961-1970.
[39] T.P. Gabb, S.L. Draper, D.R. Hull, R.A. Mackay, M.V. Nathal: *Mat. Sci. Eng. A*, 1989, 118, pp. 59-69.
[40] A. Royer, P. Bastie, D. Bellet, J.L. Strudel: *Phil. Mag. A*, 1995, 72, pp. 669-689.
[41] Y. Koizumi, J.X. Zhang, T. Kobayashi, T. Yokokawa, H. Harada, Y. Aoki, M. Arai: *J. Jpn Inst. Met*, 2003, 67, pp. 468-471.
[42] M. Véron, Y. Bréchet, F. Louchet: *Acta Mater.*, 1996, 44, pp. 3633-3641.
[43] O. Paris, M. Fahrmann, E. Fahrmann, T.M. Pollock, P. Fratzl: *Acta Mater.*, 1997, 45, pp. 1085-1097.
[44] T.M. Pollock, A.S. Argon: *Acta Metall. Mater.*, 1994, 42, pp. 1859-1874.
[45] M. Fahrmann, W. Hermann, E. Fahrmann, A. Boegli, T.M. Pollock, H.G. Sockel: *Mat. Sci. Eng. A*, 1999, 260, pp. 212-221.
[46] A. Volek, F. Pyczak, R.F. Singer, H. Mughrabi: *Scr. Mater.*, 2005, 52, pp. 141-145.
[47] M.V. Nathal, R.A. Mackay: *Mat. Sci. Eng.*, 1987, 85, pp. 127-138.
[48] H. Mughrabi: *Mat. Sci. Tech.*, 2009, 25, pp. 191-204.
[49] F.R.N. Nabarro: in *Intl. Conf. Mat.*, Cape Town, South Africa, 1993, pp. 167-171.
[50] M. Probst-Hein, A. Dlouhy, G. Eggeler: *Acta Mater.*, 1999, 47, pp. 2497-2510.
[51] J. Zhang, T. Murakumo, Y. Koizumi, T. Kobayashi, H. Harada, S. Masaki, *Met. Trans. A*, 2002, 33, pp. 3741-3746.
[52] L. Rowland: *PhD Thesis*, University of Michigan, Ann Arbor, 2005.
[53] T.G. Langdon: *J. Mat. Sci.*, 2006, 41, pp. 597-609.
[54] Q. Feng, T.K. Nandy, S. Tin, T.M. Pollock: *Acta Mater.*, 2003, 51, pp. 269-284.

[55] S. Tin, L. Zhang, G. Brewster, M.K. Miller: *Met. Trans. A*, 2006, 37A, pp. 1389-1396.
[56] A. Sato, H. Harada, T. Yokokawa, T. Murakumo, Y. Koizumi, T. Kobayashi, H. Imai: *Scr. Mater.*, 2006, 54, pp. 1679-1684.
[57] F. Pyczak, B. Devrient, F.C. Neuner, H. Mughrabi: *Acta Mater.*, 2005, 53, pp. 3879-3891.
[58] C.M.F. Rae, R.C. Reed: *Acta Mater.*, 2001, 49, pp. 4113-4125.
[59] R. Darolia, D.F. Lahrman, R.D. Fields, R. Sisson: in *Superalloys 1988*, D.N. Duhl, G. Maurer, S. Antolovich, C. Lund, S. Reichman, eds., Seven Spring, PA, TMS, 1988, pp. 255-264.
[60] W.S. Walston, K.S. O'Hara, E.W. Ross, T.M. Pollock, W.H. Murphy: in *Superalloys 1996*, R.D. Kissinger, D.J. Deye, D.L. Anton, A.D. Cetel, M.V. Nathal, T.M. Pollock, D.A. Woodford, eds., Seven Springs, PA, TMS, pp. 27-34.
[61] N. Birks, G.H. Meier, F.S. Pettit: *Introduction to High Temperature Oxidation of Metals*, Cambridge University, UK, 2006.
[62] S. Bose: *High Temperature Coatings*, Butterworth-Heinemann, Burlington, MA, 2007.
[63] D.R. Coupland, I.R. McGill, C.W. Cortil: *J. Metals*, 1982, 35, pp. A76-A76.
[64] D.R. Coupland, C.W. Corti, G.L. Selman: in *Behavior of High Temperature Alloys in Aggressive Environments*, Petten, Netherlands, 1979, pp. 525-536.
[65] H. Murakami, T. Honma, Y. Koizumi, H. Harada: in *Superalloys 2000*, T.M. Pollock, R.D. Kissinger, R.R. Bowman, K.A. Green, M. McLean, S.L. Olson, J.J. Schirra eds., Seven Springs, PA, TMS, 2000, pp. 747-756.
[66] A.P. Ofori, C.J. Humphreys, S. Tin, C.N. Jones: in *Superalloys 2004*, K.A. Green, T.M. Pollock, H. Harada, T.E. Howson, R.C. Reed, J.J. Schirra, S. Walston, eds., Seven Springs, PA, TMS, 2004, pp. 787-794.
[67] T. Yokokawa, M. Osawa, K. Nishida, T. Kobayashi, Y. Koizumi, H. Harada: *Scr. Mater.*, 2003, 49, pp. 1041-1046.
[68] S. Hayashi, S.I. Ford, D.J. Young, D.J. Sordelet, M.F. Besser, B. Gleeson: *Acta Mater.*, 2005, 53, pp. 3319-3328.
[69] J.A. Haynes, B.A. Pint, Y. Zhang, I.G. Wright: in *34th International Conference on Metallurgical Coatings and Thin Films*, San Diego, CA, 2007, pp. 730-734.
[70] J.X. Zhang, J.C. Wang, H. Harada, Y. Koizumi: *Acta Mater.*, 2005, 53, pp. 4623-4633.
[71] S. Tin, A.C. Yeh, A.P. Ofori, R.C. Reed, S.S. Babu, M.K. Miller: in *Superalloys 2004*, K.A. Green, T.M. Pollock, H. Harada, T.E. Howson, R.C. Reed, J.J. Schirra, S. Walston, eds., Seven Springs, PA, TMS, 2004, pp. 735-741.
[72] T. Kobayashi, H. Harada, M. Osawa, A. Sato: *J. Jpn. Met.*, 2005, 69, pp. 1099-1103.
[73] G.L. Selman, R.J. Midgley, 1987, US Patent #4,683,119.
[74] D.R. Clarke, C.G. Levi: *Ann. Rev. Mat. Res.*, 2003, 33, pp. 383-417.
[75] B. Gleeson: *J. Prop. Pwr.*, 2006, 22, pp. 375-383.
[76] P.K. Wright, A.G. Evans: *Sol. St. Mat. Sci.*, 1999, 4, pp. 255-265.
[77] B.A. Pint, J.R. DiStefano, I.G. Wright: *Mat. Sci. Eng. A*, 2006, 415, pp. 255-263.
[78] B. Tryon, Q. Feng, R.G. Wellman, K.S. Murphy, J. Yang, C.G. Levi, J.R. Nicholls, T.M. Pollock: *Met. Trans. A*, 2006, 37A, pp. 3347-3358.

[79] M. Schutze: *Corrosion and Environmental Degradation, Vol II*, Wiley-VHC, London, 2000.
[80] Y. Minamino, H. Yoshida, S.B. Jung, K. Hirao, T. Yamane: in *DIMAT 96*, Trans Tech-Sci. Pub. Ltd., Nordkirchen, Germany, 1996, pp. 257-262.
[81] D. Pan, M.W. Chen, P.K. Wright, K.J. Hemker: *Acta Mater.*, 2003, 51, pp. 2205-2217.
[82] M.P. Taylor, H.E. Evans, E.P. Busso, Z.Q. Qian: *Acta Mater.*, 2006, 54, pp. 3241-3252.
[83] T. Izumi, N. Mu, L. Zhang, B. Gleeson: in *34th International Conference on Metallurgical Coatings and Thin Films*, San Diego, CA, 2007, pp. 628-631.
[84] J. Antony: *Design of Experiments for Scientists and Engineers*, Elsevier, Burlington, MA, 2003.
[85] R.C. Reed, T. Tao, N. Warnken: *Acta Mater.*, 2009, 57, pp. 5898-5913.
[86] F.C. Hull: *Metal Progress*, 1969, 96, p. 139.
[87] P. Caron, T. Khan: *Aero. Sci. Tech.*, 1999, 3, pp. 513-523.
[88] A.J. Elliott, S. Tin, W.T. King, S.C. Huang, M.F.X. Gigliotti, T.M. Pollock: *Met. Trans. A*, 2004, 35A, pp. 3221-3231.
[89] W. Boettinger, U. Kattner, K. Moon, J. Perepezko, *DTA and Heat-Flux DSC Measurements of Alloy Melting and Freezing*, NIST 960-15, Washington DC, 2006.
[90] R.T. Dehoff, F.N. Rhines: *Quantitative Microscopy*, McGraw-Hill, NY, 1968.
[91] M. Loretto: *Electron Beam Analysis of Materials*, Chapman and Hall, New York, 1984.
[92] D. Williams, C. Carter: *Transmission Electron Microscopy: Imaging*, Springer, New York, 1996.
[93] J.P. MacSleyne, J.P. Simmons, M. De Graef: *Acta Mater.*, 2008, 56, pp. 427-437.
[94] J.P. MacSleyne, J.P. Simmons, M. De Graef: *Mod. Sim. Mat. Sci.*, 2008, 16.
[95] M.V. Nathal, L.J. Ebert: *Met. Trans. A*, 1985, 16, pp. 1849-1862.
[96] F.J. Bois, L.G. Remy, J.C. Theret: in *SNECMA*, France, 1989.
[97] O.M. Barabash, R.I. Barabash, S.A. David, G.E. Ice: *Adv. Eng. Mat.*, 2006, 8, pp. 202-205.
[98] G.E. Fuchs: *Mat. Sci. Eng. A*, 2001, 300, pp. 52-60.
[99] K.S. O'Hara, E.W. Ross, R. Darolia: 1996, US Patent #5,482,789.
[100] R.C. Reed, A.C. Yeh, S. Tin, S.S. Babu, M.K. Miller: *Scr. Mater.*, 2004, 51, pp. 327-331.
[101] J. Zhu, W. Cao, Y. Yang, F. Zhang, S. Chen, W.A. Oates, Y.A. Chang: *Acta Mater.*, 2007, 55, pp. 4545-4551.
[102] J. Zhu, C. Zhang, W. Cao, Y. Yang, F. Zhang, S. Chen, D. Morgan, Y.A. Chang: *Acta Mater.*, 2009, 57, pp. 202-212.
[103] F. Pyczak, B. Devrient, H. Mughrabi: in *Superalloys 2004*, K.A. Green, T.M. Pollock, H. Harada, T.E. Howson, R.C. Reed, J.J. Schirra, S. Walston, eds., Seven Springs, PA, TMS, 2004, pp. 827-836.
[104] V. Raghavan: *J. Phase Eq.*, 2008, 29, p. 61.
[105] C.K. Sudbrack, D. Isheim, R.D. Noebe, N.S. Jacobson, D.N. Seidman: in *Microscopy and Microanalysis 2002 Meeting*, Quebec City, Canada, 2002, pp. 355-365.
[106] J. Popovic, P. Broz, J. Bursik: *Intermetallics*, 2008, 16, pp. 884-888.

[107] J. Tiley, G.B. Viswanathan, R. Srinivasan, R. Banerjee, D.M. Dimiduk, H.L. Fraser: *Acta Mater.*, 2009, 57, pp. 2538-2549.
[108] A.M. Ges, O. Fornaro, H.A. Palacio: *Mat. Sci. Eng. A*, 2007, 458, pp. 96-100.
[109] H.Y. Li, L.L. Zuo, X.P. Song, Y.L. Wang, G.L. Chen: *Rare Metals*, 2009, 28, pp. 197-201.
[110] A.J. Heidloff, J. Van Sluytman, T.M. Pollock, B. Gleeson: *Met. Trans. A*, 2009, 40A, pp. 1529-1540.
[111] F. Cao, B. Tryon, C.J. Torbet, T.M. Pollock: *Acta Mater.*, 2009, 57, pp. 3885-3894.
[112] M. Fahrmann, E. Fahrmann, T.M. Pollock, W.C. Johnson: *Met. Trans. A*, 1997, 28, pp. 1943-1945.
[113] J.S. Van Sluytman, A. Suzuki, A. Bolcavage, R.C. Helmink, D.L. Ballard, T.M. Pollock: in *Superalloys 2008*, R.C. Reed, K.A. Green, P. Caron, T.P. Gabb, M.G. Fahrmann, E.S. Huron, eds., Seven Springs, PA, TMS, 2008, pp. 499-508.
[114] A. J. Ardell: *Scr. Metal. Mater.*, 1990, 24, pp. 343-346.
[115] B. Roebuck, D. Cox, R. Reed: *Scr. Mater.*, 2001, 44, pp. 917-921.
[116] A. Royer, P. Bastie, M. Veron: *Acta Mater.*, 1998, 46, pp. 5357-5368.
[117] M.S.A. Karunaratne, P. Carter, R.C. Reed: *Mat. Sci. Eng. A*, 2000, 281, pp. 229-233.
[118] G.F. Hancock, B.R. McDonnel: *Phys. Stat. Sol.*, 1971, 4, pp. 143-150.
[119] J.K. Tien, S.M. Copley: *Met. Trans.*, 1971, 2, p. 543.
[120] C. Wagner: *Zeit. Elektrochemie*, 1961, 65, pp. 581-591.
[121] I.M. Lifshitz, V.V. Slyozov: *J. Phys. Chem.*, 1961, 19, pp. 35-50.
[122] C.K. Sudbrack, T.D. Ziebell, R.D. Noebe, D.N. Seidman: *Acta Mater.*, 2008, 56, pp. 448-463.
[123] J.L. Kamm, W.W. Milligan: *Scr. Metal. Mater.*, 1994, 31, pp. 1461-1464.
[124] R. Yu, P.Y. Hou: *App. Phys. Lett.*, 2007, 91.
[125] H. Harada: in *Computational Materials Design*, T. Saito, ed., Springer, 2001, pp. 39-67.
[126] T. Murakumo, T. Kobayashi, Y. Koizumi, H. Harada: *Acta Mater.*, 2004, 52, pp. 3737-3744.
[127] L.J. Carroll, Q. Feng, J.F. Mansfield, T.M. Pollock: *Met. Trans. A*, 2006, 37A, pp. 2927-2938.
[128] H. Harada, N. Sakuma, H. Koizumi, S. Nakazawa, I. Tomizuka, M. Yamazaki: *Tetsu-to-Hagane*, 1983, 69, p. S615.
[129] L. Ajdelsztajn, D. Hulbert, A. Mukherjee, J.M. Schoenung: *Surf. Coat. Tech.*, 2007, 201, pp. 9462-9467.
[130] M.F. Ashby, S.D. Hallam: *Acta Metal.*, 1986, 34, pp. 497-510.
[131] S. Tin, L. Zhang, A.P. Ofori, M.K. Miller: in *Beijing International Materials Week*, S. Long, F.H. Pan, K.U. Kainer, Y.F. Han, W. Ke, B. Liu, X.M. Zhang, C.Q. Peng, X.Q. Zhao, Q. Feng, Y.F. Lu, P.X. Zhang, C.B. Jiang, eds., Beijing, PEOPLES R CHINA, 2006, pp. 1187-1194.
[132] J.S. Van Sluytman, A. La Fontaine, J.M. Cairney, T.M. Pollock: *Acta Mater.*, 2010, 58, pp. 1952-1962.
[133] R. Srinivasan, G.F. Eggeler, M.J. Mills: *Acta Mater.*, 2000, 48, pp. 4867-4878.
[134] A. Ma, D. Dye, R.C. Reed: *Acta Mater.*, 2008, 56, pp. 1657-1670.

[135] T. M. Pollock, A.S. Argon: *Acta Metall. Mater.*, 1992, 40, pp. 1-30.
[136] R.E. Stoller, S.J. Zinkle: *J. Nuc. Mater.*, 2000, 283-287, pp. 349-352.
[137] G.I. Taylor: *J. Inst. Met.*, 1938, 62, pp. 307-324.
[138] T.E. Howson, D.A. Mervyn, J.K. Tien: *Met. Trans. A*, 1980, 11, pp. 1609-1616.
[139] S.V. Raj, S.C. Farmer: *Met. Trans. A*, 1995, 26, pp. 343-356.
[140] F.A. Mohamed, T.G. Langdon: *Met. Trans. A*, 1975, 6, pp. 927-928.
[141] M.V. Nathal, J.O. Diaz, R.V. Miner: in *High Temperature Ordered Intermetallic Alloys III, vol 133*, C.T. Liu, A.I. Taub, N.S. Stoloff, C.C. Koch, eds., 1989, pp. 269-274.
[142] W. Rosenhain, D. Ewen: J. Inst. Met., 1913, 10, pp. 119-149.
[143] W. Rosenhain, D. Ewen: J. Inst. Met., 1912, 8, pp. 149-180.
[144] C.M.F. Rae, M.S.A. Karunaratne, C.J. Small, R.W. Broomfield, C.N. Jones, R.C. Reed: in *Superalloys 2000*, T.M. Pollock, R.D. Kissinger, R.R. Bowman, K.A. Green, M. McLean, S.L. Olson, J.J. Schirra, eds., Seven Springs, PA, TMS, 2000, pp. 767-776.
[145] F.T. Furillo, J.M. Davidson, J.K. Tien, L.A. Jackman: *Mat. Sci. Eng.*, 1979, 39, pp. 267-273.
[146] R.F. Decker, J.W. Freeman: *Trans. AIMM*, 1960, 218, pp. 277-285.
[147] B.H. Kear, B.J. Piearcey: *Trans. AIMM*, 1967, 239, p. 1209.
[148] T.J. Garosshen, T.D. Tillman, G.P. McCarthy: *Met. Trans. A*, 1987, 18, pp. 69-77.
[149] X. Wu, A. Koul: *Met. Trans. A*, 1995, 26, pp. 905-914.
[150] R.F. Decker: *Met. Trans.*, 1973, 4, pp. 2495-2518.
[151] J. Friedel: *Dislocations*, Pergamon Press, Reading, MA, Oxford, 1964, p. 491.
[152] J.P. Hirth, J. Lothe: *Theory of Dislocations, 2nd Ed.*, John Wiley and Sons, New York, 1982.
[153] D. Gan: *J. Mat. Sci.*, 1982, 17, pp. 89-99.
[154] S. Ojediran, O. Ajaja: *J. Mat. Sci.*, 1988, 23, pp. 4037-4040.
[155] R.A. Mackay, L.J. Ebert: in *Superalloys 1984*, M. Gell, C.S. Kortovich, R.H. Bricknell, W.B. Kent, J.F. Radavich, eds., Seven Springs, PA, TMS, 1984, pp. 127-136.
[156] G. Eggeler, A. Dlouhy: *Acta Mater.*, 1997, 45, pp. 4251-4262.
[157] P.M. Sarosi, R. Srinivasan, G.F. Eggeler, M.V. Nathal, M.J. Mills: *Acta Mater.*, 2007, 55, pp. 2509-2518.
[158] F. Louchet, M. Ignat: *Acta Metal.*, 1986, 34, pp. 1681-1685.
[159] T. Link, A. Epishin, M. Klaus, U. Bruckner, A. Reznicek: *Mat. Sci. Eng. A*, 2005, 405, pp. 254-265.
[160] J.X. Zhang, H. Harada, Y. Koizumi: *J. Mat. Res.*, 2006, 21, pp. 647-654.
[161] J.Y. Buffiere, M. Ignat: *Acta Metal. Mater.*, 1995, 43, pp. 1791-1797.
[162] J.A. del Valle, A.C. Picasso, R. Romero: *Acta Mater.*, 1998, 46, pp. 1981-1988.
[163] F.R.N. Nabarro, H.L. de Villiers, *The Physics of Creep*, Taylor & Francis Inc., Bristol, PA, 1995, p. 1-403.
[164] U. Tetzlaff, H. Mughrabi: in *Superalloys 2000*, T.M. Pollock, R.D. Kissinger, R.R. Bowman, K.A. Green, M. McLean, S.L. Olson, J.J. Schirra, eds., Seven Springs, PA, TMS, 2000, pp. 273-282.
[165] M.V. Acharya, G.E. Fuchs: *Scr. Mater.*, 2006, 54, pp. 61-64.
[166] N. Baluc, H.P. Karnthaler, M.J. Mills: *Phil. Mag. A*, 1991, 64, pp. 137-150.
[167] N. Baluc, R. Schaoublin, K.J. Hemker: *Phil. Mag. Lett.*, 1991, 64, pp. 327 - 334.
[168] M. Vittori, A. Mignone: *Mat. Sci. Eng.*, 1985, 74, pp. 29-37.

[169] P. Caron: in *Superalloys 2000*, T.M. Pollock, R.D. Kissinger, R.R. Bowman, K.A. Green, M. McLean, S.L. Olson, J.J. Schirra, eds., Seven Springs, PA, TMS, 2000, pp. 737-746.
[170] W. Schroeder, D.A. Webster: *J. App. Mech.*, 1949, 16, pp. 289-294.
[171] M. McLean, B.F. Dyson: *J. Eng. Mat. Tech.*, 2000, 122, pp. 273-278.